Università degli Studi di Parma
Facoltà di Ingegneria

Dottorato di Ricerca in Ingegneria Civile – XX Ciclo
Curriculum: Strade, Ferrovie ed Aeroporti (ICAR/04)

Elena Romeo

Measurement and Prediction of Fundamental Tensile Failure Limits of Hot Mix Asphalt (HMA)

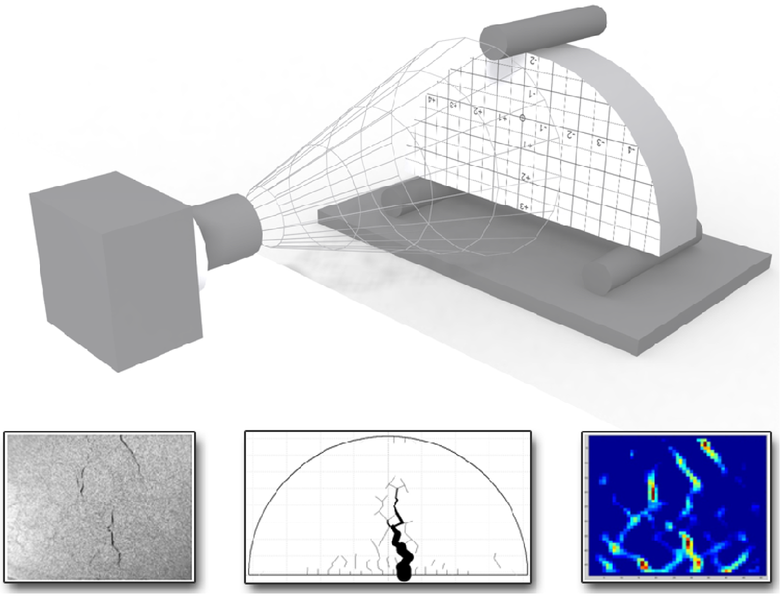

Dissertazione per il conseguimento del titolo di Dottore di Ricerca

Tutori: Prof. Ing. Antonio Montepara, Prof. Björn Birgisson
Coordinatore del Dottorato: Prof. Ing. Paolo Mignosa

Parma, Gennaio 2008

Università degli Studi di Parma
Facoltà di Ingegneria

Dottorato di Ricerca in Ingegneria Civile
Curriculum: Strade, Ferrovie ed Aeroporti (ICAR/04)
(XX Ciclo)

Elena Romeo

Measurement and Prediction of Fundamental Tensile Failure Limits of Hot Mix Asphalt (HMA)

Dissertazione per il conseguimento del titolo di Dottore di Ricerca

Tutori: Prof. Ing. Antonio Montepara, Prof. Björn Birgisson
Coordinatore del Dottorato: Prof. Ing. Paolo Mignosa

Parma, Gennaio 2008

ACKNOWLEDGMENTS

It is a great pleasure for me to thank and acknowledge those individuals who were involved in the advancement of this research, helping me with their assistance, support, suggestions and comments, or just by listening to my ideas.

First of all, my sincere thanks and deep appreciation go to my “national” advisor, Professor Antonio Montepara, for his unfailing support and guidance during my doctoral program and for having offered me the wonderful opportunity to be schooled at such a prestigious University, as the University of Florida. I owe enormous gratitude to my “international” advisor, Professor Bjorn Birgisson, who has been a continuous source of knowledge, encouragement and guidance in both academic and non-academic life and who taught me how to think critically, develop research skills and write scientific papers.

I am deeply thankful to Professor Reynaldo Roque for the generous contribution of his discussion and thinking to this work; his insightful comments and constructive criticisms led my research to a successful achievement. I am grateful to Dr. Gabriele Tebaldi who spent much of his time on supporting and helping me to solve the many problems I faced from time to time.

My sincerest thanks go to Professor Gianfranco Forlani and Dr. Riccardo Roncella for their assistance and valuable contributions in developing the DIC system and for their true friendship. Many thanks and appreciation go to Mr. George Lopp for his time, expertise and patience in teaching me all the laboratory testing procedures. Special thanks go to Dr. John A.L. Napier, who let us use his boundary element code.

I would like to take this opportunity to acknowledge the Association of Asphalt Pavement Technologists (AAPT) for the scholarship they awarded me, which supported part of my travel expenses for going back and forward from Parma to Gainesville.

I would like to thank all those members of the Department of Civil Engineering at the University of Parma who have made me feel “part of the team”.

A very special acknowledgement is sent to all the “GNV’s Italian Buddies”, and everyone in the Materials Group at the University of Florida whose friendship and help made my experience there something I will always remember.

Last but not least, my eternal thanks go to my parents, my brother and Riccardo for their love, encouragement and constant advice throughout my academic life, especially away from home.

To my father, who has always been a role model,
instilling me his passion for the research since I was child.
Thanks Daddy!

You could cover the whole earth with asphalt,
but sooner or later green grass would break through.
Ilya Ehrenburg

Science is the attempt to make the chaotic diversity of our sense experience
correspond to a logically uniform system of thought.
Albert Einstein

Dubium sapientiae initium
Cartesio

TABLE OF CONTENTS

APPENDICES

CHAPTER 1

Literature Review

The primary purpose of this section is to summarize theoretical background and experimental confirmations that have supplied the motivations for this research. Current understanding of cracking mechanism and damage criteria in the area of design and evaluation of flexible pavement were examined.

1.1 Crack Initiation and Propagation

Observation of crack initiation and propagation in asphalt mixture indicates that cracks may start as microcracks that later propagate, densify and coalesce to from macrocracks as the mixture is subjected to tensile stresses, shear stresses or a combination of both. An improved understanding of the mechanism of cracking would lead to improved mixture tests, materials and pavement models to predict the field performance of asphalt mixtures more reliably. Recognizing that both crack initiation and propagation processes are directly related to stress-strain fields in asphalt layers, researchers recently have focused on developing constitutive relationships that can describe the cracking response of asphalt mixtures under realistic traffic conditions composed of multiple load levels and random rest periods.

The cracking mechanism of asphalt pavements have been studied since the early 70s when several researchers began to apply fracture mechanics to analyze the fatigue behavior in asphalt materials (Majidzadeh et al. 1971; Schapery, 1973). Unfortunately, the complexity of crack propagation in HMA mixtures has been an obstacle to the incorporation of fracture mechanics-based approaches in the bituminous pavement area.

In recent years, it was found that asphalt mixture's cracking mechanism can be simulated using nonlinear models with an appropriate constitutive law for the damaged material in the fracture process zone (FPZ), identified as a strongly nonlinear region ahead of the crack tip where intense damage and microcrack coalescence occur (Figure 1.1 Wagoner and Buttlar, 2007). Specifically, the FPZ ahead of the crack tip has complex phenomena where aggregates can slide along the crack face, bridge the crack face, and the asphalt binder can yield under high strain (Wagoner & Buttlar, 2007). This approach, named Cohesive Crack Model (CCM), introduced the concept of a nonlinear fracture model appropriate for quasi-brittle materials (concrete, asphalt concrete, ceramics, etc.).

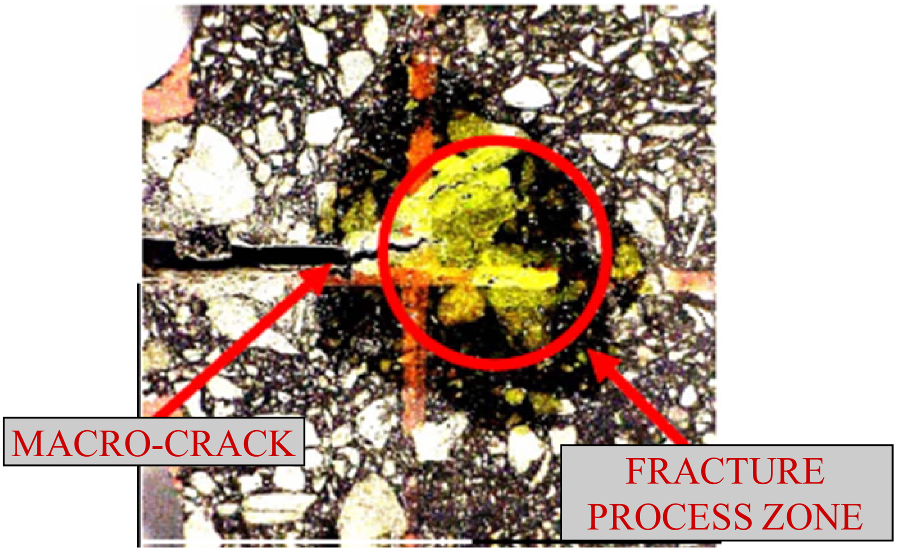

Figure 1.1: Fracture process zone in asphalt mixtures (Wagoner and Buttlar, 2007)

A further pavement cracking model entitled "HMA Fracture Mechanics" was recently developed at the University of Florida by Zhang et al. (2001) and Roque et al. (2002) observing that crack in HMA grows in a stepwise rather than a continuous manner. Central to this framework is the concept of the existence of a fundamental crack growth threshold as the key element in defining the cracking mechanism and fracture resistance of asphalt mixtures.

1.2 Conventional Fracture Mechanics

The science of fracture mechanics was firstly introduced in the 1920s by Griffith to describe the propagation of cracks through materials. Griffith invoked the first law of thermodynamics to formulate a fracture theory based on a simple energy balance: the crack will increase in size if sufficient potential energy is greater than the surface energy of the material.

Since then, fracture mechanics concepts were adopted by several researchers to quantify fracture resistance of asphalt mixtures developing fracture mechanics-based models to predict crack growth in materials.

1.2.1 Linear Elastic Fracture Mechanics (LEFM)

The Linear Elastic Fracture Mechanics (LEFM) presumes that in a material there are intrinsic flaws from which, at critical conditions, a crack initiates and propagates continuously. The most common parameter used in LEFM is the stress intensity factor K, which characterizes the stress distribution in the vicinity of a macro-crack.

Crack growth rate of linear-elastic materials is generally assumed to follow Paris law (Paris and Erdogan, 1963), in which:

$$\frac{da}{dN} = A\left(\Delta K\right)^n \qquad [1.1]$$

where a is the crack length, N is the number of repeated loads, K is the stress intensity factor, A and n are material parameters determined from fitting fatigue test data.

ΔK is the range in stress intensity factor and K_{th} represents a material related threshold, below which no fatigue is assumed to occur (Figure 1.2). Fracture toughness K_c represents the resistance of the material to failure from fracture and is considered an intrinsic material constant.

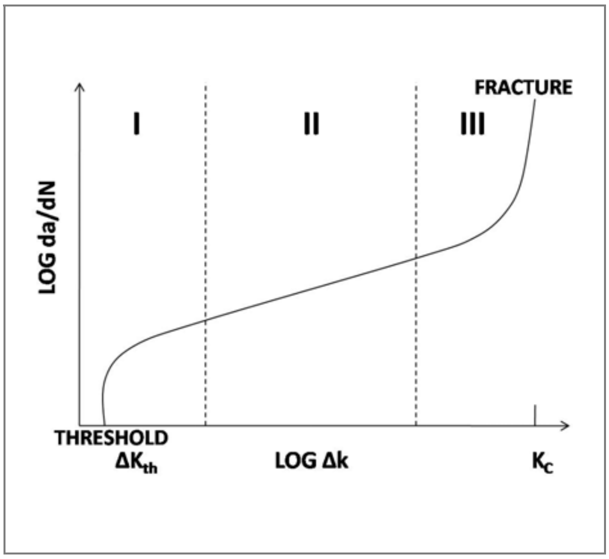

Figure 1.2: Typical Fatigue Crack Growth Behavior

The sigmoidal curve contains three distinct regions: in region I, da/dN approaches zero at the threshold ΔK_{th}; in region II, the crack growth rate deviates from the linear trend at high and low ΔK levels; in region III, the crack growth rate accelerates as K_{max} approaches K_{crit}, the fracture toughness of the material (Anderson, 1995).

Lately, several researchers have developed equations that modeled all or part of the sigmoidal da/dN-ΔK relationship (Foreman, 1967; Weertman, 1966; Klesnil and Lukas, 1972; McEvily, 1988).

As Paris law became widely used for prediction of fatigue crack growth, it was realized that this simple expression was not universally applicable. Therefore, further research work led to insight into crack performance. For example, in 1970, Elber proposed a modified Paris law:

$$\frac{da}{dN} = C\Delta K_{eff}^{m} \qquad [1.2]$$

where ΔK_{eff} is the effective stress intensity range, defined as K_{max}-K_{op}, where K_{op} is the stress intensity factor at which the crack opens.

Recently, Roque et al. (1999) investigated the possibility of developing a fracture method to indirectly measure crack growth rates (A and n) in the laboratory. Using the linear elastic finite element method to simulate specimens under Indirect Tensile Test (IDT) condition at different crack length series, they found a relationship between the theoretical length and the deformation between two gauge points located across the crack line. The theoretical crack length allowed them to monitor the crack growth corresponding to the increment of cycling loading. This method was further investigated by Zhang et al. (2001) by comparing crack growth rates measured in the lab from 4 Superpave mixtures with field performance. They found that laboratory crack growth rates did not correlate with the observed field cracking performance and did not agree with expected trends for the Superpave mixtures. They concluded that Paris law does not incorporate all aspects involved in the mechanism of cracking of asphalt mixtures subjected to generalized loading conditions, such as those encountered in the field.

1.2.2 Non Linear Fracture Mechanics (NLFM)

The Non-Linear Fracture Mechanics (NLFM) theory allows to extend fracture mechanics methodology beyond the validity limits of LEFM.

The most common parameter for characterizing non-linear materials is the J integral, firstly introduced by Rice (1968). The J integral has physical meaning for both non-linear elastic and elastic-plastic behaviors, and can be used as an energy parameter as well as a stress intensity parameter (Anderson, 1995):

$$J = \int_{\Gamma} \left(Wdy - \sigma_{ij} n_j \frac{\partial u_i}{\partial x} ds \right) \qquad [1.3]$$

where W is the strain energy density, Γ is any boundary around the crack and ds is a length increment along the boundary. Several studies based on J-integral theory have been conducted to characterize fracture resistance, low temperature properties and fatigue properties of asphalt mixtures (Abdulshafi & Majidzadeh, 1985; Little et al., 1987; Button et al., 1987; Sulaiman & Stock, 1995; Mull et al., 2002).

A more mechanics-based model was developed by Ramsamooj (1980). He used the nonlinear differential equation governing subcritical growth of a crack embedded in an elastic-plastic matrix up to the point of gross instability derived by Wnuk (1971), to formulate a fatigue crack growth model for a beam on elastic foundation:

$$\frac{da}{dN} = \frac{\pi}{24 K_{IC}^2 \sigma_t^2} \left(\Delta K_I^4 - K_0^4 \right) \qquad [1.4]$$

where:

σ_t = yield stress in flexural tension;

K_I = stress intensity at service load;

K_0 = value of stress intensity at endurance limit.

Ramsamooj (1991) then again used the same nonlinear differential equation with an estimated value of plastic zone for asphalt concrete $\Delta = 0.125(K_I/\sigma_t)^2$ to formulate a general expression for fatigue behavior of asphalt concrete under any configuration of loading and boundary conditions.

A further approach is the viscoelatic fracture mechanics theory developed by Schapery (1973). This approach evaluates fatigue crack growth in homogeneous linear viscoelastic materials by estimating the parameters A and n (equation [1.1]) from mechanical, chemical and thermodynamics characteristics , such as creep compliance, tensile strength and adhesive and cohesive surface energy density. According to Schapery's theory, the parameters A and n are given as follows:

$$A = \frac{\pi}{6\sigma_m^2 I_1^2}\left(\frac{\left(1-\nu^2\right)D_2}{2\Gamma}\right)^{\frac{1}{m}}\left(\int_0^{\Delta t} w(t)^n\,dt\right) \qquad [1.5]$$

$$n = 2\left(1+\frac{1}{m}\right) \qquad \text{for force controlled tests}$$

$$n = \frac{2}{m} \qquad \text{for displacement controlled tests}$$

where:

σ_m = tensile strength;

I_1 = result of the integration of stress near the crack tip over a small region ahead of the crack tip known as the failure zone;

ν = Poisson's ratio;

D_2 = compliance at t = 1s;

m = slope of the creep compliance curve (log-log scale);

Γ = energy needed to produce a unit surface of fracture;

w(t) = wave shape of stress intensity factor;

Δt = the period of loading to complete one cycle of loading.

1.2.3 Application of Conventional Fracture Mechanics

Since the fracture mechanics approach has been well accepted for analyzing crack growth in materials, many researchers have adopted the concepts and applied them to the field of pavements.

Jacobs (1995 and 1996) used fracture mechanics principles to characterize fracture toughness and construct master curves. He conducted uniaxial static testing on double edge notched specimen (50x50x150mm) to obtain maximum tensile strength (σ_m) and fracture energy (Γ). He also conducted fatigue tests of the double edge notched specimen to determine material parameters A and n. According to this research, he concluded that theoretical derivations for A and n for viscoelastic materials by Schapery (1973, 1975, 1978) appeared to be valid.

Ramsamooj (1993) modified an analytical solution for a thin plate resting on elastic foundation by including 3 cracking conditions: crack through in transverse direction, crack through in longitudinal direction and semi elliptical crack at the bottom of the plate. The equations can be used to evaluate stress intensity factor ahead of the crack tip for those three types of cracking in pavement.

Collop and Cebon (1995) investigated the causes of cracking on the top and bottom layer of an asphalt concrete pavement. According to their findings, the surface cracking was caused by transverse shear stress of a radial tire and perhaps combined with the presence of stiffness gradients due to aging and thermal effects. They also formulated an analytical solution for determining stress intensity factor for a surface crack in a semi-infinite plate subjected to a general remote stress. They also derived a formula based on parametric studies to quantify the stress intensity factor due to traffic and thermal loading for various pavement structures at progressive crack growth in pavement.

Myers (2000) and Myers et al. and (2001) also investigated the mechanism of surface initiated cracking along the wheel path but they used measured tire contact stresses instead of the traditionally assumed circular load. According to their findings, the surface cracking was caused by transverse shear stress of a radial tire and perhaps combined with thermal stress due to rapid cooling. Then they used a fracture mechanics approach with the finite element software ABAQUS® to study propagation of top-down cracking. By assuming cracks propagate perpendicular to the major principal (tensile) stress, they found the cracks grew down vertically in the pavement and the bent 30 degrees toward the wheel load. The predicted crack path was found similar to what has been observed in the field. They also performed parametric studies to quantify the stress intensity factor ahead of the crack tip for various load positions, stiffness ratios and thickness ratios for progressive crack growth in a flexible pavement.

1.2.4 Cohesive Crack Model

The Cohesive Crack Model (CCM) is a simple model that used to describe a nonlinear fracture process at the front of a pre-existing crack. This model was firstly introduced by Dugdale (1960) and Barenblatt (1962) to account for a relatively large plastic yield zone ahead of a crack tip. Hillerborg et al. (1976) extended this model to concrete fracture and described a fairly large FPZ. According to this model, the material can be characterized by a couple of constitutive laws: a stress–strain relationship, valid for the undamaged material, and a stress–crack opening displacement relationship, the so-called cohesive law (Figure 1.3).

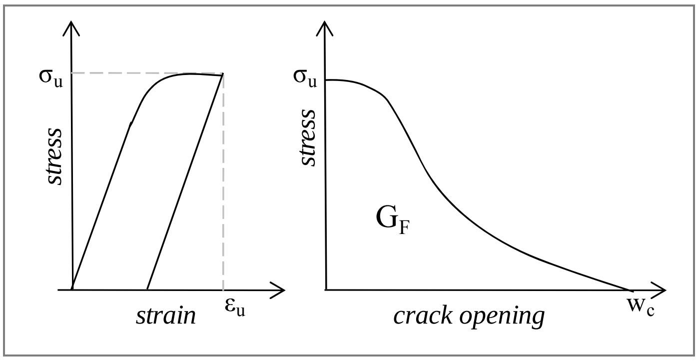

Figure 1.3 Cohesive Crack Model. Left: elastic stress-strain curve. Right: cohesive stress-crack opening displacement law

This law describes how the stress decreases from its maximum value to zero as the distance between the crack lips increases from zero to the critical displacement w_c. The area below the stress–crack opening displacement curve represents the energy spent to create the unit crack surface (Fracture Energy G_F). If the two portions into which the specimen is separated undergo elastic unloading, the work done to split the specimen can be considered to be exactly equal to the product of G_F times the cracked area.

The fracture energy G_F can be obtained from:

$$G_F = \int_0^{\infty} \sigma dw = \int_0^{\infty} f(w) dw \qquad [1.6]$$

According to Hillerborg's work, the cohesive crack model is able to explain different size effects encountered in concrete structures. More in detail, the model is able to simulate tests where high stress gradients are present, i.e. tests on pre-notched specimens. In these cases, the cohesive crack model captures the ductile–brittle transition occurring by increasing the size of the structure. On the other hand, relevant scale effects are encountered also in uniaxial tension tests on dog-bone shaped specimens, where much smaller stress gradients are present. In this case, size effects should be inherent to the material behavior rather than to the stress intensification.

Works conducted by Carpinteri & Ferro (1994, 1998) and Mier & Vliet (1999) proved that the physical parameters characterizing the cohesive law are scale dependent, thus showing the limits of Hillerborg's model. In fact, by increasing the size of the specimen, the ultimate stress decreases while the fracture energy increases.

The CCM has been applied extensively to Portland cement concrete and has only recently been investigated for asphalt mixture. Jenq et al. (1991) used both indirect tensile tests and notched beams to assess the tensile strength and fracture energy of asphalt mixes. Seo et al. (2004) determined the cohesive model parameters using constant crosshead rate monotonic tension tests using double-edge notched specimens. They calculated the fracture energy using the crack opening displacement within the FPZ indentified as a 5 mm high band between notches.

Following are the basic hypotheses of the CCM:

- A crack is assumed to form at a point when the maximum principal stress at that point reaches the tensile strength. The crack forms perpendicular to the maximum principal stress direction (i.e., crack initiation and propagation criteria).
- The properties of the material outside the process zone are governed by the undamaged state.
- The stress transferred between the faces of the crack is described by a post-peak function (i.e., softening function).

1.3 Continuum Damage Approach

The Continuum Damage approach analyzes microcracks in asphalt mixtures under realistic loading conditions and healing effect. A research conducted by Kim et al. (1990) has shown that continuous cycles of loading at a constant strain or stress amplitude, which are generally applied in laboratory test, differ to the realistic field loading conditions. The major cause is attributed to the rest period between loading applications, which in the field occurs with random length. It was observed (Kim et al., 1990) that in a partially cracked asphalt pavement, two different mechanisms occur during rest periods: the relaxation of stresses in the system due to the viscoelastic nature of asphalt concrete and the chemical healing across microcrak and macrocrak faces.

A mechanics approach to fatigue characterization of asphalt mixture using viscoelasticity and continuum damage theory was introduced by Kim Y.R. et al. (1997). They modeled damage accumulation (assumed to grow continuously under uniaxial tensile cyclic loading), and microdamage healing during rest periods using the visco-elastic correspondence principle developed by Schapery (1984). Schapery stated that constitutive equations for certain viscoelastic media are identical to those for the elastic cases, but stresses and strains are not necessarily physical quantities in the viscoelastic body; instead they are pseudo variables (e.g. pseudo-stress, pseudo-strain). According to Schapery's theory, the pseudo-strain is defined as:

$$\varepsilon^R = \frac{1}{E_R}\int_0^t E(t-\tau)\frac{d\varepsilon}{d\tau}d\tau \qquad [1.7]$$

where:

ε_R = pseudo-strain;

ε = time-dependent strain;

E_R = reference modulus (arbitrary constant);

$E(t)$ = relaxation modulus at time t.

If there is no damage contributed in the loading response, the stress-pseudo strain relationship can be represented by an elastic-like equation:

$$\sigma = E_R\varepsilon^R \qquad [1.8]$$

When the material experiences significant damage due to higher tensile loading the stress-pseudo strain relationship is represented by a nonlinear response with a hysteresis loop. Damage accumulation can be demonstrated by observing changes in the loop area and loop secant slope during fatigue tests.

Based on the relationship between the pseudo strain and physical stress, Kim et al. (1994, 1995) introduced the pseudo stiffness parameter (S^R) to characterize the change in slope of each σ-ε^R cycle and give a quantitative measure of microdamage:

$$S^R = \frac{\sigma_m}{\varepsilon_m^R} \qquad [1.9]$$

where ε_m^R is peak pseudo strain in each stress-pseudo strain cycle, and σ_m is the stress corresponding to ε_m^R. The pseudo stiffness decreases as repeated loading continues. The material is considered to fail when the stiffness is reduced to 50% its original value (Kim Y.R. et at., 1997).

Based on experimental data of asphalt concrete subjected to continuous and uniaxial loading in tension, Lee and Kim (1998a) proposed a constitutive model that describes the mechanical behavior of the material under these conditions:

$$\sigma = I\left(\varepsilon_e^R\right)\left[F + G\right] \qquad [1.10]$$

where:

I = initial pseudo stiffness;

ε = effective pseudo strain;

F = damage function;

G = hysteresis function.

The effective pseudo strain accounts for the accumulating pseudo strain in a controlled stress mode. A mode factor is also applied to the damage function, F, to allow a single expression for both modes of loading. The parameter I is used to account for specimens variability. The damage function F represents the change in slope of the stress-pseudo strain loop as damage accumulates in the specimen. The hysteresis function G describes the difference in the loading and unloading paths.

Lee and Kim (1998b) also proposed a model to describe the fatigue life for controlled-strain testing mode, finding that in these conditions, the hysteresis function G is not to be taken in account:

$$\sigma = I\left(\varepsilon_e^R\right)\left[CS\right] \qquad [1.11]$$

where:

C = coefficient of secant pseudo stiffness reduction;

S = internal state variable.

The disadvantage of the continuum damage method is the requirement of numerous functions such as relaxation modulus to determine pseudo strain, as well as the F and G functions to describe the damage process. In addition, given the fact that only a continuum can be modeled, continuum damage mechanics is incapable of properly addressing the mechanics of crack propagation (i.e., once a crack develops, the system is no longer a continuum). Finally, damage mechanics does not provide a realistic physical interpretation of damage, since failure is generally assumed to coincide with a 50-percent reduction in pseudo-stiffness, which is not applicable to the field, as a failure criterion.

1.4 HMA Fracture Mechanics

Previous work by Zhang et al. (2001) and Roque et al. (2002) has shown that the fracture properties of mixtures can be described within a viscoelastic fracture mechanics-based framework, entitled "HMA Fracture Mechanics", recently developed at the University of Florida. They observed that a crack in HMA grows in a stepwise rather than in a continuous manner, as shown in Figure 1.4.

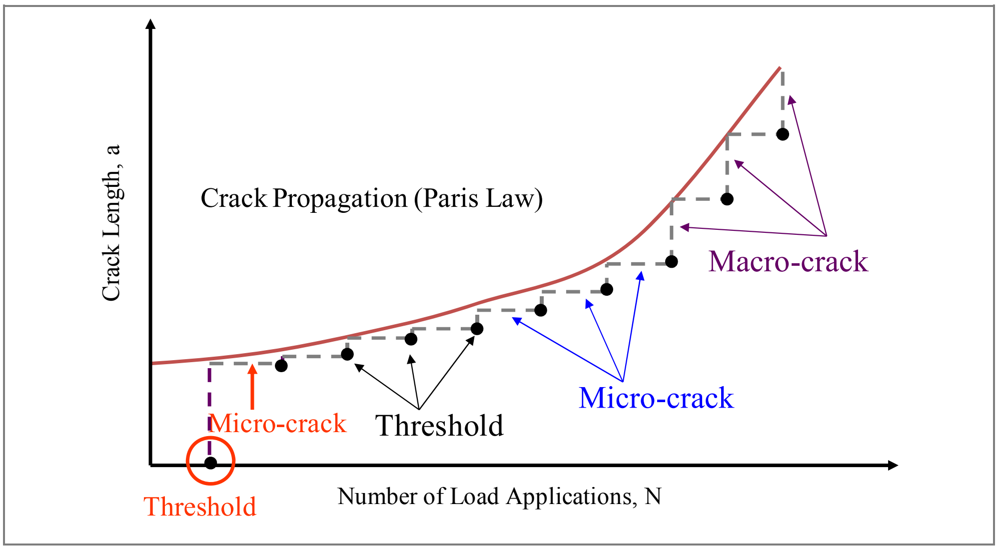

Figure 1.4 Crack propagation in Asphalt Mixtures according to "HMA Fracture Mechanics"

The implication with this work is that it may not be sufficient to monitor changes in a single parameter such as strength or stiffness to evaluate the effects of micro- and macro-damage in mixtures. Rather, changes in stiffness and strength are typically accommodated by changes in the viscoelastic properties of mixtures, as well as strength and stiffness.

The topic of the framework presented by Zhang et al (2001) is the concept of the existence of a fundamental crack growth threshold. The concept is based on the observation that micro-damage (i.e., damage not associated with crack initiation or crack growth) appears to be fully healable, while macro-damage (i.e., damage associated with crack initiation or growth) does not appear to be healable. This indicates that a damage threshold exists below which damage is fully healable. Therefore, the threshold defines the development of macro-cracks, at any time during either crack initiation or propagation, at any point in the mixture. If loading and healing conditions are such that the induced energy does not exceed the mixture threshold, then the mixture may never crack, regardless of the number of loads applied.

As discussed by Roque et al. (2002), fracture (crack initiation or crack growth) can develop in asphalt mixtures in two distinct ways, defined by two distinct thresholds (Figure 1.5). The lower threshold is associated with continuous repeated loading. When cyclic stresses significantly below the tensile strength occur, cracking will eventually occur if the rate of damage accumulation exceeds the rate of healing during the loading period. In contrast, the upper energy threshold corresponds to that threshold required to fracture the mixture with a single load application. In this case, fracture would occur if any single load applied during the loading cycle exceeds the threshold required to fracture the mixture with a single load application. Essentially, fracture would not occur during a single load application unless the upper threshold is exceeded, even when the lower threshold is exceeded.

It has been determined that the dissipated creep strain energy (DCSE) limit and the fracture energy (FE) limit of asphalt mixtures suitably define the lower and the upper threshold values. These parameters can be easily determined from the stress-strain response of an Indirect Tensile strength Test (IDT), as shown in Figure 1.6 and discussed by Roque et al. (2002). The fracture energy limit is determined as the area under the stress-strain curve at first fracture, while the dissipated creep strain energy limit is the fracture energy minus the elastic energy. First fracture in the IDT specimen is determined by plotting the deformation differential (V - H), and visually observing the point at which the deformation differential starts to deviate from a smooth curve.

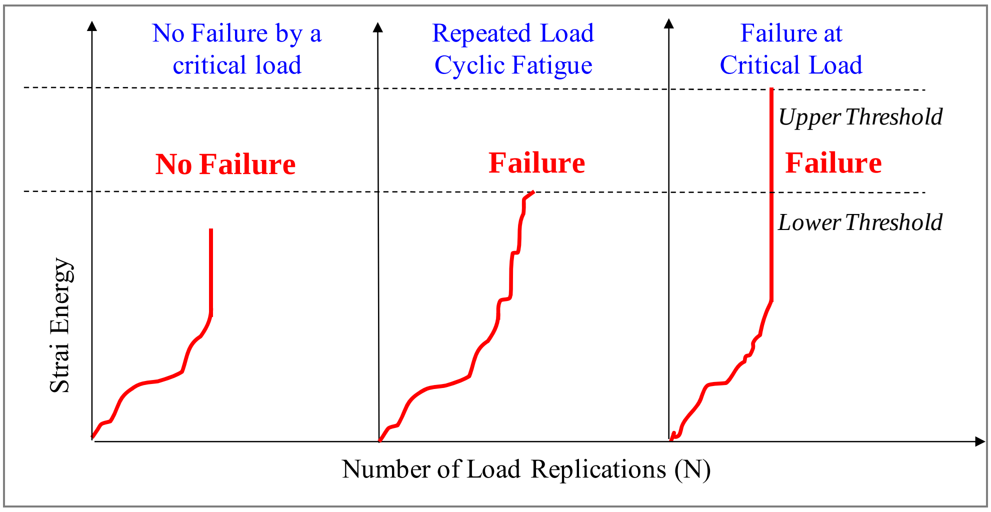

Figure 1.5 Crack initiation or crack growth development in asphalt mixtures

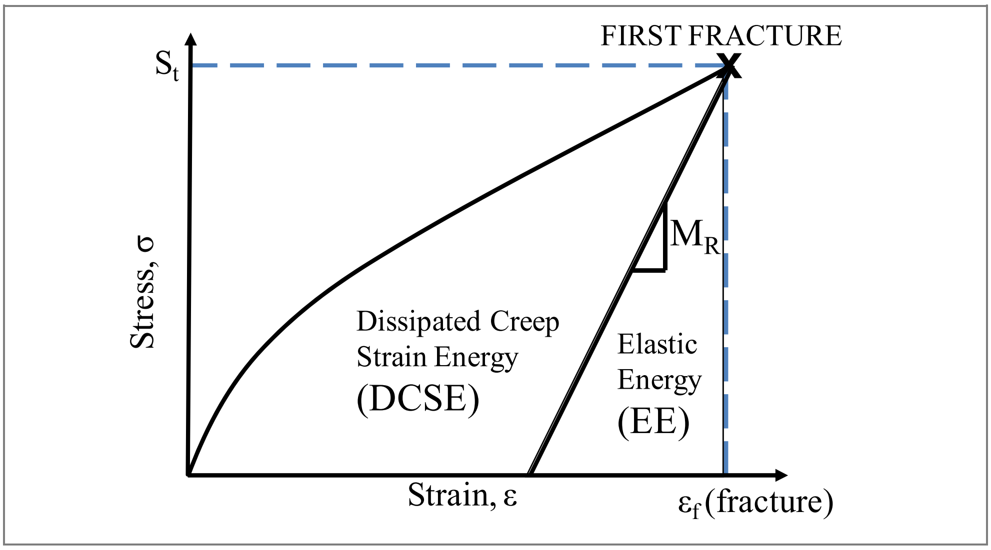

Figure 1.6 Determination of the lower and upper thresholds for asphalt mixtures

1.5 Tensile Failure Limits of HMA Mixes

The critical location for load-induced cracking is generally considered to be at the bottom of the asphalt mixture layer, where the stress state is longitudinal. Cracks are initiated at the bottom of this layer and later propagate due to the repeated stressing in tension caused by bending beneath the wheel loads.

HMA failure limits are needed to determine whether the induced pavement response is critical enough to result in failure under one or more load applications. Several testing modes can generally be used to obtain these properties, but if the property is not fundamental, then different testing modes may yield different results. Fundamental properties of asphalt mixture can be obtained from multiple testing configurations when appropriate test procedures, measurement systems and analytical methods are used.

1.5.1 Tensile Strength

Tensile strength is one of the critical parameter to be always taken into consideration for HMA performance evaluation. Several laboratory testing methods have been proposed and used to evaluate mixture's tensile strength, which is usually calculated from the overall response of a specimen subjected to a specific monotonic load. It must be pointed out that the response of the material is controlled by the specimen geometry and material factors, thus the simpler is the stress field applied to the specimen, the easier is the material characterization.

One of the most popular test methods for HMA tensile strength estimation at low and intermediate pavement temperature is the Superpave Indirect Tension Test (IDT), developed by Roque & Buttlar (1992) and Buttlar & Roque (1994) under the Strategic Highway Research Program (SHRP). A compressive load is applied along the diametral axis of a 150mm diameter specimen in an indirect tensile test device at a controlled vertical deformation rate until failure. The mechanics of the test are such that a nearly uniform state of tensile stress is achieved across the vertical diametral plane. In particular, both the vertical and horizontal stress distribution is fairly uniform near the center of the face of the indirect tensile specimen as discussed by Roque & Buttlar (1992). Vertical and horizontal deformations are measured by two strain gauges with a length of 38.1 mm placed at the center of the circular specimen. According to the Superpave Indirect Tension test procedure, the horizontal stress at the center of the specimen is computed using the following IDT plane stress equation:

$$\sigma_h = \frac{2P}{\pi Dt} \qquad [1.12]$$

where:

σ_h = maximum tensile stress (MPa),

P = load of the specimen (N),

D = diameter of the specimen (mm);

t = thickness of the specimen(mm).

The load for estimating the tensile strength is determined from the point at which the vertical minus horizontal deformation is maximum.

The Semi-Circular Bending (SCB) test on semi-circular specimens as been proposed in the recent past as an alternative to the Indirect Tension Test to determine the fracture properties of HMA mixes. The SCB test was firstly introduced by Lim et al. (1994) to conduct mode I and mix mode fracture toughness experiments on rock materials. Afterwards, Krans et al. (1996) and Van de Ven et al. (1997) investigated the possibilities of the SCB test as a practical crack growth test for asphalt mixtures. They developed a load-stress relationship using a 2-D linear-elastic finite element analysis for maximum horizontal tensile stress:

$$\sigma_x = 4.263\frac{P}{D} \qquad [1.13]$$

where:

$\sigma_{x =}$ maximum horizontal tensile stress (MPa);

P = load per unit thickness of the specimen (N/mm);

D = diameter of the specimen (mm).

However, this relationship appeared to be not adequate for describing the stress state of a semi-circular bending specimen since the resulting tensile strength was structurally higher than the tensile strength determined with the IDT. Molenaar et al. (2002) investigated the stress field development in a SCB specimen by means of a finite element program, assuming that the material behaves linear elastic. They proposed the following equation for SCB horizontal stress computation:

$$\sigma_t = 4.8\frac{F}{D} \qquad [1.14]$$

where:

σ_t = maximum tensile stress at the bottom of the specimen (MPa),

F = load per unit width of the specimen at failure (N/mm)

D = diameter of the specimen (mm).

It was pointed out that in SCB specimens tension might be the dominant failure mode but that damage due to compression develops within the specimen during loading. Equation [1.14] has proved to be not adequate for SCB tensile strength analysis since large differences were observed between tensile strength values obtained from the SCB and the IDT (2.1 times higher than the real tensile strength). It has also been shown that the tensile strength as calculated by means of equation [1.14] is not the true tensile strength but only an indication of the tensile strength characteristics of the material. Li and Marasteanu (2004) used the SCB to evaluate the low-temperature fracture resistance of asphalt mixtures. They performed a finite element stress analysis to identify the correct specimen thickness for assuming plane stress conditions, resulting in a 25 mm thick specimen.

A further test which can be widely found in literature as a candidate for HMA fracture properties determination is the Single Edge Notched Beam (SENB) test. The SENB is a three point bending test which uses beam specimens obtained from slabs. Various beam sizes, test temperatures and testing procedures have been employed (Majidzadeh et al., 1971; Mobasher et al., 1997; Kim & El Hussein, 1997; Marasteanu et al., 2002; Wendling et al, 2004; Wagoner et al., 2005a). The test procedures are usually developed with guidance from the ASTM E399 (2002) and ASTM 1820 (2002) standards for fracture testing of metallic specimens. The loading configuration allows simple stress states and ease of test control with closed-loop servo-hydraulic equipment, as indicated by Wagoner et al. (2005a). The SENB test is not commonly performed to estimate the tensile strength of the material, but rather to estimate the fracture energy parameter (load-deformation response), meant as the energy required to initiate and fully break a unit surface of crack. However, it is possible to determine the maximum tensile strength at the bottom edge of the beam using the tension bending beam equation (Kaloush et al., 2003):

$$\sigma_t = 0.375 \frac{P}{bh^2} \tag{1.15}$$

where:

σ_t = maximum tensile stress (MPa);

P = applied load (N);

b = average specimen width (mm);

h = average specimen height (mm).

1.5.2 Fracture Energy

The fracture energy is one of the most important parameters for describing and modeling the fracture behavior of cohesive materials. It is defined as the amount of energy required to create a unit area of a crack. The objective definition of fracture energy and optimal testing procedure for its determination is a hot topic, recently studied by committees of the American Society for Testing and Materials (ASTM) and thoroughly discussed by many researchers.

According to LEFM theory, energy dissipation takes place only at the crack tip; thus fracture energy is directly related to the separation energy required to create a new surface by a clean cut in the material. However, the assumptions of LEFM lead to a singularity at the crack tip and to unbounded stress field. In real materials, stresses cannot become arbitrarily large, and the crack tip is always surrounded by a process zone in which the material response is not elastic.

In 1985, the RILEM Technical Committee 50-FMC (Fracture Mechanics of Concrete Test Methods), proposed a draft recommendation to determine the material fracture energy using a three-point beam bending test. In the RILEM test, the experimental beams are notched and subjected to a three point loading while a clip gage measures the load point displacement.

The typical load-deflection plot obtained from a RILEM test is shown in Figure 1.7. During a formation of a crack, a certain amount of energy is dissipated in the process zone, and the fracture energy (G_F) is considered as the total energy dissipation (W_0) per unit area of the ligament (A_{lig}) that represents the idealized (smooth) crack trajectory:

$$G_F = \frac{W_0}{A_{lig}} \qquad [1.16]$$

where A_{lig} is defined as the projection of the fracture process zone on a plane parallel to the main crack direction.

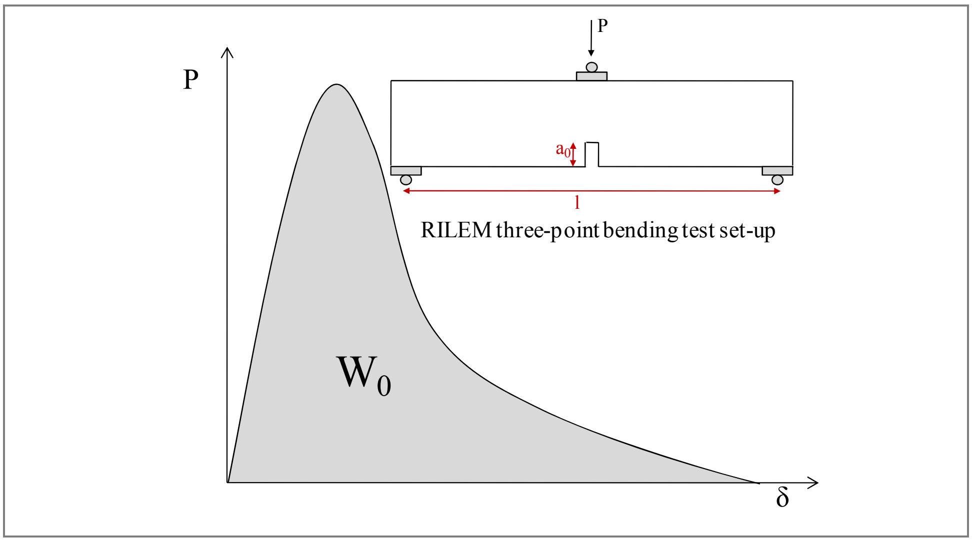

Figure 1.7 Load-deflection plot from RILEM test

The problem with this definition is that it does not specify an objective material property that would be independent of the size and shape of the tested specimen. Indeed, measured values of G_F obtained using the RILEM procedure, in general, increase with increasing size specimen (Hillerborg, 1985; Wittmann, 1986; Mihashi et al., 1989; Swartz et al., 1987; Xu & Zhao, 1991). Even if one considers only pure Mode-I fracture (only normal crack opening, no relative sliding of the crack faces), measurements on different specimens lead to different results for the same material. Also for a fixed specimen geometry and type of loading, fracture energy defined in this way depends on the specimen size (Abdalla & Karihaloo, 2003; Carpinteri et al., 1994; Elices et al., 1992; Wittmann et al., 1990) and therefore it should be considered only a “nominal fracture energy”.

Even though the RILEM procedure was developed specifically for mortar and concrete specimens, in the recent past it has also been used for asphalt concrete fracture analysis. In 1999, Hossain et al. conducted an experimental study for investigating the fracture and tensile properties of asphalt-rubber concrete mixtures using the RILEM three point bending test. Wagoner et al. (2005a) used the Cohesive Zone Model (CZM) to describe the fracture characteristics of asphalt concrete for which the critical tip opening and the fracture energy (as previously defined) are two of the three required material properties. Afterwards, they developed a Disk-Shaped Compact Tension (DCT) specimen geometry that maximizes the ligament length to easier determine the fracture energy parameter (Wagoner et al. 2005b). Li & Marasteanu (2004) investigated the use of a Semi Circular Bend (SCB) test as a candidate for a low-temperature asphalt mixture cracking specifications calculating the fracture energy on the base of the RILEM procedure.

Seo et at. (2004) adopted a cohesive crack model-based approach to calculate the fracture energy on a single asphalt mixture using monotonic and cyclic tension tests performed on prismatic, double-edge notched specimens. The fracture energy was represented by the area below the stress-elongation curve (Equation [1.6]), as previously discussed. The crack opening displacement (w) was measured from a 5 mm thick band between the notches of the specimen. Then, fracture energy was obtained by subtracting the area that is surrounded by stress-elongation outside the cracked section from the area under the stress-crack opening displacement.

The limitations developing when applying the RILEM model to asphalt mixtures can be summarized as follows:

- The area of ligament in asphalt mixtures is very hard to measure due to its high variability from a cut plane, which is due to the random effects of aggregate arrangements and their influence on crack path.
- The properties of the material outside the FPZ are assumed to be governed by the undamaged state, which is inconsistent for asphalt mixtures in which cracks occur randomly at the same time at different locations.
- A notch is required to address crack initiation and FPZ preventing the identification of a real fracture initiation.

The discussion presented above leads to the HMA Fracture Mechanics as a promising model for determining HMA failure limits, since it provides a more fundamental approach. HMA Fracture Mechanics accounts for both crack initiation and propagation which are governed by the same mixture parameters, considers generalized loading conditions, models HMA as a viscoelastic material in which cracks are assumed to grow discontinuously, describes crack initiation and propagation using only four parameters easily obtainable performing a Superpave IDT test and finally introduces the threshold concept as a key element in the cracking process.

1.6 SBS Polymer Modified Mixtures

Cracking is widely recognized as an asphalt binder-related distress, thus the fracture resistance of asphalt mixtures is strictly correlated to its properties. Polymer modifiers are introduced in an attempt to increase the mixture's high temperature stiffness to resist rutting and low temperature flexibility to resist fatigue and thermal cracking. Previous research has indicated that polymer-modified asphalt binder has the ability to improve asphalt pavement's resistance to permanent deformation (Freeman et al., 1997; Bahia et al., 2001; Sargand & Kim, 2001). However, polymer modified asphalt mixtures may either degrade or enhance asphalt mixture fatigue life (Aglan, 1997; Deacon et al., 1997; Khattak & Baladi, 1998; Newman, 2000; Romero et al. 2000; Bahia et al., 2001, Lundström & Isacsson, 2004). Studies by Harvey and Monismith (1995, 1997) and Bahia et al. (2001) have shown that the addition of the same modifier to different asphalt binders may lead to contrasting results in terms of fatigue resistance. These studies indicate that modifiers had different effects on mix stiffness, fatigue life and cumulative dissipated energy. The addition of polymers to asphalt binders may also increase the resistance to low-temperature cracking of asphalt pavements (King et al., 1993; Lu & Isacsson, 1997; Pucci et al., 2004; Khattak et al., 2007). However, studies conducted on low temperature properties of polymer-modified mixtures have shown that polymer modification does not show benefits as compared to the corresponding base asphalt binder (Lu et al., 2003).

Currently, the most commonly used polymer for binder modification is the elastomer Styrene Butadiene Styrene (SBS) (Airey, 2004). It belongs to the class of copolymers, defined as polymers made up of two or more different repeating units in the molecular chain. The structure of a SBS copolymer consists of styrene butadiene styrene tri-block chains, having a two-phase morphology of spherical polystyrene block domains within a matrix of polybutabiene (Isacsson & Lu, 1995). SBS copolymers derive their strength and elasticity from physical cross-linking of the molecules into a three-dimensional network. The polystyrene end-blocks impart the strength to the polymer, while the polybutadiene rubbery matrix mid-blocks give the material elasticity. When SBS is blended with asphalt, the elastometric phase of the SBS copolymer absorbs the maltenes (oil fractions) from the asphalt and swells up to nine times its initial volume. At suitable SBS concentrations, a continuous polymer network (phase) is formed throughout the polymer modified binder, significantly modifying its properties (Airey, 2004).

Recent research conducted by Kim et al. (2003) showed that the SBS modified mixtures generally have a lower creep rate than unmodified ones resulting in a reduced rate of micro-damage accumulation without a reduction in fracture energy limit or healing rates. Kim et al. (2003) also found that the asphalt mixture fracture limits as measured by the fracture energy density and the dissipated creep strain energy did not change with the 3 percent SBS polymer modification as percent of the binder used. They claimed that the reduction in tensile creep rate observed could either be explained as a benefit associated with SBS modification or possibly with age-hardening or further combined effects.

In summary, it appears that polymers may improve the cracking resistance of asphalt mixtures through the reduction of tensile creep rate. However, the effect of higher percent of polymer modification on the fracture resistance and tensile creep rate of asphalt mixtures has not been thoroughly investigated.

CHAPTER 2

Materials and Methods

Tensile failure limits were evaluated from three different test configurations: the Indirect Tensile Test (IDT), the Semi-Circular Bending Test (SCB) and the Three Point Bending Beam Test (3PB). Six different 12.5-mm nominal maximum size fine-graded Marshall mixtures with the same aggregate type and gradation but different asphalt binders were investigated. All the mixtures were prepared in laboratory, while the asphalt binders were provided by Valli Zabban Asphalt Refining Company.

2.1 Materials

2.1.1 Aggregates

The gradation selected is a fine-graded mix which had been successfully used to produce acceptable mix designs in the past. The batch is composed by limestone and marly limestone, calcarenite and fine and coarse sand, mined from Parma, North Italy by Spotti Srl. The aggregate gradation and curve of the six mixtures are given in Table 2.1 and Figure 2.1.

2.1.2 Asphalt Binders

Six different asphalt binders were used in this research, named as N1, N2, RM3.5, RM5.0, LM3.5 and LM6.5. N1 and N2 are two unmodified binders, graded as PG64-22 and PG58-22 respectively. RM3.5 and LM3.5 are two polymer modified binders obtained blending the N2 unmodified one with a 3.5% of SBS cross-linked and SBS linear polymers respectively. RM5.0 and LM6.5 are two heavily polymer modified binders prepared blending the N2 virgin binder with the maximum percentage of polymer modifier to maintain asphalt stable, resulting in 5% for the cross-linked polymer and 6.5% for the linear polymer. The SBS were blended with the base asphalt by the manufacturer using high shear milling. Details on the asphalt binder composition and PG grading test results are listed in Table 2.2.

Sieve size (mm)	% Passing
19.00	100
12.500	93
9.500	82
4.750	51
2.360	39
1.180	27
0.600	19
0.300	14
0.150	11
0.075	8

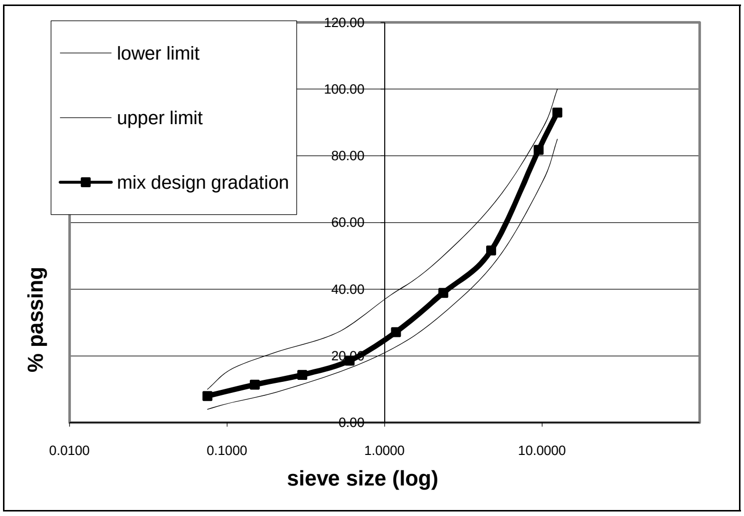

Table 2.1 Aggregate gradation; **Figure 2.1** Aggregate curve of the six mixtures

Table 2.2. Asphalt binder properties

ASPHALT BINDER	**N1**	**N2**	**RM3.5**	**RM5.0**	**LM3.5**	**LM6.5**
Performance Grade	PG 64-22	PG 58-22	PG 64-22	PG 70-22	PG 70-22	PG 76-22
Blend	Unmodified	Unmodified	N2+3.5% SBS cross-linked	N2+5.0% SBS cross-linked	N2+3.5% SBS linear	N2+6.5% SBS linear
UN-AGED ASPHALT						
Dynamic Shear (10rad/sec) $G^*/\sin\delta$, kPa	2.52@64°C	2.58@58°C	2.46@64°C	1.55@70°C	1.40@70°C	2.12@76°C
RTFO AGED RESIDUE						
Dynamic Shear (10rad/sec) $G^*/\sin\delta$, kPa	4.71@64°C	4.77@58°C	4.64@64°C	4.64@70°C	2.35@70°C	3.05@76°C
PAV AGED RESIDUE @ 100°C						
Creep Stiffness and m-value, 60 sec.	154 and 0.329 @-22°C	179 and 0.353 @-22°C	130 and 0.335 @-22°C	147 and 0.323 @-22°C	173 and 0.311 @-22°C	150 and 0.324 @-22°C

2.2 Specimen Preparation

The two unmodified asphalt mixtures (N1 and N2) were designed according to the Marshall mix design procedure, resulting in 5.4% and 5.2% design asphalt content, respectively (medium traffic level). All the modified mixtures were prepared with the same effective asphalt content as the N2 unmodified one to assure that the SBS modifier was the only factor affecting the test results.

For each mixture, five 4500 g and one 15000 g aggregate batches were prepared to produce a total of 30-152 mm diameter cylindrical specimens and six 300x300x75 mm slabs. The aggregates, the asphalt binders and mixing equipment were heated for three hours at 150°C for unmodified mixes and at 175°C for the modified ones to achieve appropriate uniform mixing temperature. The batches were then mixed with the design asphalt content percentage and heated for another two hours at 135°C for short-term aging.

The cylindrical specimens were obtained compacting the mixes to 6 (± 0.5) percent air voids into 152 mm diameter specimens using the Superpave Gyratory Compactor. The slabs were compacted on a proper compactor set to produce 300 mm long by 300 mm wide by 75 mm tall specimens. This equipment is made up of a cylindrical horizontally pivoted steel cup upon which a 3ton maximum load hydraulic press is placed. Below the press, a 300x300 mm mobile basement is placed with the formwork containing the material. This formwork moves while the pivoted element applies a given pressure to compact the material to the desired air void percentage, in this case 6 (± 0.5) percent. After compaction and cooling of the specimens, volumetric analyses of the mixtures were performed, as shown in Table 2.3.

Each cylindrical specimen was sawn to obtain two effective plates, each 30 mm thick discarding the top and the bottom plates for reducing density gradient effects. For each mixture, three circular shaped specimens were used to perform resilient modulus, creep compliance, and strength test at 10° C according to the Superpave IDT procedure developed by Roque and Buttlar (1992) and Buttlar and Roque (1994). Three other specimens were used to perform IDT fracture tests using the Digital Image Correlation system. Three final plates were sawn in half to obtain 76 mm height Semi-Circular specimens for performing SCB fracture tests. The slabs were cut to produce 3 beam specimens for each mixture to the final dimension of 300 mm long by 75 mm tall by 100 mm wide.

Table 2.3 Volumetric properties for the six mixtures

ASPHALT MIXTURE	N1	N2	RM3.5	RM5.0	LM3.5	LM6.5
Asphalt content, AC%	5.4	5.2	5.2	5.2	5.2	5.2
Theoretical maximum specific gravity, G_{mm}	2.456	2.585	2.557	2.546	2.581	2.595
Bulk specific gravity of compacted mix ,G_{mb}	2.305	2.429	2.399	2.391	2.416	2.432
Bulk specific gravity of aggregate, G_{sb}	2.632	2.632	2.632	2.632	2.632	2.632
Effective specific gravity of aggregate, G_{se}	2.650	2.650	2.650	2.650	2.650	2.650
Percent VMA in compacted mix ,VMA	17.15	12.45	13.62	13.88	12.99	12.41
Percent air voids in compacted mix, Av	6.1	6.0	6.2	6.1	6.4	6.3
Percent VFA in compacted mix, VFA	64.43	51.95	54.48	56.07	50.73	49.25

In summary, the following specimens were prepared:

- Three 152 mm diameter (30 mm thick) circular shaped specimens for each mixture to perform resilient modulus, creep compliance and strength tests;
- Three 152 mm diameter (30 mm thick) circular shaped specimens for each mixture to perform IDT fracture analysis by Digital Image Correlation;
- Three 152 mm diameter and 76 mm height (30 mm thick) Semi-Circular specimens for each mixture to perform SCB fracture tests using both traditional strain measurement devices (strain gauges) and Digital Image Correlation;
- Three 300 mm long, 100 mm thick, 75 mm height beam specimens for each mixture to perform Three Point Bending fracture tests using both traditional strain measurement devices (strain gauges) and Digital Image Correlation.

2.3 Test Methods

Three different test methods, the Indirect Tensile Test (IDT), the Semi-Circular Bending Test (SCB) and the Three Point Bending Beam Test (3PB) were performed on three replicates at 10°C, using an MTS closed-loop servo-hydraulic loading system. The specimens were conditioned inside a MTS Environmental Chamber enabling the testing of materials and components within a range of high and low temperature environments. A temperature controller associated with the Environmental Chamber monitors the temperature to a desired point. Temperature stability inside the chamber is within ±0.5°C.

2.3.1 Indirect Tension Fracture Test

The IDT fracture test loads monotonically a 152 mm diameter circular specimen to failure applying a constant stroke of 0.084mm/sec. The top and the bottom loading plates are 25.4 mm wide and 50.8 mm long. Two strain gauges with a length of 38.1 mm are placed at the center of the specimen to measure vertical and horizontal deformations during loading. The IDT experimental setup is shown in Figure 2.2. To take into account 3D effects, the procedure described by Roque and Buttlar (2002) and Buttlar and Roque (1994) was applied. According to this procedure, bulging correction factors are needed to correct the measured horizontal and vertical deformation to fit the deformation in a flat plane. These are then divided with the gauge length GL to obtain the average strain. Finally, center correction factors are used to correct the strain values at the center of specimen.

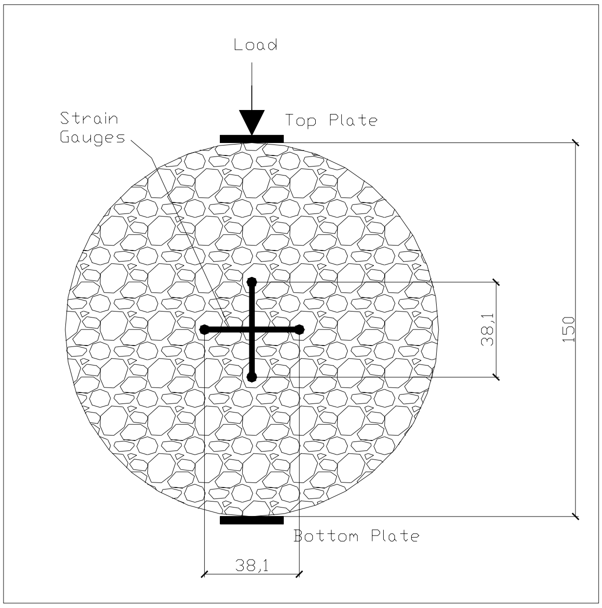

Figure 2.2 Indirect Tensile Test setup

The horizontal stress at the center of the specimen was computed using the following IDT plane stress equation, according to the Superpave Indirect Tension test procedure (Roque and Buttlar, 2002; Buttlar and Roque, 1994):

$$\sigma_h = \frac{2P}{\pi Dt} \qquad [2.1]$$

where:

σ_h = tensile stress at the center of the specimens (MPa),

P = load of the specimen (N),

D = diameter of the specimen (mm),

t = thickness of the specimen (mm).

2.3.2 *Semi-Circular Bending Test*

The Semi-Circular Bending Test was performed applying a static load on a semi-circular specimen with a length of 152 mm and a height of 76 mm placed under a loading ring. The diameter of the top and bottom rings (which function as supports) is 30 mm.

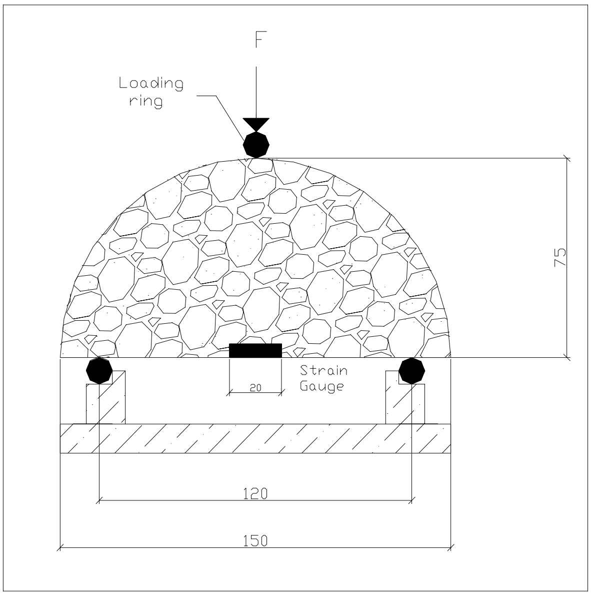

The load transmission occurs with a displacement control system, where the top loading ring drops with a 0.084mm/sec speed. One HBM-Y series strain gauge, arranged in a quarter Wheatstone bridge, with a length of 20 mm is mounted on the central bottom edge of the specimen to measure horizontal deformations during fracture testing. The Semi-Circular Bending test experimental setup is shown in Figure 2.3. Strain gauge specifications are listed in Table 2.4.

Figure 2.3 Semi-Circular Bending test setup

Table 2.4. HBM-Y series strain gauge specifications

Maximum elongation (μm/m)	50,000 (5%)
Fatigue life	> 10^7
Operating temperature range (°C)	-70…+200
Mechanical hysteresis (μm/m)	1

Strain gauge signals are acquired by a National Instrument SCXI Chassis which scans input channels at rates up to 333kS/s. A commercial software developed in a LabView environment was used to calculate stain gauge parameters and acquire output signals. Strain measurements were acquired at a frequency of 10Hz.

The stress field in a SCB specimen was previously studied by Van de Ven et al. (1997) and Molenaar et al. (2002). In these studies both tensile and compressive stresses were computed by means of a finite element analysis. It was pointed out that in SCB specimens tension might be the dominant failure mode but that damage due to compression develops within the specimen during loading. The development of a compression arch was considered in this research work observing the full field strain maps obtained by Digital Image Correlation analyses. However, the damage due to compression appears strongly less predominant than the tension one in the area of interest, as shown in Figure 2.4 (where x and y axes are the lengths of the Region of Interest in mm). The length covered by the strain gauge in Figure 2.4 is from 20 mm to 40 mm (x axis).

Initially, the SCB horizontal stress was computed using the equation proposed by Molenaar et al (2002):

$$\sigma_h = 4.8\frac{P}{Dt} \qquad [2.2]$$

where:

σ_h = tensile stress at the central bottom area of the specimens (MPa),

P = load of the specimen (N),

D = diameter of the specimen (mm),

t = thickness of the specimen (mm).

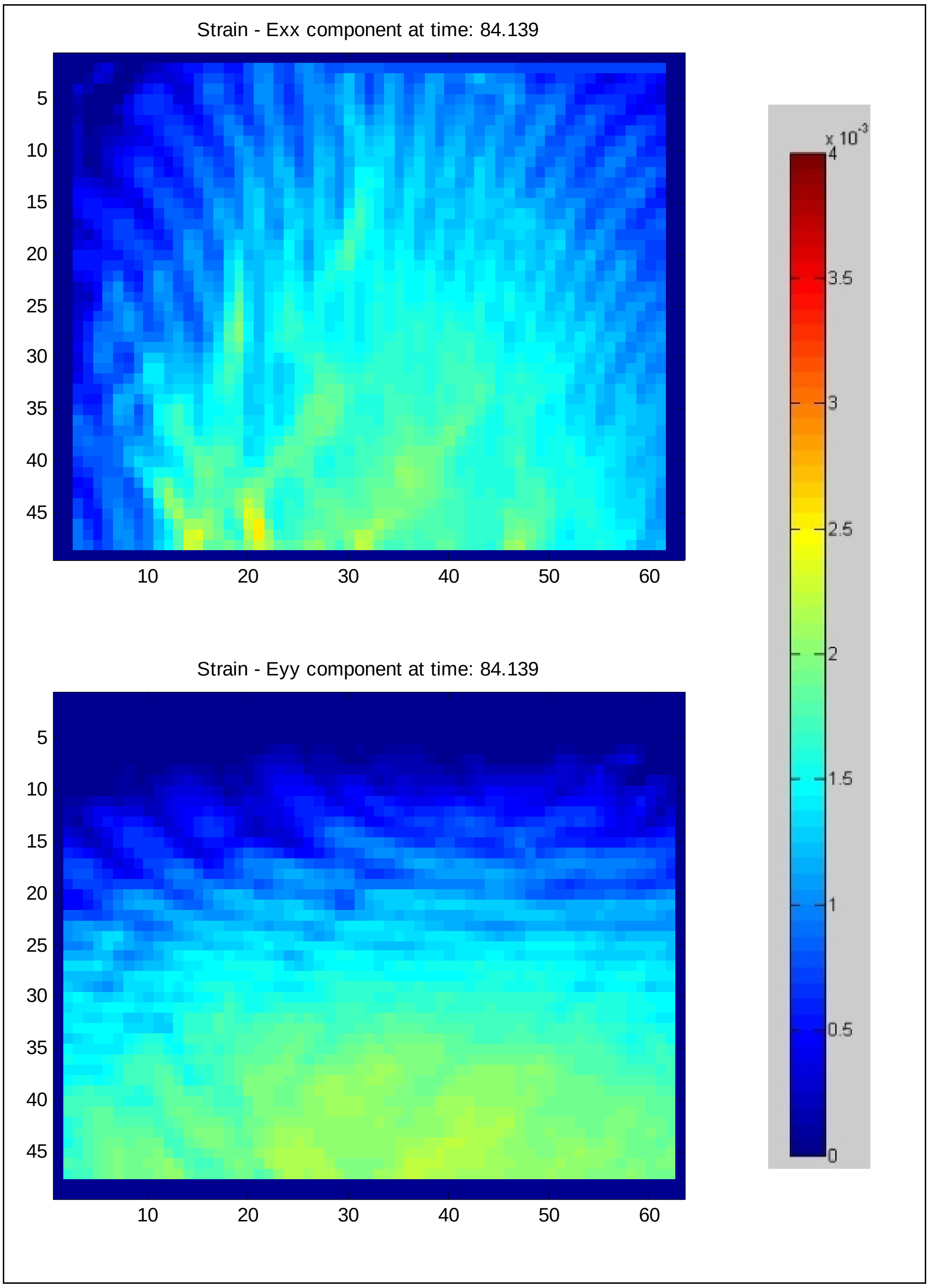

Figure 2.4 Horizontal and vertical SCB strain maps of mix N2 at crack opening

Equation [2.2] has proved to be not adequate for SCB tensile strength analysis since large differences were observed between tensile strength values obtained from the SCB (2.1 times higher than the real tensile strength) and the IDT. It has also been shown that the tensile strength as calculated by means of equation [2.2] is not the true tensile strength but only an indication of the tensile strength characteristics of the material. For these reasons the SCB tensile stress at the bottom edge of the specimen was evaluated by means of a Displacement Discontinuity (DD) boundary element method adopting a nonlinear failure law for the cracking criterion. From the results, the following equation has been proposed:

$$\sigma_h = 2.2\frac{P}{Dt} \qquad [2.3]$$

where:

σ_h = tensile stress at the central bottom area of the specimens (MPa),

P = load of the specimen (N),

D = diameter of the specimen (mm),

t = thickness of the specimen (mm).

Equation [2.3] was estimated modeling all the six mixtures used in this research work. Input parameters for the SCB test simulations were obtained from Superpave IDT testing and simulation, followed by the interpretation approach developed by Birgisson et al. (2003) for obtaining a suitable set of material parameters for the micromechanical displacement discontinuity modeling of mixtures. Further discussion is provided in chapter 4.

2.3.3 Three Point Bending Beam Test

The three point bending fracture test procedure was developed with guidance from the SCB test. The same test equipment consisting of loading and supporting rings, type of strain gauge and data acquisition system was used. The beam dimension was selected based on the capability of the beam compactor resulting in 300 mm long by 75 mm tall by 100 mm wide beam specimens. The span length of the specimen is settled at 0.8 of the beam length (240 mm). A static load is applied in the middle section of the beam by the upper loading ring which applies a constant stroke of 0.084mm/sec. One HBM-Y series strain gauge (see Table 2.4 for specifications) with a length of 50 mm is placed on the surface of the specimen in the central bottom area to measure horizontal deformations. The Three Point Bending Beam test experimental setup is shown in Figure 2.5.

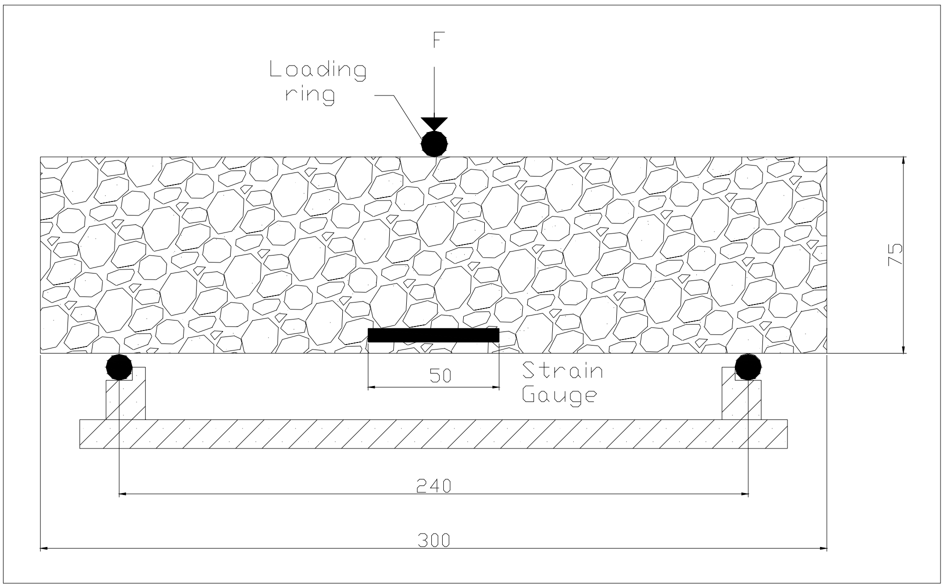

Figure 2.5 Three Point Bending Beam Test setup

The tensile stress at the bottom edge of the beam is calculated using the tension bending beam equation:

$$\sigma_h = 1.5\frac{PL}{th^2} \quad [2.4]$$

where:

σ_h = tensile stress at the central bottom area of the specimens (MPa),

P = load of the specimen (N),

L = span of the specimen (mm),

t = thickness of the specimen (mm),

h = height of the specimen (mm).

CHAPTER 3

Digital Image Correlation (DIC) System

The evaluation of HMA material properties (such as tensile strength and fracture energy density) rests on the accuracy of displacement and strain measurements. The most common fracture tests performed on asphalt mixture specimens employ on-specimen mechanical strain measurement techniques (e.g. strain gauges and LVDTs). These devices are simple to use, but their drawback is not being capable of accurately capturing localized or non-uniform strain distributions, thus not allowing for true point-wise analyses of a strain field. This prevents the exact determination of the important location of crack initiation, not easily allowing the determination of the strain values at the instance and location of which a crack initiates. Traditional on-specimen strain measurement techniques also do not provide flexibility, because the measurement location must be decided prior to the test. This precludes the possibility of a "back analysis" of the resulting strain field over an area of finite extent, and, above all, does not capture full field displacement/strain measurements in the specimen. In comparison, the detection of crack initiation in HMA specimens is simplified by field measurements of deformation over an area of finite extent, since typically cracks appear in somewhat non predictable locations.

During the last decade, several types of full-field deformation measurement techniques have been proposed for composite material characterization, as described by Grédiac (2004). Since the advent of target location in digital or digitized images (Van den Heuvel & Kroon, 1992), alternatives based on analogue photogrammetry and vision metrology have also become viable (Crippa et al., 1993). Digital image correlation was proposed in the 1980's as an automated approach for the computation of surface strains and displacements (Sutton et al, 1983; Chu et al., 1985; Sutton et al., 1986; Ranson et al, 1987; Bruck et al., 1989). It was later advanced to study 2-D solid mechanics problems, being successfully applied to determine strains in specimens of resin films (Muszynski et al., 2002), fiber reinforced polymer composites (Melrose et al., 2004), and concrete (Choi & Shah, 1997).

Kim & Wen (2002) first proposed the use of a DIC technique as a possible displacement/strain measurement method for asphalt mixtures. They applied the DIC technique to determine the proper gauge length for a 100-mm diameter IDT specimen. They also demonstrated that the DIC technique is a good alternative to the LVDTs for HMA noncontact deformation/strain measurements. Seo et al. (2004) and Chehab et al. (2007) utilized a DIC technique to investigate the size and shape of the fracture process zone for asphalt mixtures performing uniaxial monotonic and cyclic tension tests on prismatic specimens with symmetric double notches and on cylindrical specimens cored from Superpave gyratory compacted specimens.

However, all these studies were conducted adopting a commercial package for two-dimensional digital image correlations, which has the drawback of not providing flexibility. Conversely, an in-house developed DIC system gives important advantages brought by the ability to customize the system for specific applications. In particular, the current Digital Image Correlation (DIC)-based method was developed specifically for imaging asphalt specimens. This means that the software was designed to facilitate the quantification of large strains in the mastic in between the aggregates in a typical asphalt mixture.

The Least Squares Matching technique (Forstner, 1982; Ackermann, 1984; Gruen, 1985) was employed for the purpose of providing matches with sub-pixel accuracy. Finally, an efficient optimization of the algorithm was developed to achieve accurate image correlations.

The DIC technique involves: specimen surface treatment, appropriate illumination, and a suitable equipment placement. A sequence of images is then acquired with a digital camera during the tensile fracture testing of the HMA specimen; a dense set of features, artificially generated on the specimen surface, is accurately tracked by the algorithm along the image sequence. From the image coordinates, displacements and deformations can be evaluated in image space and, with an appropriate transformation, in object space.

3.1 Image System Characteristics

The system is composed of three elements: the hardware (i.e. the digital camera and the illumination devices), the specimen set up, and the software (image acquisition and processing).

3.1.1 Experimental setup

A digital camera Basler AF 101 (resolution 1300x1030, focal length 8mm, pixel size 6.7 micrometers, 12 fps@max resolution) is currently employed. The optics adopted at maximum magnification allow 30 μm per pixel resolution. The camera which is directly connected with a personal computer, is located on a support inside the climatic chamber, focusing up to 3.5 cm from the area of most interest of the specimen (i.e. the most stressed area). A lighting system, created for the purpose of providing adequate illumination of the specimen inside the climatic chamber, is composed of 4 white lights, which can be oriented according to the specimen shape and/or dimensions: two horizontal guide rails allow horizontal movements while two 20 cm eyelets in which the lights are embedded, allow vertical settings. The experimental setup is shown in Figure 3.1

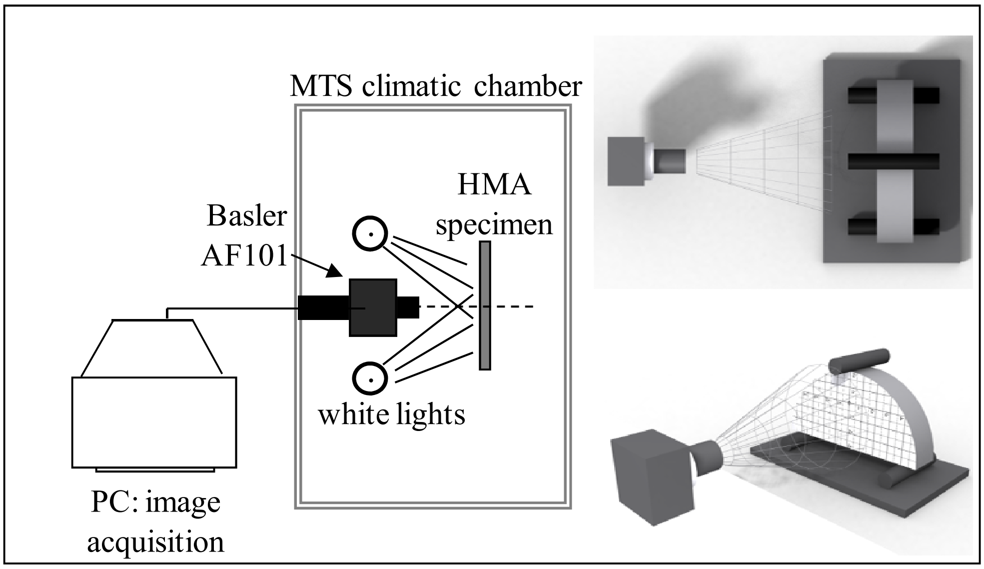

Figure 3.1: DIC System experimental setup

3.1.2 Specimen preparation

The specimen requires a preliminary surface treatment to ensure a successful imaging acquisition and the subsequent application of the DIC method. The technique involves measurements of the greyscale level at each pixel location of the image, thus very well-contrasted images are fundamental for achieving a high measurement accuracy.

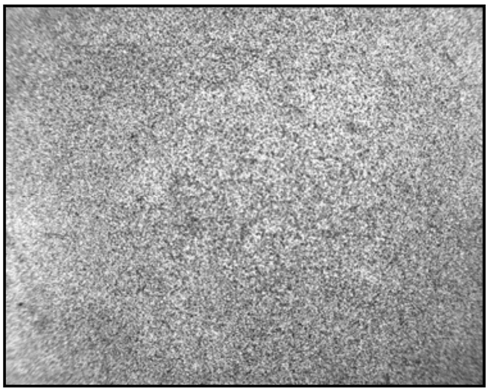

Figure 3.2: Specimen surface treatment

The surface treatment adopted for asphalt mixtures consists of the application of thin white paint overprinted by a speckle pattern of black, resulting in a homogeneous randomly oriented texture (Figure 3.2). Care must be taken in ensuring thin enough layer thickness to avoid tracking the deformation of the paint film rather than the specimen deformation. The paint adopted was a water-based paint, which is lightly absorbed by the asphalt mixture so as not to affect the estimation of the real cracking behavior of the specimen.

3.2 Theoretical Principles

The feature tracking is achieved using Area Based Matching (ABM), a long established technique for the extraction of image correspondences based on similarities between grey values (g.v.). In ABM, each image point to be matched is the centre of a small window of pixels (template) in an undeformed reference image (master image), which usually corresponds to the first image in the sequence of frames. The grey values of the template are statistically compared with those of an equally sized window of pixels (patch) in a deformed search image (slave image), which corresponds to another image in the sequence of frames (Figure 3.3).

Two different approaches can be adopted for the evaluation of the similarities between patch and template's grey values: cross-correlation and least squares matching. The former uses a proper correlation function to determine a coefficient which establishes whether a point in the template corresponds to another in the patch, while the latter is based on an iterative least-squares resolution algorithm.

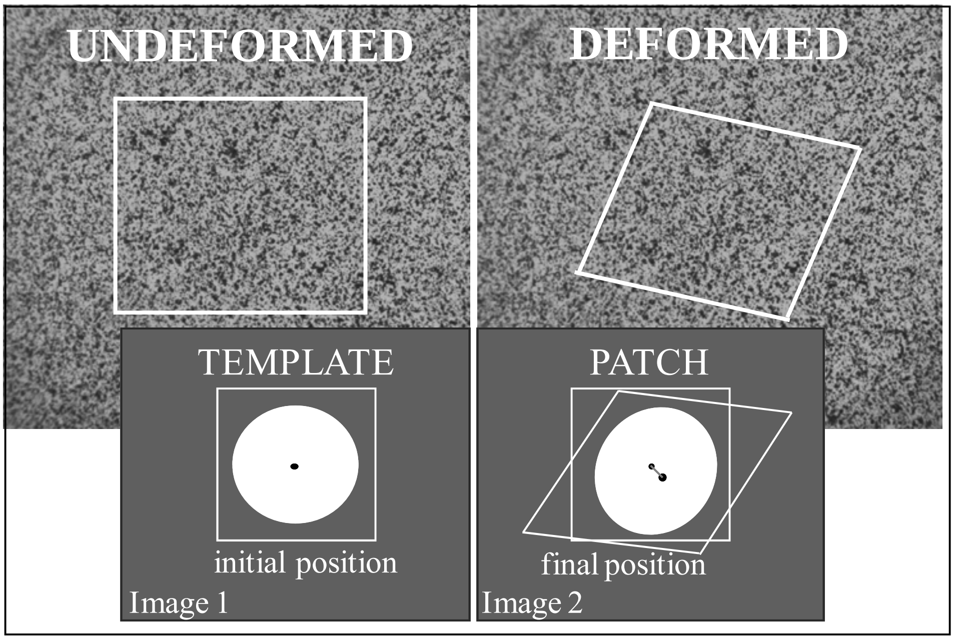

Figure 3.3: Area Based Matching principles

The maximum correspondence between the grey values of the two windows is established if patch and template are exactly the same. However, grey value correspondences always differ since the patch is affected by both radiometric and geometric differences.

Radiometric differences are due to sensor response, illumination changes, and object reflective changes. Geometric differences arise from object movements (translations and rotations), object deformation, and perspective effects (camera location and object shape).

The DIC system developed for HMA full field displacement/strain estimation was developed using the least squares matching approach; however, a brief description of the two techniques is provided.

3.2.1 Cross-Correlation

The cross-correlation function tracks the interested point by shifting pixel by pixel the template window within a specific range in the patch window using a simple translation, as shown in Figure 3.4. The nearest location at the pixel level is selected based on the occurrence of the best-matched pattern, which has the minimum value of the mutual cross-correlation coefficient ρ. Essentially, the cross-correlation function is estimated over the search area: its maximum provides the best match position. The coefficient ρ is computed as a discrete function of patch displacement (Δ_x, Δ_y):

$$\rho = \frac{\sum_x \sum_y (f(x,y) - \bar{f}) \times (g(x + \Delta_{x,y} + \Delta_y) - \bar{g})}{(\sum_x \sum_y (f(x,y) - \bar{f})^2 \times \sum_x \sum_y (g(x + \Delta_{x,y} + \Delta_y) - \bar{g})^2)^{1/2}} = \frac{\sigma_{fg}}{\sigma_f \cdot \sigma_g} \qquad [3.1]$$

where $\bar{f}$ and $\bar{g}$ are the mean values of the grey levels of the template and patch windows respectively.

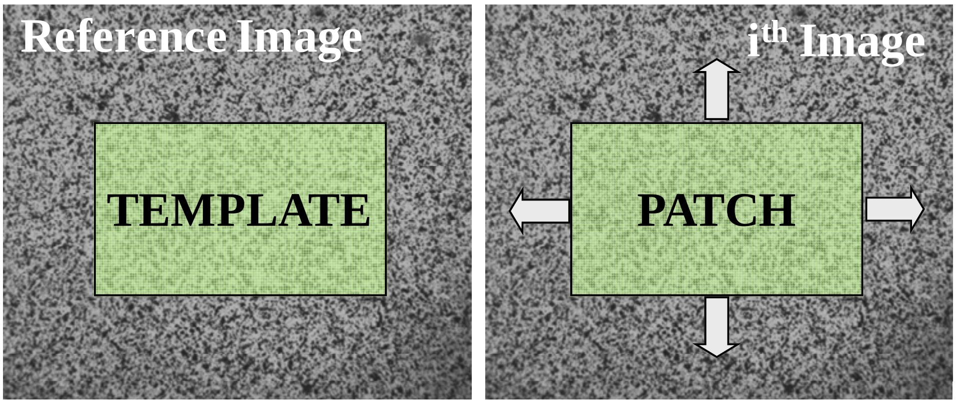

Figure 3.4: Cross-correlation approach

Sub-pixel accuracy can be obtained by interpolating the cross-correlation coefficient ρ using a smooth continuous function, thus allowing for the analytical checking of its maximum.

Cross-correlation is a method of choice in computer science, since it is faster to implement and results in a more efficient computational performance. However cross-correlation tracks the interested point only by shifting the template along the horizontal and /or vertical axes, not accounting for rotations. Thus it works well only if geometric and radiometric distortions of the patches are kept at the minimum.

During Hot Mix Asphalt fracture tests, rotations and/or scale changes between two images always occur, thus the cross-correlation approach appears not adequate for these kind of analysis. In contrast, the Least Squares Matching technique uses a more complete functional model, providing matches with sub pixel accuracy while accounting for both translation and rotations.

3.2.2 Least Squares Matching (LSM)

The LSM method is based on the minimization of the squared differences of the grey values between patch and template.

Given two image points, LSM considers the two conjugate image regions as discrete two-dimensional functions: the template $f(x_1,y_1)$ and the patch $g(x_2,y_2)$. The matching process establishes a correspondence if:

$$f(x_1,y_1) = g(x_2,y_2) \qquad [3.2]$$

However, equation [3.2] is not consistent due to radiometric and geometric differences, as previously discussed. Therefore, the patch $g(x_2,y_2)$ is transformed applying both radiometric and geometric corrections to obtain a new, more reliable, patch $g^{'}(x_2,y_2)$.

$$f(x_1,y_1) - g^{'}(x_2,y_2) = e(x_1,y_1) \qquad [3.3]$$

where $e(x_1,y_1)$ is the residual for the point (x_1,y_1) in the master image reference system.

Radiometric changes during testing are easily modeled accounting for brightness and contrast changes of grey values in the patch function:

$$g'(x_2,y_2) = r_0 + (1 + r_1) \cdot g(x_2,y_2) \qquad [3.4]$$

where r_0 and r_1 are two parameters accounting respectively for brightness and contrast changes in the slave image.

Geometric corrections are achieved by minimizing a goal function, which measures the distances between the gray levels in the template and in the patch. The goal function to be minimized is the L2-norm of the residuals of least squares estimation. The new location $g^{'}(x_2,y_2)$ is generally described by shift parameters which are estimated with respect to the initial position of $g(x_2,y_2)$ by means of an affine transformation:

$$g(x_2, y_2) = g\left(x_2(u,v), y_2(u,v)\right) \tag{3.5}$$

$$\begin{cases} x_2 = a_1 u + a_2 v + a_3 \\ y_2 = b_1 u + b_2 v + b_3 \end{cases} \tag{3.6}$$

where (a_1, a_2 , b_1, b_2) are model shape differences, while (a_3, b_3) are the shift parameters.

Radiometric and geometric correction parameters are then estimated solving, for $||e(x_1,y_1)||$ = min, the following least squares system, obtained by substituting the transformed functions in equation [3.3]:

$$f(x_1, y_1) + e(x_1, y_1) = r_0 + r_1 \cdot g\left(x_2(u,v), y_2(u,v)\right) = \overline{g}(r_0, r_1, a_1, a_2, a_3, b_1, b_2, b_3) \tag{3.7}$$

The function $\overline{g}(r_0, r_1, a_1, a_2, a_3, b_1, b_2, b_3)$ is linearized and the system is solved with Gauss-Markov least squares estimation model.

3.2.3 LSM optimization

When proper illumination is provided, the two radiometric parameters r_0 and r_1 tend to be zero, while showing high correlation coefficients. In this case, the use of both parameters may lead to numerical instability of the estimation process, resulting in high computational efforts. To overcome these drawbacks, a parameter rejection algorithm was developed to check if one or more function parameters are highly correlated with others and must be fixed during the estimation.

To account for geometric corrections, different shape functions were tested (Sutton et al., 1988; Bruck et al., 1989; Lu & Cary, 2000). It was found that the use of a simplified shape function leads to lower computational efforts but provides inaccuracies when significant deformations occur. In contrast, higher shape function polynomial orders lead to numerical instability from the over-parameterization of the system of equations, even when the parameter rejection algorithm is employed. In this case, good accuracies can be achieved only using a bigger template window to maintain high redundancy in the system of equations. However, the larger the templates, the lower the correspondence between the shape function and the real local deformation of the specimen, which means that accuracies do not improve.

The affine transformation seemed to provide the best performance even when high local deformation gradients occur. Indeed, the affine shaping function is capable of describing a transformation corresponding to a shear deformation plus a compressive and a tensile deformation along two mutual orthogonal directions; thus providing a correct geometric description of the specimen deformation in a localized area.

At the end of the estimation, the initial assumption ($e(x_1,y_1)$ = random error vector) must be verified to account for potential discrepancies between the numerical image correlation model and the real image acquisition (i.e. specimen flat surface, C_0 continuity of the displacement field, ideal sensor without noise, etc.). An iterative statistical procedure, named data snooping (Schwarz & Kok, 1993), was employed for this purpose. Data snooping discards all the observations which show a normalized residual a posterior higher than a threshold. The solution is then re-evaluated until no further gross errors are identified.

3.2.4 Data extraction

The image correlation technique tracks a dense set of features along the acquired image sequence using an approximate value of the patch position estimated at the previous frame. The displacement is computed as the difference of the feature location between each image frame in the sequence and the reference one (which is fixed). Displacement estimation depends mostly on two concurrent factors: the partial or total rigid displacement of the specimen and the displacements occurring in the image system, e.g. camera vibrations.

These effects must be minimized to recover only strain field information. Thus, in each sequence, a point is selected as the origin of a reference system attached to the specimen (Figure 3.5). The origin is selected as a distinct point feature, with high and consistent correlation values between epochs and located on a specimen area not significantly stressed. The region of interest (ROI) is then meshed regularly in both (x,y) directions. The displacements are computed at the nodes of the regular grid by linear

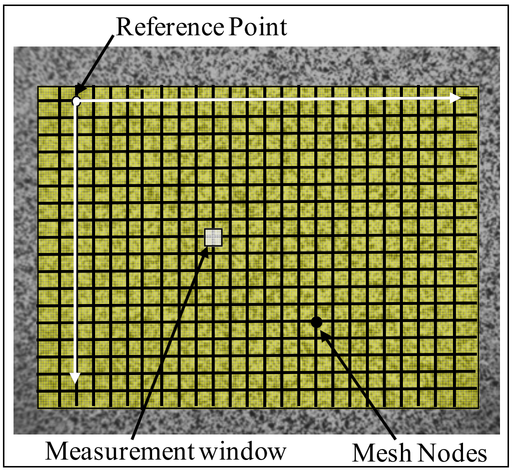

Figure 3.5: ROI meshing

interpolation of the displacement values estimated by LSM over the template bordering the same nodes.

Strains are finally estimated by using a finite difference scheme at the double ends of the template window. If u and v are the displacement components in x and y directions, the strain tensor can be computed as:

$$S=\begin{pmatrix} \dfrac{\Delta u_x}{\Delta x} & \dfrac{1}{2}\left(\dfrac{\Delta u_y}{\Delta y}+\dfrac{\Delta v_x}{\Delta x}\right) \\ \dfrac{1}{2}\left(\dfrac{\Delta u_y}{\Delta y}+\dfrac{\Delta v_x}{\Delta x}\right) & \dfrac{\Delta v_y}{\Delta y} \end{pmatrix} \quad \text{with} \quad \begin{aligned} \Delta u_x &= u(i+1,j)-u(i,j) \\ \Delta u_y &= u(i,j+1)-u(i,j) \\ \Delta v_x &= v(i+1,j)-v(i,j) \\ \Delta v_y &= v(i,j+1)-v(i,j) \end{aligned} \qquad [3.8]$$

Strain values outside the mesh nodes are estimated by bilinear or bicubic interpolation. The accuracy achievable in the strain tensor components depends on the Least Square Matching accuracy. Let assume that displacement measurements are independent. This is true when the mesh step is larger than the template size and the accuracy is uniform ($\sigma_u = \sigma_v$) such as in the case of assumed isotropic specimen texture. Assuming no uncertainty in the determination of the mesh step Δx, and according to the error propagation law:

$$\begin{aligned} &\varepsilon_{xx}=\frac{u(i+1,j)-u(i,j)}{\Delta x}\Rightarrow\sigma_\varepsilon=\frac{\sqrt{2}}{\Delta_x}\times\sigma_u \\ &\varepsilon_{xy}=\frac{1}{2}\left(\frac{u(i,j+1)-u(i,j)}{\Delta y}+\frac{\nu(i+1,j)-\nu(i,j)}{\Delta x}\right) \\ &\Rightarrow\sigma_\varepsilon=\sqrt{\frac{1}{2\Delta^2 x}+\frac{1}{2\Delta^2 y}}\cdot\sigma_u=\frac{1}{\Delta_x}\cdot\sigma_u \quad (\Delta x=\Delta y) \end{aligned} \qquad [3.9]$$

The mesh step directly affects the uncertainty in the strain estimation: a small one provides a point strain description but with less accuracy; a larger one gives an average value of the strain with better accuracy. Thus, considering that both σ_u and σ_v depend on the accuracy in the image space, the pixel size in the object space directly defines the achievable accuracy.

3.3 Verification of the method accuracy

The performance of the method was investigated by means of several tests, aimed to assess its accuracy for both displacement and strain measurements. Comparisons between the image method strain measurements and strain gauge ones were also observed.

3.3.1 Accuracy in Displacement Measurements

The accuracy in the displacement measurements is affected by both LSM performance and template dimension. Using a small template, the assumption of strain isotropy and affine deformations becomes more realistic but the measurement redundancy drastically decreases (in terms of number of pixels considered, number of equations involved, and the likelihood of finding well-contrasted pixels). On the other hand, the use of large templates improves the redundancy but adversely affects initial assumptions of affine deformations. Indeed, the use of larger templates makes the approximation of local displacements by affine transformations harder.

The displacement measurements accuracy was assessed performing two different kinds of tests. The first set of tests was performed on synthetic images, re-sampling the original one with different transformations (translation, rotation, non-isotropic scaling and shear). The second set of tests was performed using a micrometric 10 μm slide. This kind of test was selected to account only for translations, thus neglecting the possible development of local deformations. An enlarged picture of the specimen surface was glued on the micrometer slide and imaged at each 100 μm shift. An appropriate distance between the camera and the target texture was chosen to achieve an object space accuracy of the slide of 1/1000 pixel in image space.

Figure 3.6 shows the accuracies estimated according to the template size performing the 10 μm micrometric slide test. The theoretical ε_{xx} accuracy for locally homogeneous strain fields according to the ROI dimension and the mesh step size are listed in Table 1 assuming a sensor with 1300x1000 pixels and σ_u = 1/100 pixel. For instance, for a 4 cm wide ROI and a 1300 pixel resolution in x direction, the pixel size in object space is 30 μm. Least Square Matching accuracy between 1/100 pixel and 1/150 pixel was achieved corresponding to value between 0.30 μm and 0.20 μm in image space. Assuming $\Delta x = \Delta y$ = 1mm (1200 measurement nodes), the1σ accuracy of the tensor components is:

$$\begin{aligned} \varepsilon_{xx} &: \sigma_{\varepsilon} = 0.03\% \div 0.04\% \\ \varepsilon_{xy} &: \sigma_{\varepsilon} = 0.02\% \div 0.03\% \end{aligned} \quad [3.10]$$

Table 3.1: Theoretical image system accuracy

ROI	1cm	3 cm	5 cm	10 cm
Displ Accuracy (μm)	0.08	0.23	0.38	0.77
ε grid 1mm	0.011%	0.033%	0.054%	0.109%
ε grid 2mm	0.005%	0.016%	0.027%	0.054%
ε grid 5mm	-	0.007%	0.011%	0.022%

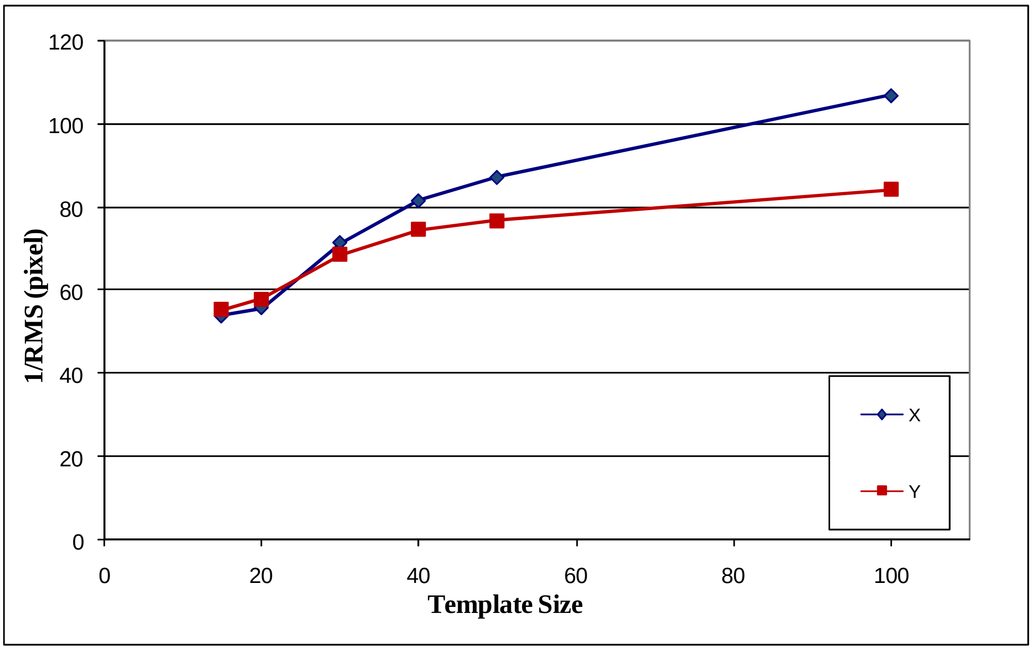

Figure 3.6: Accuracies achievable according to the template size

3.3.2 Accuracy in Strain Measurements

The accuracy achievable in the strain measurements rests on the distribution of the measurement points on the specimen surface. If the nodes are too close to each other, even a small inaccuracy in the displacement measurements may lead to large errors in the strain values as can be observed in equation [3.9]. On the other hand, if the reciprocal nodes are too distant, the local effects can be lost due to the interpolation process.

The accuracy in the strain measurements was assessed performing a test in which results obtained from the image method was compared to results obtained with on-specimen strain gauge measurements. A strain gauge, arranged in a quarter Wheatstone bridge, was mounted on an aluminum bar, machined to a dog-bone shape for an uniaxial tensile test. The strain gauge was painted to obtain a dotted pattern and imaged during the testing. Strain gauge and digital image measurements were recorded. The strain values obtained with the digital image correlation method were averaged over the strain gauge area; their differences were computed during the linear elastic portion of the stress-strain response as well as during the initial yielding stage. The ROI was about 1 cm wide and the displacement measurement grid was 0.5 mm spaced. The root mean square of the differences between the strain gauge measurement and the DIC mean strain value over the strain gauge length was about 0.003%. as shown in Figure 3.7. The result agree with the variance propagation law:

$$\sigma_{mean} = \frac{\sigma_{\varepsilon}}{\sqrt{n}} \qquad [3.11]$$

where σ_{mean} is the error in the mean value and n is the number of measurement points. Indeed, 100 measurement points uniformly distributed over the strain gauge area (with expected local accuracy σ_{ε} = 0.02÷0.03%) were used to obtain the mean strain value at each epoch.

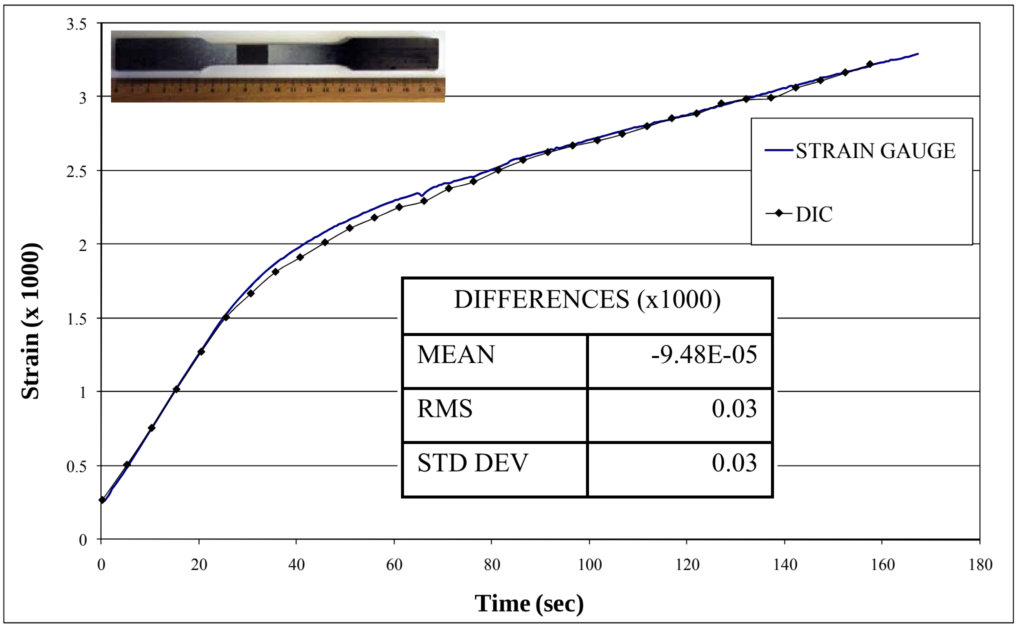

Figure 3.7: Comparison between image correlation and strain gauge measurements in uniaxial tensile test.

3.3.3 Potential measurement errors

The DIC method can be affected by measurement inaccuracy due to both test defaults and image peculiarities. The first source of errors develops when the specimen and the load direction are not parallel to the camera sensor (Figure 3.8a). In this case, perspective transformation of the object plane in the image space precludes a scale reproduction picture of the specimen surface.

Perspective projection are described by a mathematical framework, namely the collinearity equations which are commonly satisfied by a transformation. Assuming a planar specimen surface, the most generic transformation is the homography.

Collinearity equations are described as follows:

$$\begin{cases} x = \dfrac{a_1\xi + a_2\eta + a_3}{c_1\xi + c_2\eta + 1} \\ y = \dfrac{b_1\xi + b_2\eta + b_3}{c_1\xi + c_2\eta + 1} \end{cases} \qquad [3.12]$$

where (x,y) represent image space coordinates of the specimen surface, (ξ,η) represent the corresponding coordinates in a planar reference system in object space and $a_{1..3}$, $b_{1...3}$, $c_{1...2}$,are the eight parameters of the homography itself.

Drawing reference targets on the boundaries of the grabbed area by means of a calibrated mould to standardize both target dimensions and their mutual distances (Figure 3.8b), allows for the estimation of the homography (a_i, b_i and c_i parameters in eq. [3.12]) and then for the correction of specimen point coordinates (and thus their correct displacements) in object space. Nonetheless, providing a good orientation of the specimen with respect to the camera sensor ensures that all the specimen regions are imaged with the same resolution, leading to approximately the same level of accuracy at all points.

A more serious issue develops when the specimen is affected by out of plane movements during test conditioning (along the image sequence) as shown in Figure 3.8c. When the specimen or part of it moves forward or backward, a perspective deformation is registered by the camera (its picture suddenly becomes wider or smaller) leading to unreliable displacement estimation. This drawback cannot be solved with a monoscopic approach. However, using two (or more) synchronized cameras (stereoscopic approach), the 3D object displacements can be computed and relative motion between the specimen and the camera can be determined.

Specimen roughness, shown in Figure 3.8e, is the last issue of concern related to test setup. It occurs in the case of non-smooth specimen surfaces and it appears troublesome since it invalidates both the assumption that an affine transformation can approximately model the mapping between the patch and the template picture, and the hypothesis that the specimen can be approximated with a planar surface. The former issue usually becomes significant only for very rough surfaces. The template size represents just a small part of the specimen area: if the roughness is not too high, its local roughness might be well described by the affine transformation. The latter issue still remains a main concern for correct global strain field evaluation. Since homographic mapping between object and image space is strictly corrected for planar transfers, errors arise during specimen displacement estimation. The out-of-plane mapping error can be observed as a miscalculated image scale factor varying linearly on the specimen surface with the out-of-plane entity itself and the point distance from the principal point (projection of the projective centre on the image frame) in image space. In other words, the displacements in some areas of the image become larger or smaller than they really are, due to perspective effects not properly corrected by the homographic transformation. Even in this case the only practical way to solve the issue is a stereoscopic or multi-image approach. In Table 3.2, errors in terms of displacement are presented with respect to local roughness (difference between the points set nearer and farther from the camera) in specimen regions with only two points using a common camera and test set-ups and assuming a 10 pixel overall displacement (Figure 3.8e). It can be observed that even with a small out-of-plane inaccuracy (0.1 mm) with a region of interest smaller than 40x30 mm the final strain error is not negligible.

Table 3.2: Displacement and strain errors for a common camera set up (focal length 8mm, 1300x1000 resolution) due to out of plane specimen roughness. DZ is the error due to local roughness; DL is the spacing between the points in the mesh.

ROI (mm)	Out of plane displacement DZ (mm) (for a point on the frame border)							
	0.1		0.2		0.5		1.0	
	Displ(pix)	**Strain ‰**	**Displ(pix)**	**Strain ‰**	**Displ(pix)**	**Strain ‰**	**Displ(pix)**	**Strain ‰**
20x15 (Δx = 0.5 mm)	0.054	1.0	0.109	2.1	0.272	5.2	0.544	10.3
40x30 (Δx = 1 mm)	0.027	0.3	0.054	0.5	0.136	1.3	0.272	2.6
60x45 (Δx = 1.5 mm)	0.018	0.1	0.036	0.2	0.091	0.6	0.181	1.1
100x75 (Δx = 2.5 mm)	0.011	0.0	0.022	0.1	0.054	0.2	0.109	0.4

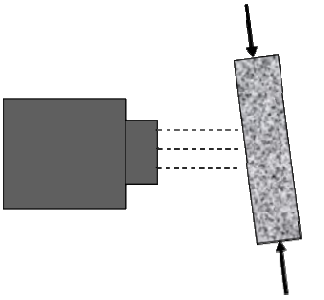

(a) specimen and load direction out of plane

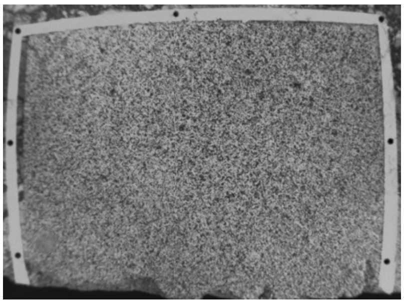

(b) reference target to control unparallelism

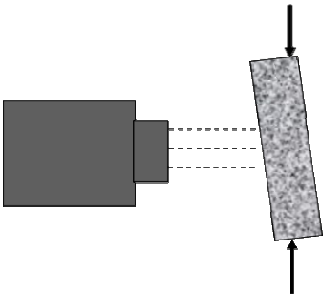

(c) specimen out of plane movement

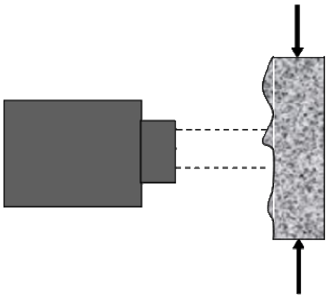

(d) specimen unflatness

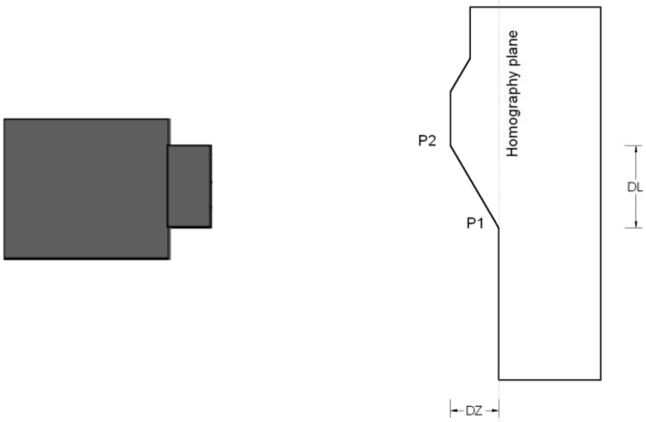

(e) local roughness

Figure 3.8: Potential elements leading to measurement errors

3.4 Tests on asphalt mixture specimens

For verifying the accuracy obtainable from the DIC measurements during HMA strength test, a single mixture (the unmodified N1) was tested using all the three configurations: IDT, SCB, 3PB. The camera, placed inside the climatic chamber on an adequate support, was set at 5 frames per second (fps) and focused at the shortest distance, providing a 5x4cm ROI located in the more stressed area of the opposite face of the specimen. The measurement grid spacing was set equal to 1mm; the pattern size was in the range of 30÷40 pixels, dot size is about 3 pixels. The origin point of the reference system attached to the specimen was selected according to the highest values of correlation between epochs and in an area not significantly stressed during all test long.

3.4.1 Accuracy achievable in HMA strength tests

The results obtained from the three HMA strength tests are shown. For each test setup one strain gauge was mounted on one face of the specimen. The same face was then treated to obtain the required texture for digital image analysis. The test was imaged and processed; then the mean strain value of the length covered by the strain gauge was estimated by the digital image system interpolating all the strain values of the grid points located at the strain gauge length. Strains registered by the strain gauge were finally compared with those estimated with the DIC System.

Computing the Root Mean Square (RMS) of the differences between measured and estimated strain values, accuracies of 0.015% for the IDT test, 0.034% for the SCB test, and 0.017% for the 3PB were obtained, as shown in Figure 3.9. These results agree well with the mean error previously estimated (~0.03%). The DIC System accuracy matches that obtained with strain gauges, while allowing a dense description of the field of interest where the cracking is developing. A big advantage resulting from the method is the opportunity of locating the specific point(s) at which cracks initiate and propagate, without constraining the analysis of HMA cracking behavior in a larger area of interest.

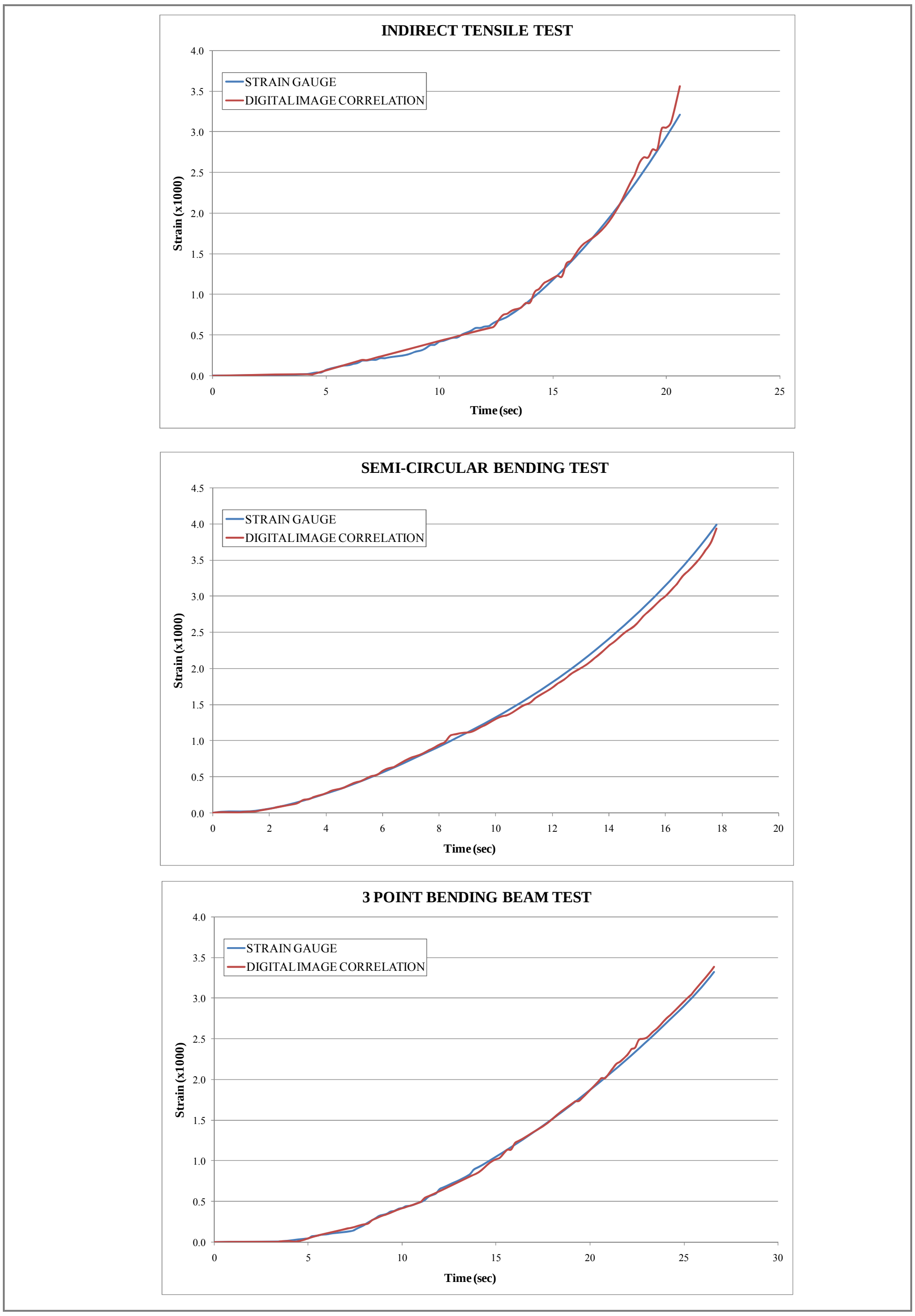

Figure 3.9: Comparison between image correlation and strain gauge measurements

3.4.2 Description of Software Tools

The visual graphic interface of the image correlation software was conceived on purpose to pick the point of interest, choosing which information is requested (horizontal/vertical/shear strains, horizontal/vertical displacements).

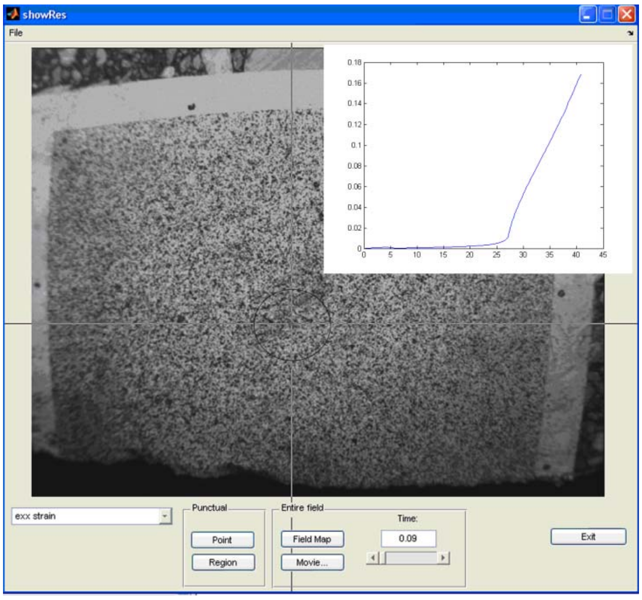

Figure 3.10 DIC System visual graphic interface

The strain values are then exported to plot stress-strain responses at the specific chosen point, as shown in Figure 3.10. This tool is very convenient for fracture mechanics analysis since it allows for strain response estimation at the accurate point in which a crack initiates.

Figure 3.11 shows an example of a comparison between horizontal strain map for the mixture during IDT test at major crack opening and the correspondent specimen image. The Figure emphasizes the capability of the DIC method to catch strain values and to visualize crack patterns at crack initiation and propagation.

Full field strain estimations allow for a comprehensive analysis of HMA cracking behavior since strains vary within the overall ROI. Traditionally, for wide area analysis, users mount multiple sensors with different lengths and positions; while in the image correlation system a single camera functions as a single sensor from which information from all the grabbed area is achievable.

Moreover, since the strain field is evaluated frame by frame, it is possible to analyze at each load step the current mechanical behavior of the specimen, selecting the option of making denser the measurement grid where a fracture opening can be spotted by looking for large gradients of the strain field. (Figure 3.12).

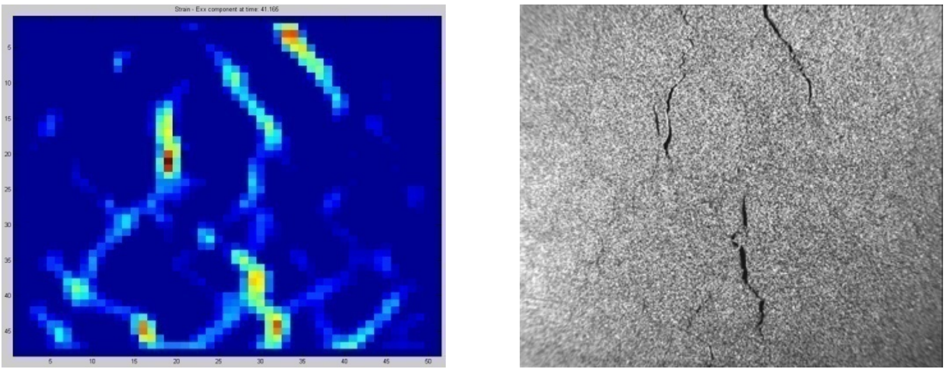

Figure 3.11 Comparison between full-field tensile strain map and the correspondent specimen image for mixture N1 during IDT test

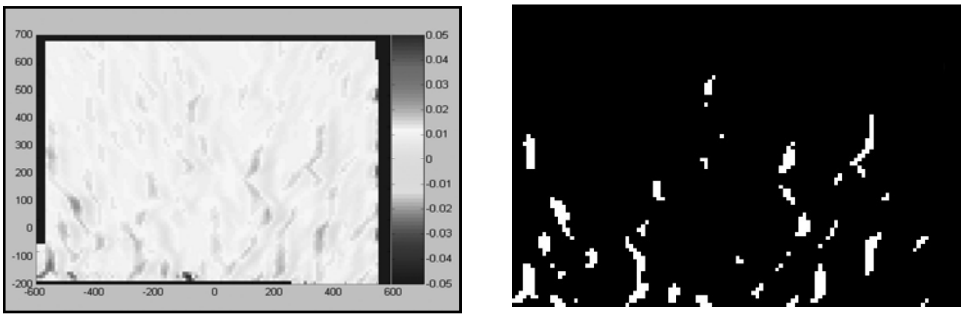

Figure 3.12 Left: Colormap of gradient value of tensile strain; right: Thresholding of the gradient field to obtain growing fracture zones.

Finally, other information not achievable by direct strain measurements can be collected. The DIC system allows for taking into account the mechanical behavior of the mastic and aggregates. Using reference marks and an image acquired before the specimen is painted, it is possible to automatically or manually generate the aggregate map, which can be used during strain field estimation to obtain correct strain values (Figure 3.13).

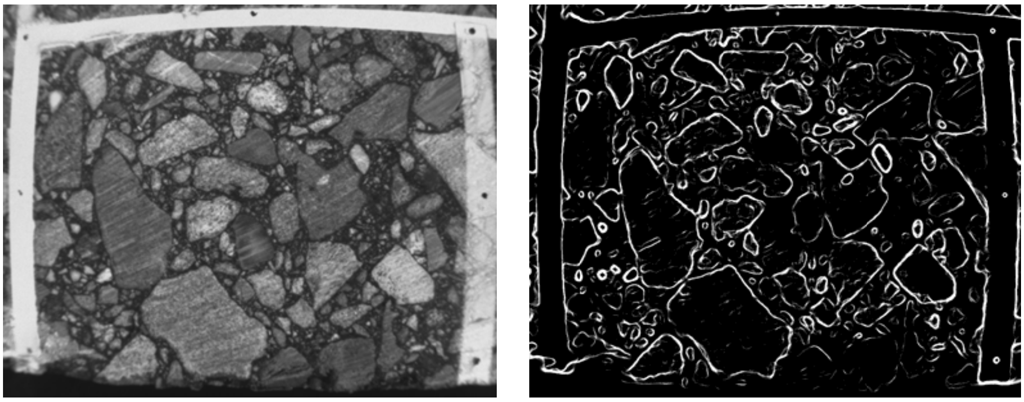

Figure 3.13 Left: Image acquired before the specimen is painted; Right: Aggregate map

3.4.3 Potential measurement errors in HMA tests

As previously described, the following elements can affect DIC measurement accuracy:

- Unparallelism between specimen/load direction and camera sensor;
- Specimen's out of plane movements during loading;
- Specimen roughness.

Two of these source of error have shown to occur in typical asphalt mixture testing configurations. The first may be checked when the specimen is affected by out of plane movements. These out-of-plane movements may occur when the specimen is not cut perpendicular to its axis, or when the specimen supports are not fully aligned.

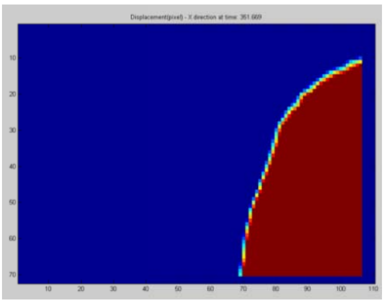

Figure 3.14 Example of a potential measurement error in HMA tests

Figure 3.14 shows the horizontal displacements of a semi-circular HMA specimen: during test loading the right side shifted forward so that artificially large displacements have been registered by the DIC system. The second source of error is due to excessive specimen surface roughness, it is therefore recommended to thoroughly clean and in case etch the specimen surface before painting.

CHAPTER 4

Prediction of HMA Crack Initiation and Propagation

The main obstacle to improved understanding of fracture mechanics-based approaches consists in the complexity of modeling crack propagation. Various models for cracks in granular materials have received considerable attention among researchers. Bazant (1986) provided a good review of existing cracking models that have been used to analyze brittle materials such as rock and concrete.

The analysis of cracks is commonly carried out by either a fracture mechanics approach or a smeared crack approach. The former assumes that a crack can be represented as a series of connected single line segments, which initiate from one or more pre-existing flaws and which propagates through the material according to certain crack growth criteria, such as maximum energy release rate. Alternatively, the smeared crack approach assumes that cracks are distributed over a finite region such that an average tensile strain adequately represents the physical presence of the cracks. With appropriate material models for compression and tension, the smeared crack approach can reasonably predict the cracking behavior of materials. Nevertheless, both methods cannot fully capture the nature of cracks in granular materials, where cracks randomly initiate along weak planes, coalesce to form a major crack band and propagate through the material.

Explicit fracture modeling using random assemblies of displacement discontinuity boundary elements provides a more realistic approach in the simulation of discrete cracks in granular materials, as discussed by Steen et al. (2001). The method employs known stress and displacement field influence functions due to defined displacement discontinuity elements that are distributed through the region of interest. The change in geometry due to crack propagation is easily handled by allowing cracks to grow only along the predefined crack paths, which can be assumed to be along aggregate boundaries or to follow internally defined fracture paths within the aggregates.

The complexity of modeling the mechanics of crack initiation and crack growth with traditional numerical methods, such as the finite element method (FEM) has been an obstacle to the incorporation of fracture mechanics-based approaches in the bituminous pavement area, as discussed in Birgisson et al. (2002). The FEM requires highly refined meshes around the cracking area in order to simulate the stresses in the vicinity of the crack tip. Improper mesh generation will result in a failure to capture the very important stress singularity at the crack tip. The simulation of crack growth with the FEM also requires elaborate re-meshing to simulate the geometry of a growing crack. The computational intensity required puts these types of problems out of the realm of reasonableness for the typical capabilities of personal computers, which means that only select research organizations and major universities have the capabilities to perform these types of calculations.

The Displacement Discontinuity (DD) Boundary Element Method (BEM) provides an attractive alternative to finite element-based methods for modeling crack initiation and crack growth. The DD method requires meshes only on the boundaries of an object or pavement, including cracks. This means that the number of elements required is reduced significantly. Also, the stress singularity at the crack tip is naturally included in the DD by using a representative displacement distribution around the crack tip. Crack growth is addressed simply by adding more DD elements in regions of crack growth.

Birgisson et al. (2002; 2003) first used the DD to assess the mechanics of fracture in the Superpave Indirect Tension Test (IDT). The same method was applied and improved in this research work to model the microstructure of asphalt mixtures and predict fracture energy density as well as crack initiation and propagation in the IDT, the SCB and the 3PB tests for all the six mixtures.

4.1 Displacement Discontinuity (DD) Boundary Element Method with Tessellation

The Displacement Discontinuity method is an indirect boundary element method developed by Crawford & Curran (1982) and Crouch & Starfield (1983) which has been extensively used in the fields of rock mechanics and geological engineering. The method has the potential to be an analytical tool for assessing cracking in granular materials such as asphalt concrete.

The numerical model consists of two types of elements: exterior boundary elements and potential crack elements. The exterior boundary elements are placed along the boundary of a problem to simulate the edge of specimen, while potential crack elements are randomly placed inside the specimen to simulate predefined crack paths, which normally are assumed to be along the grain boundary or perhaps trough grain as well.

The displacement discontinuity boundary element method can be used coupled with various tessellation schemes. The use of tessellations to represent granular structure in simulation of fracture process zone is very well accepted. It improves the realism of predicted failure mechanisms at the particle level.

Two basic tessellation schemes Delanuay and Voronoi have been used in various fields. Both tessellations can be used to simulate polycrystalline of ductile material (Van der Burg & Giessen, 1993; Helms et al., 1999). The tessellation schemes are also applicable to simulate granular structure of brittle rocks, as discussed by Napier & Peirce (1995), Napier & Malan (1997), Napier et al. (1997) and Steen et al. (2001). The suitable choice of tessellations to represent granular structure depends on the realistic looks of failure pattern and observed responses.

In 1995, Napier and Peirce developed a new boundary element solution technique, termed the "multipole method" for solving multiple interacting crack problem that involve several thousand boundary elements. They applied the new technique to study the different failure mechanisms of a rectangular rock sample under displacement control using two tessellations schemes (Delaunay and Voronoi) for three levels of grain densities. It appeared that Voronoi assemblies are less prone to shed load than the Delanuay triangulations. With increasing the density of Voronoi polygons, it seemed to not change this conclusion.

Steen et al. (2001) introduced a new type of tessellation pattern, the Voronoi tessellation with internal fracture path to simulate a confined compression test of a rock sample. From this study they found that the use of Voronoi tessellations with internal fracture paths best simulate the formation of shear band in the specimen. Also, both Rankine and Coulomb failure criteria were analyzed to identify the appropriate failure law that allowed the formation of shear bands. The results of the simulation revealed that only Coulomb failure criterion enabled localization of shear band.

Birgisson et al. (2002; 2003) used exterior boundary elements to create a 2D plain stress IDT specimen and randomly laid down potential crack elements forming Voronoi tessellation inside the specimen. With an appropriate set of material parameters for local failure at potential crack elements, the numerical prediction was found to be suitable for capturing stress strain responses and crack patterns. They found that the method was capable of evaluating mixture properties with acceptable accuracy. Also, they proved that the DD is suitable for modeling aggregate and mastic separately such that the detail of aggregate structure and strength of mastic can be investigated.

4.1.1 Theoretical Background

The DD method assumes displacements in a body are continuous everywhere except at a line of discontinuity (Figure 4.1). When the displacement crosses the line of discontinuity, its value jumps by the amount of the displacement discontinuity D_i, in which its component in local axis coordinates *y-z* are:

$$D_i(y_q) = u_i(y_q, 0) - u(y_q, 0_+) \qquad i = y,z \quad -b < y_q < b \tag{4.1}$$

where $z = 0_+$ is the positive side and $z = 0_-$ is the negative side of the discontinuity element.

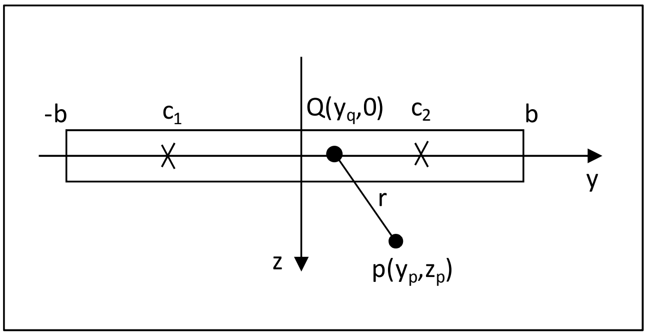

Figure 4.1 Displacement discontinuity element in local coordinates (y-z).

A linear discontinuity element has the total length of 2b with two collocation points (c_1 and c_2) at $y = \pm(\sqrt{2}/2)b$. The distance r is measured from the field point $p(y_p,z_p)$ in the domain to the source point $Q(y_q,0)$ at boundary.

Napier and Pierce (1995) have show that in two-dimensional plane strain problems, if the line of discontinuity has a length of 2b, centered on the y-axis of a local coordinate system y-z, and has normal vector components n_y and n_z along the surfaces, the contribution of a given element to the total displacement components at point p is:

$$\begin{pmatrix} u_y(p) \\ u_z(p) \end{pmatrix} = \frac{1}{8\pi(1-\nu)} \int_{-b}^{b} \begin{bmatrix} L_y & M_y & N_y \\ L_z & M_z & N_z \end{bmatrix} \begin{bmatrix} D_y(y_q)n_y \\ \frac{1}{2}(D_y(y_q)n_z + D_z(y_q)n_y \\ D_z(y_q)n_z \end{bmatrix} dy_q \tag{4.2}$$

where u_y, u_z are the local components of the displacement vector, ν is Poisson ratio and the symbols in matrix are given by:

$$\begin{aligned}
L_y &= (1-\nu)\Psi_{,yyy} + (2-\nu)\Psi_{,yzz} \\
M_y &= -\nu\Psi_{,yyz} + (1-\nu)\Psi_{,zzz} \\
N_y &= \nu\Psi_{,yyy} - (1-\nu)\Psi_{,yzz} \\
L_z &= -(1-\nu)\Psi_{,yyz} + \nu\Psi_{,yzz} \\
M_z &= (1-\nu)\Psi_{,yyy} - \nu\Psi_{,yzz} \\
L_z &= (2-\nu)\Psi_{,yyz} + (1-\nu)\Psi_{,zzz}
\end{aligned} \quad [4.3]$$

The biharmonic function for plain strain problem is given by:

$$\Psi = \frac{1}{2}(r^2 - r^2 \log r^2) \qquad \text{and} \qquad r^2 = (y_p - y_q)^2 + z_p{}^2 \quad [4.4]$$

As discussed by Napier and Peirce (1995), the contribution of the element to the total stress tensor components at point p is given by:

$$\begin{bmatrix} \sigma_{yy}(y_p, q_p) \\ \sigma_{yz}(y_p, q_p) \\ \sigma_{zz}(y_p, q_p) \end{bmatrix} = \frac{E}{8\pi(1-\nu^2)} \int_{-b}^{b} \begin{bmatrix} -\Psi_{,zzzz} & \Psi_{,yzzz} & -\Psi_{,yyzz} \\ \Psi_{,yzzz} & -\Psi_{,yyzz} & \Psi_{,yyyz} \\ -\Psi_{,yyzz} & \Psi_{,yyyz} & -\Psi_{,yyyy} \end{bmatrix} \begin{bmatrix} D_y(y_q)n_y \\ D_y(y_q)n_z + D_z(y_q)n_y \\ D_z(y_q)n_z \end{bmatrix} dy_q \quad [4.5]$$

For numerical implementation, the displacement discontinuity D_i is approximated by a polynomial function:

$$y = a_0 + a_1 x^1 + a_2 x^2 + \ldots + a_n x^n \quad [4.6]$$

More accurate results can be obtained by using several terms in the approximation, but increasing computing time. For most practical applications it is better to approximate the displacement discontinuity with a linear function as done for the Discontinuity Interaction and Growth Simulation (DIGS) (Napier, 1990; Napier & Hildyard, 1992; Napier & Peirce, 1995; Malan & Napier, 1995; Kuijpers & Napier, 1996; Napier et al., 1997, Napier & Malan, 1997). The linear variation of discontinuity can be written as:

$$D_i(y_q) = a_i + b_i y_q \qquad a_i \text{ and } b_i \text{ are constants} \quad [4.7]$$

By substituting [4.7] into [4.6], and carrying out the mathematical manipulation, the analytical solution for normal stress on the y-axis of the local coordinates system (y-z) is given by:

$$\sigma_{zz}(y,0)=\frac{E}{8\pi(1-\nu^2)}\left[2(\alpha_z+\beta_z y)\left(\frac{1}{y+b}-\frac{1}{y-b}\right)+\beta_z\log\left(\frac{y+b}{y-b}\right)^2\right] \qquad [4.8]$$

It is obvious from equation [4.8] that the analytical normal stress σ_{zz} approaches infinity as y approaches the tip of the element y = ±b. However, in boundary element formulations, stress in equation [4.8] is evaluated at suitable collocation points y = ±c, namely the Gauss-Chebyshev points, as described by Crawford and Curran (1982):

$$y_i=\cos(2i-1)\frac{\pi}{2n} \qquad i = 1, 2, \ldots, n \qquad [4.9]$$

The stresses at collocation points will have finite values and are solvable using a numerical algorithm.

4.1.2 Numerical Implementation

The DD method employs the fundamental solutions of a discontinuity surface (or crack) to formulate a system of governing equations. For a problem with one crack in an infinite elastic body without far field stresses, the general system of governing equations can be written as:

$$\begin{aligned}\sigma_s^i&=\sum_j\left(A_{ss}^{ij}D_s^j+A_{sn}^{ij}D_n^j\right)\\ \sigma_n^i&=\sum_j\left(A_{ns}^{ij}D_s^j+A_{nn}^{ij}D_n^j\right)\end{aligned} \qquad [4.10]$$

where σ^i_s and σ^i_n are the shear and normal stress of the element i, respectively; A^{ij}_{ss}, A^{ij}_{sn}, A^{ij}_{ns} and A^{ij}_{nn} are the influence coefficients due to element j on element i, and D^j_s and D^j_n and are the displacement discontinuity components of the element *j*, which are the unknowns of the system.

In simulations of crack interaction problems, a displacement discontinuity element can either slide if the driving shear stress exceeds the shear strength or open up if the applied tensile stress exceeds the tensile strength. Although the DDM was initially developed for an open crack, it can be easily extended to include contacting crack surfaces and sliding cracks in softening mode.

When two crack surfaces are in contact at collocation point I, the shear and normal stress components σ^i_s and σ^i_n depend on the stiffness (K_s and K_n) and the displacement discontinuity components (D^j_s and D^j_n). The relationships can be written in matrix forms as follows:

$$\begin{aligned} \sigma^i_s &= K_s D^i_s \\ \sigma^i_n &= K_n D^i_n \end{aligned} \qquad [4.11]$$

By substituting [4.11] into [4.10] and rearranging the terms so that the unknowns are on the right hand side, the system of governing equations then becomes:

$$\begin{aligned} 0 &= \sum_j \left(A^{ij}_{ss} D^j_s + A^{ij}_{sn} D^j_n \right) - K_s D^i_s \\ 0 &= \sum_j \left(A^{ij}_{ns} D^j_s + A^{ij}_{nn} D^j_n \right) - K_n D^i_n \end{aligned} \qquad [4.12]$$

When an element is mobilized, the crack surface will deform according to the softening models, which will be described shortly in the next session. The residual strength of the element i, namely σ^i_s and σ^i_n can be assumed to decrease as a function of the discontinuities D^j_s and D^j_n, which are expressed as follows:

$$\begin{aligned} \sigma^i_s &= f_s(D^i_s, D^i_n) \\ \sigma^i_n &= f_n(D^i_s, D^i_n) \end{aligned} \qquad [4.13]$$

Substituting equation [4.13] in equation [4.10] and rearranging the unknowns to the right hand side, the system of equations becomes:

$$\begin{aligned} 0 &= \sum_j \left(A^{ij}_{ss} D^j_s + A^{ij}_{sn} D^j_n \right) - f_s\left(D^i_s, D^i_n \right) \\ 0 &= \sum_j \left(A^{ij}_{ns} D^j_s + A^{ij}_{nn} D^j_n \right) - f_n\left(D^i_s, D^i_n \right) \end{aligned} \qquad [4.14]$$

Finally, a set of algebraic equations that consists of known driving forces, influence coefficients and the unknown displacement discontinuities can be written in matrix form:

$$\{\sigma\} = [A]\{D\} \quad [4.15]$$

Since the mobilization of cracks is associated with a softening model in which stresses depend on the unknown discontinuities, an interactive technique needs to be employed in solving the equations. Once displacement discontinuities at all boundary elements have been determined, displacements and stresses at any designated points can be computed by using known solutions of discontinuity surfaces as discussed by Napier and Peirce (1995).

4.1.3 Crack Growth Algorithm

The numerical model consists of two types of elements: exterior boundary elements and potential crack elements (Figure 4.2). These represent respectively, the boundary surface of the specimen and internal sites where potential crack elements are selected for mobilization (slip or tensile opening modes). The Voronoi tessellation approach is adopted to account for the presence of aggregates in which displacement discontinuity elements are randomly placed inside the specimen forming Voronoi patterns of predefined paths. At each load step, stresses are computed at collocation points inside the potential crack elements; these stresses are then checked against a failure limit to determine whether or not a crack has been activated.

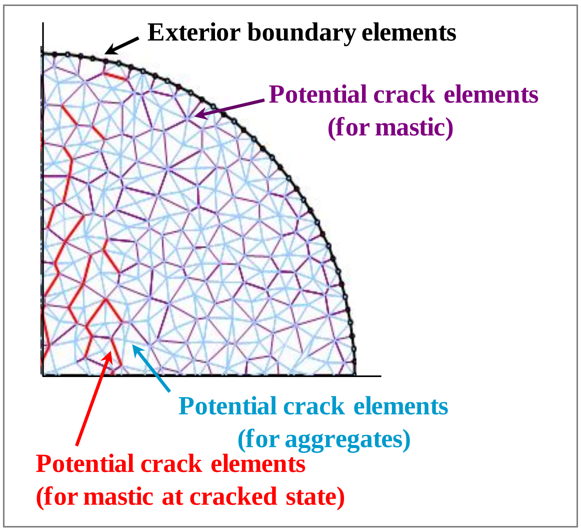

Figure 4.2 Voronoi tessellations with internal fracture paths representing the aggregate structure

A nonlinear Mohr-Coulomb type of failure law, shown in Figure 4.3, is adopted for the cracking criterion.

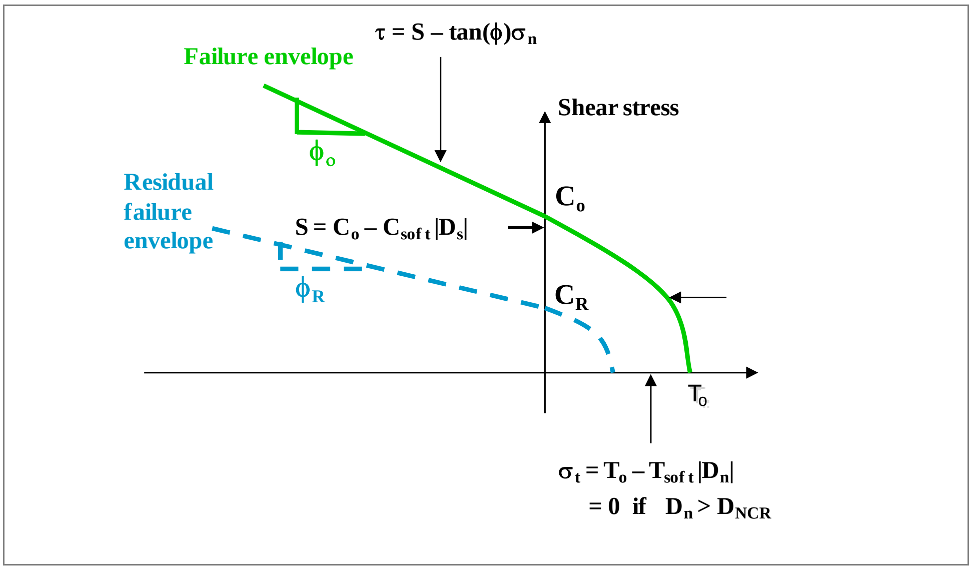

Figure 4.3 Failure criterion for determining crack mobilization

The failure law comprises a linear portion in the compression region that changes over to a power law curve in the tension region, with a continuous slope at $\sigma_n = 0$.

The linear portion has the following form:

$$\tau = S - \tan(\Phi)\sigma_n \qquad \text{when } \sigma_n = 0 \qquad [4.16]$$

where S is the cohesion, Φ is the friction angle and σ_n is the normal stress across the discontinuity that is assumed to be negative when compressive.

The power law curve is defined by:

$$\tau = a(\sigma_t - \sigma_n)^b \qquad \text{when } 0 < \sigma_n < \sigma_t \qquad [4.17]$$

where σ_t is the tensile strength and the two constants a and b are chosen to match the value and the slope of the linear portion of the failure envelope when $\sigma_n = 0$.

For every load step, a crack search algorithm is performed to detect cracks that may occur in the specimen. At the end of each search step, the detected cracks are added to the system and resolved for determining new cracks in the next search step, until no more cracks are found.

When a potential crack element is mobilized, the cohesion S is assumed to weaken as a linear function of the slip Ds:

$$S = C_0 - C_{soft} \left| D_s \right| \qquad [4.18]$$

where C_o is the original cohesion intercept and C_{soft} is the rate of cohesion softening.

Similarly, the tensile strength σ_t is also assumed to weaken as a linear function of the opening displacement D_n:

$$\sigma_t = T_0 - T_{soft} \left| D_n \right| \qquad [4.19]$$

where T_o is the tension cutoff and T_{soft} is the rate of tension softening. When crack slip occurs, the tensile strength is implicitly degraded as the cohesion softens, congruently with the extent of cohesion softening.

4.2 HMA Fracture Test Models

The IDT, SCB and 3PB specimens geometries were modeled using an appropriate number of discontinuity elements defining the relevant load or displacement conditions on the boundary. The regions inside the specimen models are covered by a random mesh of Voronoi polygons, providing a specific number of potential crack elements according to the aggregate nominal maximum size; additional crack paths are obtained in the Voronoi tessellation by connecting the geometric center of the Voronoi polygons with the vertices of the polygons, to simulate potential fracturing of aggregates. A preliminary study to evaluate the optimal average Voronoi particle sizes for the mixtures were performed. The IDT tessellation has 503 particles filling the circular area of 17662.5 mm^2, the SCB tessellation has 251 particles filling the semi-circular area of 8831.2 mm^2 and the 3PB tessellation has 618 particles filling the rectangular area of 22500 mm^2. Thus, it was found that for realistic simulations, Voronoi particles with an average size of 6.8 mm diameter or D_{50} (aggregate size at 50% passing of the gradation) represented the aggregate structure of the mixes reasonably well.

4.2.1 IDT Model

The IDT specimen model is shown in Figure 4.4.

The perimeter of the modeled specimen is defined using 152 appropriately located displacement discontinuity elements; of those, 8 elements are placed at the top and forced to move downward to simulate displacement control; other 8 elements at the top are fixed to provide a static condition. The remaining 136 elements along the circumference are specified with zero traction to simulate traction free surface. Inside the specimen model, the random mesh of Voronoi polygons provides 1826 potential crack elements (for mastic) and 3549 additional potential aggregate fracture paths.

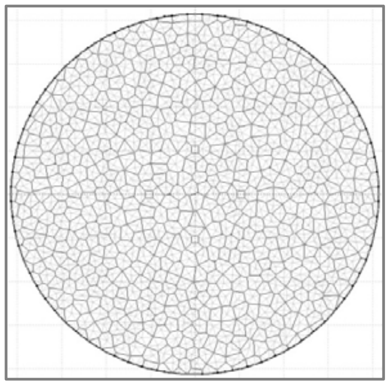

Figure 4.4 IDT specimen model

The elements under the top platen were subsequently displaced in 16 equal steps to simulate the total measured vertical displacement. For each load step, horizontal and vertical stresses are evaluated at the center of the specimen using 2D plane stress formulas:

$$\begin{aligned} \sigma_v &= 6P / (\pi D t) \\ \varepsilon_v &= \Delta V / L_{gauge} \\ \sigma_h &= 2P / (\pi D t) \\ \varepsilon_h &= \Delta H / L_{gauge} \end{aligned} \qquad [4.20]$$

where, σ_v is the vertical stress at the center of the specimen, P is a total applied load, D is the diameter of the specimen, t is the thickness of the specimen, ε_v is an average vertical strain over a vertical strain gauge, ΔV is a vertical deformation measured at a vertical strain gauge, L_{gauge} is a gauge length (38.1 mm). The stress component σ_h is the theoretical uniform tensile stress across the depth of the IDT specimen, ε_h is an average horizontal strain over a horizontal strain gauge, ΔH is a horizontal deformation measured at a horizontal strain gauge.

4.2.2 SCB model

The SCB model is shown in Figure 4.5.

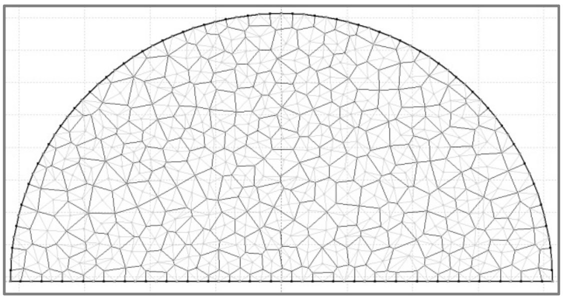

Figure 4.5 Semi-Circular Bending specimen model

The perimeter of the modeled SCB specimen is defined using 128 appropriately located displacement discontinuity elements. The region inside the specimen model is covered by 665 (for mastic) potential crack elements and 1268 additional potential aggregate fracture paths. The edges below the SCB top ring consist of 8 elements, while the edges above each of the two SCB support rings consist of 4 elements. The remaining 112 elements along the semi circumference are specified with zero traction to simulate a traction free surface. The elements under the top ring were subsequently displaced in 16 equal load steps. For each load step, the horizontal stress was computed using equation [2.3], while the simulated horizontal deformation ε_h was computed as for the IDT but assuming a gauge length of 20mm.

4.2.3 3PB model

The 3PB specimen model is shown in Figure 4.6.

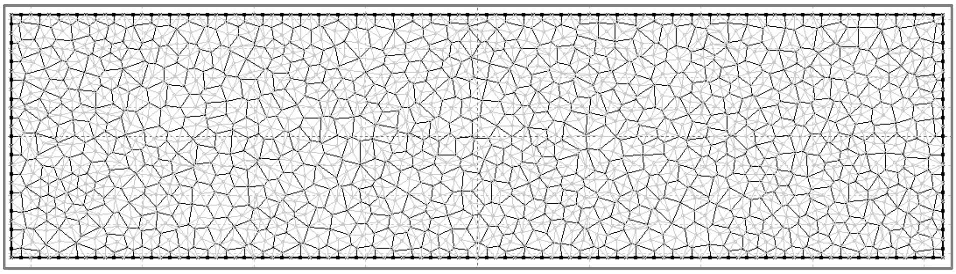

Figure 4.6 Three Point Bending Beam model

The modeled Beam specimen consists of 252 DD boundary elements, 1718 potential crack elements (for mastic) and 3562 additional potential aggregate fracture paths. As in the SCB, the edges below the top ring consist of 8 elements, while the edges above the each support ring consist of 4 elements. The remaining 236 elements along the perimeter are specified with zero traction to simulate a traction free surface. The elements under the top ring were subsequently displaced in 16 equal load steps. For each load step, the horizontal stress was computed using equation [2.4], while the simulated horizontal deformation ε_h was computed as for the IDT and the SCB but assuming a gauge length of 50mm.

4.3 HMA Parameters Calibration

The global material parameters (Young modulus and Poisson ratio) for the numerical models of the six mixtures were obtained from Superpave IDT tests. For a given stress-strain curve, the secant modulus at any point on the curve is calculated by:

$$E = \frac{1}{\varepsilon_h}(\sigma_h - \nu\sigma_v) \qquad [4.21]$$

The secant modulus at half the ultimate load seems to result in reasonable simulations of the stress-strain curves.

Local material parameters for the mastic and internal fracture paths for the three numerical models of the six mixtures were determined by numerical calibration from a parametric study based on Suerpave IDT results. In this parametric study, local material properties were varied in a systematic fashion until a reasonable fit to the experimental data (vertical and horizontal stress-strain response) was achieved. Once the input parameters were obtained for the Superpave IDT test results, these same parameters were used to predict the stress-stain response in the SCB and the 3PB tests. The resulting calibrated parameters for each mixture are listed in Table 4.1 The same local material parameters for the internal fracture paths were used for the six mixtures numerical models since all the six mixtures have the same aggregate gradation.

The plots obtained from the numerical calibration for the six mixtures are shown from Figure 4.7 to Figure 4.12. Once the stress-strain response has been determined, the tensile strength at fracture and fracture energy density were evaluated.

Table 4.1 Calibrated material parameters for the parametric study of the six mixtures

Parameters	Internal fracture paths	Mastic N1	Mastic N2	Mastic RM3.5	Mastic RM5.0	Mastic LM3.5	Mastic LM6.5
T_0 (MPa)	6.40	3.60	2.20	3.40	3.50	3.50	3.60
D_{NCR} (mm)	0.09	0.12	0.12	0.14	0.13	0.16	0.12
T_{soft} (MPa/mm)	10.0	10.0	10.0	10.0	10.0	10.0	10.0
C_0 (MPa)	6.40	3.60	2.20	3.20	3.20	3.20	3.20
C_R (MPa)	0.12	0.18	0.11	0.10	0.11	0.09	0.11
C_{soft} (MPa/mm)	1.00	1.00	1.00	1.00	1.00	1.00	1.00
ϕ_0 (degree)	40	38	44	38	40	38	40
ϕ_R (degree)	36	32	38	36	38	36	34
Young Modulus (MPa)		10500	6200	6100	4600	5800	3800
Poisson's ratio		0.36	0.35	0.26	0.26	0.29	0.29

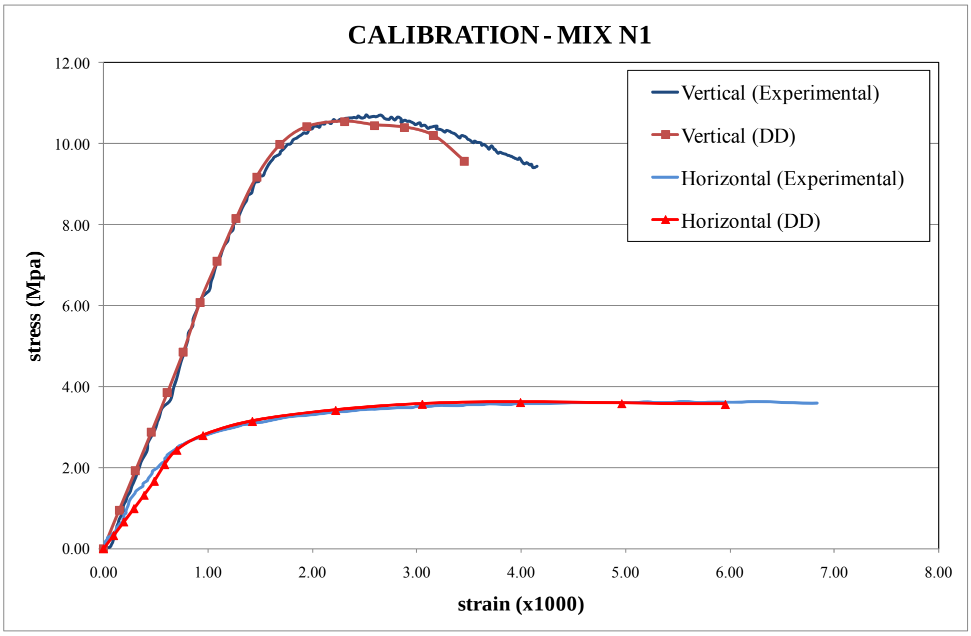

Figure 4.7 Matching of the experimental and DD stress-strain response for mixture N1

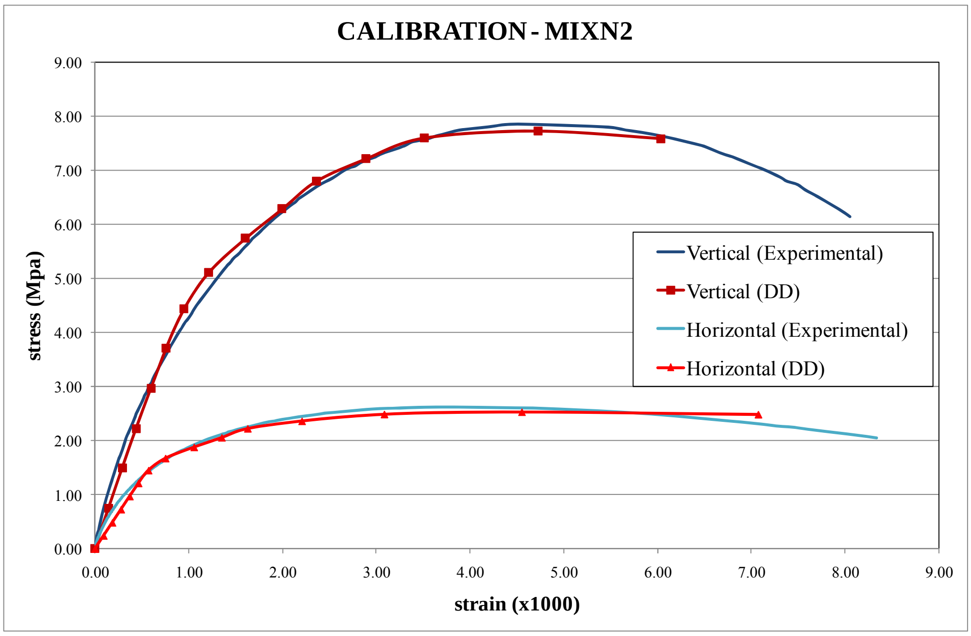

Figure 4.8 Matching of the experimental and DD stress-strain response for mixture N2

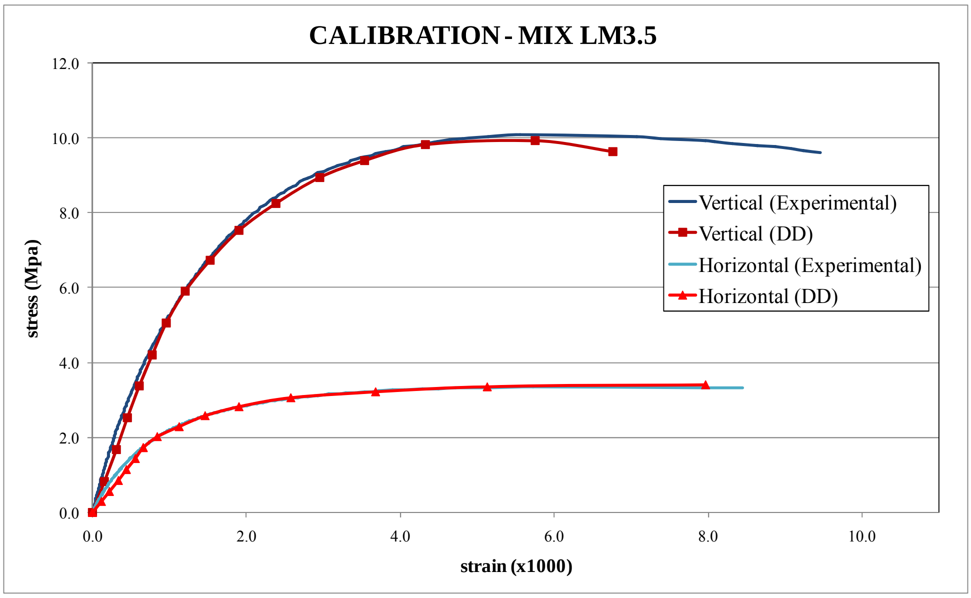

Figure 4.9 Matching of the experimental and DD stress-strain response for mixture RM3.5

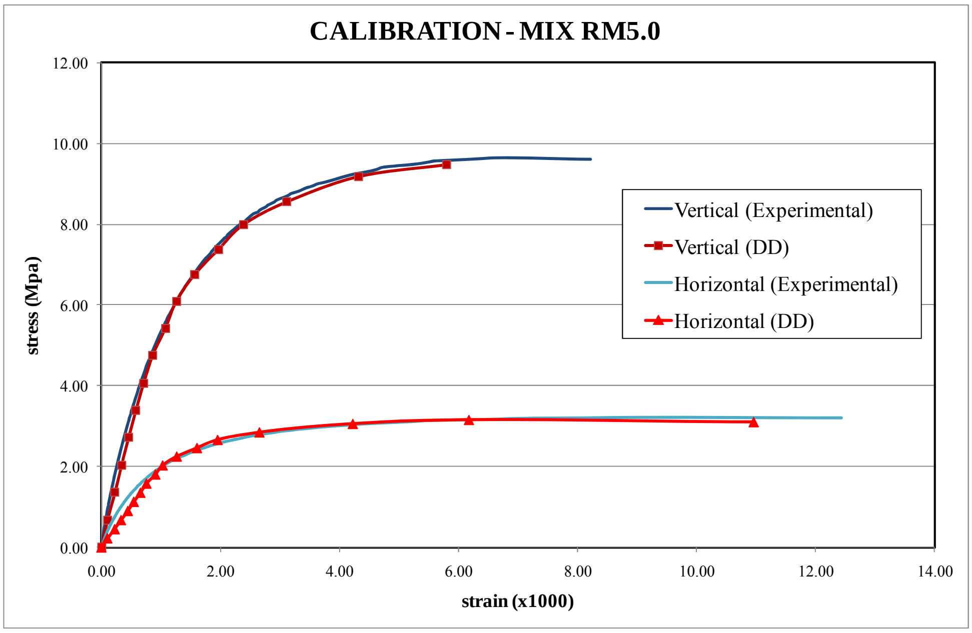

Figure 4.10 Matching of the experimental and DD stress-strain response for mixture RM5.0

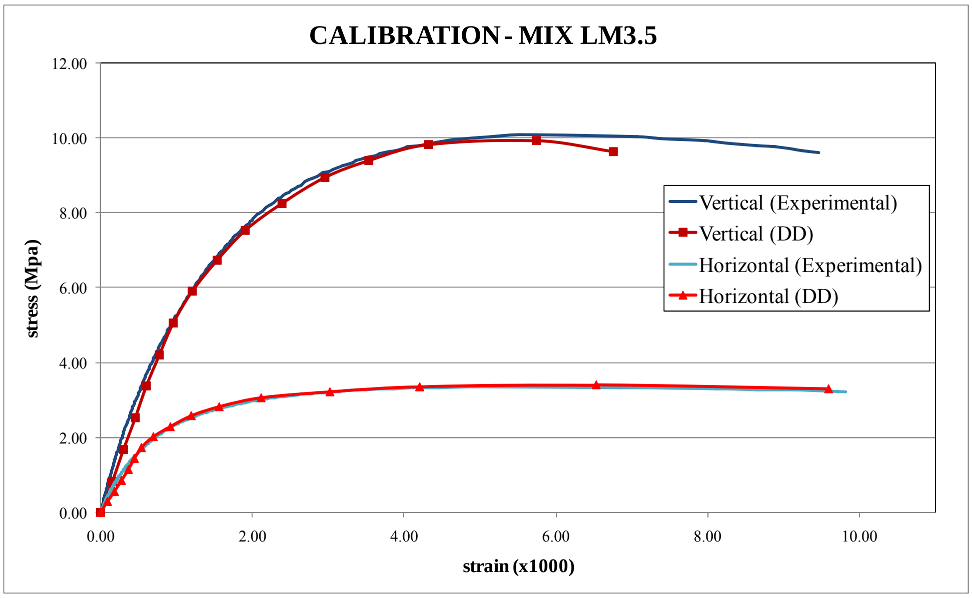

Figure 4.11 Matching of the experimental and DD stress-strain response for mixture LM3.5

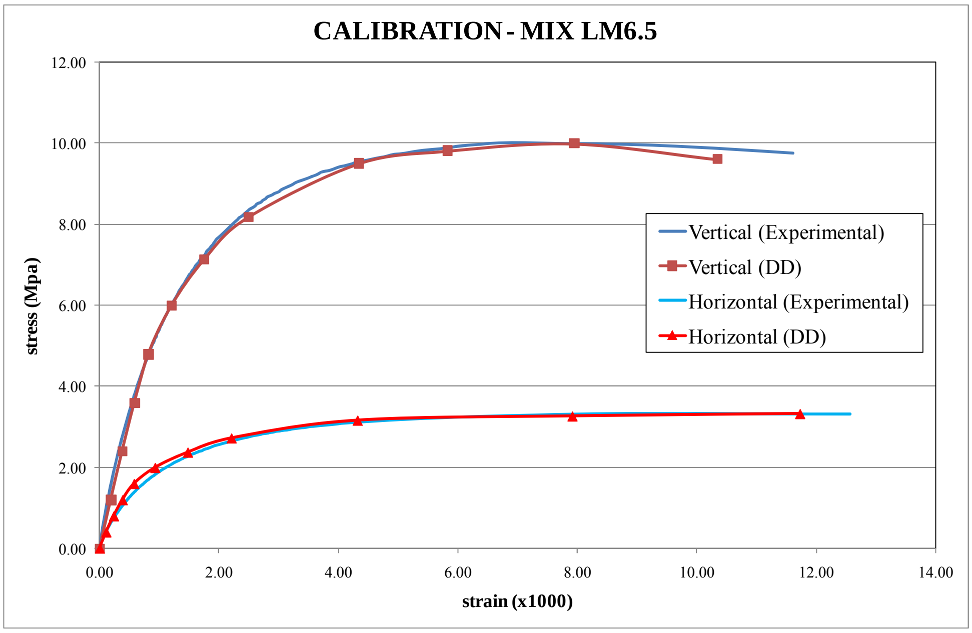

Figure 4.12 Matching of the experimental and DD stress-strain response for mixture LM6.5

4.4 Evaluation of Fracture Energy Density with DD

In the IDT simulation, "simulated strain" gauge deformation are evaluated across the center portion of the specimen at offsets of ± 19 mm horizontally away from the line of symmetry. In the SCB simulation, "simulated strain" gauge deformation values are picked over the central portion of the bottom edge of the semi-circular specimen at a vertical distance of 10.0 mm above the bottom edge of the specimen and at offsets of ±10 mm horizontally away from the line of symmetry. Similarly, in the 3PB simulation the "simulated strain" gauge deformation value is obtained over the central portion of the bottom edge of the beam specimen a vertical distance of 10.0 mm above the bottom edge of the specimen and at offsets of ±25 mm horizontally away from the line of symmetry. 3D effects are accounted for applying bulging correction factors C_{bh} and C_{bv}, shown in Table 4.2, to correct the measured horizontal and vertical deformation to fit the deformation in a flat plane, as described by Roque and Buttlar (1992) and Birgisson, et al. (2003) :

$$\begin{aligned} H_{corrected} &= H_{measured} C_{bh} \\ V_{corrected} &= V_{measured} C_{bv} \end{aligned} \quad [4.22]$$

Table 4.2 Correction Factors accounting for bulging effects

Poisson's ratio		Diameter/length – to – thickness ratio (t/D)				
	υ	0.167	0.333	0.500	0.625	0.750
C_{bh}	0.20	0.9816	0.9638	0.9461	0.9358	0.9294
	0.35	0.9751	0.9518	0.9299	0.9179	0.9108
	0.45	0.9722	0.9466	0.9234	0.9111	0.9040
C_{bv}	0.20	0.9886	0.9748	0.9677	0.9674	0.9688
	0.35	0.9808	0.9588	0.9479	0.9473	0.9493
	0.45	0.9759	0.9492	0.9361	0.9358	0.9380

The corrected horizontal and vertical deformation is then divided with the gauge length GL to obtain the average strain. Finally, center correction factors C_{eh} = 1.072 and C_{ev} = 0.977 are used to correct the strain values:

$$\varepsilon_{h\_corrected} = \frac{H_{corrected}}{GL} C_{eh}$$
$$\varepsilon_{v\_corrected} = \frac{V_{corrected}}{GL} C_{ev} \qquad [4.23]$$

Likewise, horizontal and vertical stresses are evaluated (at the center of the specimen for IDT test and at central portion of the bottom edge for SCB and 3PB tests), using 2D plane stress formulas and then are corrected with the stress correction factors $C_{\sigma h}$ and $C_{\sigma v}$ to convert 2D plane stress to the stresses on the surface of a 3D specimen:

$$\sigma_{h\_corrected} = \frac{2P}{\pi Dt} C_{\sigma h}$$
$$\sigma_{v\_corrected} = \frac{6P}{\pi Dt} C_{\sigma v} \qquad \text{for IDT} \qquad [4.24]$$

$$\sigma_{h\_corrected} = 2.2 \frac{P}{Dt} C_{\sigma h} \qquad \text{for SCB} \qquad [4.25]$$

$$\sigma_{h\_corrected} = 1.5 \frac{PL}{th^2} C_{\sigma h} \qquad \text{for 3PB} \qquad [4.26]$$

The fracture point in the specimens were determined by plotting the deformation differential ($V_{corrected}$ - $H_{corrected}$) during the numerical simulation, and visually observing the point at which the deformation differential starts to deviate from a smooth curve.

Figures from 4.13 to 4.19 show the predicted deformation differential for each mixture determined for each test simulation. Based on the fracture point, the predicted horizontal deformations were used to evaluate the fracture energy density.

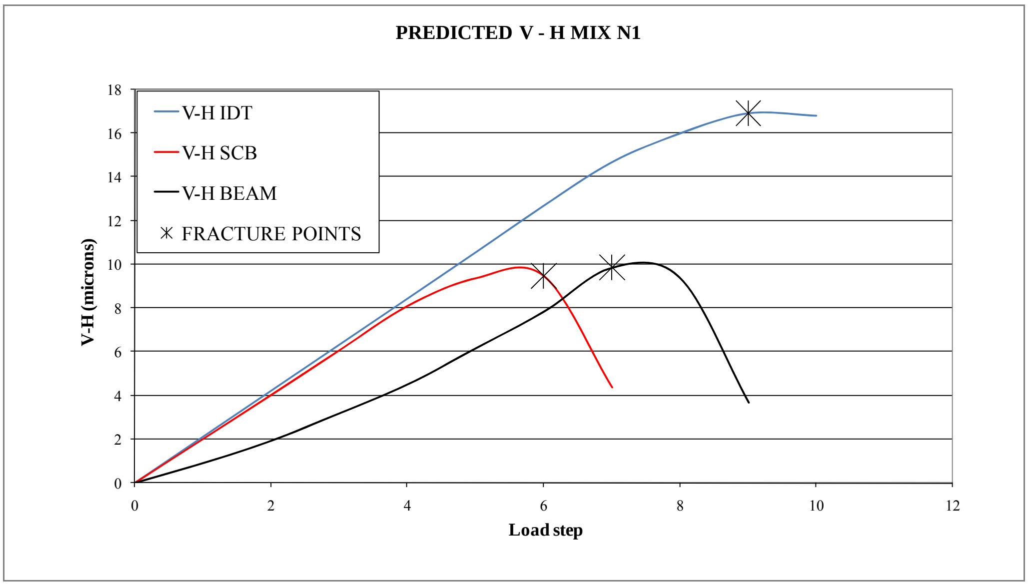

Figure 4.13 Simulated deformation differential for mix N1 during IDT, SCB and 3PB tests.

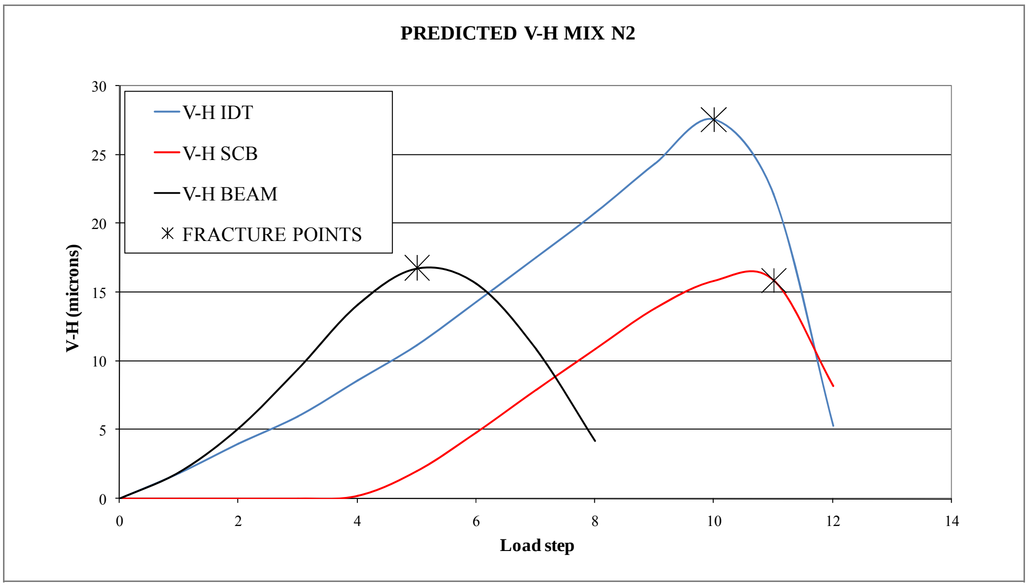

Figure 4.14 Simulated deformation differential for mix N2 during IDT, SCB and 3PB tests.

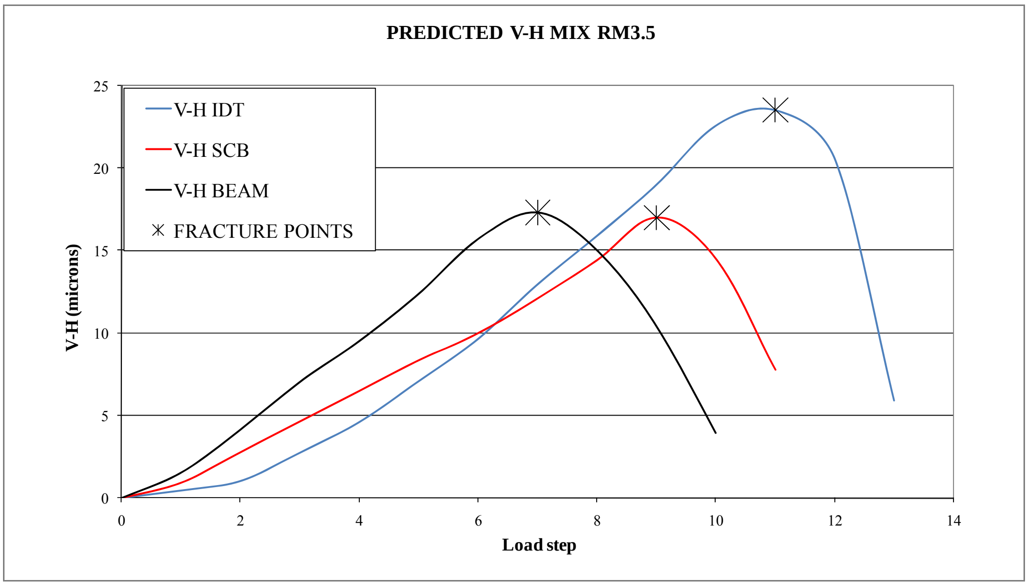

Figure 4.15 Simulated deformation differential for mix RM3.5 during IDT, SCB and 3PB tests.

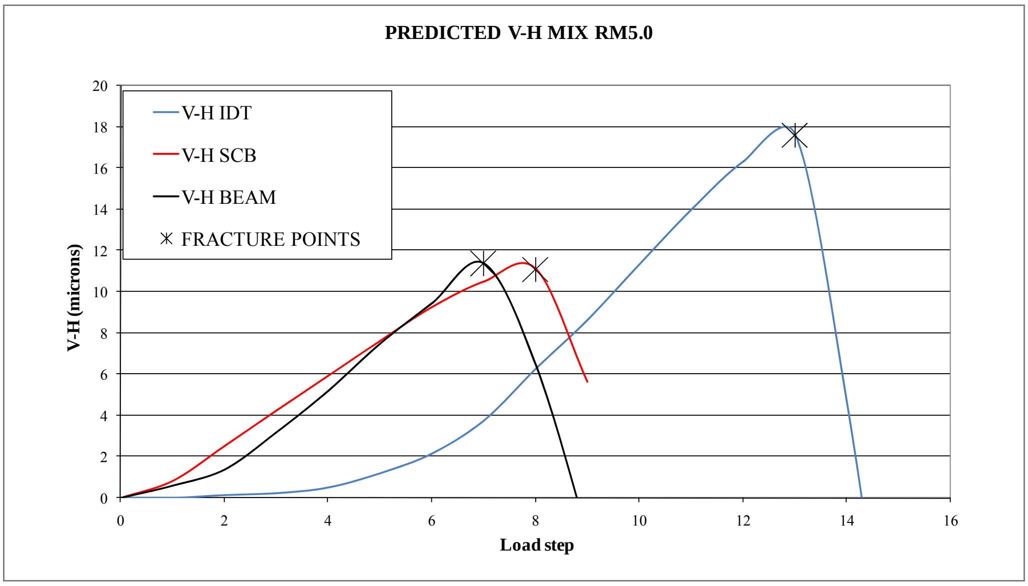

Figure 4.16 Simulated deformation differential for mix RM5.0 during IDT, SCB and 3PB tests.

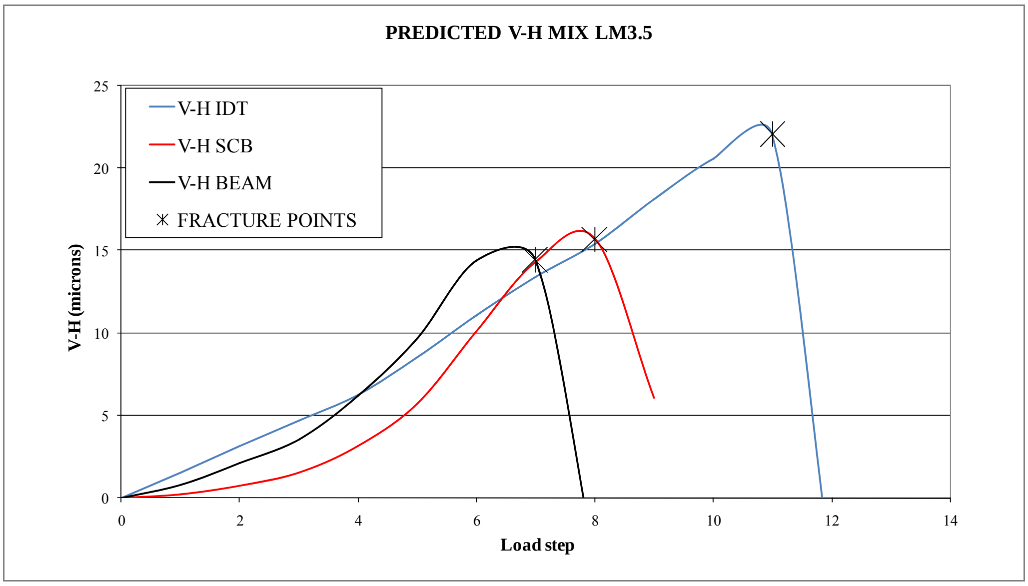

Figure 4.17 Simulated deformation differential for mix LM3.5 during IDT, SCB and 3PB tests.

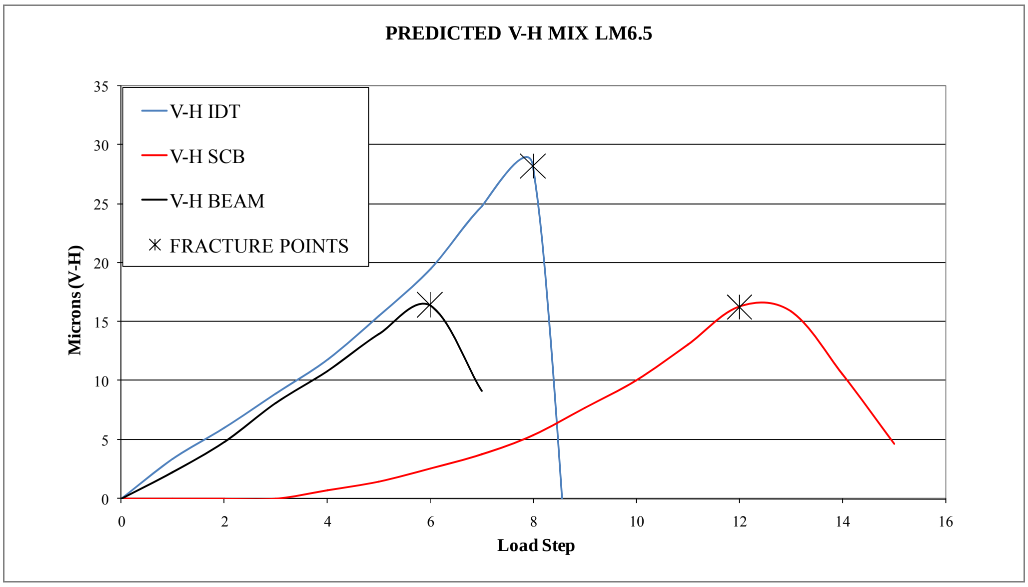

Figure 4.18 Simulated deformation differential for mix LM6.5 during IDT, SCB and 3PB tests.

CHAPTER 5

Finding and Analysis

Results from laboratory investigation and numerical predictions are shown and discussed in this chapter.

5.1 Fracture Tests Results

A total of 54 specimens, 9 for each mixture (3 IDT, 3 SCB, 3 3PB) were tested at 10 °C. For each testing setup, three replicates were performed monitoring strains with both strain gauge and digital image correlation analyses. The tests were imaged and processed; two different strain curves were estimated with the DIC System: a “pinpoint” one obtained estimating the strain value at the specific point in which a crack develops and an “average” one obtained estimating the mean strain value of the length covered by the strain gauge. The mean strain value was estimated interpolating all the strain values computed over the strain gauge length. It must be highlighted that the strain gauge was mounted on the opposite face of the imaged one.

In the tests performed, fracture points were identified as the point in the instant in which a crack was found to have visibly initiated, then fracture energy densities were computed as the resulting area under the stress-strain curve up to the fracture point

Figures from 5.1 to 5.18 compare the horizontal stress-strain responses of the three tests, evaluated by strain gauge and image correlation as mean values. Fracture points obtained by the DIC System match very well with the strain gauge results. This means that fracture energy corresponds to that specific strain energy value at the point of impending macro-cracking.

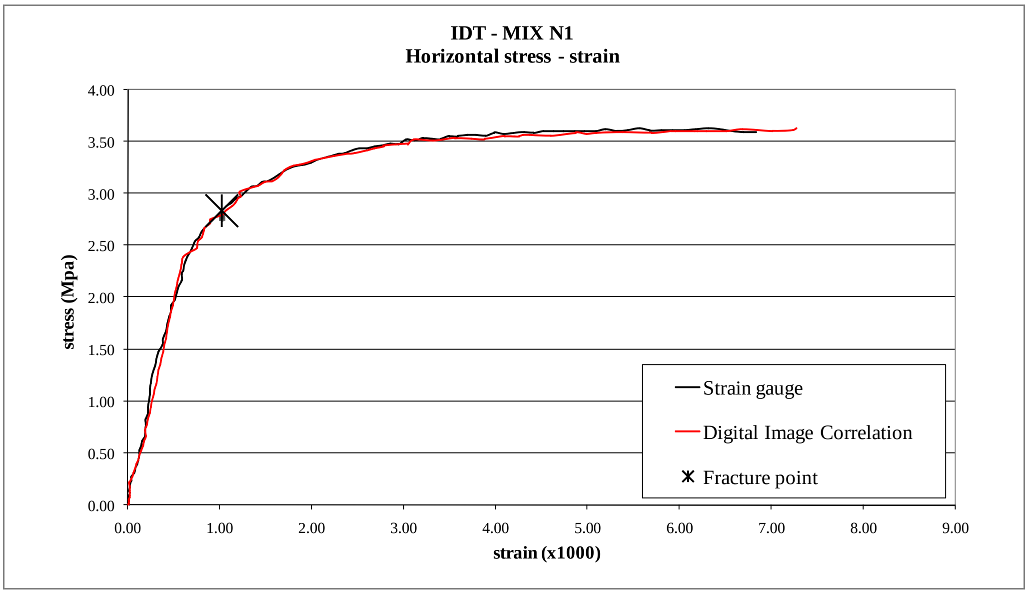

Figure 5.1 Comparison between experimental and mean image correlation horizontal stress-strain response for mixture N1 (virgin; PG 64-22) during IDT.

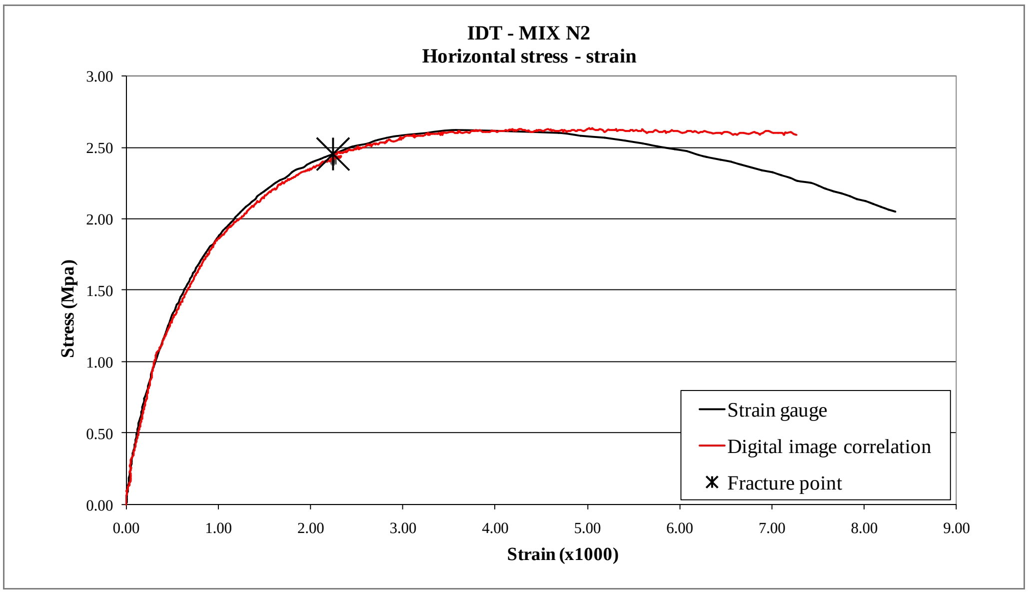

Figure 5.2 Comparison between experimental and mean image correlation horizontal stress-strain response for mixture N2 (virgin; PG 58-22) during IDT.

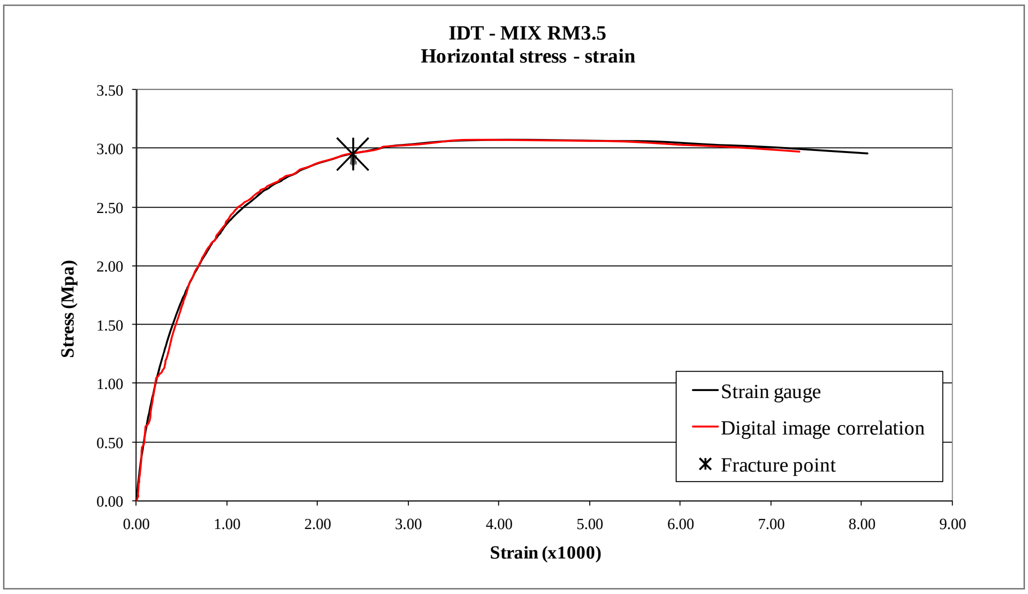

Figure 5.3 Comparison between experimental and mean image correlation horizontal stress-strain response for mixture RM3.5 (cross-linked polymer modified PG 64-22) during IDT.

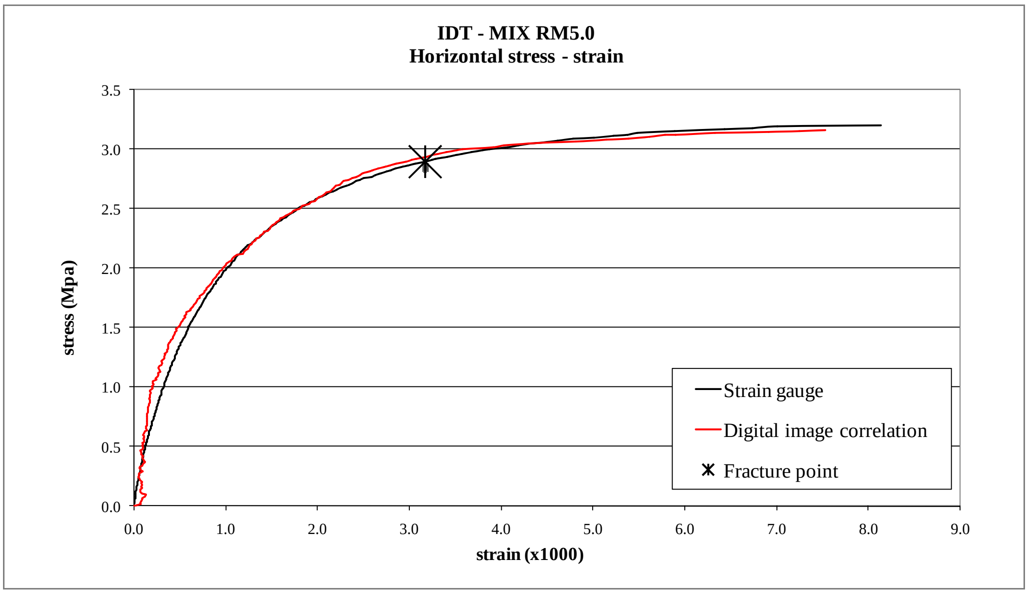

Figure 5.4 Comparison between experimental and mean image correlation horizontal stress-strain response for mixture RM5.0 (cross-kinked polymer modified PG 70-22) during IDT.

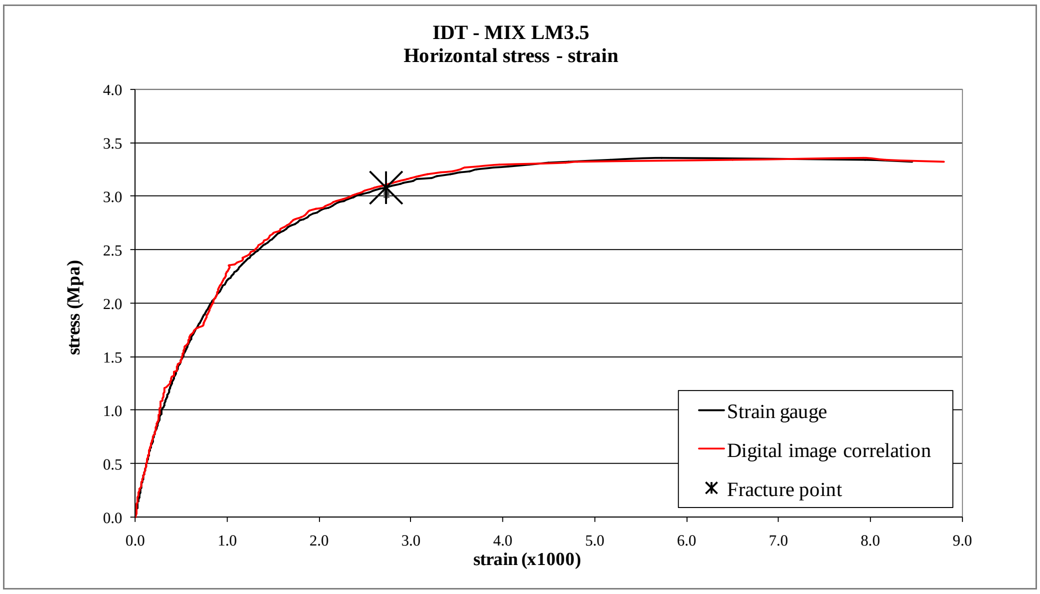

Figure 5.5 Comparison between experimental and mean image correlation horizontal stress-strain response for mixture LM3.5 (linear polymer modified PG 70-22) during IDT.

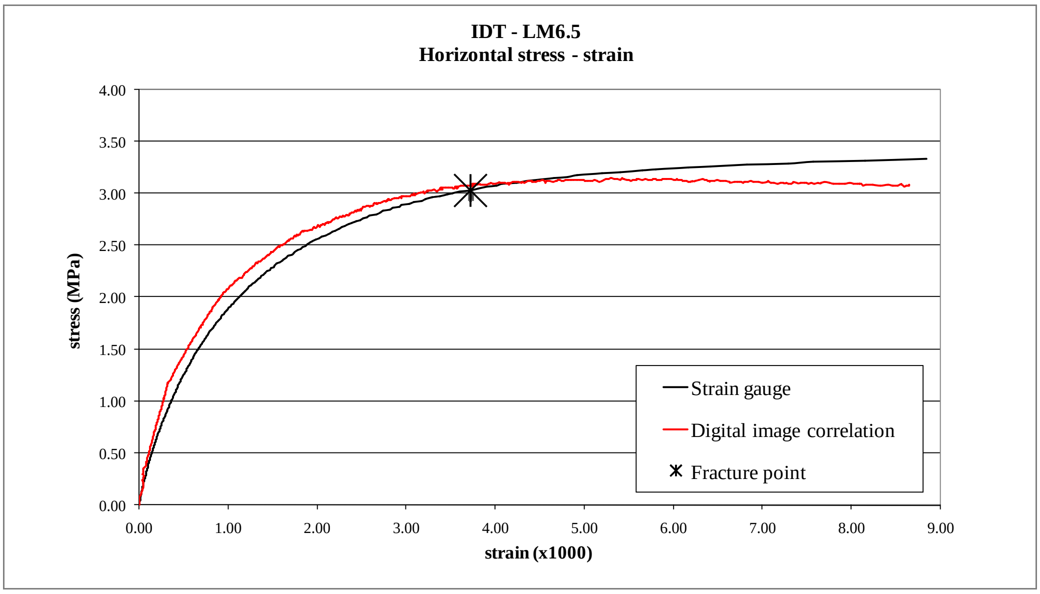

Figure 5.6 Comparison between experimental and mean image correlation horizontal stress-strain response for mixture LM6.5 (linear polymer modified PG 76-22) during IDT.

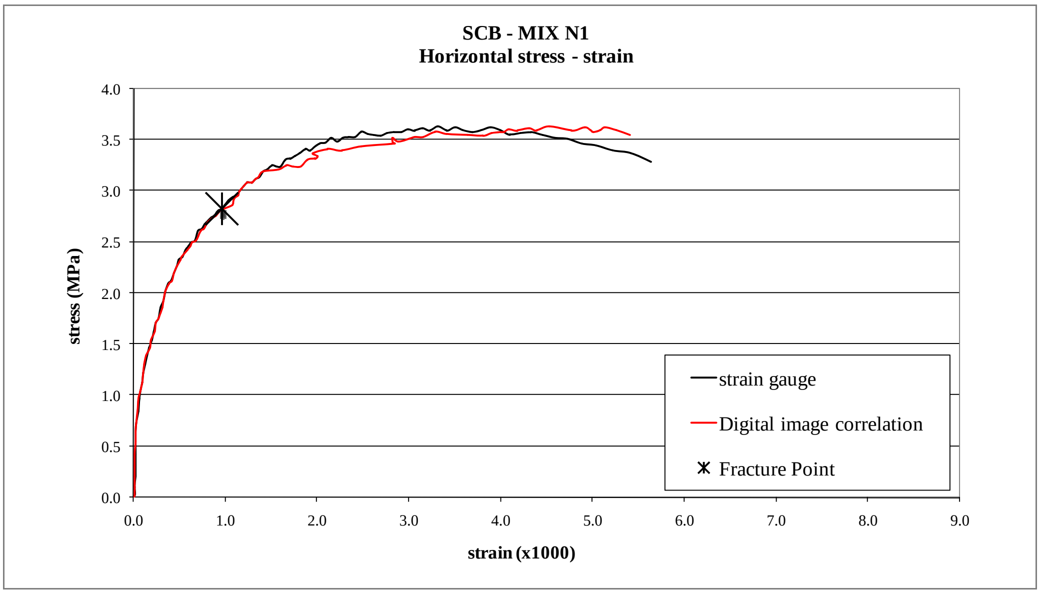

Figure 5.7 Comparison between experimental and mean image correlation horizontal stress-strain response for mixture N1 (virgin; PG 64-22) during SCB.

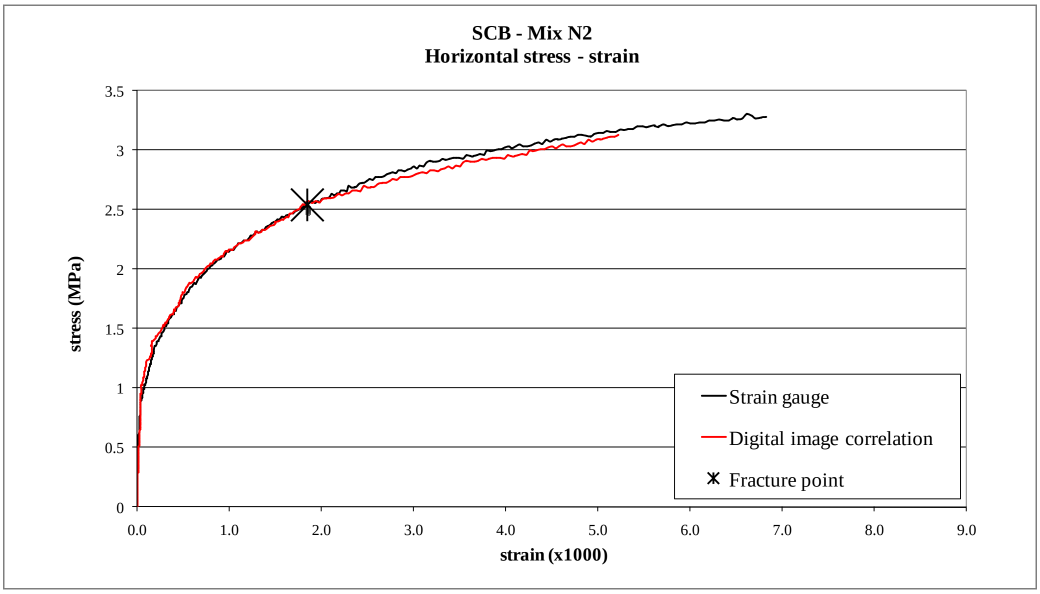

Figure 5.8 Comparison between experimental and mean image correlation horizontal stress-strain response for mixture N2 (virgin; PG 58-22) during SCB.

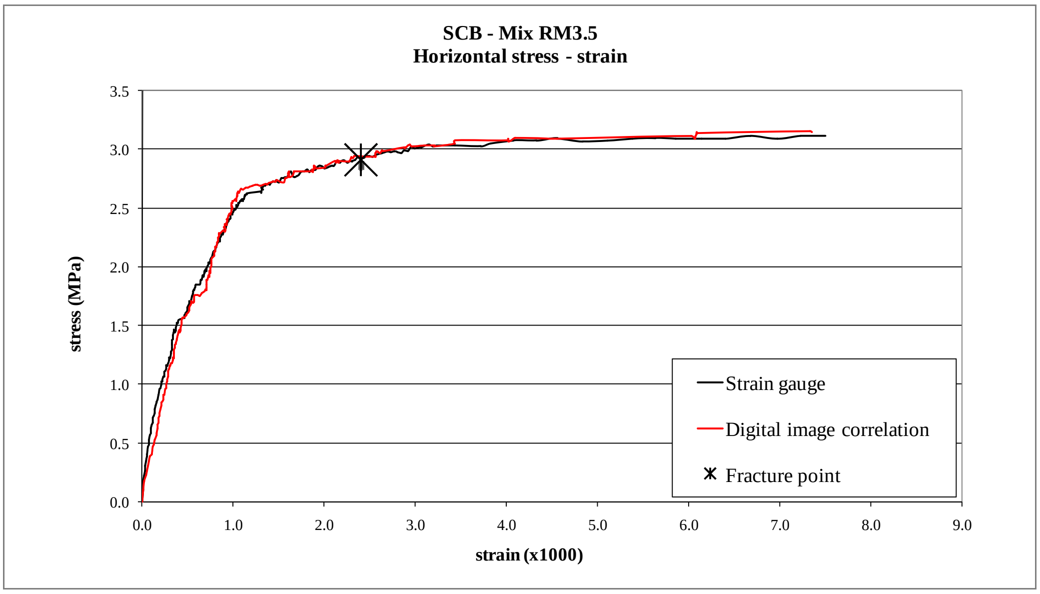

Figure 5.9 Comparison between experimental and mean image correlation horizontal stress-strain response for mixture RM3.5 (cross-linked polymer modified PG 64-22) during SCB.

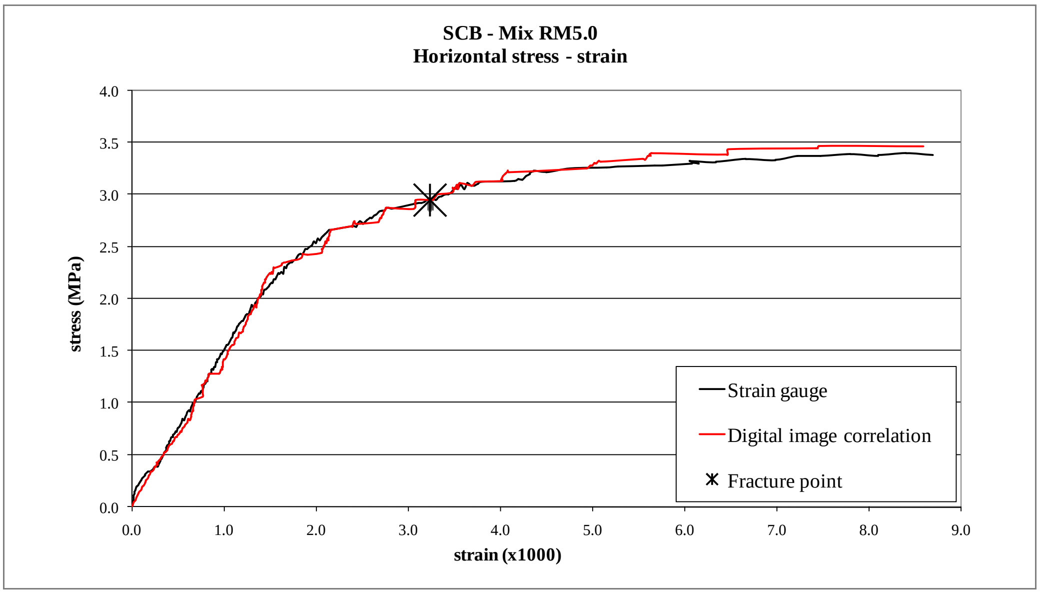

Figure 5.10 Comparison between experimental and mean image correlation horizontal stress-strain response for mixture RM5.0 (cross-kinked polymer modified PG 70-22) during SCB.

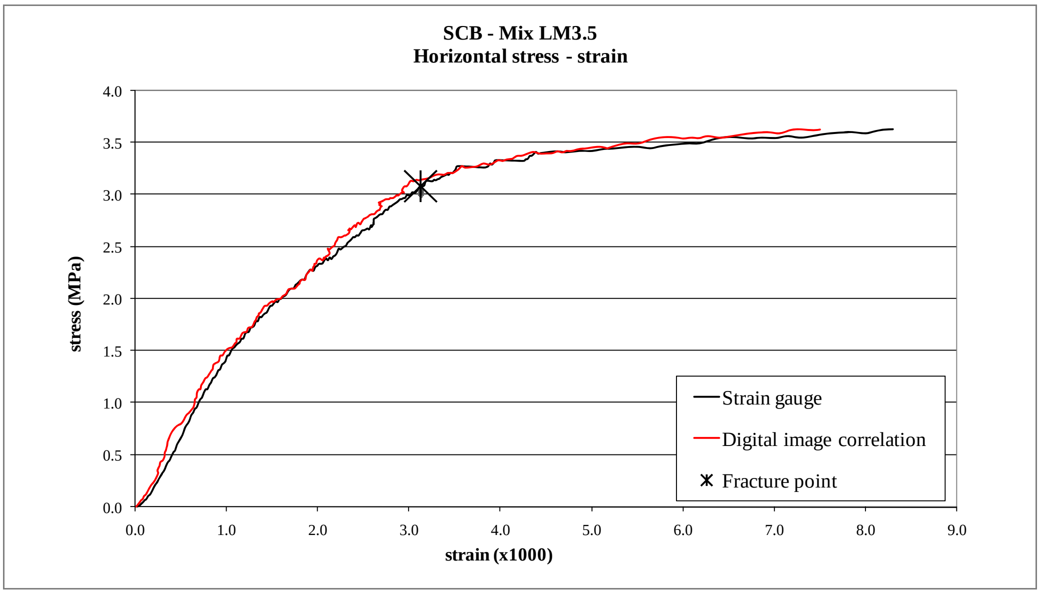

Figure 5.11 Comparison between experimental and mean image correlation horizontal stress-strain response for mixture LM3.5 (linear polymer modified PG 70-22) during SCB.

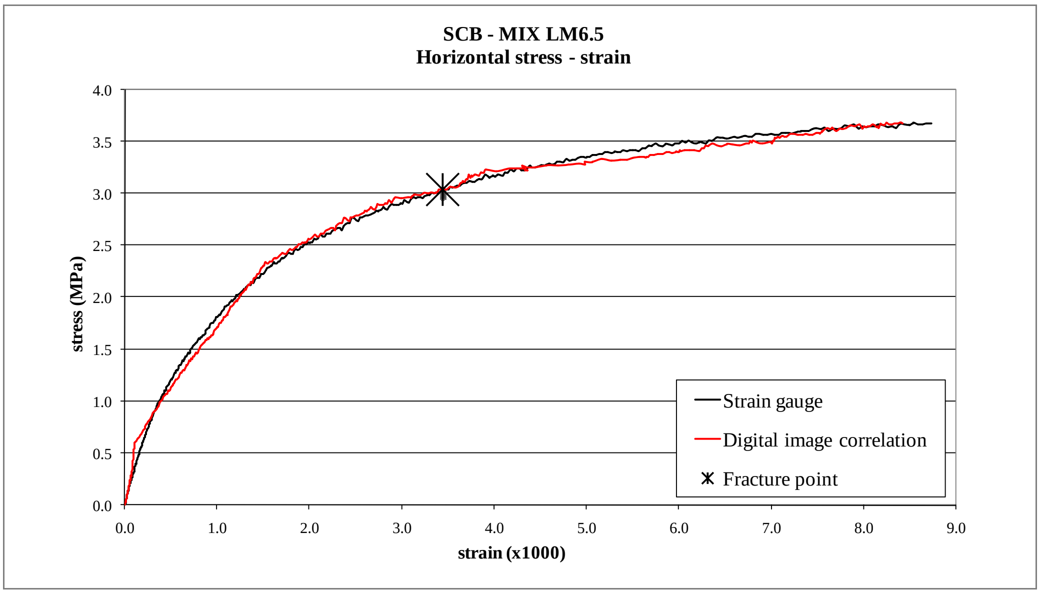

Figure 5.12 Comparison between experimental and mean image correlation horizontal stress-strain response for mixture LM6.5 (linear polymer modified PG 76-22) during SCB.

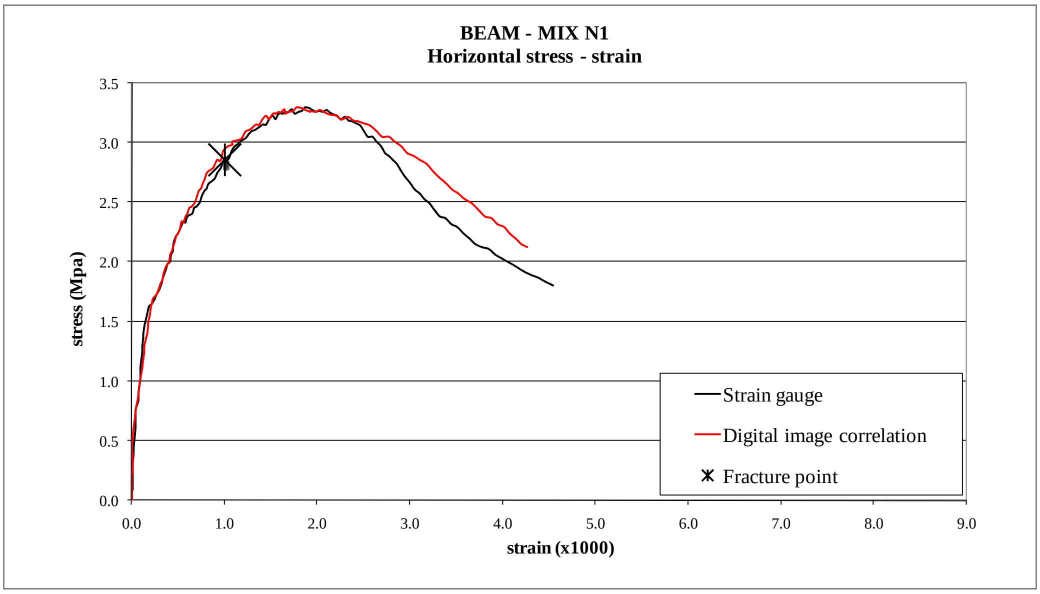

Figure 5.13 Comparison between experimental and mean image correlation horizontal stress-strain response for mixture N1 (virgin; PG 64-22) during 3PB.

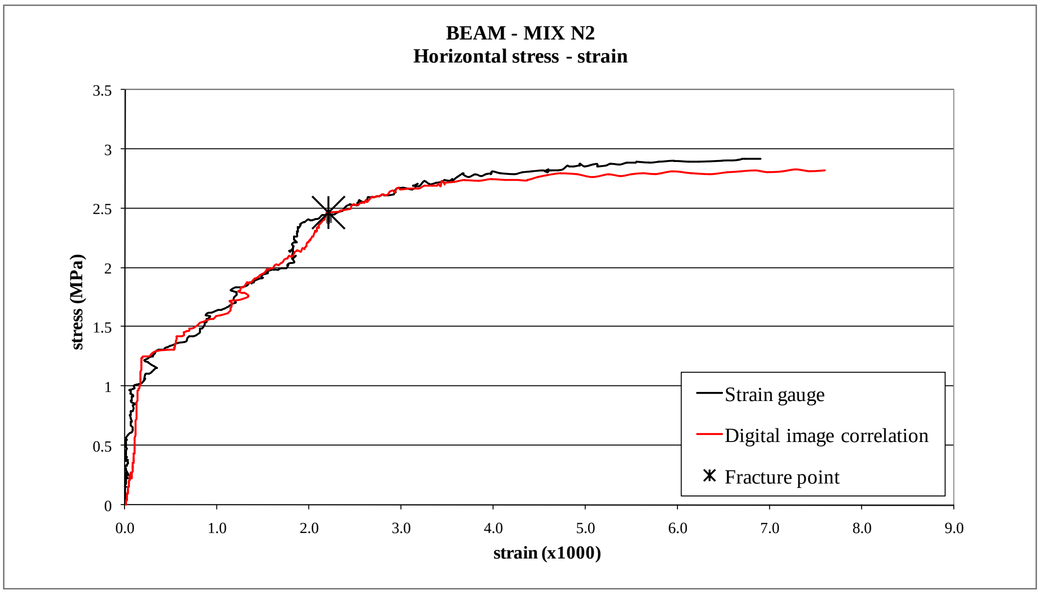

Figure 5.14 Comparison between experimental and mean image correlation horizontal stress-strain response for mixture N2 (virgin; PG 58-22) during 3PB.

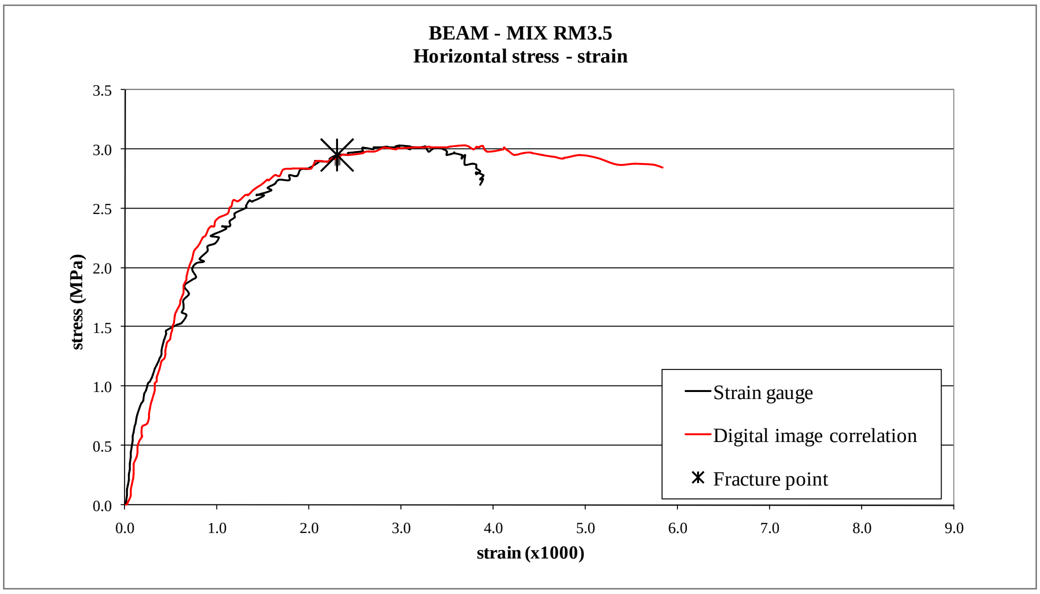

Figure 5.15 Comparison between experimental and mean image correlation horizontal stress-strain response for mixture RM3.5 (cross-linked polymer modified PG 64-22) during 3PB.

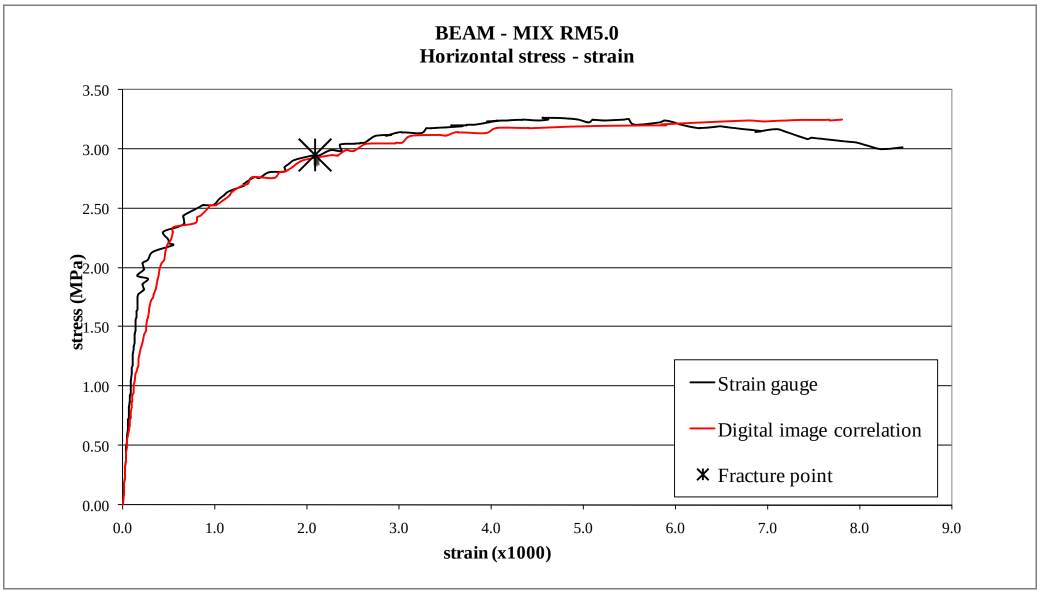

Figure 5.16 Comparison between experimental and mean image correlation horizontal stress-strain response for mixture RM5.0 (cross-kinked polymer modified PG 70-22) during 3PB.

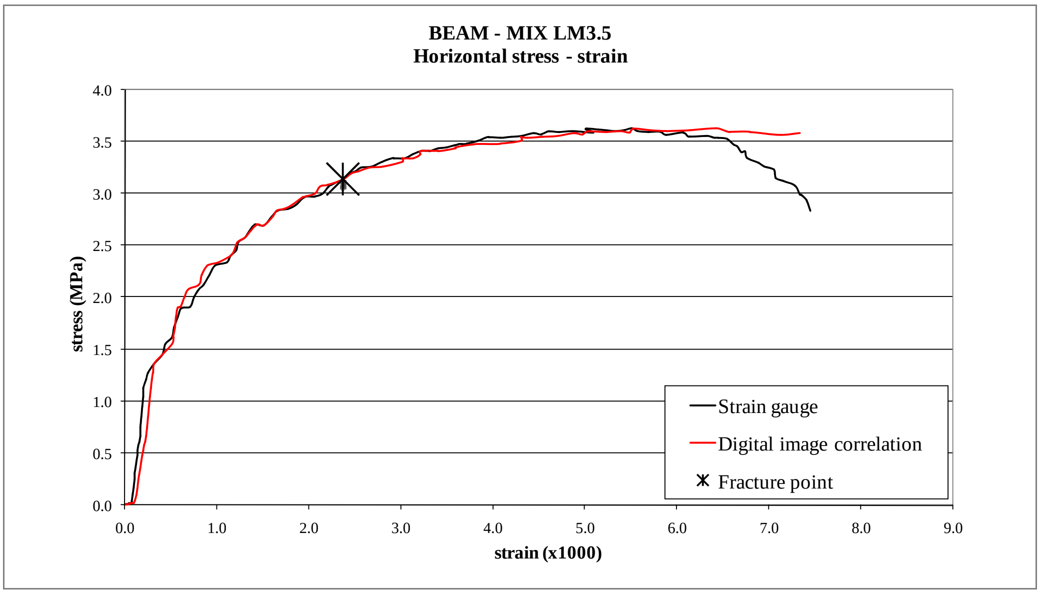

Figure 5.17 Comparison between experimental and mean image correlation horizontal stress-strain response for mixture LM3.5 (linear polymer modified PG 70-22) during SCB.

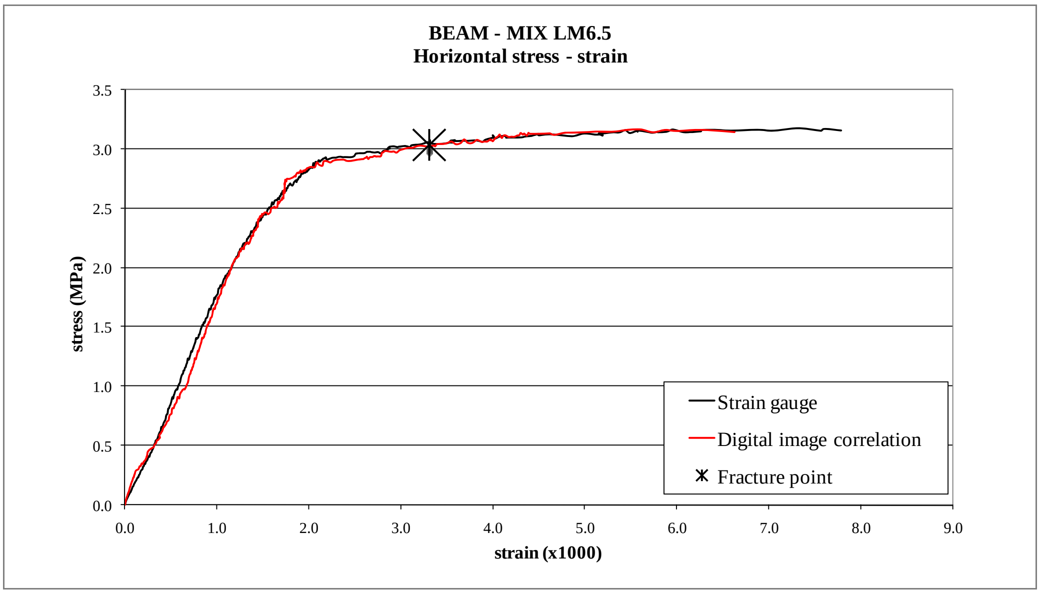

Figure 5.18 Comparison between experimental and mean image correlation horizontal stress-strain response for mixture LM6.5 (linear polymer modified PG 76-22) during 3PB.

As shown in Table 5.1, the Image Correlation and experimental fracture energy densities are well correlated with the fracture energy values obtained from the three tests test.

All of these results indicate that the fracture energy limit defines the onset of macro-cracks in the mixture, independently of mode of loading and test specimen geometry, and independently of polymer modification.

Table 5.1 Comparison between experimental and image correlation (as mean values) tensile strength and fracture energy values

	Tensile Strength from Strain gauge Acquisition of first fracture (MPa)	**Tensile Strength from Image Correlation Acquisition of first fracture (MPa)**	**Fracture Energy Density from Strain gauge Acquisition of first fracture (KJ/m^3)**	**Fracture Energy Density from Image Correlation Acquisition of first fracture (KJ/m^3)**
MIXN1				
IDT	2.84	2.84	1.99	1.93
SCB	2.83	2.81	2.00	1.96
3PB	2.86	2.86	2.04	2.03
MIX N2				
IDT	2.49	2.41	3.80	3.80
SCB	2.54	2.54	3.67	3.72
3PB	2.46	2.47	3.72	3.78
MIX RM3.5				
IDT	2.93	2.94	5.20	5.25
SCB	2.90	2.90	5.21	5.25
3PB	2.95	2.92	5.26	5.32
MIX RM5.0				
IDT	2.90	2.90	6.30	6.35
SCB	2.95	2.96	6.31	6.35
3PB	2.95	2.98	6.34	6.48
MIX LM3.5				
IDT	3.08	3.08	5.70	5.80
SCB	3.08	3.02	5.76	5.70
3PB	3.14	3.14	5.71	5.73
MIXLM6.5				
IDT	3.03	3.02	7.30	7.34
SCB	3.03	3.04	7.29	7.26
3PB	3.04	3.03	7.31	7.30

Comparisons between "pinpoint" and average tensile stress-strain responses obtained from the three tests for all the mixtures are shown in Figures from 5.19 to 5.36. Respective tensile strengths and fracture energy densities are listed in Table 6.2.

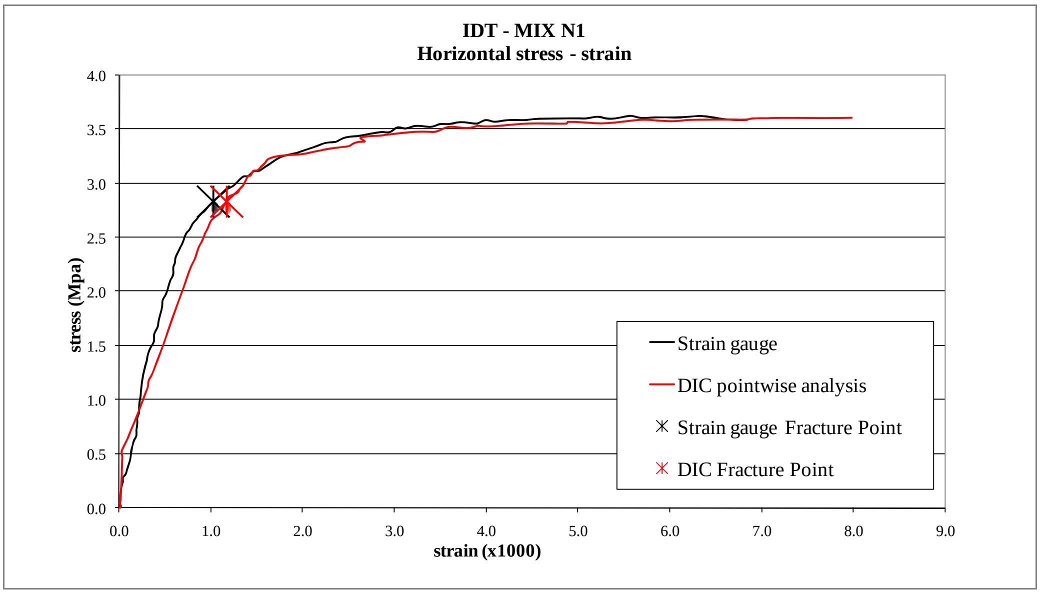

Figure 5.19 Comparison between experimental and pinpoint DIC horizontal stress-strain response for mixture N1 (virgin; PG 64-22) during IDT.

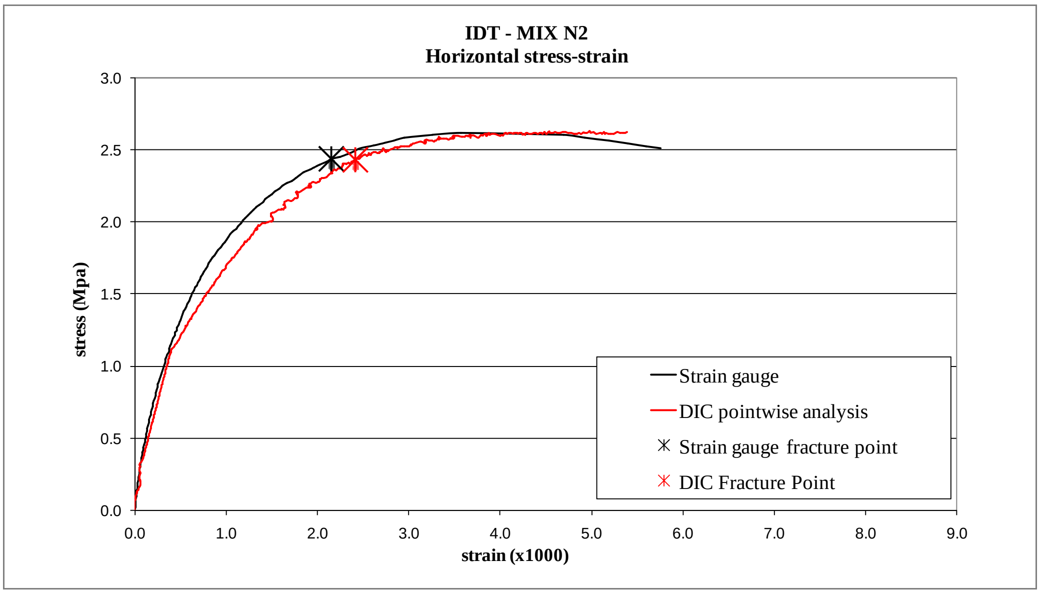

Figure 5.20 Comparison between experimental and pinpoint DIC horizontal stress-strain response for mixture N2 (virgin; PG 58-22) during IDT.

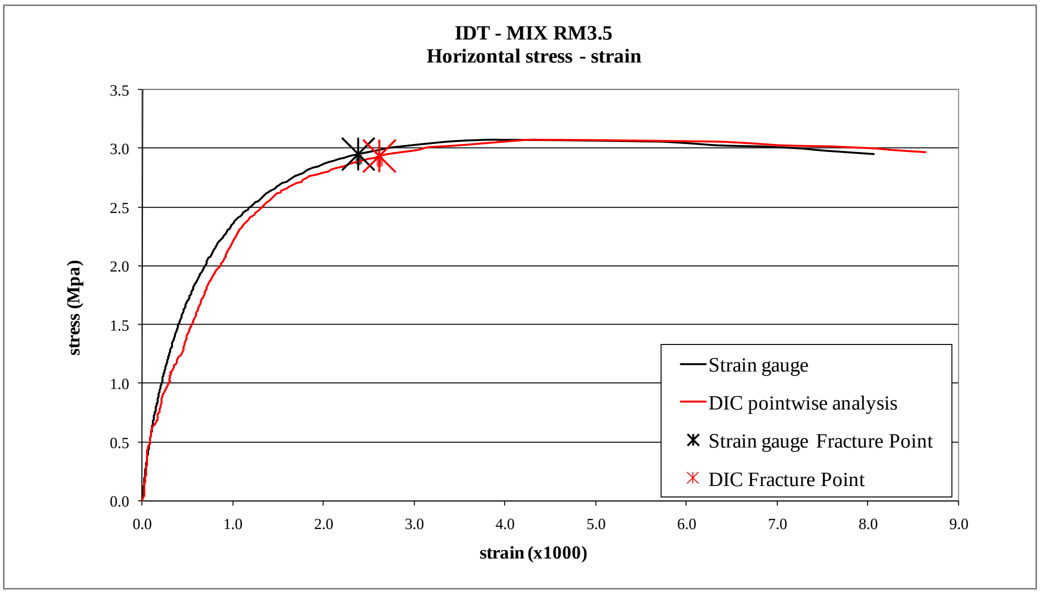

Figure 5.21 Comparison between experimental and pinpoint DIC horizontal stress-strain response for mixture RM3.5 (cross-linked polymer modified PG 64-22) during IDT.

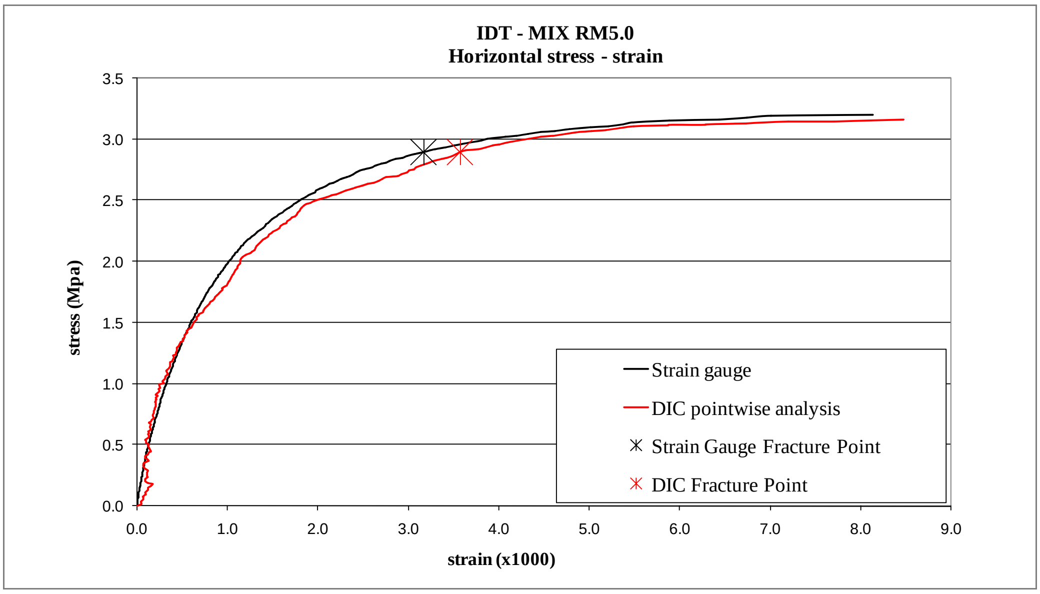

Figure 5.22 Comparison between experimental and pinpoint DIC horizontal stress-strain response for mixture RM5.0 (cross-kinked polymer modified PG 70-22) during IDT.

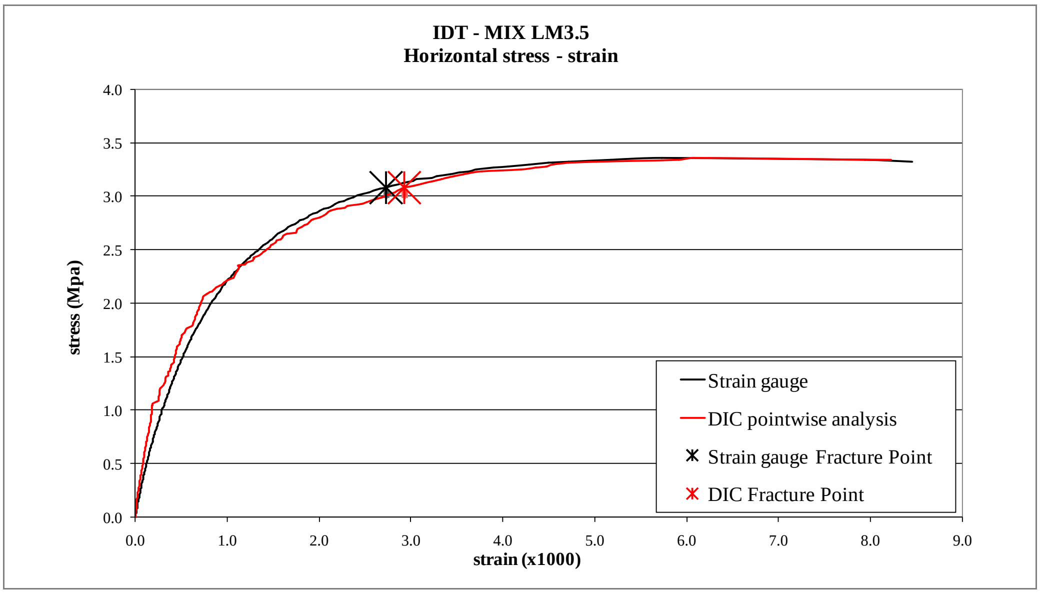

Figure 5.23 Comparison between experimental and pinpoint DIC stress-strain response for mixture LM3.5 (linear polymer modified PG 70-22) during IDT.

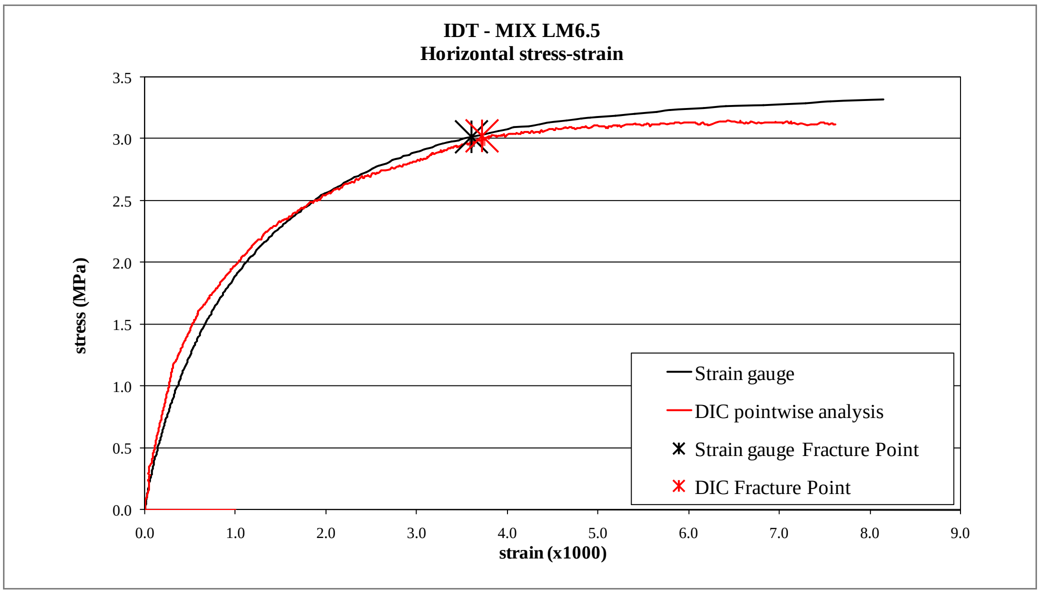

Figure 5.24 Comparison between experimental and pinpoint DIC horizontal stress-strain response for mixture LM6.5 (linear polymer modified PG 76-22) during IDT.

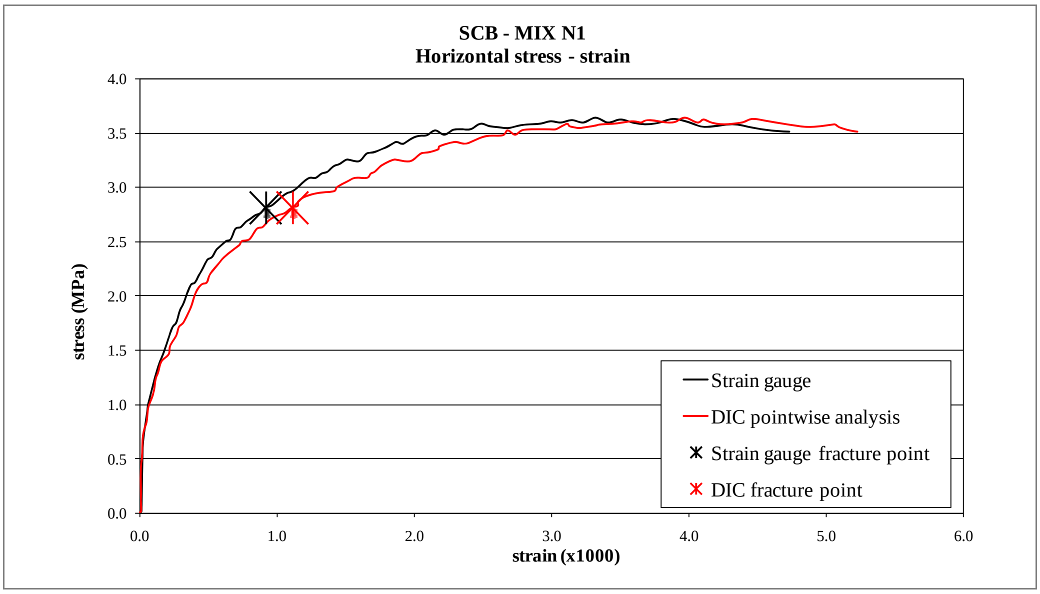

Figure 5.25 Comparison between experimental and pinpoint DIC horizontal stress-strain response for mixture N1 (virgin; PG 64-22) during SCB.

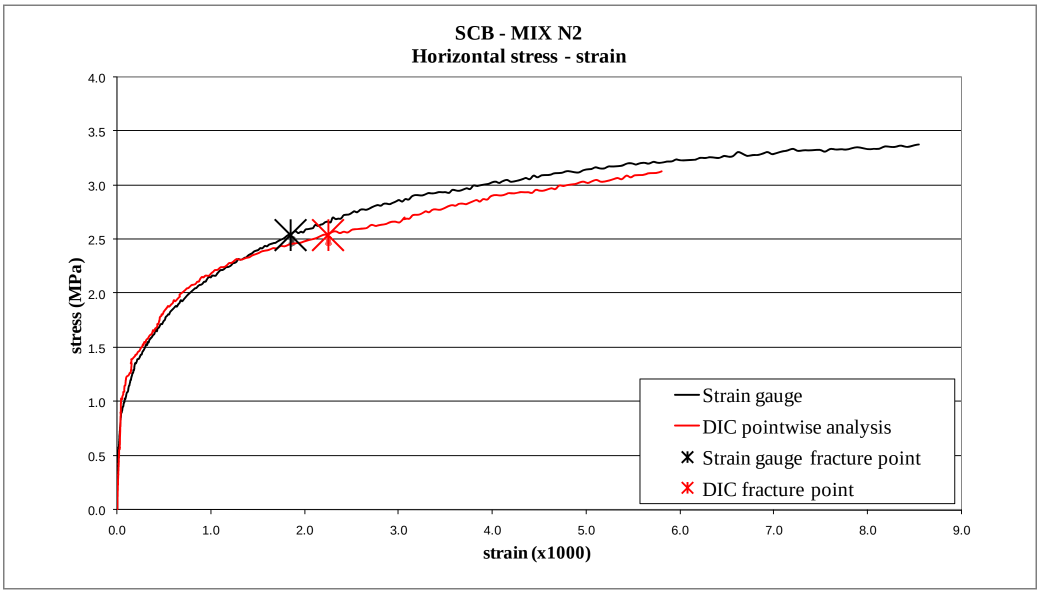

Figure 5.26 Comparison between experimental and pinpoint DIC horizontal stress-strain response for mixture N2 (virgin; PG 58-22) during SCB.

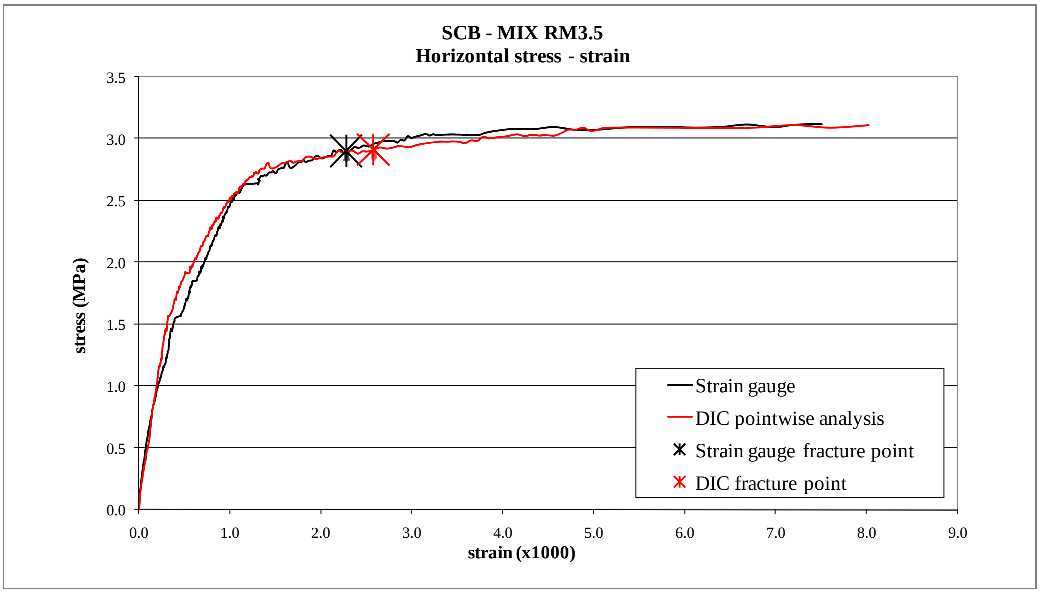

Figure 5.27 Comparison between experimental and pinpoint DIC horizontal stress-strain response for mixture RM3.5 (cross-linked polymer modified PG 64-22) during SCB.

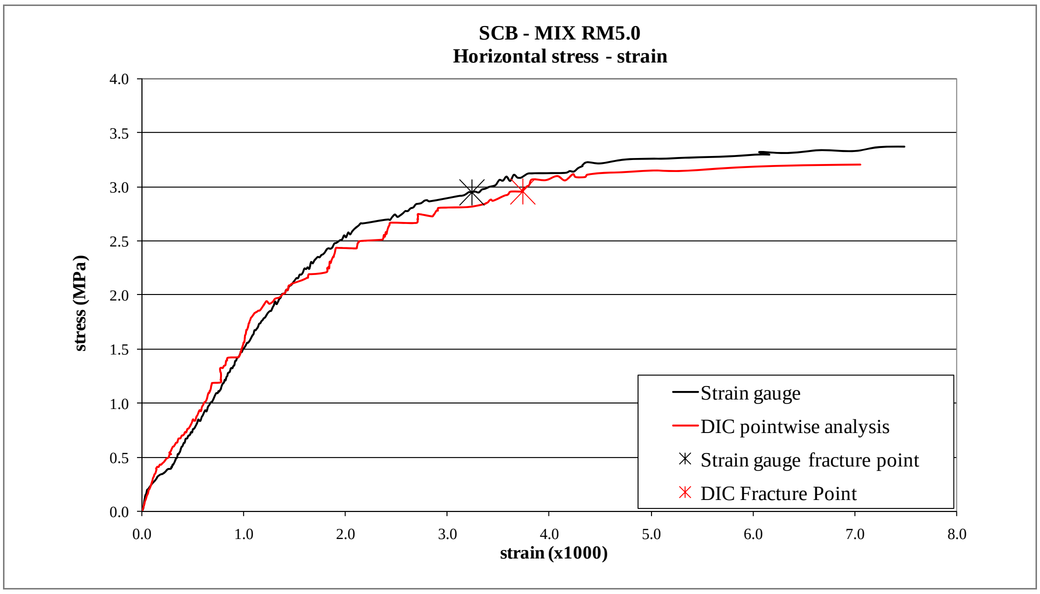

Figure 5.28 Comparison between experimental and pinpoint DIC horizontal stress-strain response for mixture RM5.0 (cross-kinked polymer modified PG 70-22) during SCB.

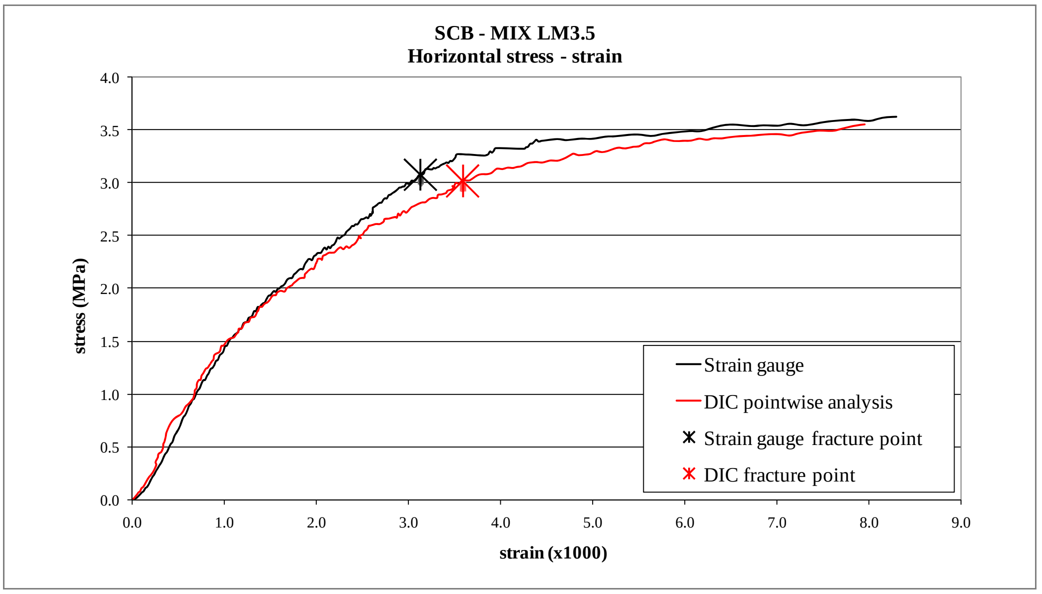

Figure 5.29 Comparison between experimental and pinpoint DIC horizontal stress-strain response for mixture LM3.5 (linear polymer modified PG 70-22) during SCB.

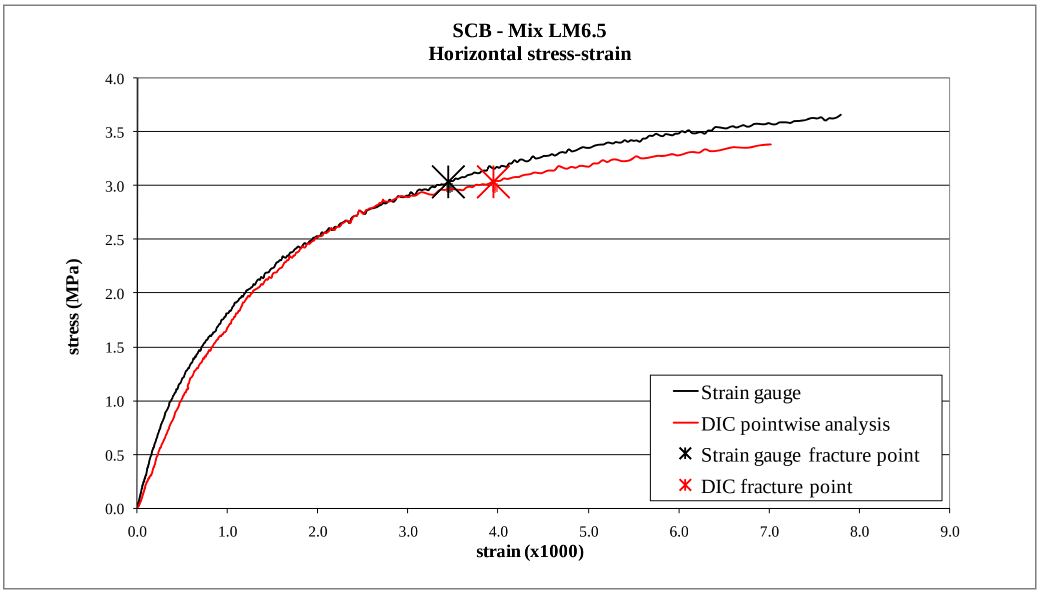

Figure 5.30 Comparison between experimental and pinpoint DIC horizontal stress-strain response for mixture LM6.5 (linear polymer modified PG 76-22) during SCB.

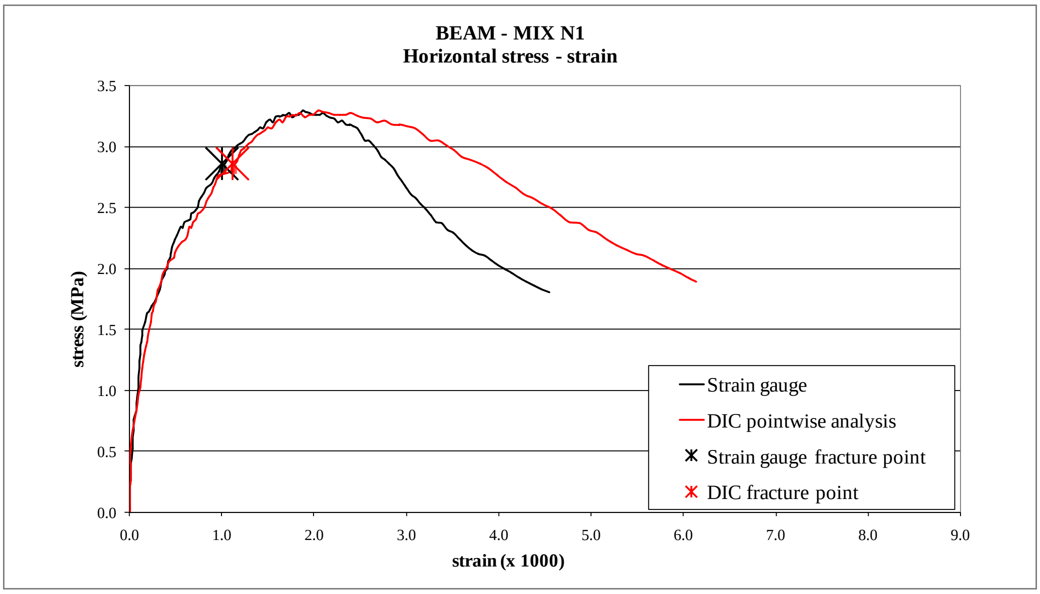

Figure 5.31 Comparison between experimental and pinpoint DIC horizontal stress-strain response for mixture N1 (virgin; PG 64-22) during 3PB.

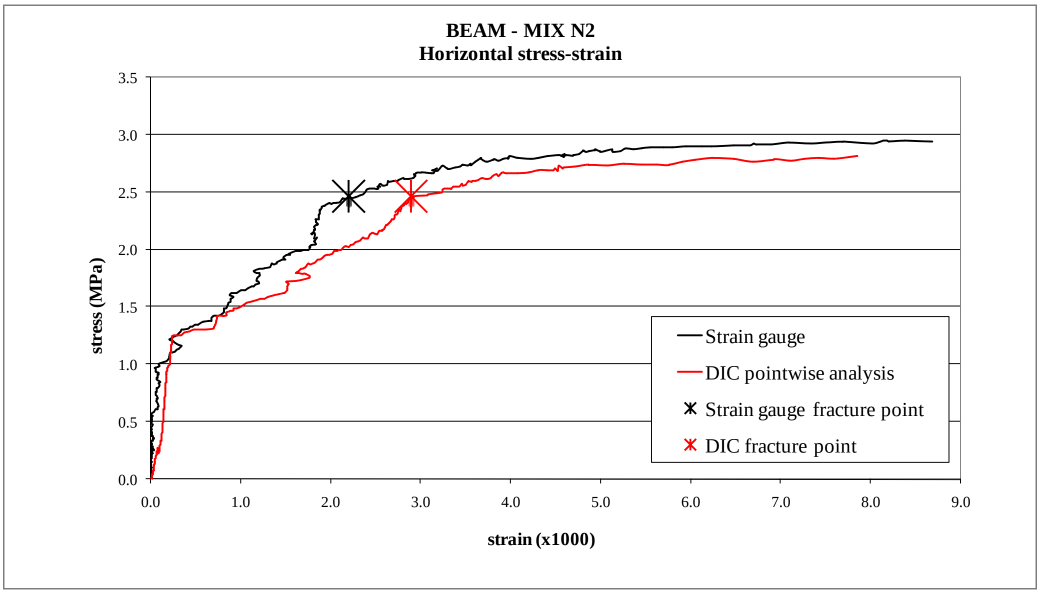

Figure 5.32 Comparison between experimental and pinpoint DIC horizontal stress-strain response for mixture N2 (virgin; PG 58-22) during 3PB.

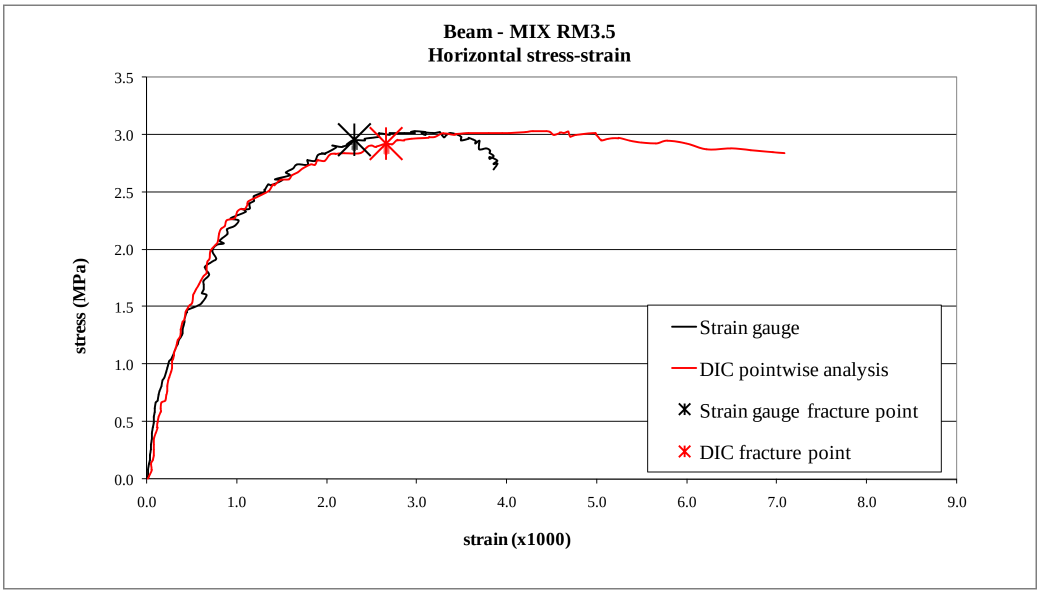

Figure 5.33 Comparison between experimental and pinpoint DIC horizontal stress-strain response for mixture RM3.5 (cross-linked polymer modified PG 64-22) during 3PB.

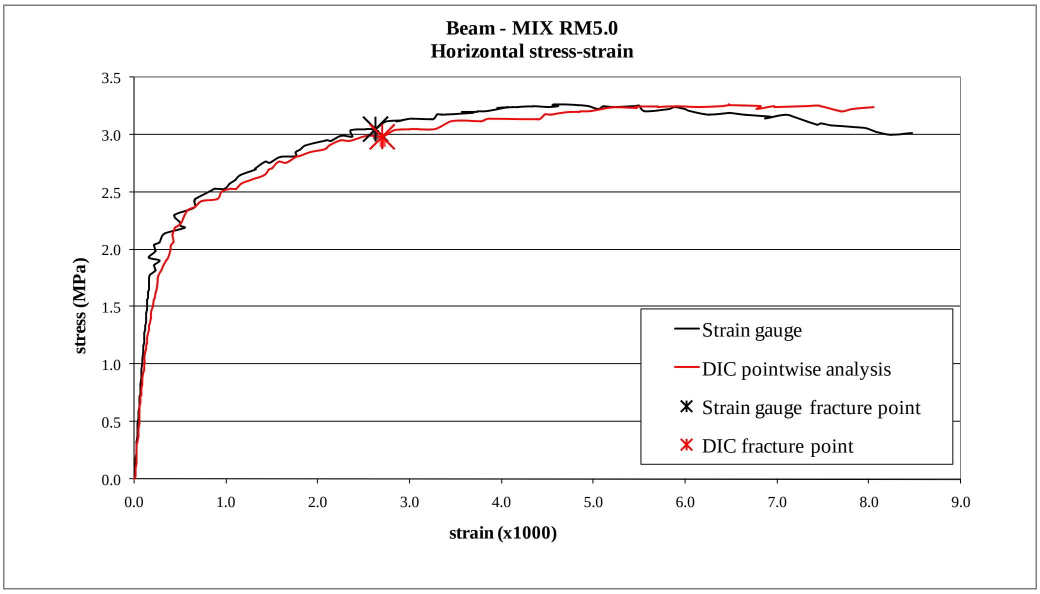

Figure 5.34 Comparison between experimental and pinpoint DIC horizontal stress-strain response for mixture RM5.0 (cross-kinked polymer modified PG 70-22) during 3PB.

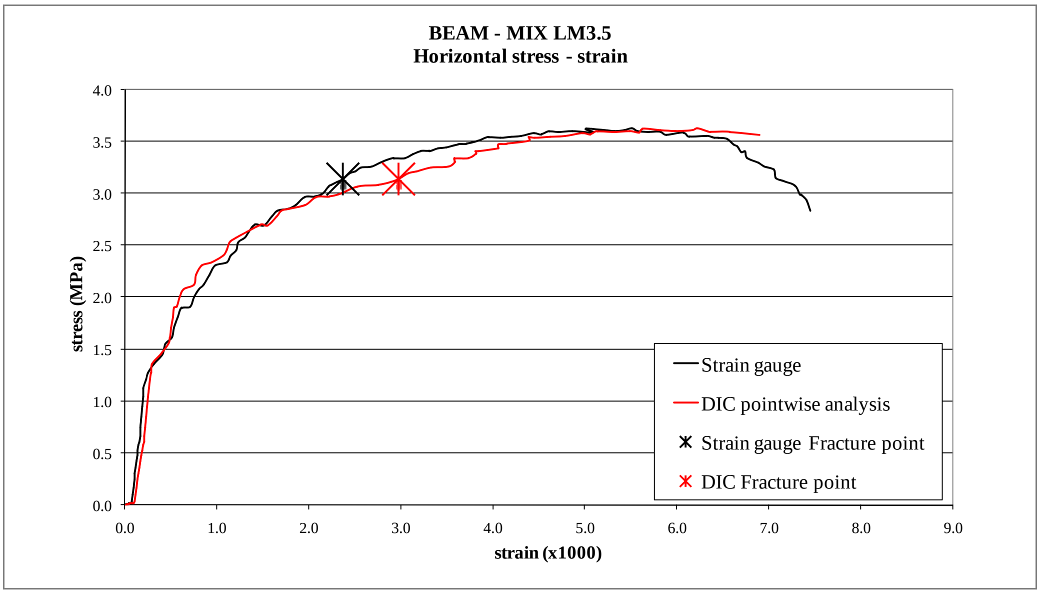

Figure 5.35 Comparison between experimental and pinpoint DIC horizontal stress-strain response for mixture LM3.5 (linear polymer modified PG 70-22) during SCB.

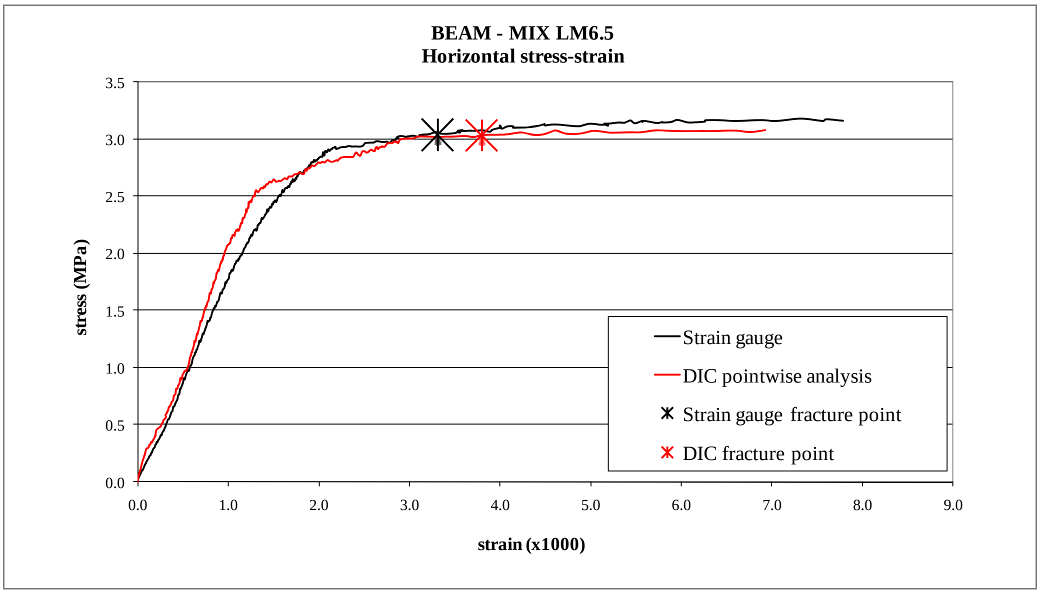

Figure 5.36 Comparison between experimental and pinpoint DIC correlation horizontal stress-strain response for mixture LM6.5 (linear polymer modified PG 76-22) during 3PB.

Table 5.2 Comparison between experimental and pinpoint tensile failure limits of the six mixtures

	Tensile Strength from Strain gauge (mean value) (MPa)	Tensile Strength from DIC (pinpoint value) (MPa)	Fracture Energy Density from Strain gauge (mean value) (KJ/m^3)	Fracture Energy Density from DIC (pinpoint value) (KJ/m^3)
MIXN1				
IDT	2.84	2.84	1.99	2.41
SCB	2.83	2.81	2.00	2.42
3PB	2.86	2.86	2.04	2.37
MIX N2				
IDT	2.49	2.41	3.80	4.61
SCB	2.54	2.54	3.67	4.70
3PB	2.46	2.47	3.72	4.77
MIX RM3.5				
IDT	2.93	2.94	5.20	6.04
SCB	2.90	2.90	5.21	6.11
3PB	2.95	2.92	5.26	6.08
MIX RM5.0				
IDT	2.90	2.90	6.30	7.66
SCB	2.95	2.96	6.31	7.72
3PB	2.95	2.98	6.34	7.67
MIX LM3.5				
IDT	3.08	3.08	5.70	6.87
SCB	3.08	3.02	5.76	6.81
3PB	3.14	3.14	5.71	6.81
MIXLM6.5				
IDT	3.03	3.02	7.30	8.76
SCB	3.03	3.04	7.29	8.86
3PB	3.04	3.03	7.31	8.83

“Pinpoint” tensile strengths do not differ significantly from those obtained with experimental analysis; conversely, fracture energy densities obtained at the specific point in which a crack has initiated are always about 20% higher than those evaluated along the strain gauge area. This means that tensile strains values obtained as average values along a finite area might be not totally representative of localized strains at impeding fracture. Rather, it may be more appropriate to perform a point-wise analysis of localized strains at the point of impending fracture. Unfortunately, the effect of stress concentration due to the impending fracture would require the introduction of a damage or fracture model, thus further complicating the analysis.

5.2 DD Predictions

Comparisons between predicted and measured horizontal stress-strain curves of the six mixtures for IDT, SCB, 3PB are shown in Figures from 5.37 to 5.54.

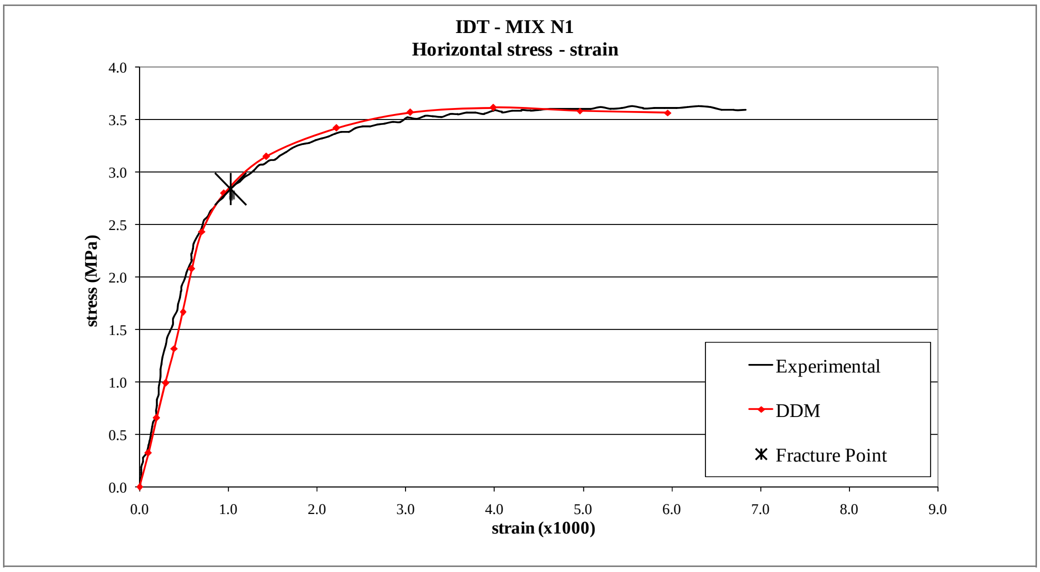

Figure 5.37 Predicted and measured horizontal stress-strain responses mix N1 (IDT)

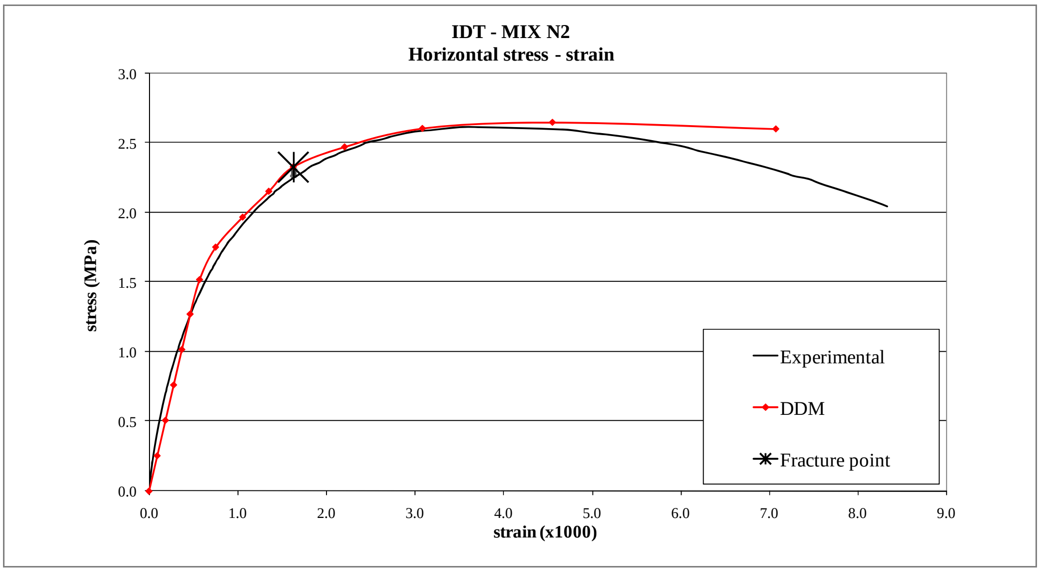

Figure 5.38 Predicted and measured horizontal stress-strain responses mix N2 (IDT)

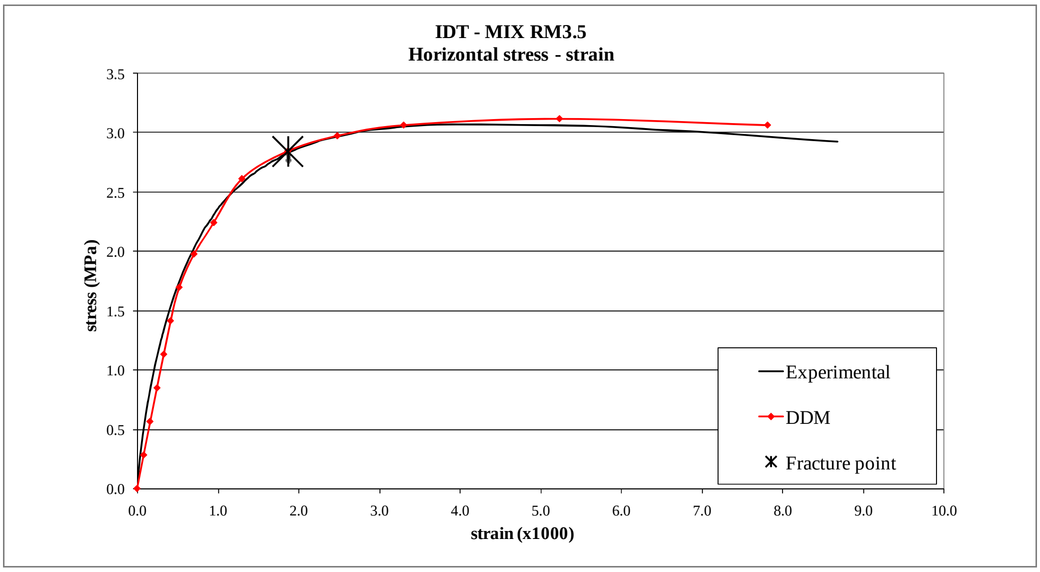

Figure 5.39 Predicted and measured horizontal stress-strain responses mix RM3.5 (IDT)

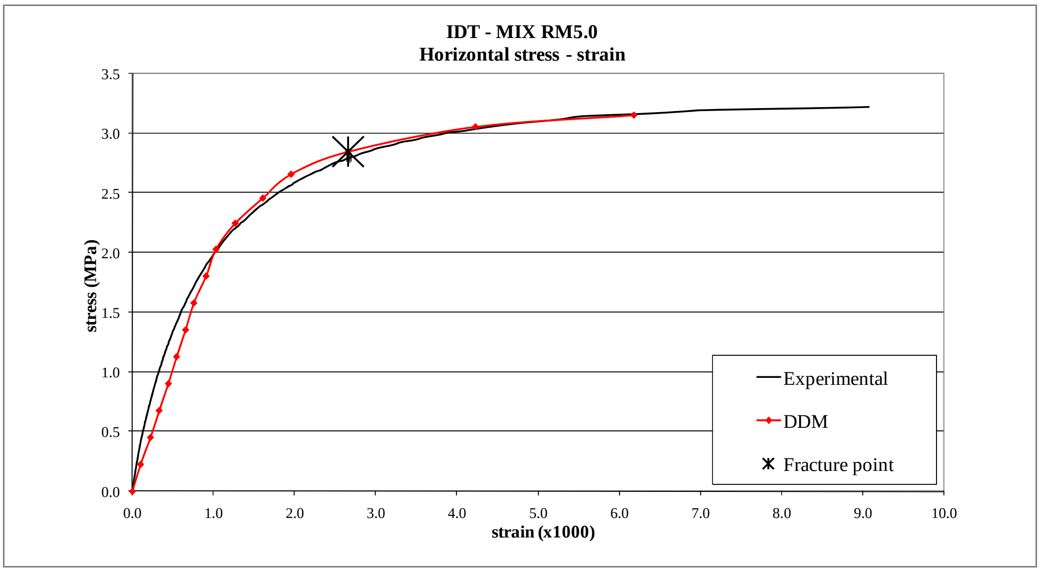

Figure 5.40 Predicted and measured horizontal stress-strain responses mix RM5.0 (IDT)

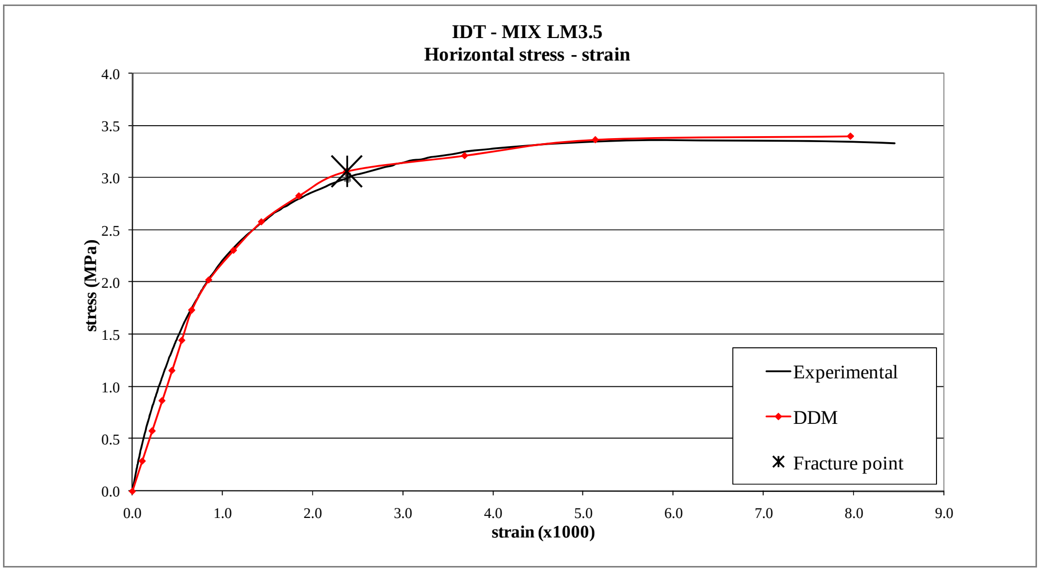

Figure 5.41 Predicted and measured horizontal stress-strain responses mix LM3.5 (IDT)

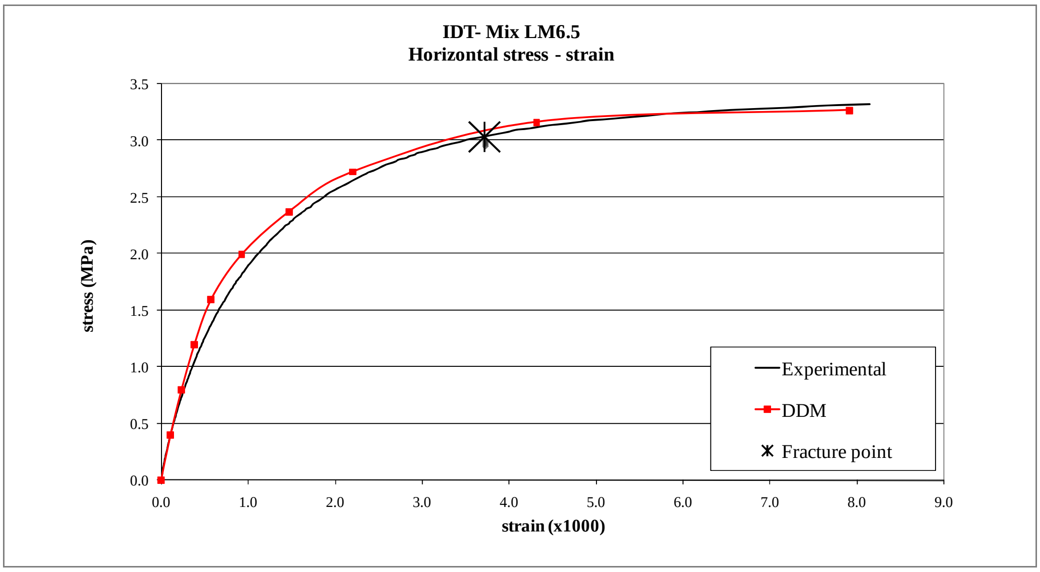

Figure 5.42 Predicted and measured horizontal stress-strain responses mix LM6.5 (IDT)

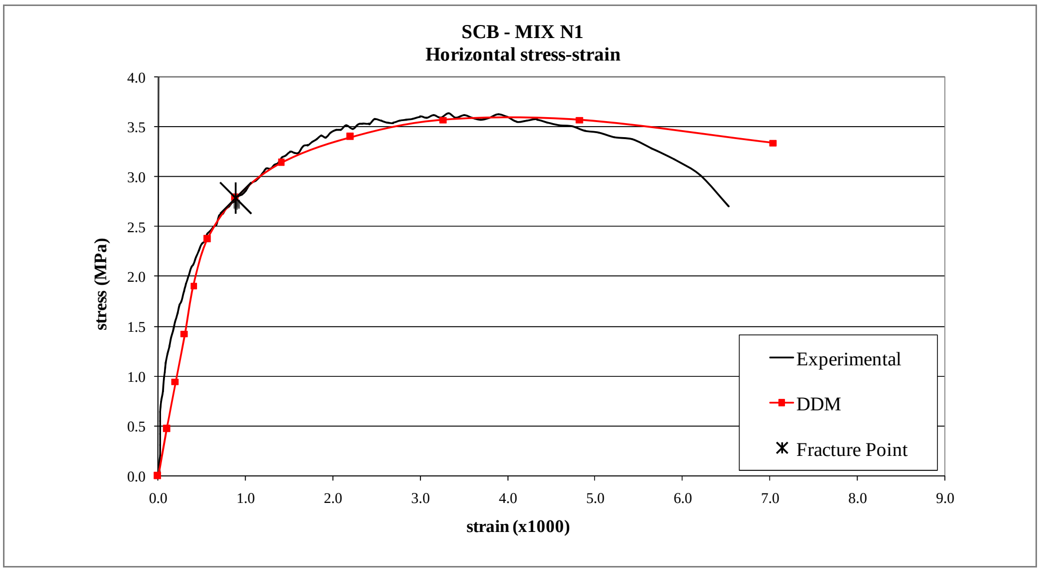

Figure 5.43 Predicted and measured horizontal stress-strain responses mix N1 (SCB)

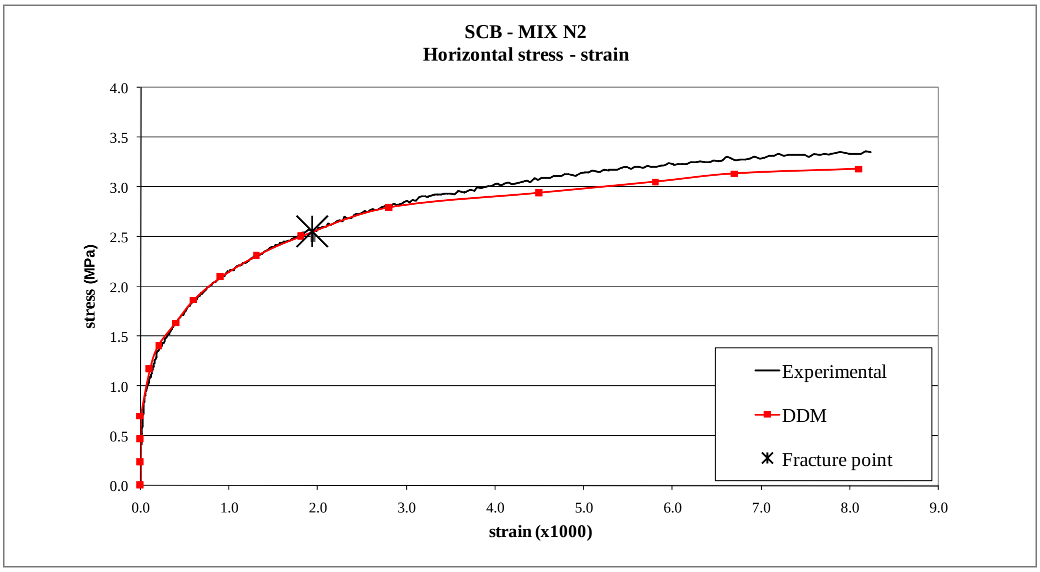

Figure 5.44 Predicted and measured horizontal stress-strain responses mix N2 (SCB)

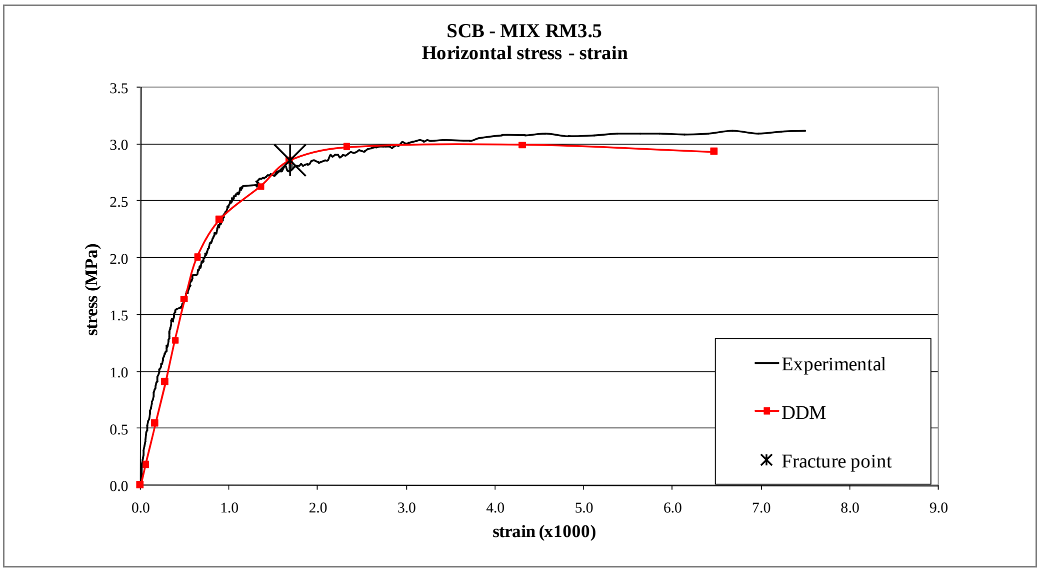

Figure 5.45 Predicted and measured horizontal stress-strain responses mix RM3.5 (SCB)

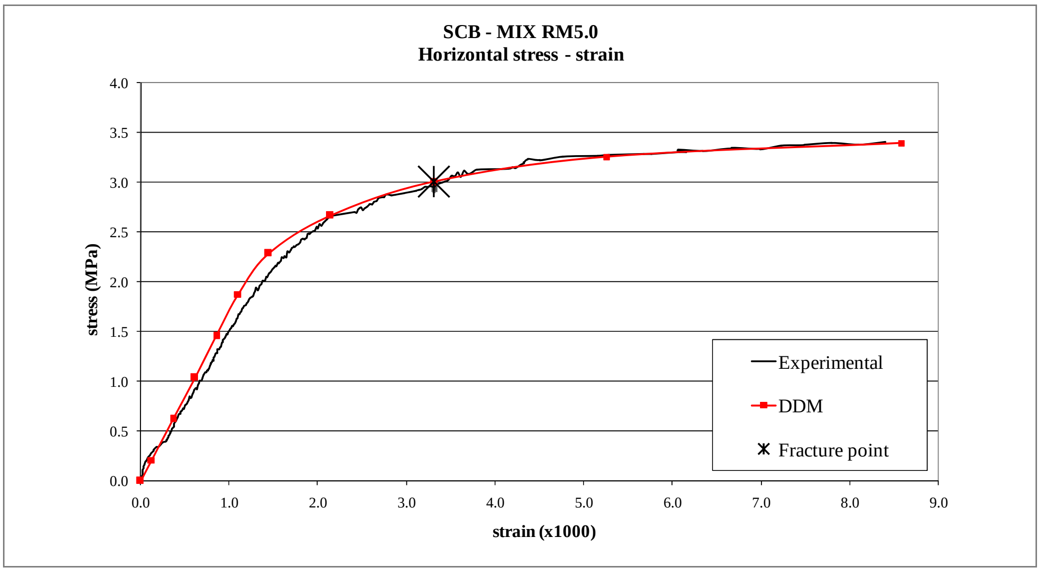

Figure 5.46 Predicted and measured horizontal stress-strain responses mix RM5.0 (SCB)

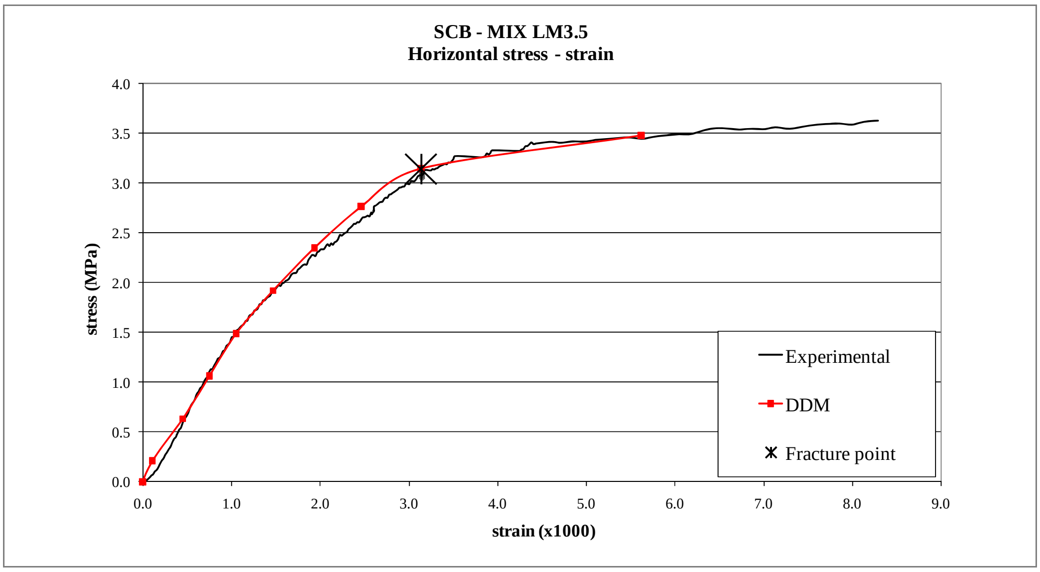

Figure 5.47 Predicted and measured horizontal stress-strain responses mix LM3.5 (SCB)

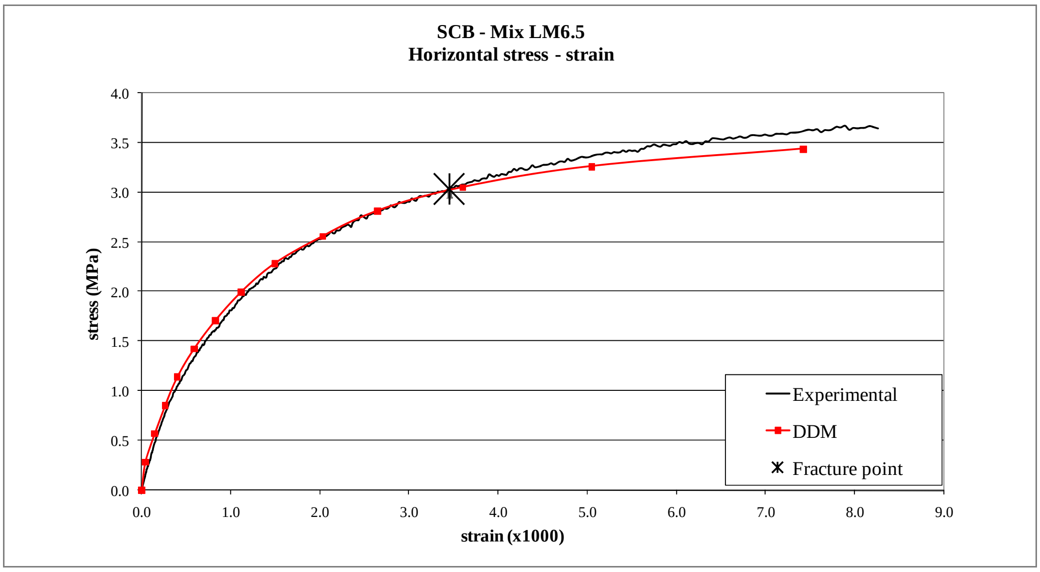

Figure 5.48 Predicted and measured horizontal stress-strain responses mix LM6.5 (SCB)

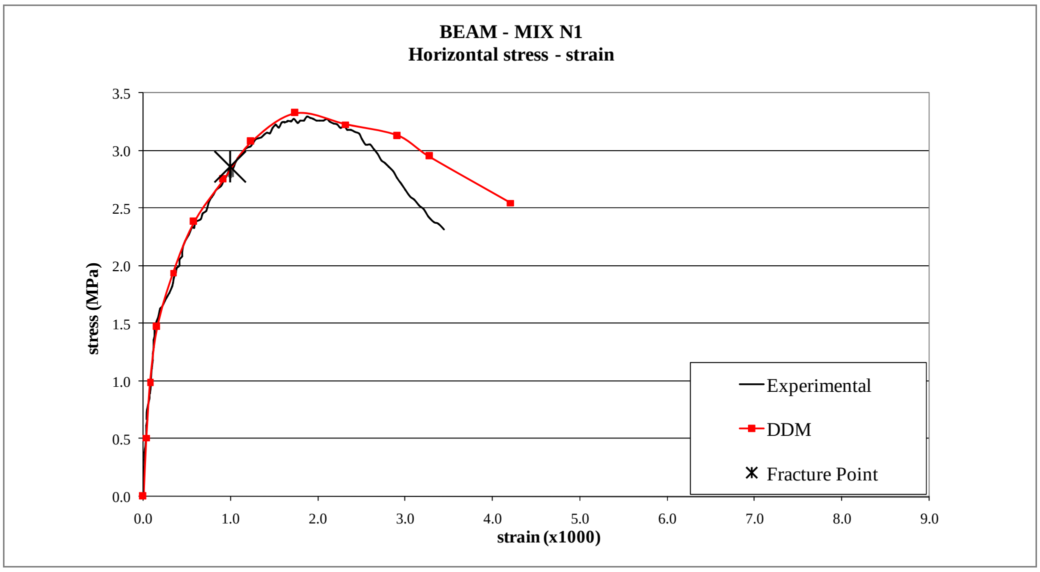

Figure 5.49 Predicted and measured horizontal stress-strain responses mix N1 (3PB)

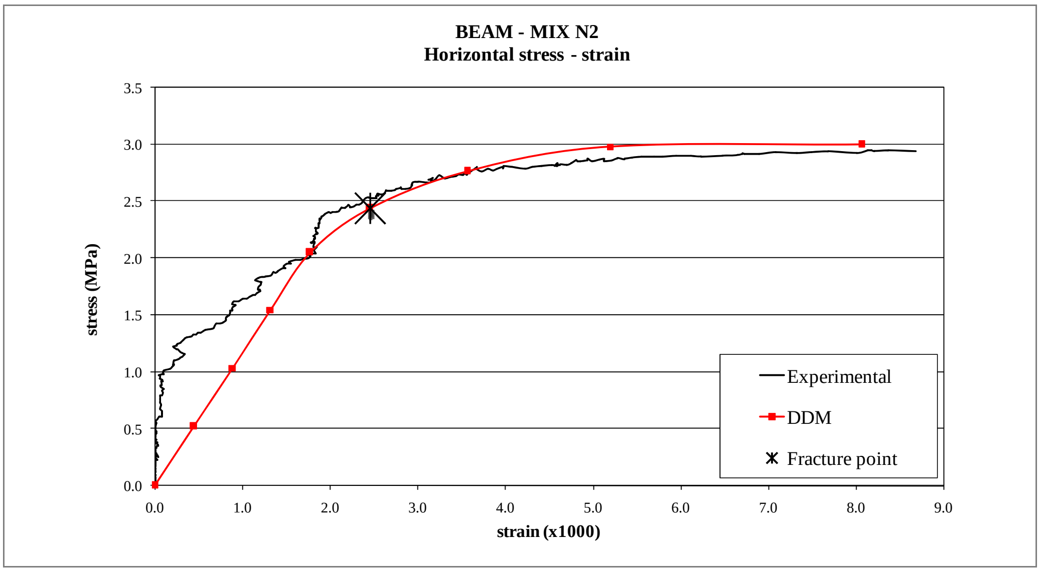

Figure 5.50 Predicted and measured horizontal stress-strain responses mix N2 (3PB)

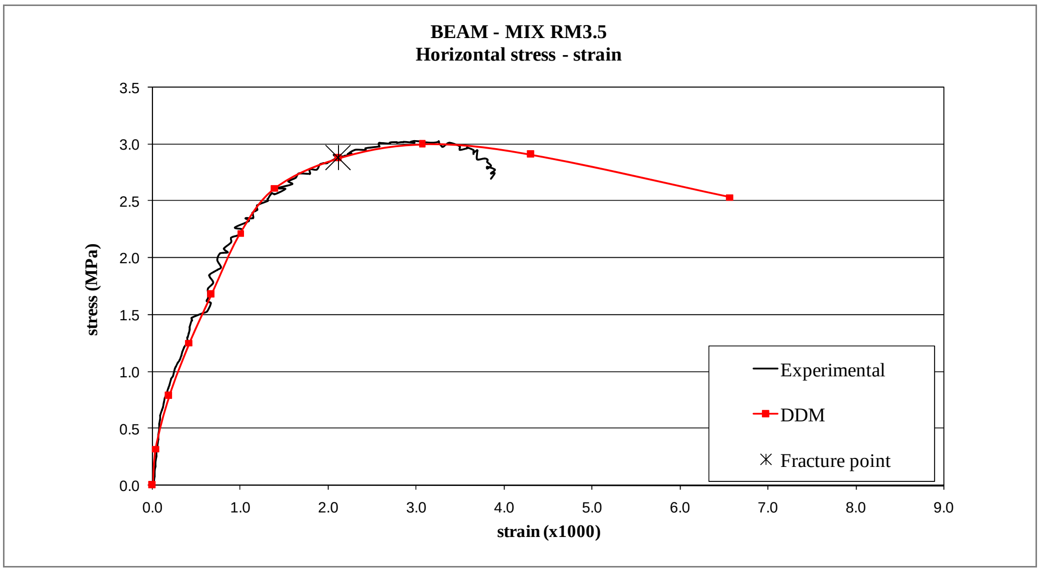

Figure 5.51 Predicted and measured horizontal stress-strain responses mix RM3.5 (3PB)

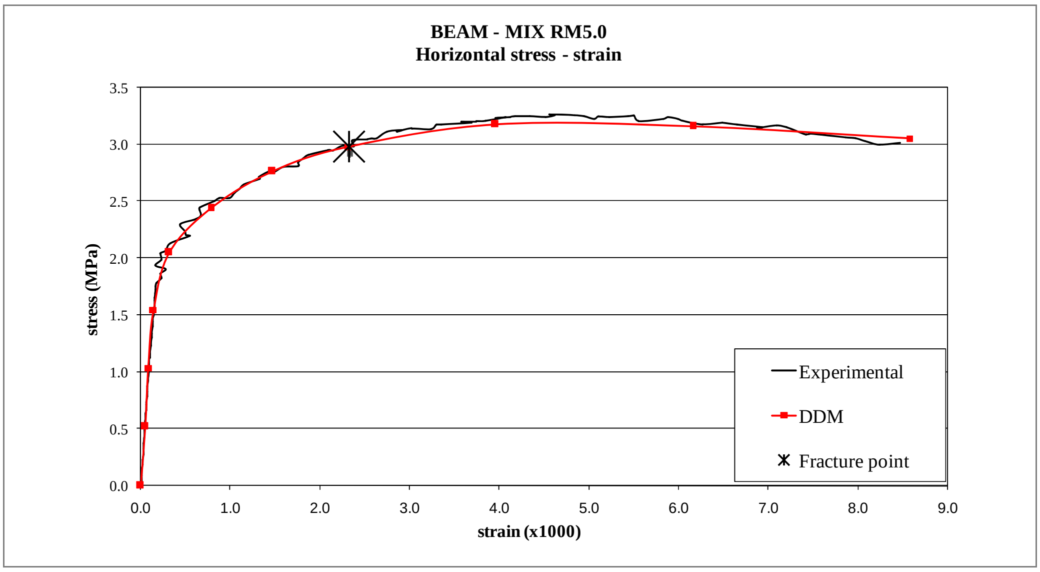

Figure 5.52 Predicted and measured horizontal stress-strain responses mix RM5.0 (3PB)

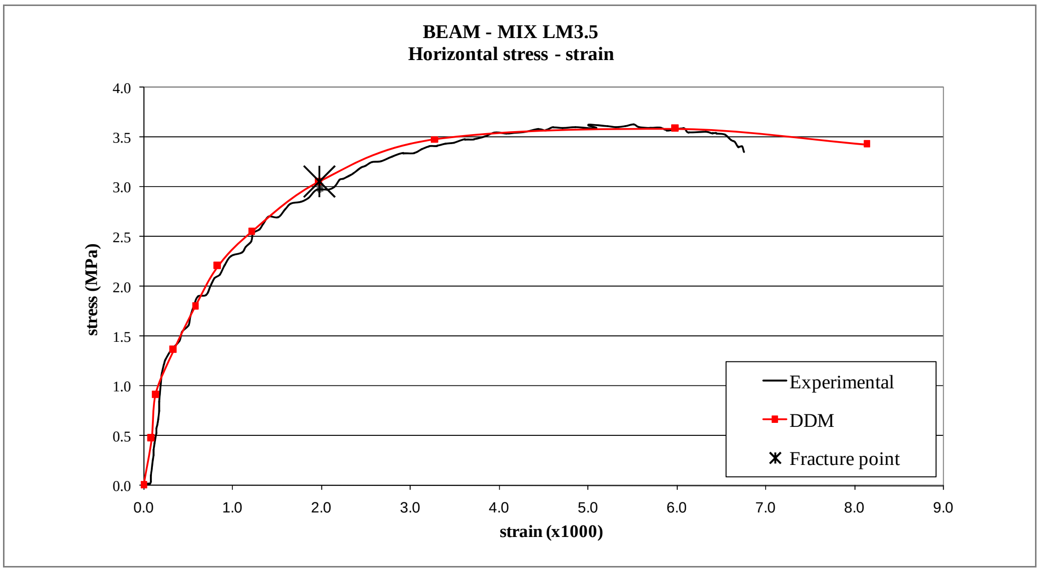

Figure 5.53 Predicted and measured horizontal stress-strain responses mix LM3.5 (3PB)

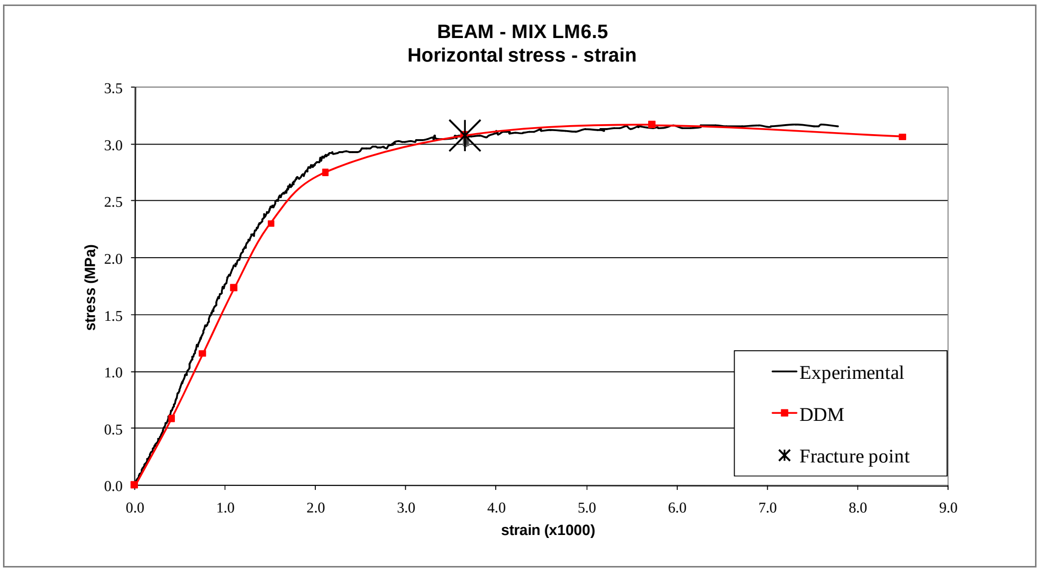

Figure 5.54 Predicted and measured horizontal stress-strain responses mix LM6.5 (3PB)

The resulting numerical simulations match the horizontal tensile stress-strain curves up to the ultimate load. The results clearly show that there is significant damage prior reaching the peak of the stress-strain curves for all the tests. The results also show that first fracture does occur well prior to peak load. In contrast, the post peak/post-first fracture interpretation is clearly very problematic. This lead to the statement that a fracture and/or damage model for the post peak cracking behavior is required.

Comparison between the predicted tensile strengths and fracture energy densities at the fracture points to the average measured ones for the mixtures are listed in Table 5.3.

Table 5.3 Comparison between predicted and measured tensile failure limits of the six mixtures

	Measured Tensile Strength from Strain gauge (MPa)	**Predicted Tensile Strength from DD (MPa)**	**Measured Fracture Energy Density from Strain gauge (KJ/m^3)**	**Predicted Fracture Energy Density from DD (KJ/m^3)**
MIXN1				
IDT	2.84	2.86	1.99	2.05
SCB	2.83	2.79	2.00	1.91
3PB	2.86	2.75	2.04	1.92
MIX N2				
IDT	2.49	2.33	3.80	3.68
SCB	2.54	2.55	3.67	3.74
3PB	2.46	2.46	3.72	3.81
MIX RM3.5				
IDT	2.93	2.97	5.20	5.24
SCB	2.90	2.86	5.21	5.14
3PB	2.95	2.88	5.26	5.21
MIX RM5.0				
IDT	2.90	2.85	6.30	6.38
SCB	2.95	3.00	6.31	6.32
3PB	2.95	2.98	6.34	6.43
MIX LM3.5				
IDT	3.08	3.06	5.70	5.65
SCB	3.08	3.14	5.76	5.83
3PB	3.14	3.05	5.71	5.72
MIXLM6.5				
IDT	3.03	3.01	7.30	7.29
SCB	3.03	3.05	7.29	7.12
3PB	3.04	3.00	7.31	7.29

The differences between predicted and measured tensile strengths and fracture energy densities at fracture for each mixture in each test are always less than 13.0%. This implies that the method is able to predict the real fracture points or rather the tensile strength of asphalt mixtures regardless of the test configuration. Indeed the fact that it is possible to obtain calibrated input parameters from the Superpave IDT test results and successfully predict the stress-strain evolution for the Superpave IDT, SCB and 3PB tests, implies that the process represented in the models is capturing a real fracture process.

5.3 Measured and Simulated Crack Patterns

Figures from 5.55 to 5.72 show both simulated crack patterns and measured full field strain maps for the six mixtures during IDT, SCB and 3PB tests at representative load steps ranging from crack initiation to major crack opening.

In the IDT test simulation, a huge number of small cracks are clearly visible within the center area of the specimen where high tensile stress is concentrated. In the following load steps, these small cracks coalesce into larger and more visible cracks until failure.

In both SCB and 3PB test simulations small cracks are visible within the center-bottom area of the specimen, which is the area of highest bending moment. Small cracks can also be noted above the specimen supports. These small cracks stabilize early not growing into larger, visible cracks. In the following load steps the central crack growth region for both SCB and 3PB region extends along the bottom edge of the specimen, coalescing into a single larger macro-crack along the vertical plane.

Measured strain maps agree well with the numerical results; high strain values develop within the whole center area of the IDT specimen, while in both SCB and 3PB specimens, the highest strain results only in a restricted zone located at the bottom edge of the specimens. From full field strain maps it can be observed how tensile strains are greatly localized in the area in which a crack initiates. The full field strain maps also allows for the observation of tensile strain development around aggregates, while no strains are registered where a coarse aggregate exists.

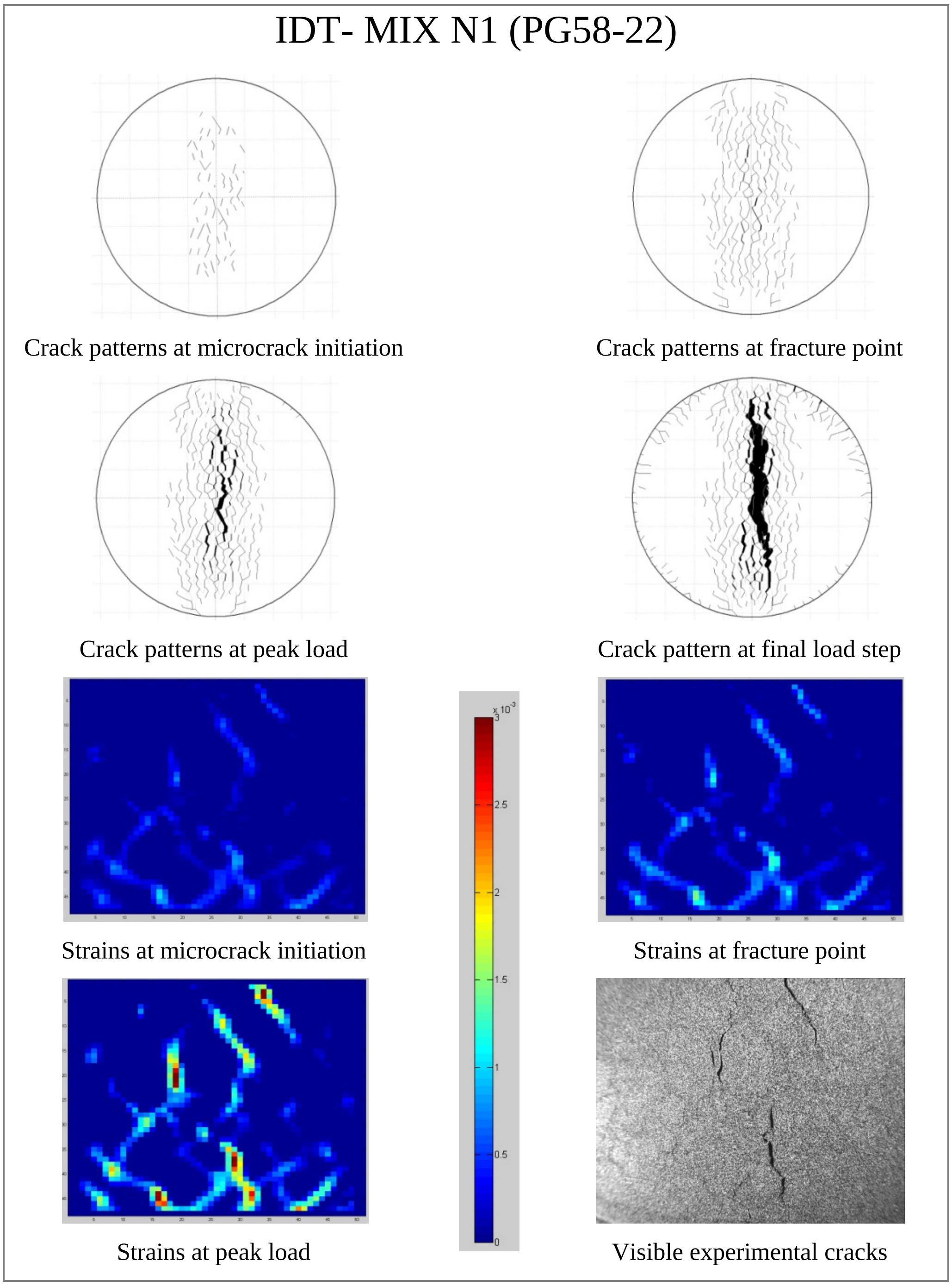

Figure 5.55 Predicted crack patterns and full field strain maps during IDT - mix N1

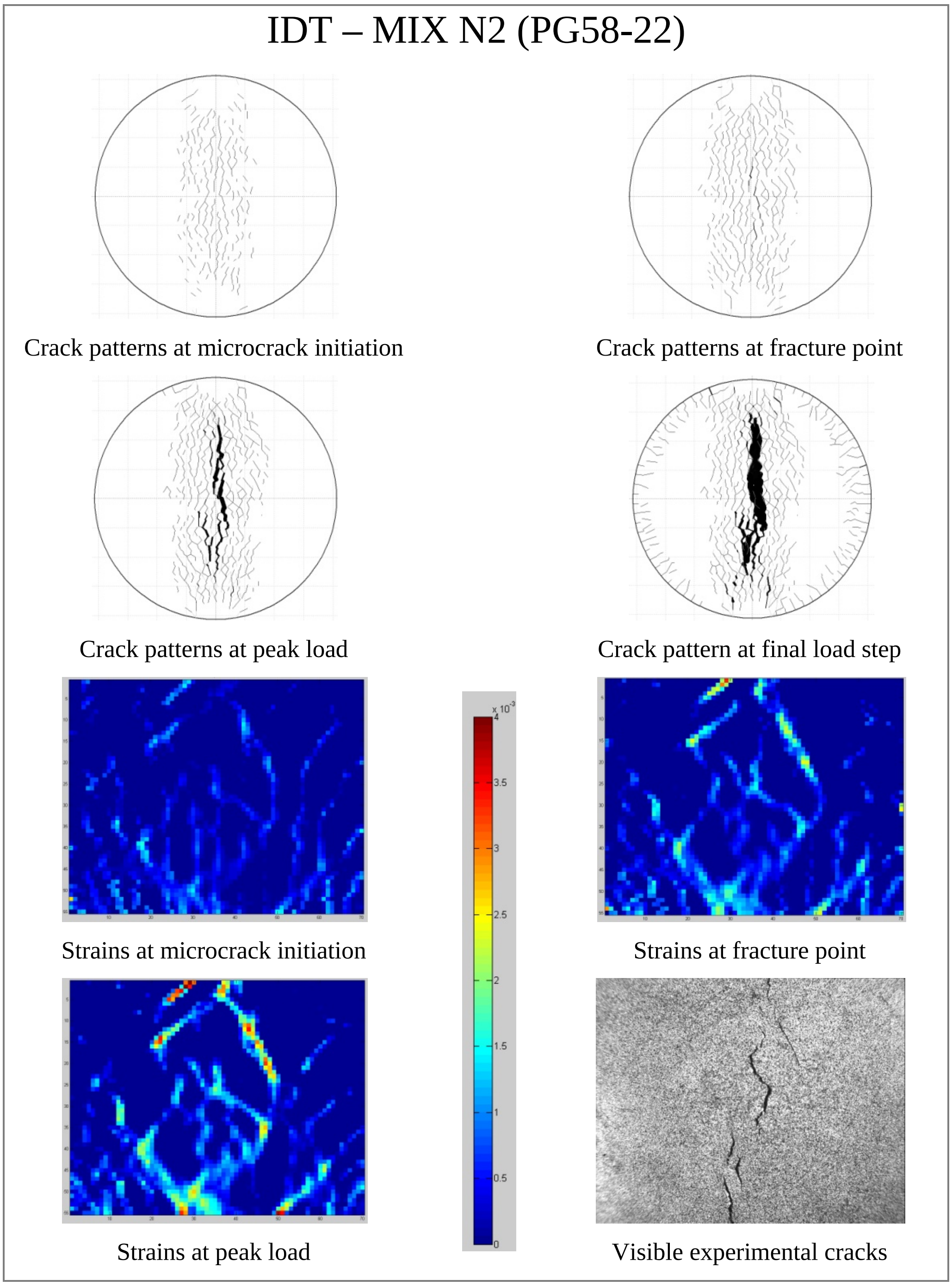

Figure 5.56 Predicted crack patterns and full field strain maps during IDT mix N2

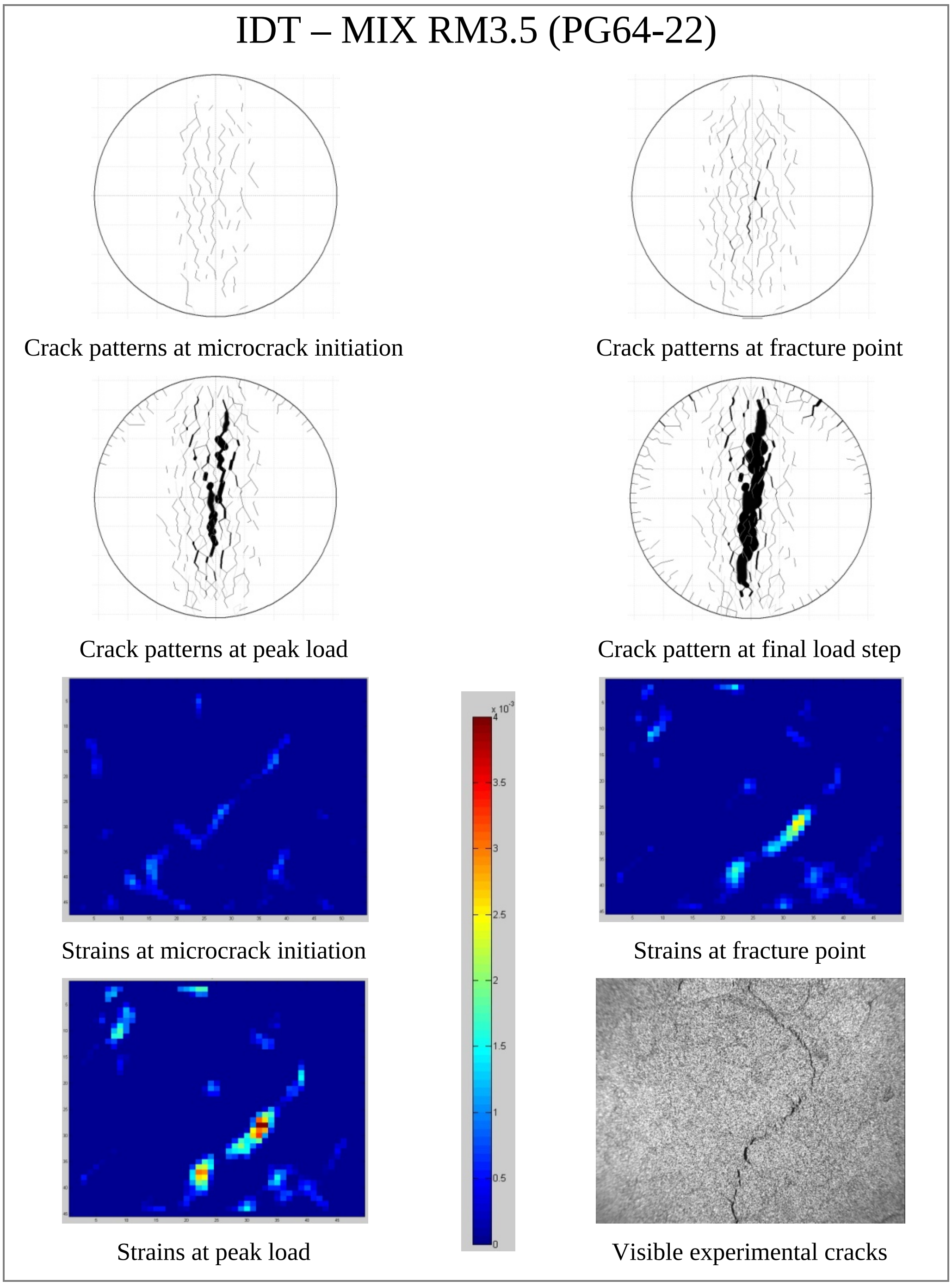

Figure 5.57 Predicted crack patterns and full field strain maps during the IDT - mix RM3.5

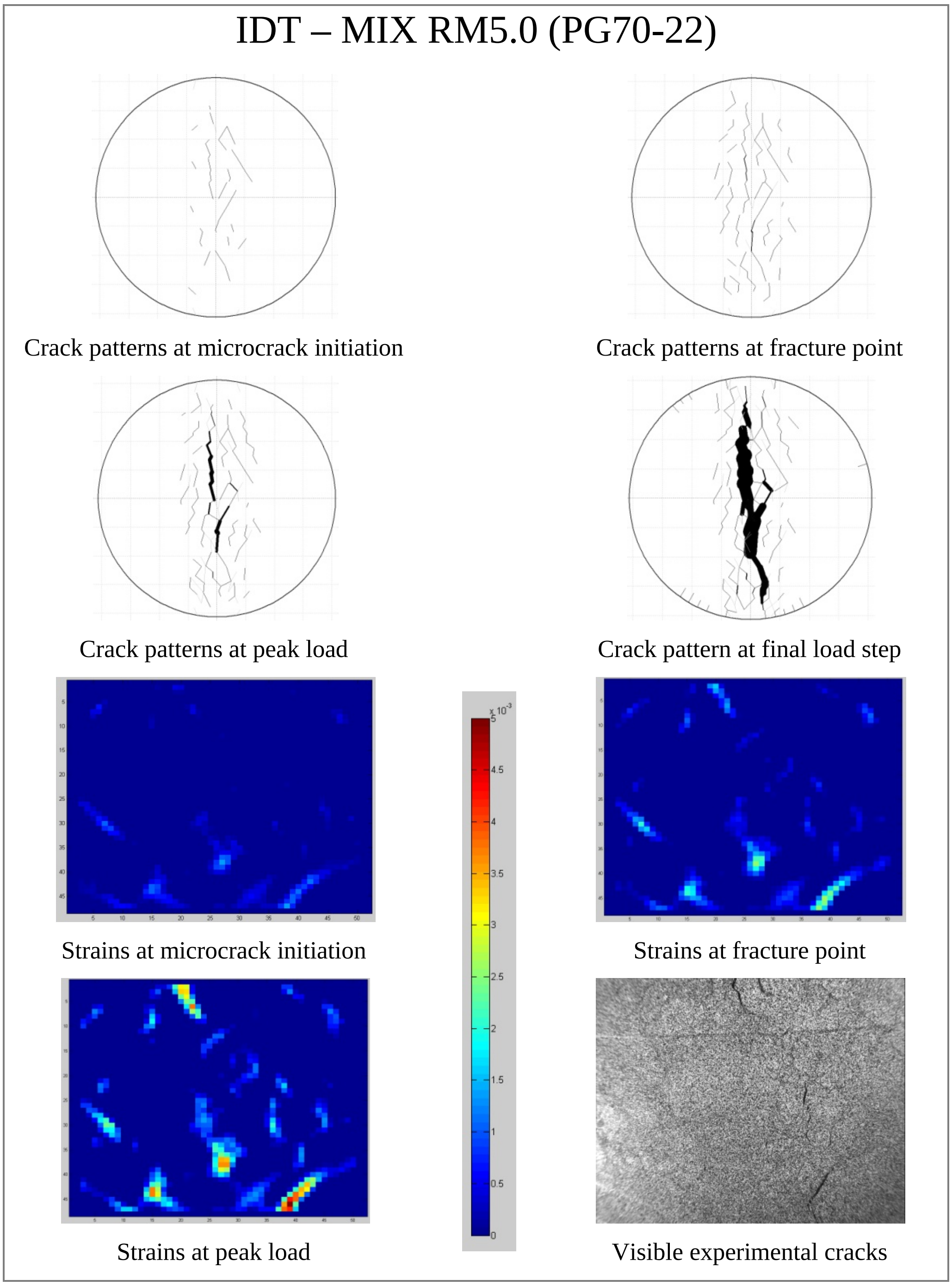

Figure 5.58 Predicted crack patterns and full field strain maps during IDT - mix RM5.0

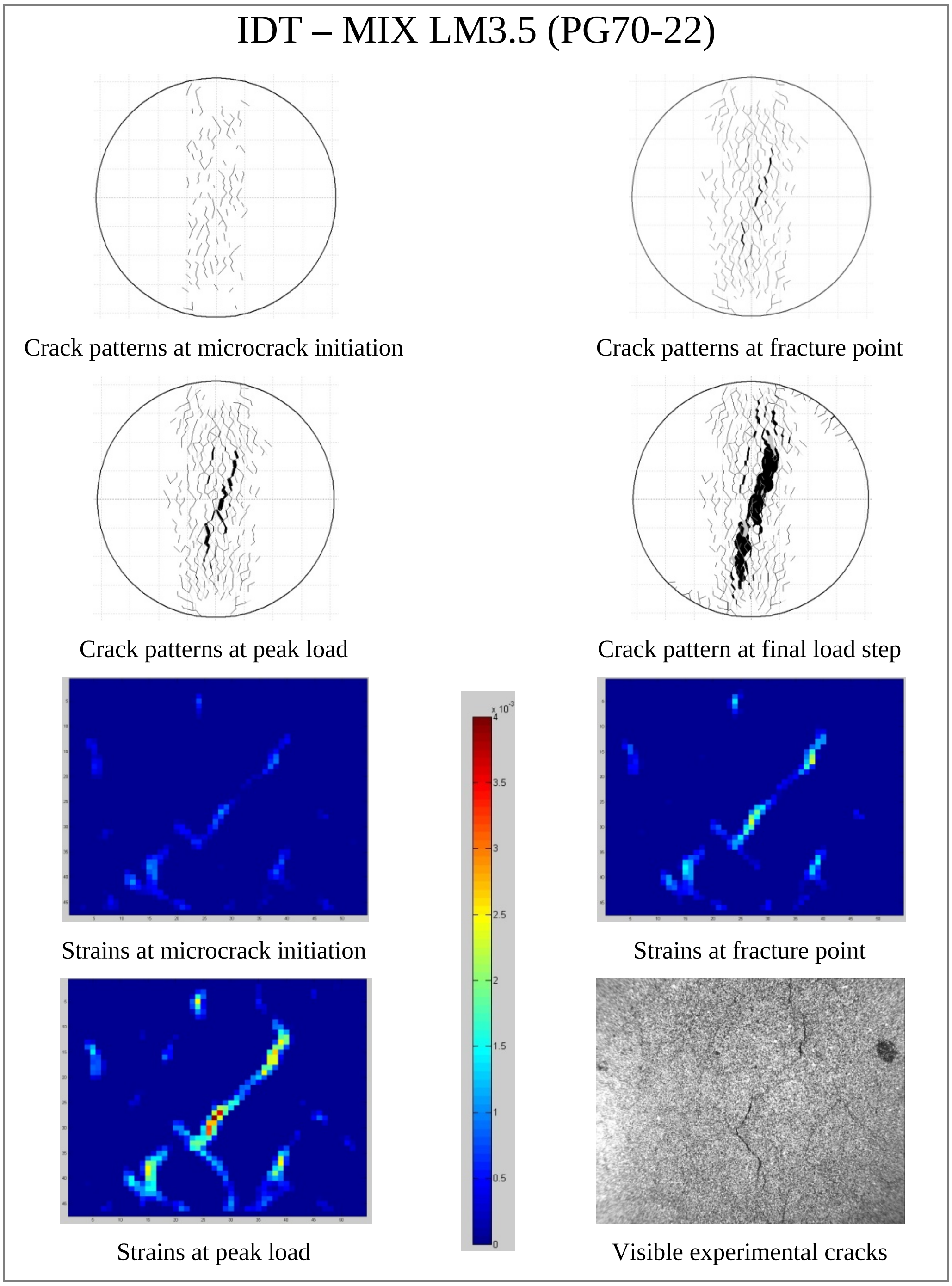

Figure 5.59 Predicted crack patterns and full field strain maps during IDT - mix LM3.5

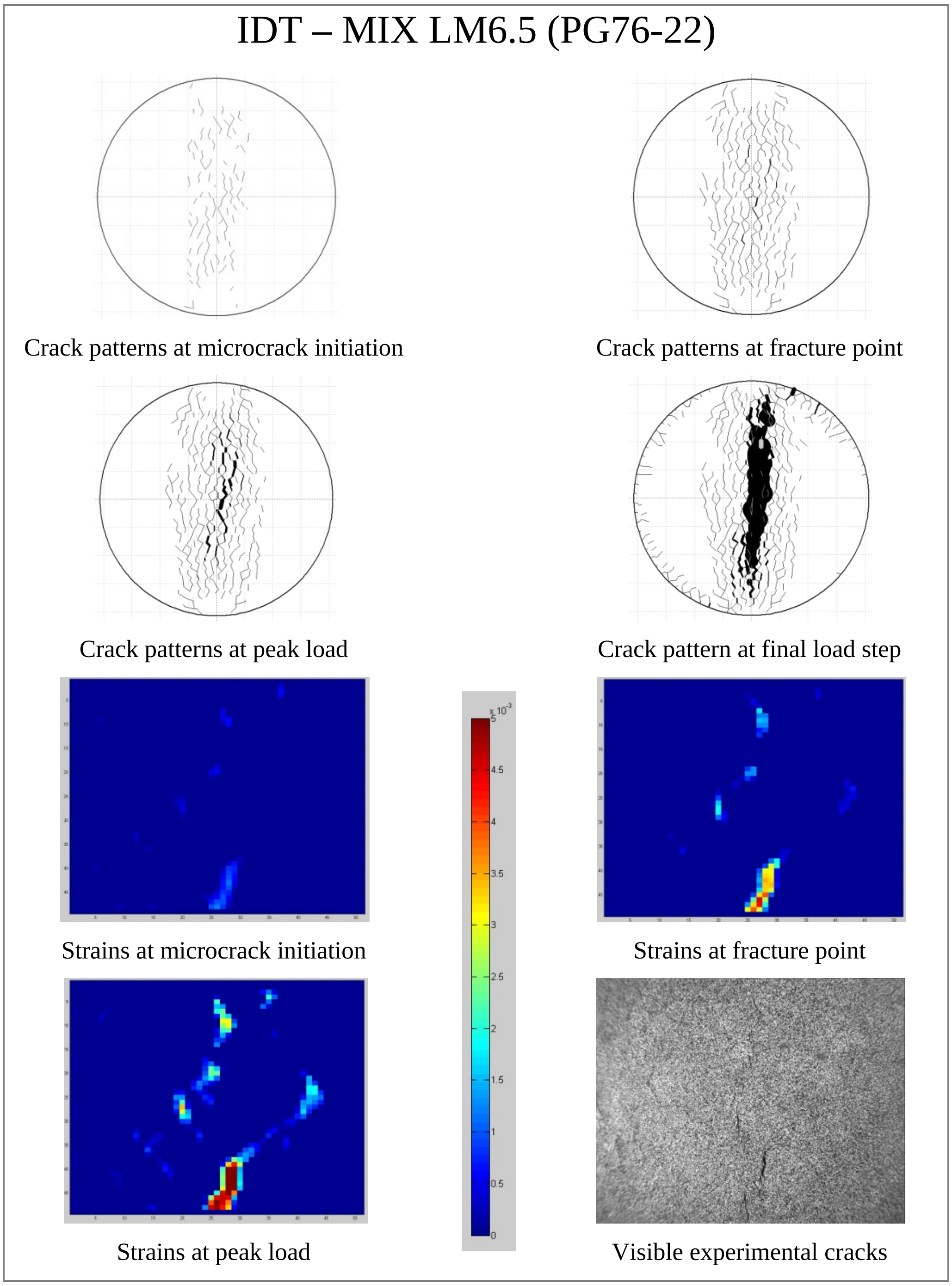

Figure 5.60 Predicted crack patterns and full field strain maps during IDT - mix LM6.5

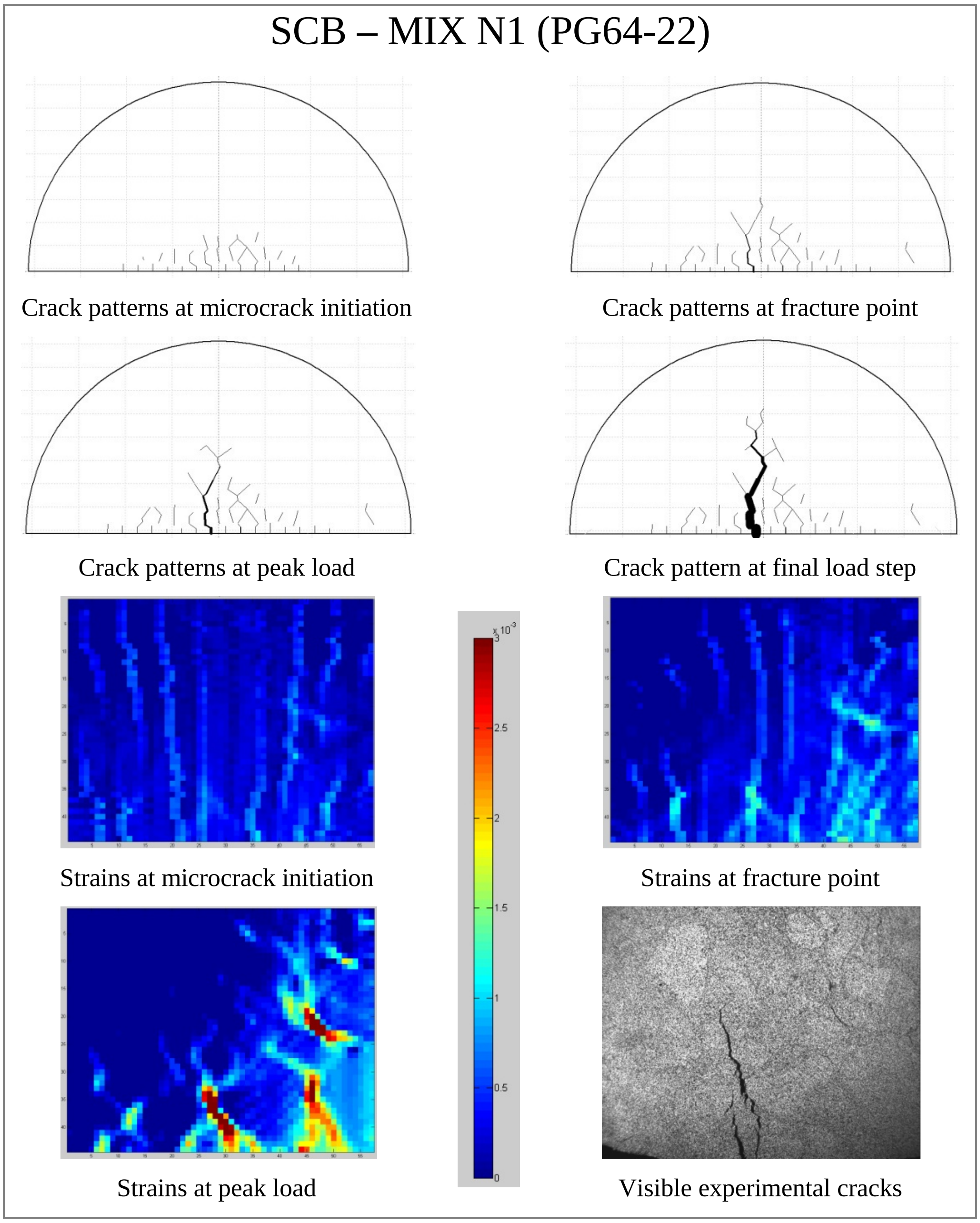

Figure 5.61 Predicted crack patterns and full field strain maps during SCB - mix N1

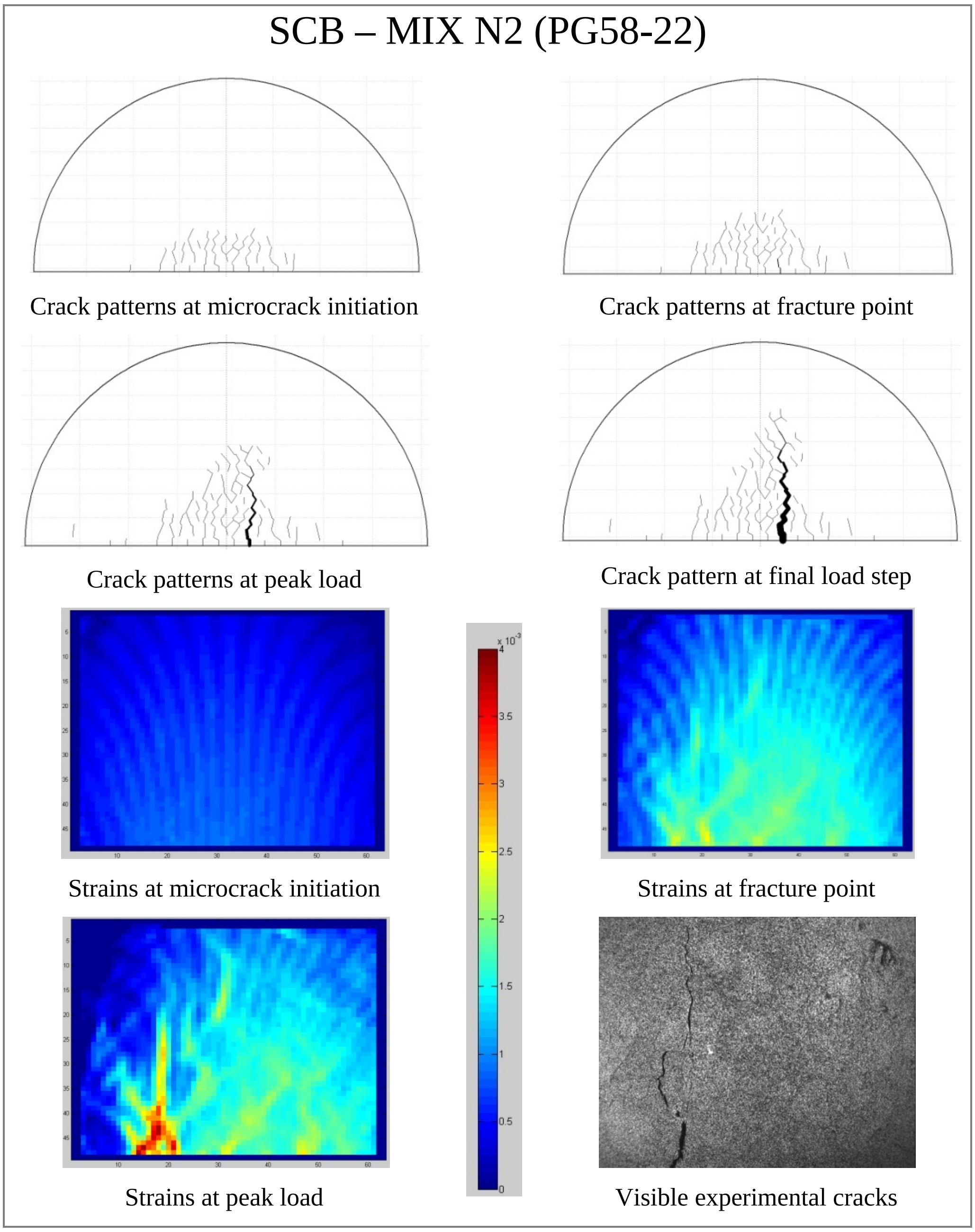

Figure 5.62 Predicted crack patterns and full field strain maps during SCB - mix N2

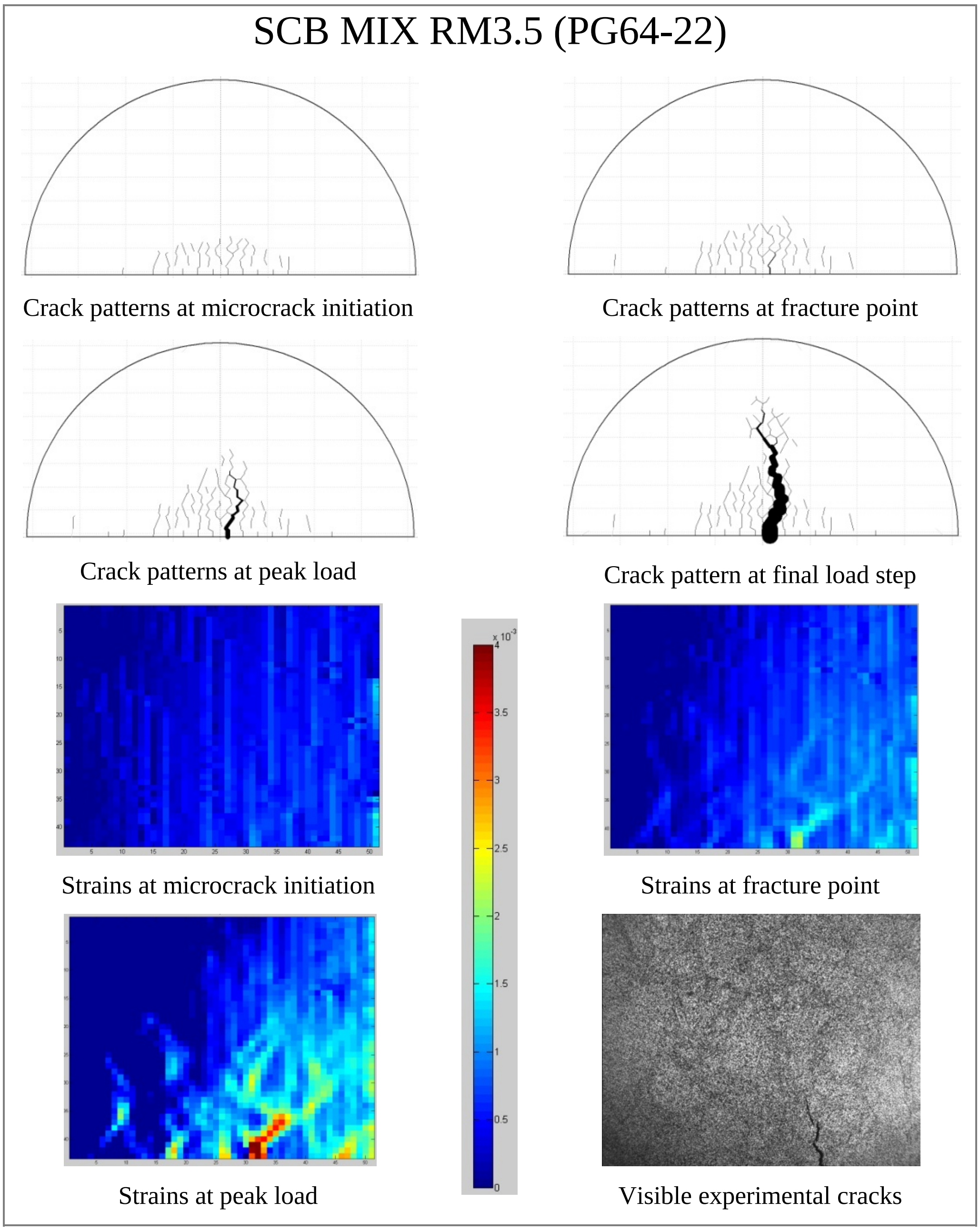

Figure 5.63 Predicted crack patterns and full field strain maps during SCB - mix RM3.5

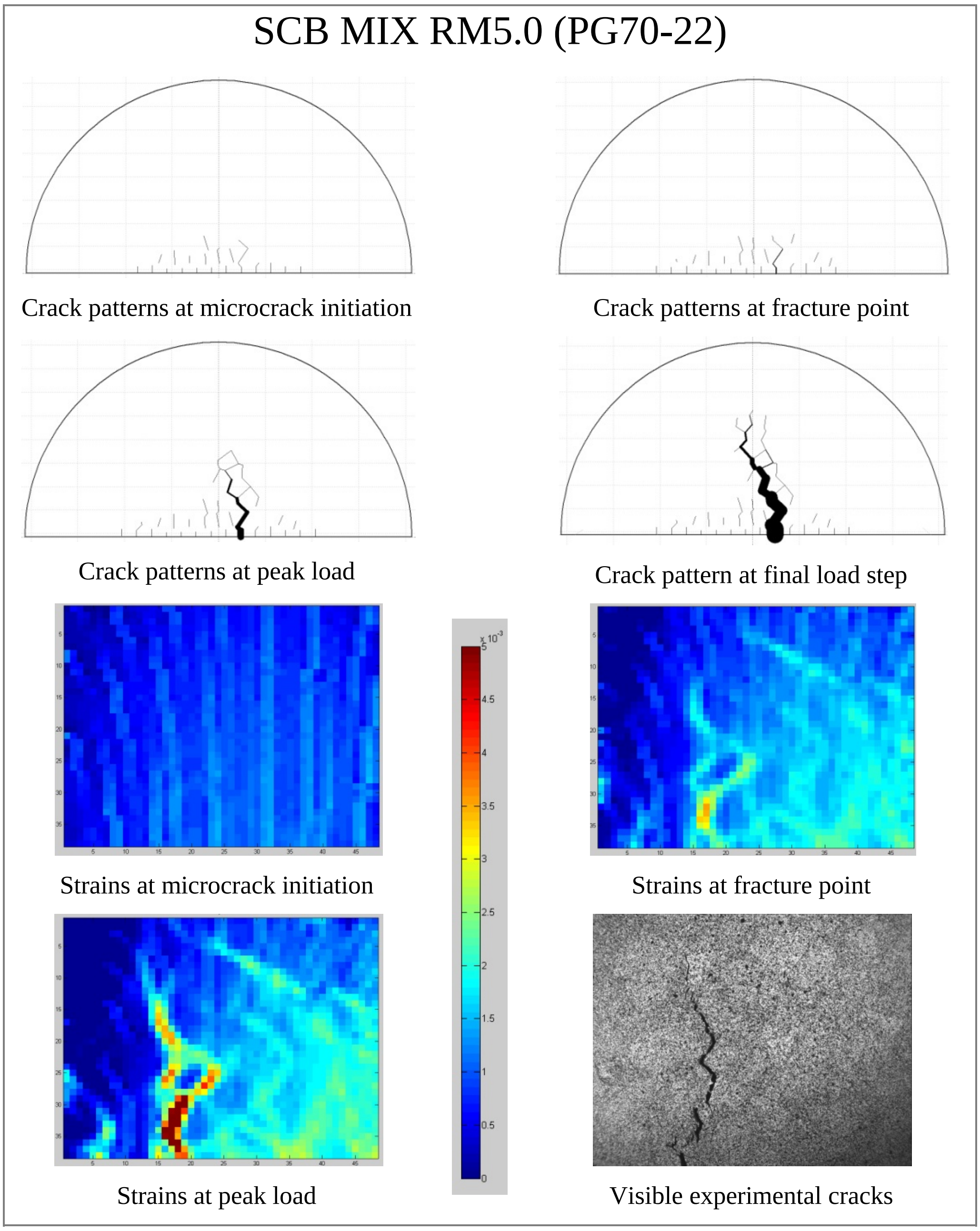

Figure 5.64 Predicted crack patterns and full field strain maps during SCB - mix RM5.0

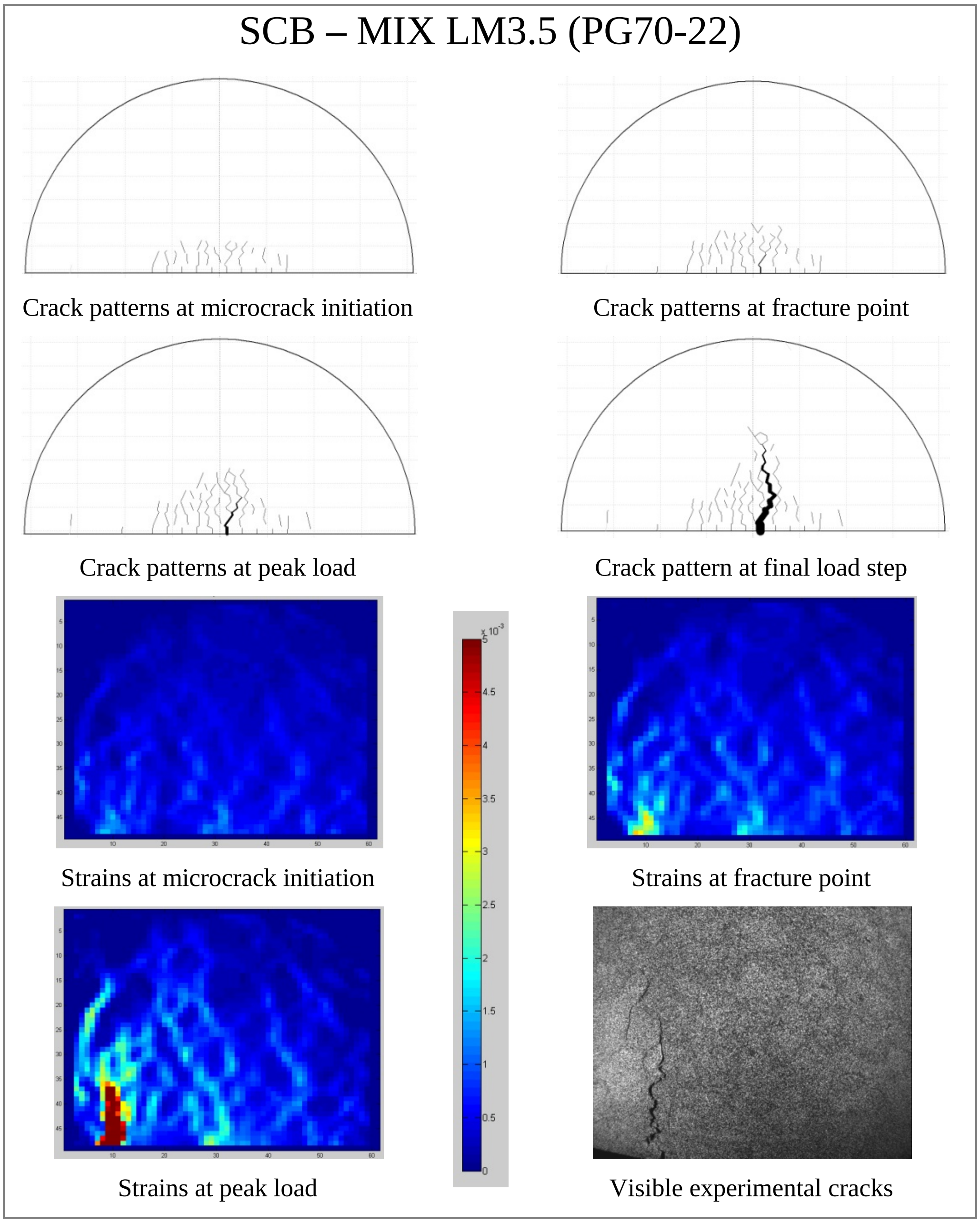

Figure 5.65 Predicted crack patterns and full field strain maps during SCB - mix LM3.5

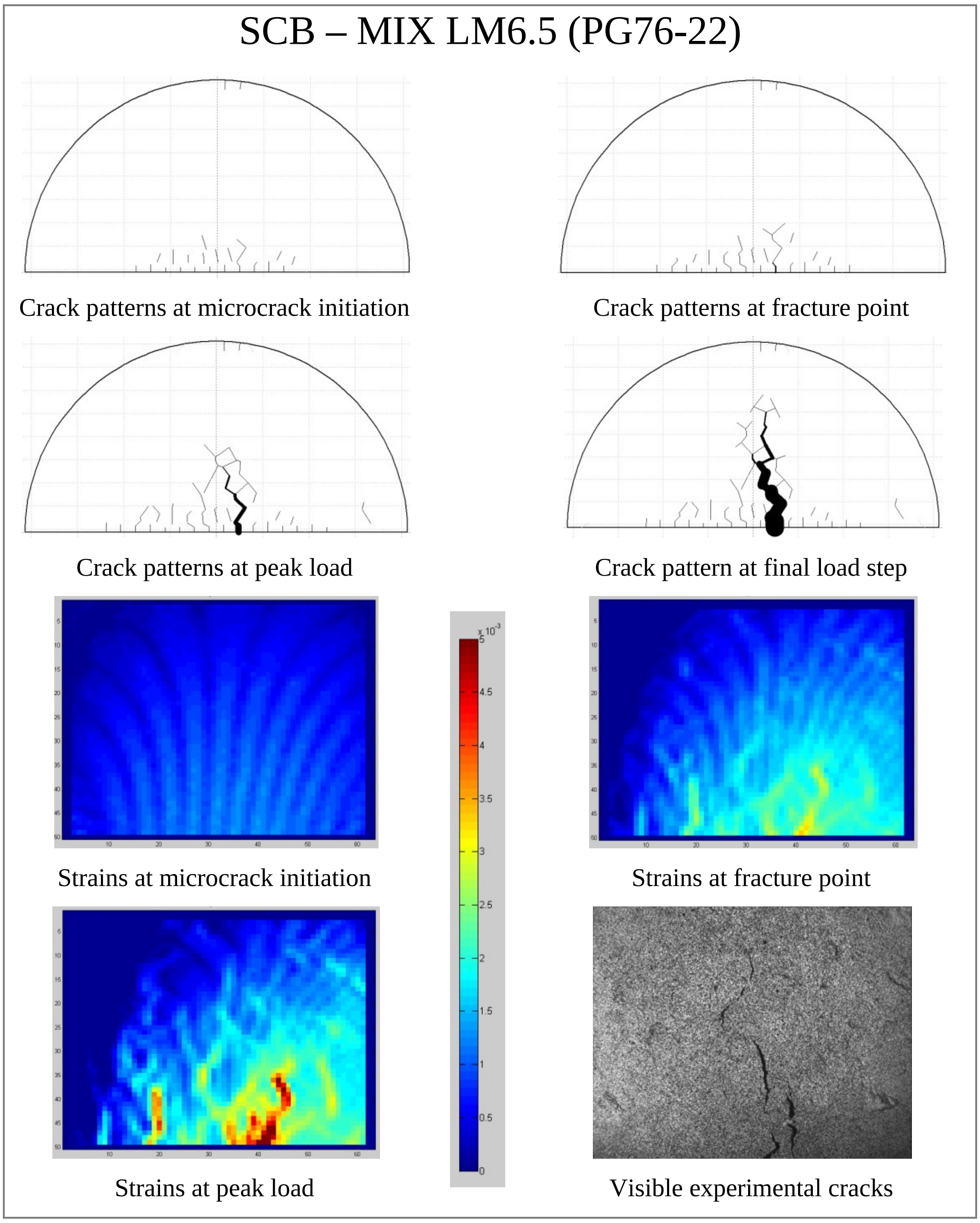

Figure 5.66 Predicted crack patterns and full field strain maps during SCB – mix LM6.5

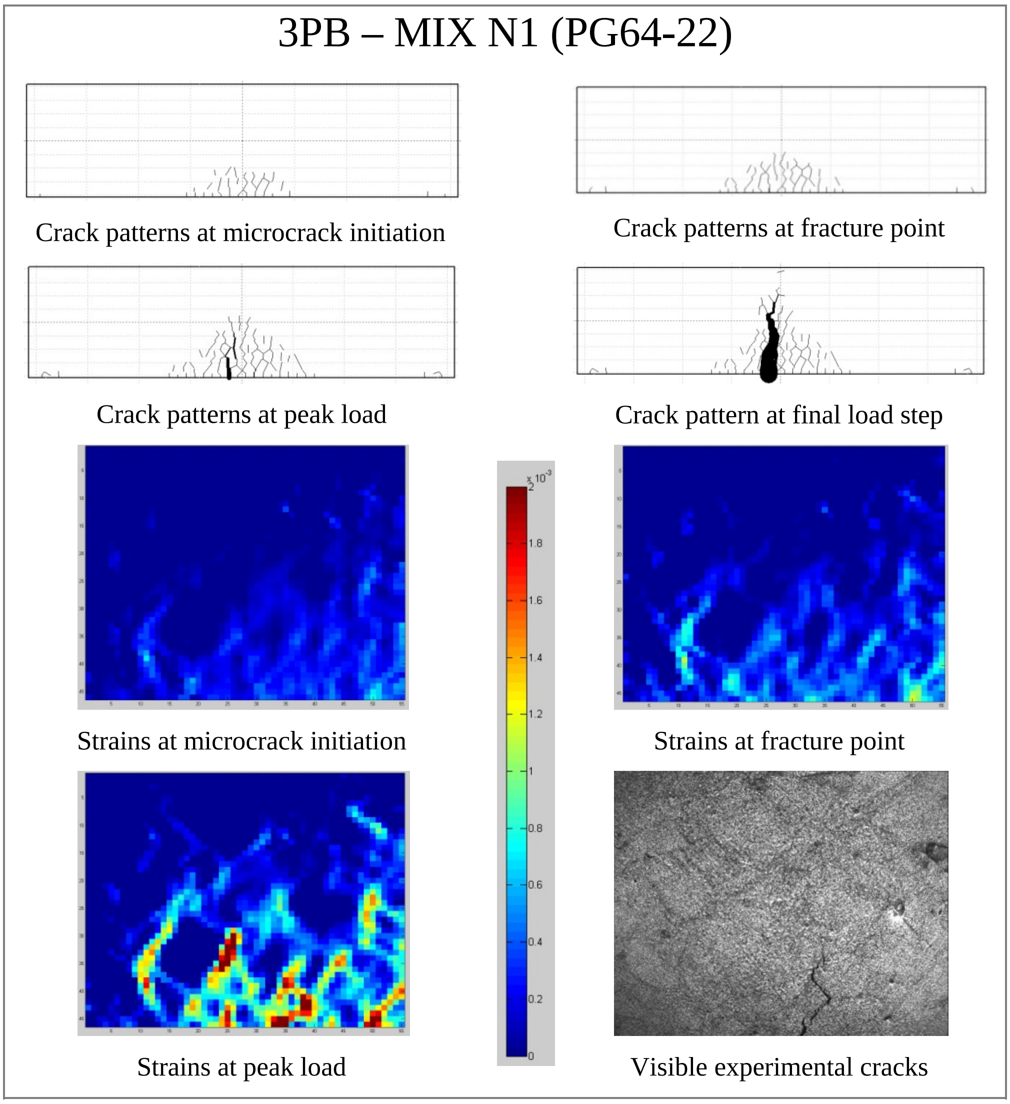

Figure 5.67 Predicted crack patterns and full field strain maps during 3PB - mix N1

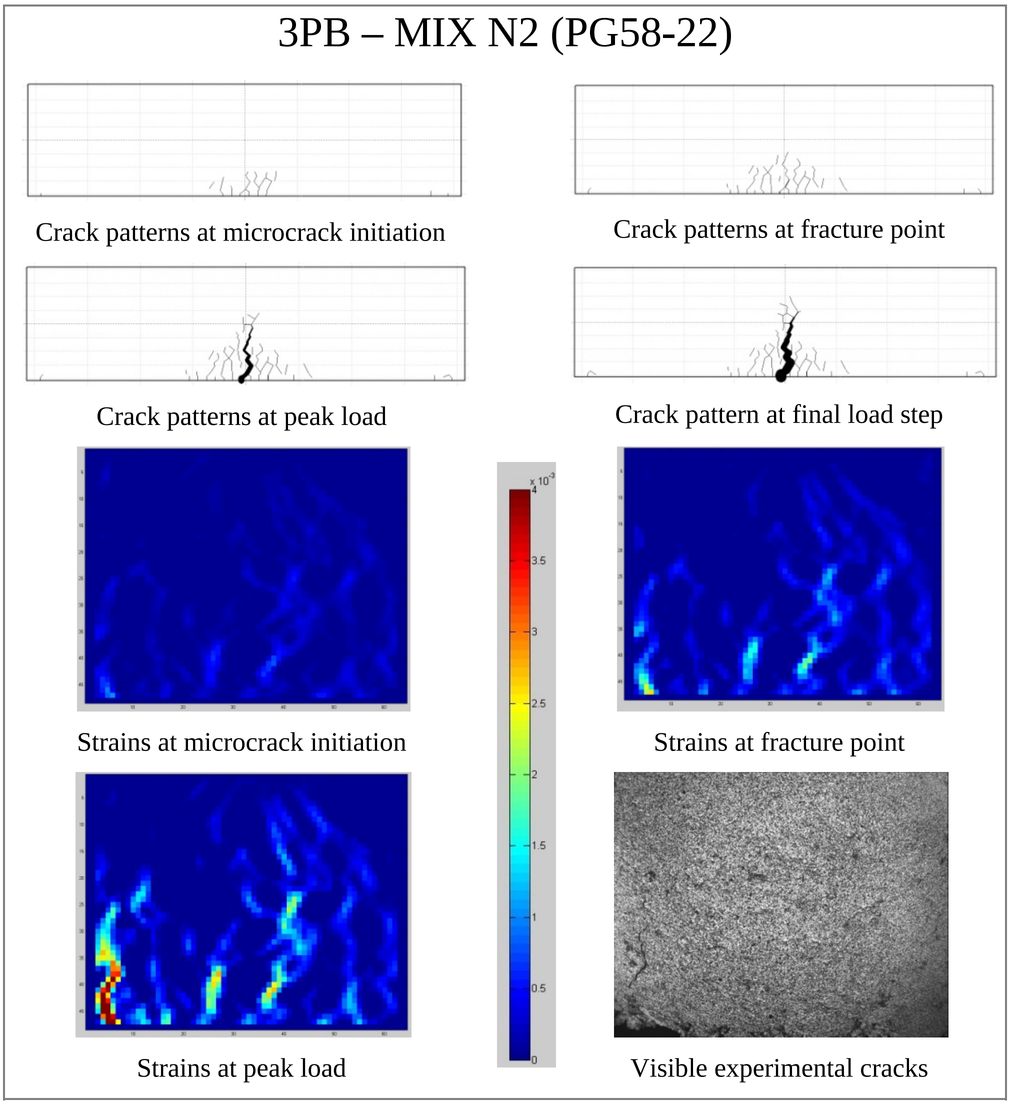

Figure 5.68 Predicted crack patterns and full field strain maps during 3PB - mix N2

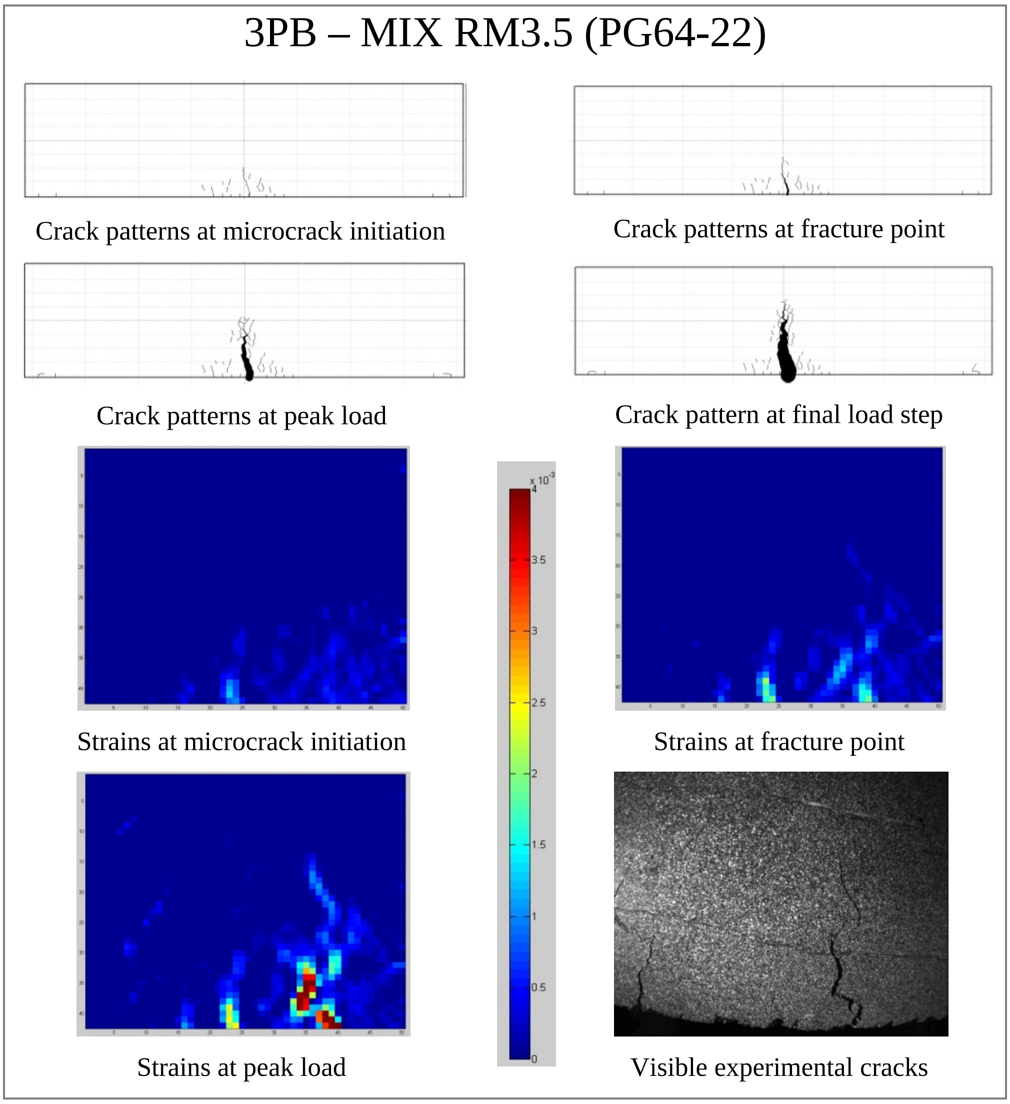

Figure 5.69 Predicted crack patterns and full field strain maps during 3PB - mix RM3.5

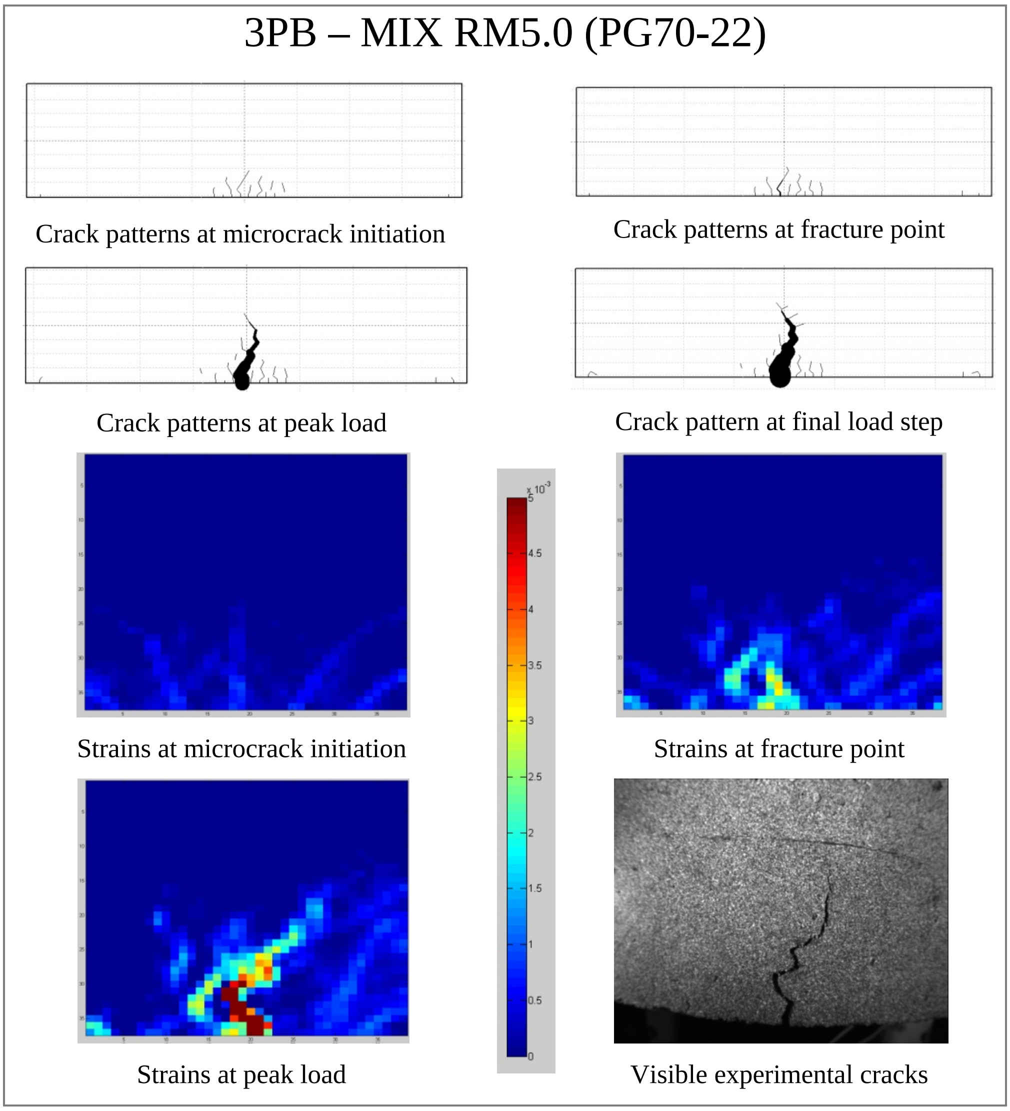

Figure 5.70 Predicted crack patterns and full field strain maps during 3PB - mix RM5.0

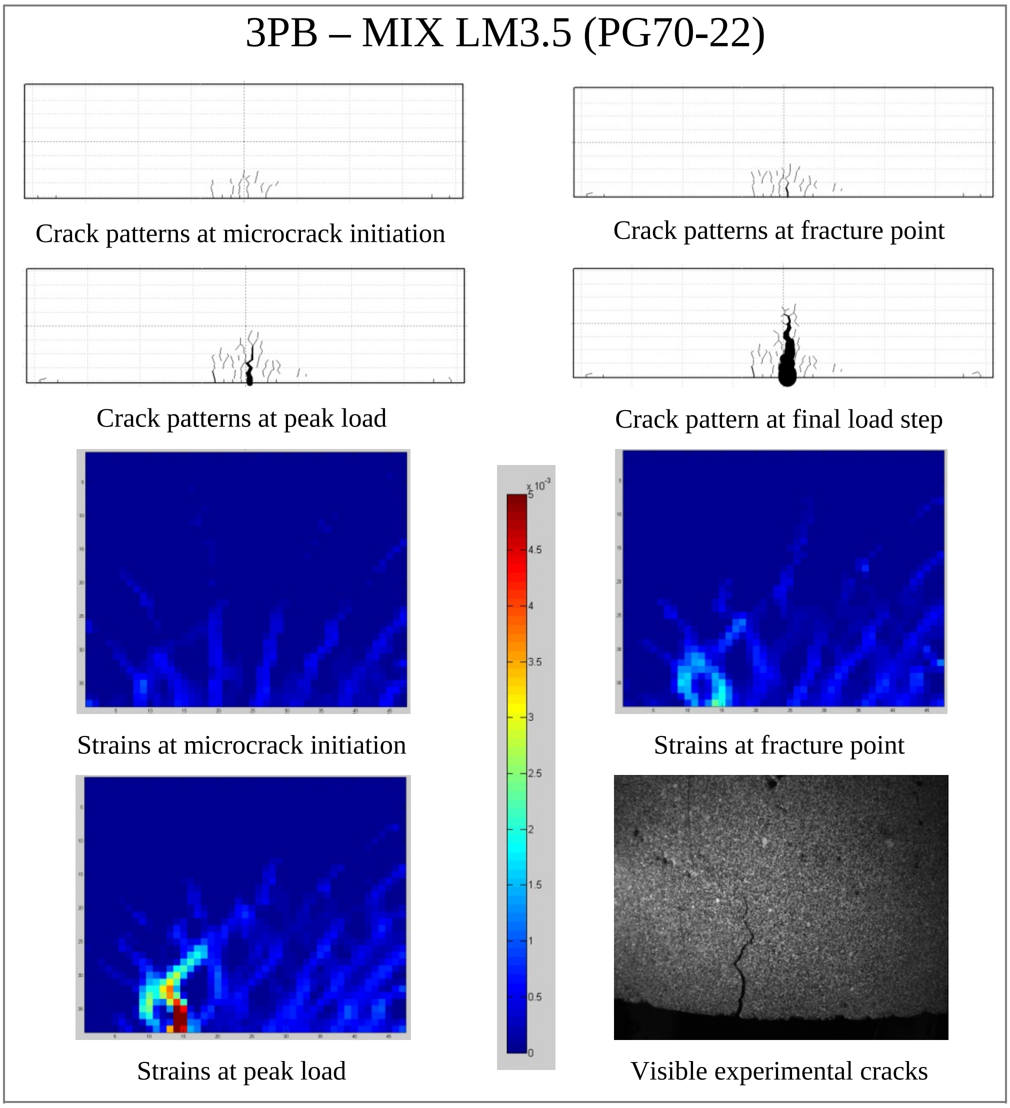

Figure 5.71 Predicted crack patterns and full field strain maps during 3PB - mix LM3.5

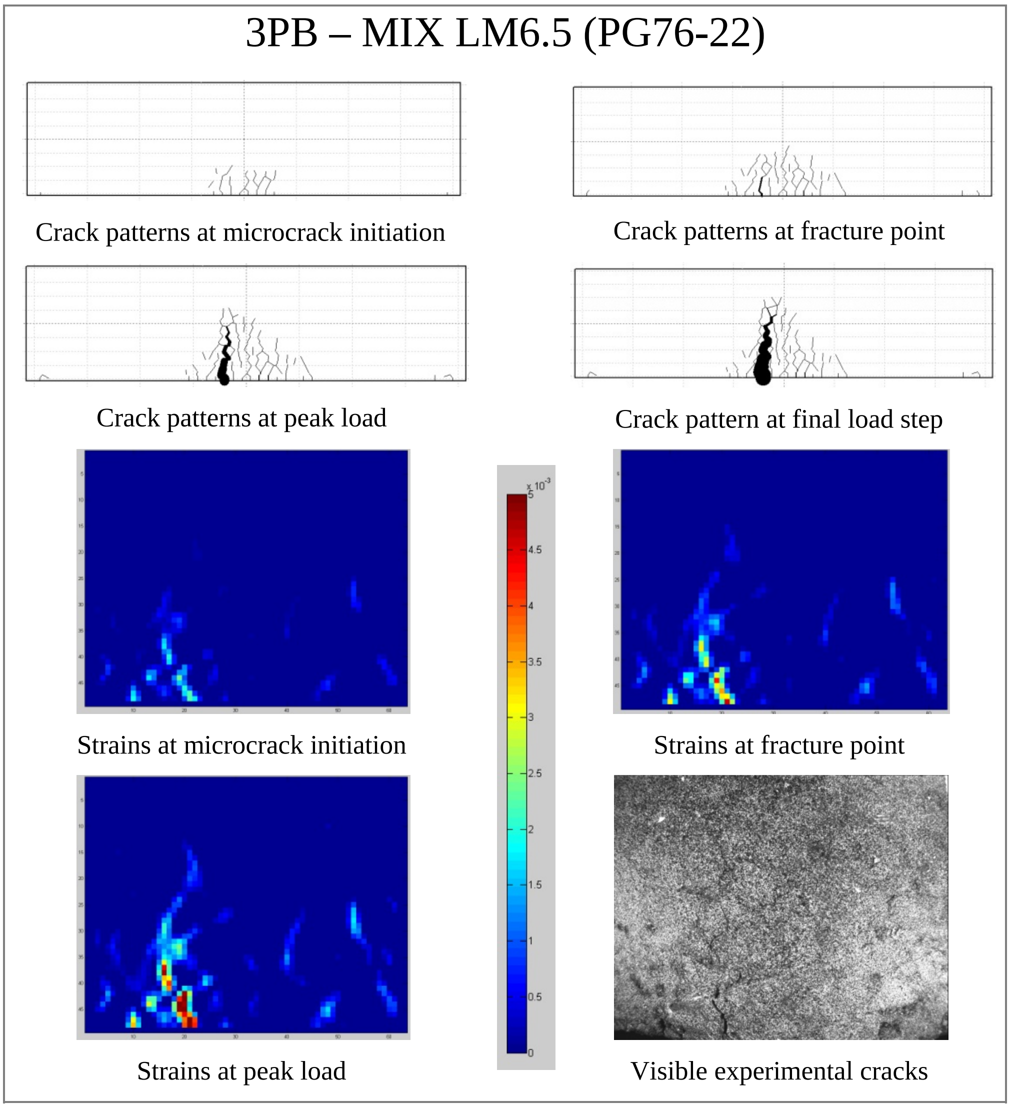

Figure 5.72 Predicted crack patterns and full field strain maps during 3PB - mix LM6.5

5.4 Effect of SBS Modifiers on HMA Cracking Resistance

The effect of SBS modifiers on HMA cracking resistance was evaluated using the five polymer modified mixtures composed by the same base binder N2 to assure that the presence of the SBS modifier was the only factor affecting the results. According to the "HMA Fracture Mechanics", mixture's cracking performance can be estimated using the following tensile asphalt mixture properties:

- Resilient Modulus (M_R)
- Creep Compliance power law parameters (D_1 and m-value)
- Tensile Strength (S_t)
- Dissipated creep strain energy to failure ($DCSE_f$)
- Fracture energy (FE)
- Energy Ratio (ER)

These properties were easily determined from the Superpave IDT test as discussed by Roque et al. (2002). A summary of Superpave IDT test results and a detailed analysis of each mixture property is presented. The relationship between mixture properties and mixture cracking performance is also described. All the results obtained from the Superpave IDT test are listed in Table 5.4.

Table 5.4. Superpave IDT test results of the five mixtures

ASPHALT MIXTURE	N2	RM3.5	RM5.0	LM3.5	LM6.5
Resilient Modulus (Gpa)	13.35	13.11	12.54	13.34	12.43
Creep Compliance @1000 seconds (1/Gpa)	4.23	2.07	1.85	2.13	1.59
m-value	0.55	0.46	0.45	0.51	0.39
D_1	6.309E-07	5.687E-07	5.584E-07	4.203E-07	7.205E-07
Tensile Strength (Mpa)	2.49	2.93	2.90	3.08	3.03
Failure Strain (10^{-6})	2061.3	2336.1	2804.4	2450.1	3176.2
$DCSE_f$ (kJ/m^3)	3.57	4.87	5.96	5.34	6.93
$DCSE_{min}$ (kJ/m^3)	2.33	1.32	1.77	1.32	1.02
Fracture Energy (kJ/m^3)	3.80	5.20	6.30	5.70	7.30
Energy Ratio	1.53	3.69	5.07	4.03	6.76

5.4.1 Resilient Modulus

The resilient modulus is defined as the ratio of the applied stress to the recoverable strain when repeated loads are applied, resulting in a measure of the material's elastic stiffness. Looking at the results listed in Table 5.4, it's clearly evident that either cross-linked and linear SBS polymer modifiers have very low effect on resilient modulus. It can be observed that the higher the percent of polymer modification, the lower is the resilient modulus value. However, this difference has shown to be not significant with respect to the unmodified mixture. The results indicate that, at small strain and/or short loading times, the amount and the type of SBS modifier do not affect the mixture's elastic response.

5.4.2 Creep Compliance

Creep compliance is a function of time-dependent strain over stress; it is related to the ability of a mixture to relax stresses. The creep compliance curve represents the time-dependent behavior of asphalt mixture, thus it is commonly used to evaluate the rate of damage accumulation of asphalt mixtures. Three mixture parameters can be obtained from creep compliance tests: D_0, D_1, and m-value. Although D_1 and m-value are related to each other, D_1 is more descriptive of the initial portion of the creep compliance curve, while m-value describes the longer-term portion of the same curve. The m-value has proved to be related to the rate of damage accumulation and the fracture resistance of asphalt mixtures (Kim et al., 2003). In detail, an asphalt mixture with a low m-value exhibits a low rate of damage accumulation.

According to the HMA Fracture Mechanics framework, the slope of the creep compliance curve at 1000 seconds is essentially a measure of the rate of permanent deformation: the higher the slope, the higher the rate of permanent deformation (Zhang et al., 2001). The crack growth process is exhibited by higher rates of permanent deformation, thus mixtures with high m-values or high creep rates exhibit higher crack growth rates. Creep compliance curves are shown in Figure 5.73. The curve trend is clearly affected by the type and the amount of SBS modifier. The results show that both cross-linked and linear SBS polymers strongly decrease the rate of permanent deformation leading to lower rate of micro-damage accumulation. Also, the higher is the amount of polymer in the asphalt binder, the lower is the mixture creep compliance. However, it should be noted that the cross-linked SBS asphalt modifier exhibits a lower creep rate than the linear one within the soft modified mixtures. In contrast, at higher percentages of modifiers, linear polymer seems to increase mixture's creep-related performance.

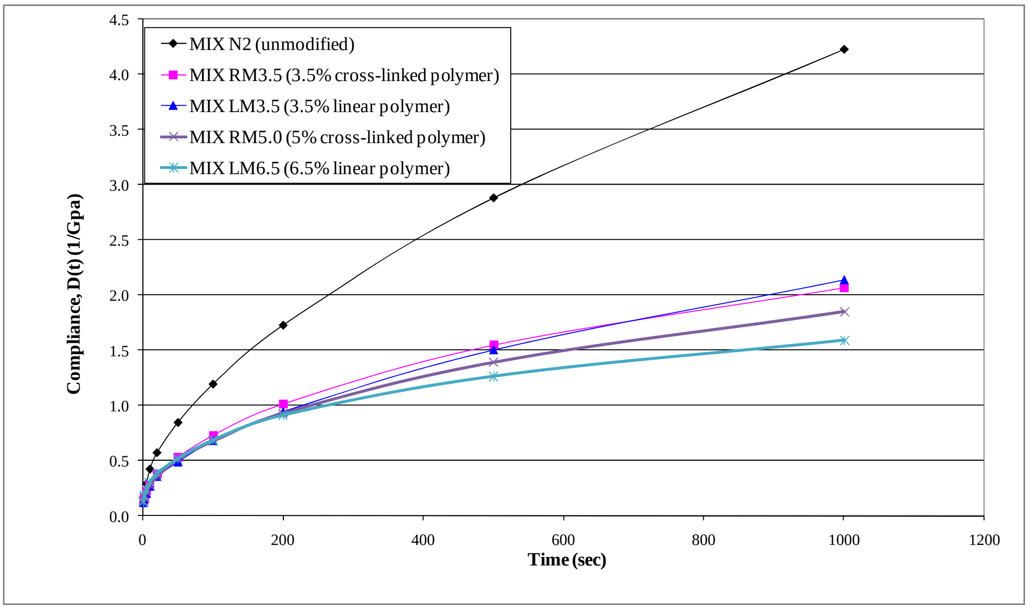

Figure 5.73 Creep Compliance Curves for the five mixtures

5.4.3 Indirect Tensile Strength and Energy-Based Parameters

As shown in Figure 5.74, the tensile strength is slightly improved by SBS polymer modification while not affected by the amount of polymer in the binder. This improvements are not significant resulting in 17% (cross-linked polymer modification) and 24% (linear polymer modification). Conversely, the dissipated creep strain energy to failure and fracture energy are strongly enhanced by polymer modifications (Figure 5.75), as well as failure strain (Figure 5.76). This means that both cross-linked and linear SBS polymers have the ability of increasing both the upper and the lower energy thresholds required to crack the mixture. Besides, linear polymers provide greater benefits in cracking resistance than the cross-linked ones.

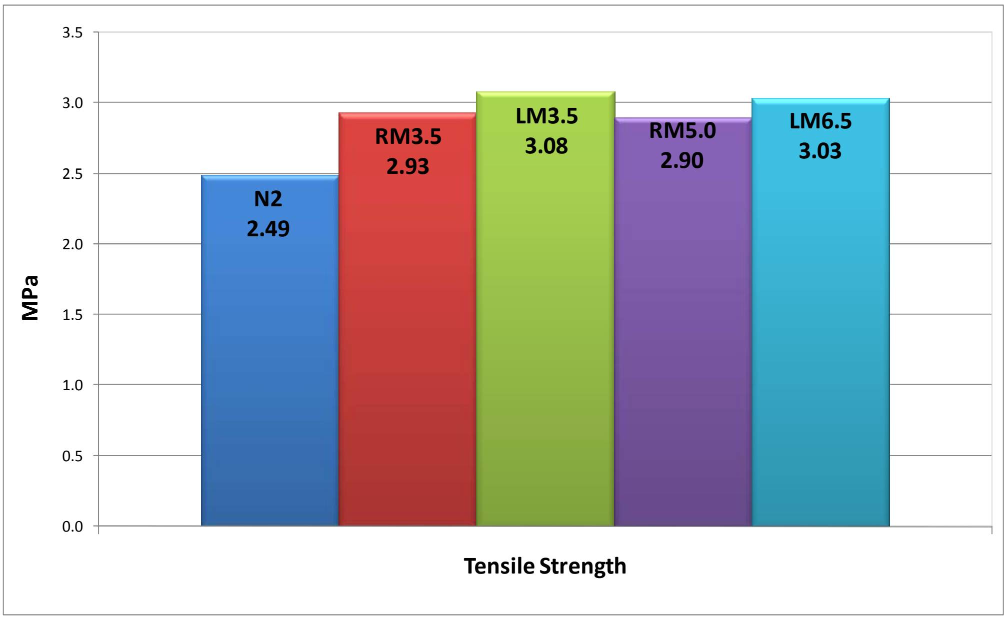

Figure 5.74 Tensile strengths obtained for the five mixes

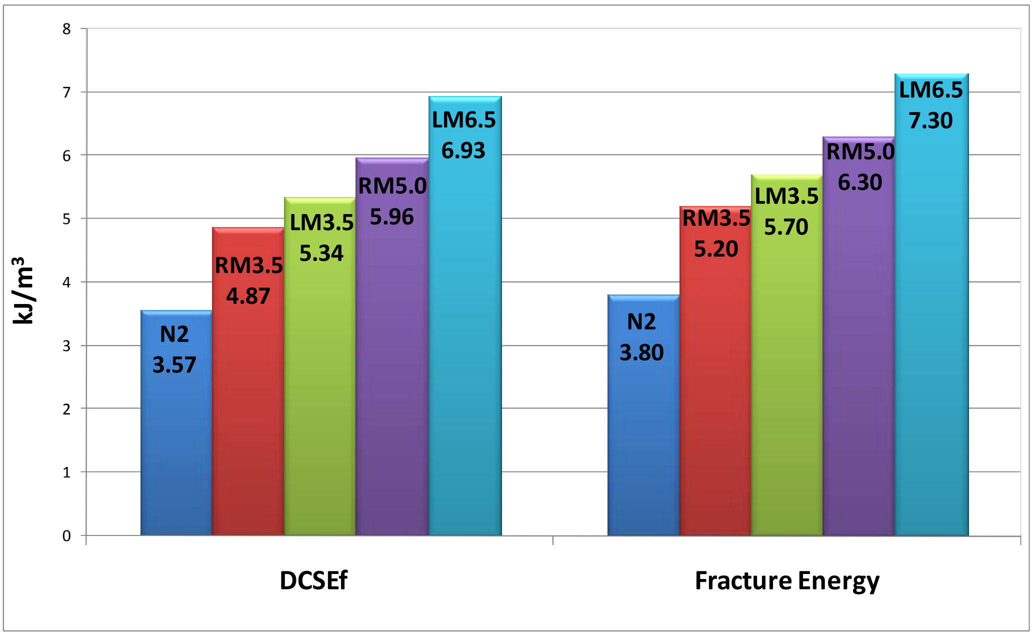

Figure 5.75 Fracture energy densities and Dissipated Creep Strain Energies for the five mixes

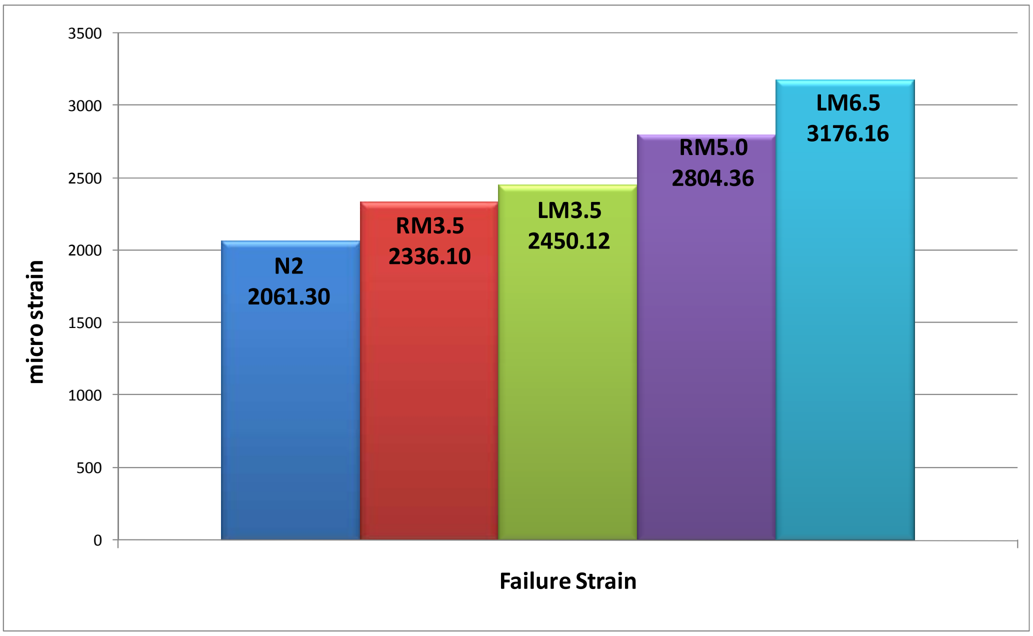

Figure 5.76 Failure strains for the five mixes

5.4.4 Energy Ratio

The Energy Ratio (ER) is a dimensionless parameter which defines a single criterion for top-down cracking performance of all mixtures in pavement structures. The Energy Ratio is defined as follows:

$$\mathrm{ER} = \mathrm{DCSE_f} \,/\, \mathrm{DCSE_{min}} \qquad [5.1]$$

where $DCSE_f$ is the dissipated creep strain energy threshold of the mixture and $DCSE_{min}$ is the minimum dissipated creep strain energy required (function of the creep compliance power low parameters). Further details are discussed by Roque et al. (2004).

According to the performance-based mixture specification developed by Roque et al. (2004), for a mixture to be acceptable, the ER should be greater than a certain value depending on the traffic volume, as detailed in Table 5.5.

Figure 5.77 shows the Energy Ratio values obtained for the five mixtures. The results highlight that the addition of SBS polymer strongly improves asphalt mixture’s resistance to top-down cracking. Even in this case, the SBS linear polymer modifier provides more benefits than the SBS cross-linked one, especially for hard modified mixtures.

Table 5.5. Energy-based mixture specification criteria

Traffic ESALS/year x 1000	Minimum Energy Ratio
< 250	1
< 500	1.3
< 1000	1.95

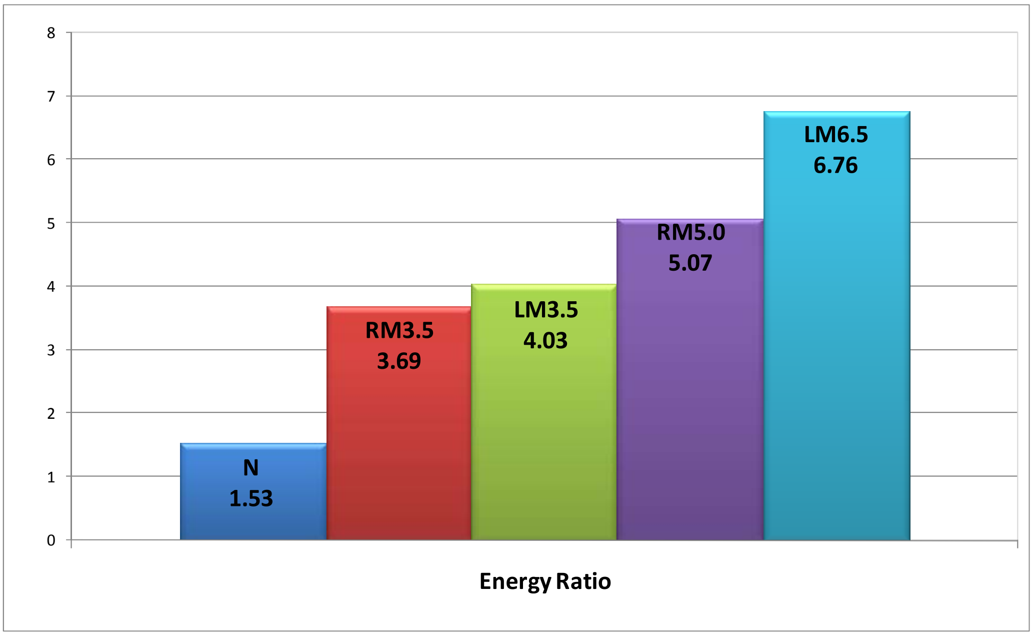

Figure 5.77 Energy Ratio values obtained for the five mixes

5.4.5 Crack Localization and Crack Growth

The previously shown (Figures from 5.55 to 5.72) measured full filed tensile strain map for the five mixes emphasize how tensile strains are greatly localized in the area in which a crack initiates. SBS polymer modified mixtures exhibit high strains only up to the location of impending fracture, while unmodified mixtures exhibit highly distributed damage in both the critical area and around the point of fracture. This is possibly attributable to the polymer network established within the modified binders. Indeed, it is possible that a continuous polymer network may form throughout the asphalt binder acting to distribute loads to some degree throughout the matrix, thus minimizing local areas of excessive damage. However, eventually a polymer modified mixture will reach its fracture limit, at which localized damage may lead to a macro-crack with any further loading.

CHAPTER 6

Summary and Conclusions

The purpose of this research program was to provide an insight into key mechanisms and asphalt mixture properties that control fracture in asphalt materials. A Digital Image Correlation (DIC) System was developed on purpose for accurately capturing localized or non-uniform stress distributions in asphalt mixtures and as a tool for detecting first fracture.

The DIC system was tested and shown to overcome the shortcomings of traditional on-specimen strain measurement devices, such as strain gauges. The major advantages of the new DIC method may be summarized as follows:

- It achieves satisfactory accuracy compared to strain gauges which is important for the investigation of fracture in HMA.
- It provides full field displacement analysis and full field compressive/tensile/shear strain analysis, thus not requiring the user to attempt to determine the location of crack initiation prior to the test or to mount multiple sensors on the specimen surface.
- It provides point-wise analysis, allowing for the exact determination of the location of crack initiation, and also for the calculation of strain values at the instance of crack initiation.
- It is a non contact measurement tool, thus further minimizing potential errors associated with on-specimen measurements.

The experimental analysis of asphalt mixture cracking behavior was based on the "HMA Fracture Mechanics" visco-elastic crack growth law recently developed at the University of Florida (Zhang et al. 2001; Roque et al.; 2002). Investigation of the asphalt cracking mechanism and identification of fundamental tensile failure limits were achieved performing multiple laboratory test configurations, namely the Superpave Indirect Tensile Test (IDT), the Semi-Circular Bending Test (SCB) and the Three Point Bending Beam Test (3PB). First fracture and crack growth in asphalt mixtures were predicted using a Displacement Discontinuity (DD) boundary element method. Finally, the effect of polymer modification on crack localization, cracking patterns and damage distribution were investigated through the use of horizontal full-field strain maps obtained from the DIC.

6.1 Summary of Findings

The major findings of this study may be summarized as follows :

- Using rigorous interpretation of test conditions and appropriate DIC analysis techniques for identification of first fracture, the same fracture energy density and tensile strength at fracture were obtained from the Superpave Indirect Test (IDT), the Semi-Circular Bending Test (SCB), and the Three Point Bending Beam Test (3PB) for both unmodified and polymer modified mixtures.
- Fracture energy densities resulting from the stress-strain response evaluated around the point of impeding fracture were 20% higher than those evaluated as a mean value along the strain gauge area. Conversely, the corresponding tensile strengths were found to not significantly differ. This means that tensile strains values obtained as average values along a finite area might be not totally representative of localized strains at impeding fracture.
- First fracture was shown to occur prior to peak load for each test configuration, meaning that post-first fracture behavior is at the present not easily interpretable, due to the highly localizing effects of cracks in the specimen.
- Using a Displacement Discontinuity (DD) boundary element method it was possible to successfully predict the stress-strain evolution for the Superpave IDT, SCB and 3PB tests, obtaining calibrated input parameters from the Superpave IDT test results. Indeed the differences between predicted and measured tensile strengths and fracture energy densities at fracture for each mixture in each test were found to be always less than 13.0%.
- The polymer modification at intermediate temperatures does not have significant effect on the resilient modulus, but during tensile creep testing, the rate of creep results lower implying less micro-damage accumulation. Polymer modification has also proven to improve tensile failure limits of mixtures, slightly increasing tensile strength and enhancing both Dissipated Creep Energy to failure and Fracture Energy density. It was

also found that SBS polymer modified mixtures exhibit a higher Energy Ratio than the unmodified one, resulting in a better top-down cracking performance.

- Polymer modified mixtures exhibit high strains only up to the location of impending fracture, while unmodified mixtures exhibit highly distributed damage in both the critical area and around the point of fracture.

6.2 Conclusions

Based on the above findings, the following conclusions were achieved :

- HMA tensile failure limits at first fracture are independent of the specimen geometry and of the test configuration. These limits are also sensitive to both presence and level of polymer modification.
- Significant damage, stress redistribution and other changes following initial fracture make the analysis at peak load difficult to interpret meaningfully. The effect of stress concentration due to the impending fracture would require the introduction of a post-first fracture damage model.
- The Displacement Discontinuity (DD) method can be used to predict fracture initiation and crack propagation for various different boundary condition problems, and not just for the calibrated laboratory test conditions.
- SBS polymer modifiers improve the cracking resistance of asphalt mixtures, by reducing the tensile creep rate and increasing the fracture energy and dissipated creep strain energy thresholds of the modified mixtures over the unmodified mixture.
- It is possible that a continuous polymer network may form throughout the asphalt binder acting to distribute loads to some degree throughout the matrix, thus minimizing local areas of excessive damage. However, eventually a polymer modified mixture will reach its fracture limit, at which localized damage may lead to a macro-crack with any further loading.

APPENDIX A

Standard Superpave IDT

From the evaluation of the SHRP Indirect Tensile Testing System developed by Roque et al. (1997), it was shown that SHRP IDT can provide reasonable and accurate asphalt mixture properties at in-service temperature where cracking is generally presumed to occur. These mixture properties (which include resilient modulus, creep compliance, m-value, failure strain, tensile strength and fracture energy), are directly and/or indirectly related to their cracking response.

The procedures for specimen preparation before testing are as follows:

- The specimens compacted are cut parallel to the top and bottom faces using a water-cooled masonry saw to produce 25/50 mm thick specimens having smooth and parallel faces.
- Four brass gage points are affixed with epoxy to each trimmed smooth face of the specimen.
- Test samples are stored in a humidity chamber at a constant relative humidity of 60 percent for at least 2 days. Specimens are then cooled at the test temperature for at least 3hours before testing.
- Extensometers are mounted and centered on the specimen to the gage points for the measurement of the horizontal and vertical deformations.

A.1 Resilient Modulus

The Resilient Modulus is defined as the ratio of the applied stress to the recoverable strain when repeated loads are applied. The Resilient Modulus test is performed in load control mode by applying a repeated haversine waveform load to the specimen for a 0.1 second followed by a rest period of 0.9 seconds. The load is selected to keep the horizontal strain in the linear viscoelastic range, in which horizontal strain is typically 150 to 350 micro-strain.

A constant pre-loading of approximately 45 N is applied to the test specimen to ensure proper contact with the loading heads before test loads are applied. If the horizontal strains are higher than 350 micron-strains, the load is immediately removed from the specimen, and specimen is allowed to recover for a minimum 3 minutes before reloading at different loading level.

When the applied load is determined, data acquisition program begins recording data. Data are acquired at a rate of 150 points per seconds.

The Resilent Modulus and Poisson's Ratio are calculated by the following equations, which were developed based on three dimensional finite element analysis conducted by Roque and Buttlar (1992). The equations are involved in the Superpave Indirect Tensile Test at Low Temperatures (ITLT) program, which was developed by Roque et al. (1997):

$$M_R = \frac{P \cdot GL}{\Delta H \cdot t \cdot D \cdot C_{cmpl}} \tag{A.1}$$

$$\nu = -0.1 + 1.480 \cdot (X/Y)^2 - 0.778 \cdot (t/D)^2 \cdot (X/Y)^2 \tag{A.2}$$

where:

M_R = Resilient Modulus

P = maximum load

GL = gauge length

ΔH = horizontal deformation

t, D = thickness, diameter

$C_{cmpl} = 0.6354 \text{ x } (X/Y)^{-1} - 0.323$

ν = Poisson's Ratio

(X/Y) = ratio of horizontal to vertical deformation

A.2 Creep Test

Creep Compliance is a function of time-dependent strain over stress. The creep compliance curve was originally developed to predict thermally induced stress in asphalt pavement. However, since it represents the time-dependent behavior of asphalt mixture, it can be used to evaluate the rate of damage accumulation of asphalt mixture.

From Creep Compliance test, three different parameters, shown in Figure A.1, can be calculated: D_0, D_1, and m-value.

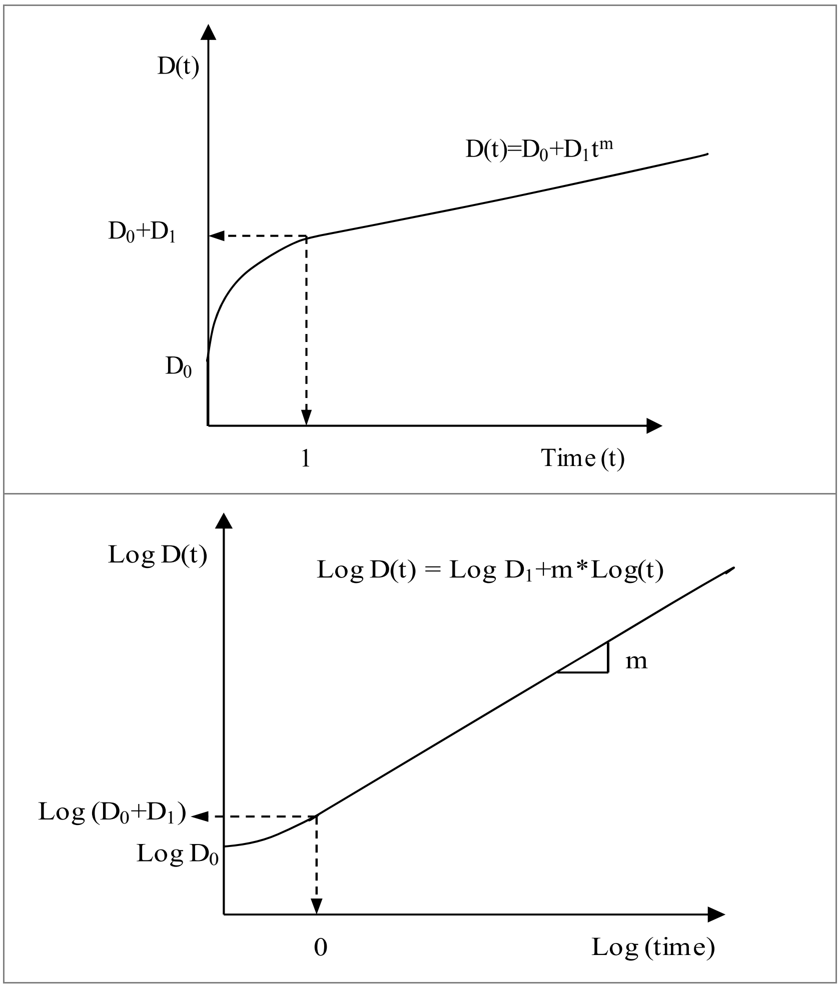

Figure A.1 Power model of the creep compliance

Although D_1 and m-value are related to each other, D_1 is more related to the initial portion of the creep compliance curve, while m-value is more related to the longer-term portion of the creep compliance curve.

The m-value has been known to be related to the rate of damage accumulation and the fracture resistance of asphalt mixtures. In other words, the lower the m-value, the lower the lower the rate of damage accumulation. However, mixtures with higher m-value typically have higher DCSE limits.

The creep compliance is a time dependant strain ε(t) divided by the applied stress σ(t). According to the analysis conducted by Roque et al. (1997), M_R is higher than creep compliance stiffness at 1 second.

The test is conducted in a load control mode by applying a static load selected to keep the horizontal strain in the linear viscoelastic range, which is below an horizontal strain of 500 micro-strain. The load is then held for 1000 seconds. If the horizontal strains are not between 150 and 200 micro-strain at 30 seconds, the load is immediately removed from the specimen, and specimen is allowed to recover for a minimum 3 minutes before reloading at a different level.

When the applied load is determined, the data acquisition program records the loads and deflections at a rate of 10 Hz for the first 10 seconds, 1 Hz for the next 290 seconds, and 0.2 Hz for the remaining 700 seconds of the creep test.

Creep compliance is computed by the following equation:

$$D(t) = \frac{\Delta H \cdot t \cdot D \cdot C_{cmpl}}{P \cdot GL} \qquad [A.3]$$

where

D(t) = creep compliance at time t,

P = maximum load

GL = gauge length

ΔH = horizontal deformation

t, D = thickness, diameter

$C_{cmpl} = 0.6354 \text{ x } (X/Y)^{-1}-0.323$

ν = Poisson's Ratio

(X/Y) = ratio of horizontal to vertical deformation

A.3 Strength Test

The strength test is conducted in a displacement control mode by applying a constant rate of displacement of 50mm/min until the specimen fails. The horizontal and vertical deformation, and the applied load are recorded at the rate of 20Hz during the test.

The maximum tensile strength is calculated as the following equation:

$$S_t = \frac{2P \cdot C_{sx}}{\pi \cdot t \cdot D} \quad [A.4]$$

where:

S_t = maximum indirect tensile strength

P = failure load at first fracture

C_{sx} = 0.984-0.01114 x (t/d) – 0.2693 x ν + 1.436 x (t/D) x ν

t, D = thickness, diameter

ν = Poisson's Ration

From the strength test and the resilient modulus test, fracture energy and dissipated creep strain energy can be determine. Fracture energy is a total energy applied to the specimen until the specimen fractures. Dissipated creep strain energy (DCSE) is the absorbed energy that damages the specimen, and dissipated creep strain energy to failure ($DCSE_f$) is the absorbed energy to fracture.

The fracture point in the IDT specimen is determined by plotting the deformation differential ($V_{corrected}$ - $H_{corrected}$) during the numerical simulation, and visually observing the point at which the deformation differential starts to deviate from a smooth curve.

As shown in Figure A.2, fracture energy and $DCSE_f$ can be determined as follows:

$$M_R = \frac{S_t}{\varepsilon_f - \varepsilon_0} \Rightarrow \varepsilon_0 = \frac{M_R \varepsilon_f - S_t}{M_R} \quad [A.5]$$

$$ElasticEnergy(EE) = \frac{1}{2} S_t (\varepsilon_f - \varepsilon_0) \quad [A.6]$$

$$FractureEnergy(FE) = \int_0^{\varepsilon_f} S(\varepsilon) d\varepsilon \quad [A.7]$$

$$DissipatedCreepStrainEnergy(DCSE_f) = FE - EE \quad [A.8]$$

where S_t = tensile strength, ε_f = failure strain.

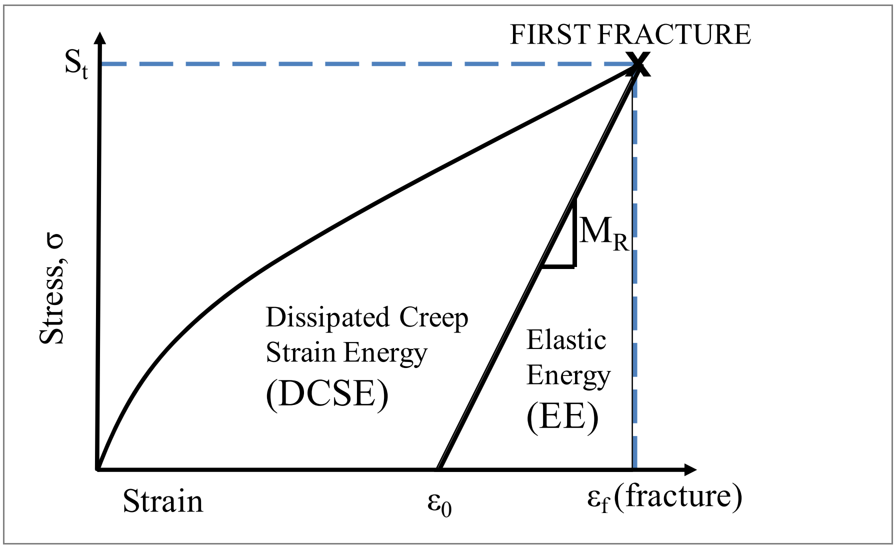

Figure A.2 Determination of Fracture Energy and Dissipated Creep Strain Energy to failure.

APPENDIX B

DD PRE/POST Processor

DD method is a graphic user interface which operates under window environment. It can read and write codes to the files associated with DIGS (Discontinuity Interaction and Growth Simulation) and DVT (Delaunay Voronoi Tessellation Generator). Three file types (*.IN,* ._SG and *.DAT) are involved with PRE processor and other three file types (*.OUT, *.REQ and *.RPT) are involved with POST processor.

DIGS is a two-dimensional (plane strain) stress analysis computer code that can be used to solve crack, fault and tabular stope interaction and intersection problems. The code is based on the displacement discontinuity boundary element method and employs linear-variation shape functions in the element. DVT is a mesh generator for Delaunay and Voronoi tessellation. The result of meshing can be used to simulate granular structure of the desired material.

Input file (*.IN) contains information of meshing parameters and boundary definition of the regions to be meshed. The IN file is used with the DVT to generate two segment files (*._SG): Delaunay (*.DSG) and Voronoi with internal fracture path (*.VSG). Segment file contains definitions of 'Line' segments that describe geometry of the problem to be solved. User can use PRE processor to open these two segment files, edit segment definitions and save them to other segment file names (*._SG) for later use.

Data file (*.DAT) contains essential information (background material properties, primitive stress fields, boundary conditions, load step, segment file name and request output report) to run boundary element analysis with DIGS.

Output file (*.OUT) contains the results from boundary element analysis. POST processor can open this file to view the result graphically. Users can also request specific output variables at desired load steps by writing command codes in the request file (*.REQ) and reporting them to the report file (*.RPT).

B.1 Coordinate Systems

The DDM assumes that all discontinuity positions are defined with respect to a global Y-Z coordinate system as depicted in Figure B.1. The X-axis is assumed to point into the plane of the diagram and all displacements in the X-direction are assumed to be zero (i.e. plane strain with respect to the Y-Z plane).

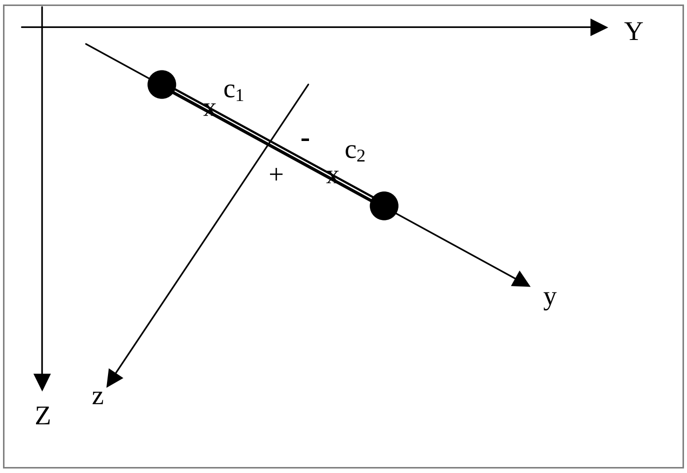

Figure B.1 Global (Y-Z) and local (y-z) coordinate systems used by DD

Each defined element is flat and has a local y-z coordinate system as shown in Figure B.1. The ends of the element are marked "o" and discontinuity values are computed at two collocation points (c_1 and c_2) within the element, marked "x". The local element axis system implies an orientation of the element with the positive (+) side in the positive z direction and the negative (-) side in the opposite direction. No continuity conditions on the discontinuity slip or opening values are enforced between adjoining elements. It is important that elements should not be defined to intersect one another but may be defined to be connected at their end points.

B.2 Text Files Associated with PRE/POST Processor

There are total 6 files (*.IN, *._SG, *.DAT, *.OUT, *.REQ and *.RPT) associated with PRE/POST Processor.

The IN file is an input text file containing computer codes for the program DVT to generate two tessellations: Delaunay and Voronoi with internal fracture path. The computer codes are written in fixed field format. That mean users have to write the codes within a specific range of columns. The structure of IN file consists of 3 coding blocks as following.

- Random point generation
- Seed triangle for creating tessellation
- Boundary definitions

The segment file is a text file containing definition of segments that describe geometry of the problem. The DVT uses the IN file to generate two segment files named Dealuanay tessellation file (*.DSG) and Voronoi with internal fracture path tessellation file (*.VSG). The computer codes of these two files are written in fixed field format. The structure of the segment file consists of several lines of segment definitions.

The DAT file is a text file that contains command codes describing background material, primitive stress fields, boundary conditions, material constitutive models, load steps and output reports. The codes are written in fixed field format. The structure of the DAT file consists of 4 coding blocks:

- General parameters for background material and primitive stress fields
- Boundary conditions
- Material constitutive models for potential crack segments
- Processing steps (or load step):

  Processing step element report requests.

  Processing step field point report requests

The OUT file contains the results obtained from DD. The OUT file first echoes the information in the DAT file and subsequently reports the requested output variables at elements and field points for each load step. The output variable names will be explained in three subsets:

- Output variables at element (requested with command code ‘RX’ or ‘RA’)
- Output variable at field point in cartesian coordinates (requested with command code ‘RC’)
- Output variables at field point in principal coordinates (requested with command code ‘RG’)

The REQ file is a text file containing request command codes to report output variables at each load step to the report file (*.RPT). The request command codes are written in free field format; separate each field with comma ",". The structure of REQ file consists of any of these coding blocks (not in particular order):

- Request output variables at elements
- Request output variables at field points (Cartesian coordinate 'RC')
- Request output variables at field points (Principal coordinate 'RG')

The RPT file is a result of using the request file (*.REQ) to request the output variables stored in the POST processor. The requested output variables are written in fixed field format, convenient to be opened with Spreadsheet program such as Excel.

B.3 Pre Processor Files for the Three Specimen Models

B.3.1 Input File (.IN)*

Figures B.2, B.3 and B.4 shows the input file for obtaining IDT, SCB and 3PB specimen models respectively.

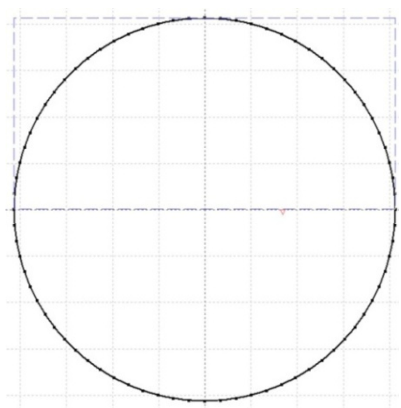

IDT.IN

```
RMG    1000      1    4.00  -76.00  -76.00    76.00   76.00  10.00
S     30.00    0.00   32.0    0.00   31.00     2.0
R/
BCB     76    7.00    0.00    0.00    76.0    0.00
B/
*** use DVT.exe to generate tessellation
*** None = 0,  Delaunay = 1,  Voronoi = 2
```

B.2 IDT.IN pre processor file

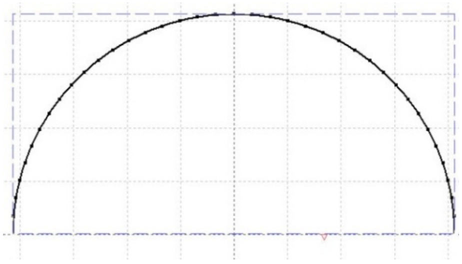

SCB.IN

```
RMG   7000   1     4   -76    -76   76    0    10
S     30   0     40     0     35    10
R/

BLB    26    5   -76      0     76    0
BCB    76    6     0      0      0   76
B/
*** use DVT.exe to generate tessellation
*** None = 0,  Delaunay = 1,  Voronoi = 2
```

B.3 SCB.IN pre processor file

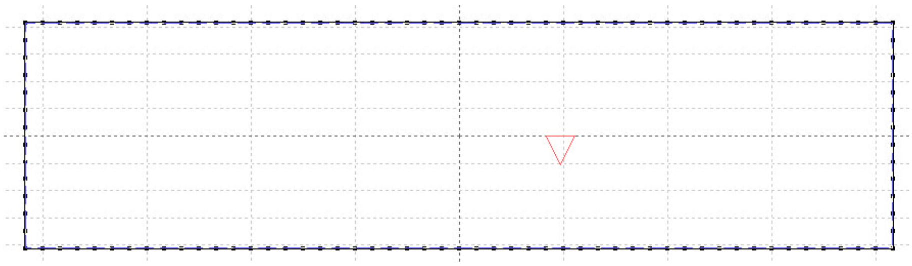

3PB.IN

```
RMG   7000   1     5   -150    -39   150    39    10
S     30   0     40     0     35    10
R/
BLB    50    5   -150    -39    150   -39
BLB    50    5   -150     39    150    39
BLB    13    5   -150    -39   -150    39
BLB    13    5    150    -39    150    39
B/
*** use DVT.exe to generate tessellation
*** None = 0,  Delaunay = 1,  Voronoi = 2
```

B.4 3PB.IN pre processor file

Random Point Generation is defined in the first line “RMG” where the nominal number of points to be generated, the minimum point spacing constraint, the starting and ending (x,y) coordinates for random points to be generated are listed. Second line defines the seed triangle for construction of tessellation. The triangle will be used as a starter to form Delaunay tessellation and construct its dual mesh Voronoi.

The codes “BLB” and “BCB” defines the boundary conditions. BLB is used to create a line, while BCB is used to create a circle. This line defines the number of elements along the boundary line, the minimum distance a point is allowed from the boundary, starting and ending coordinates of the lines or of center of the circumference.

B.3.2 Segment File (.VSG)*

The segment file is a text file containing definition of segments that describe geometry of the problem. The structure of the segment file consists of several lines of segment which define the segment type code (S for ordinary boundary segment, ? for potential crack element), the segment number, the number of elements per segment and the starting and ending coordinates for a line segment. A letter code refers to boundary condition code for ordinary boundary segment or material constitutive code for potential crack segment (i.e: 1,2,3,4,5,6,7,8, B, M, V).

Figure B.5 shows the result of using DVT with IDT.IN to generate Voronoi with internal fracture path tessellations and the code written in the segment file. The segment file can then be attached to the .DAT file to run the boundary element analysis.

```
S1   1   1 -12.542 -75.161  -9.417 -75.550    0.0    0.0     W  T T
S2   2   1  -9.417 -75.550  -6.293 -75.940    0.0    0.0     W  T T
S3   3   1  -6.293 -75.940  -3.146 -76.070    0.0    0.0     W  T T
                              .
                              .
                              .
SB   9   1  12.542  75.161   9.417  75.550    0.0    0.0     W  T T
SB  10   1   9.417  75.550   6.293  75.940    0.0    0.0     W  T T
SB  11   1   6.293  75.940   3.146  76.070    0.0    0.0     W  T T
                              .
                              .
                              .
SA  18   1  15.624 -74.515  18.706 -73.868    0.0    0.0     W  T T
SA  19   1  18.706 -73.868  21.724 -72.970    0.0    0.0     W  T T
SA  20   1  21.724 -72.970  24.742 -72.071    0.0    0.0     W  T T
                              .
                              .
                              .
?M 153   1 -20.550   1.500 -20.550  -1.500    0.0    0.0     W  T T
?M 154   1 -17.550   1.500 -17.550  -1.500    0.0    0.0     W  T T
?M 155   1 -20.550   1.500 -17.550   1.500    0.0    0.0     W  T T
                              .
                              .
                              .
?V1979   1   0.000 -22.050   1.500 -20.550    0.0    0.0     W  T T
?V1980   1   1.500 -20.550   3.000 -19.050    0.0    0.0     W  T T
?V1981   1   3.000 -19.050   1.500 -17.550    0.0    0.0     W  T T
                              .
                              .
                              .
```

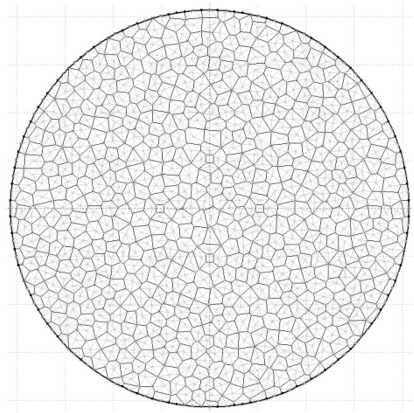

Figure B.5 IDT.VSG pre processor file

B.3.3 Data File (.DAT)*

The structure of the DAT file consists of 4 coding blocks. The first block contains general parameters for background material (Young Modulus, Poisson’s Ratio) and primitive stress fields (constant yy, yz, zz component of the primitive stress field). The second block defines the boundary conditions (shear “S” and normal “N”), where “T” is a local normal traction component specification, “D” is a local nominal discontinuity component specification, “+” is a local z displacement component specification on the “+” side of the element, “-“ is a local z displacement component specification on the “-“ side of the element. Following are the numerical value of selected normal boundary condition at collocation points 1 and 2.

The third block contains the material constitutive model for potential crack segments:

- C_0 = Initial intact cohesion (MPa);
- ϕ_o = Initial fiction angle (Degree)
- $\psi_{o\,=}$ Initial sliding dilation angle, (Degree)
- C_R = Residual cohesion, (MPa)
- ϕ_R = Residual friction angle, (Degree)
- ψ_R = Reverse dilation angle relative to initial sliding direction, (Degree)
- T_o = Tension cut off, (MPa)
- D_{NCR} = Opening crack limit over which tensile strength is lost, (This defines implicitly the tension softening slope, $T_{soft} = T_o/D_{NCR}$, with respect to the opening crack limit.
- C_{soft} = Cohesion softening slope, (MPa / mm)
- T_{soft} = Tension softening slope, (MPa / mm).
- Parameter LAMDA: it is an exponent in tension weakening law controlling residual tensile strength as a function of crack opening. LAMDA = 1 for linear tension weakening (default)
- Viscoelastic parameter 1, VP1 (mm/(s.MPa)). It is proportionality constant in relaxation creep law or may be ignored if creep not being simulated.
- Viscoelastic parameter 2, VP2. It is an exponent in creep law or ignored if creep not simulated.

The last block defines the processing steps or load steps. The first line contains the step identification name, the maximum number of crack growth search increments per time step interval, the stress tolerance for solution iteration, the maximum number of iterations allowed in each solution cycle. Following is the processing step element report request (defining which elements are to be reported) and the processing step field point report request which indicates the type of system used to report stress components (Cartesian coordinates or principal directions), the number of filed points in both Y and Z directions, the origin field point coordinates, the angle of a line of field points, the incremental distance between field points in both Y and Z directions. Figures B.6 shows the boundary conditions for IDT, SCB and 3PB respectively, while Figure B.7 shows one of the .DAT file used for simulating the IDT test.

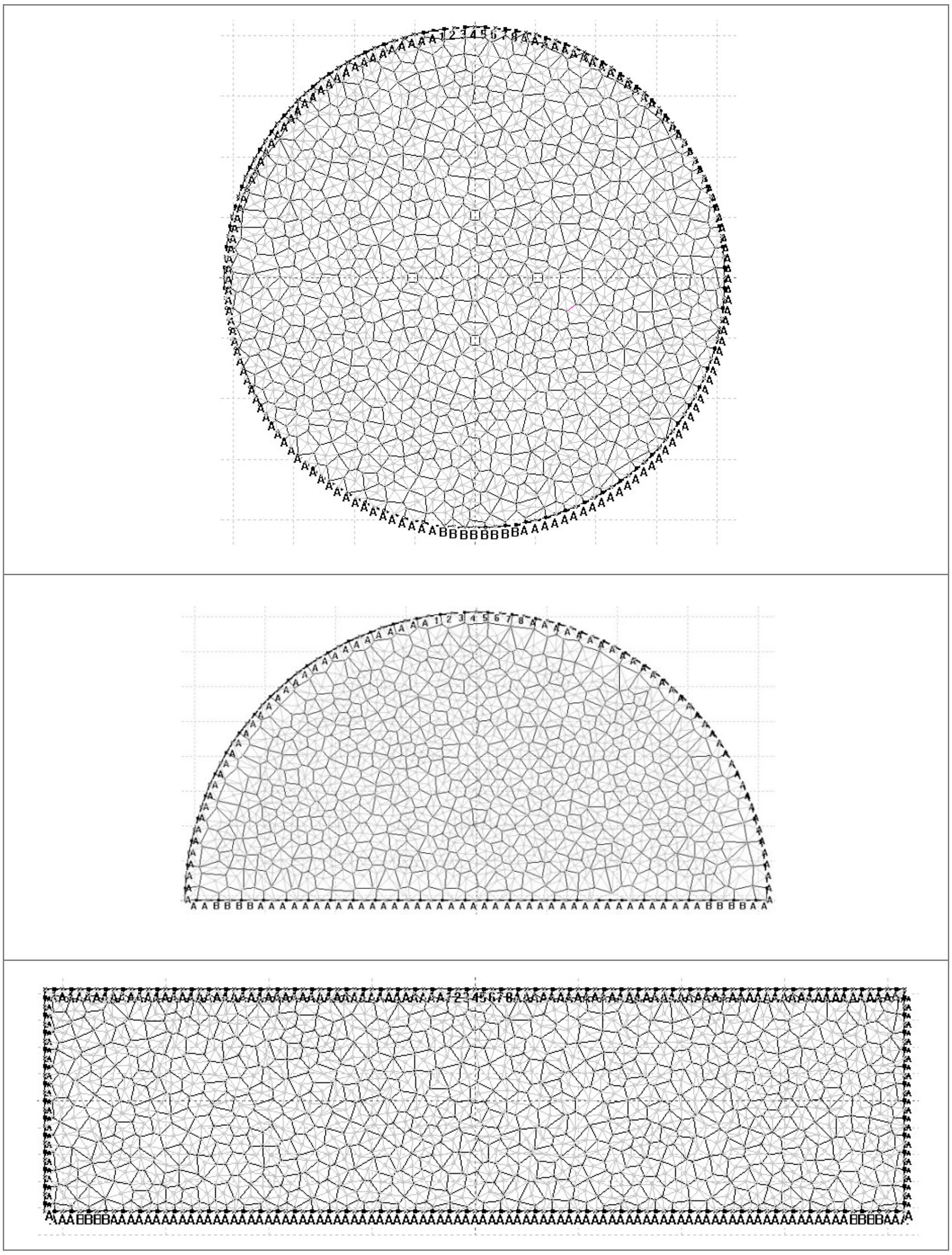

Figure B.6 Boundary conditions for IDT, SCB and 3PB models

```
**...GENERAL PARAMETERS
**    YM    PR    GY    GZ    CYY    CYZ    CZZ    CPP    PPGR
PR   6200  0.350   0.0  0.000    0.0    0.0    0.0    0.0    0.0
**
CBCS+      0.0      0.0N+      0.0      0.0
CACST      0.0      0.0NT      0.0      0.0
V1CS+-0.0006240-0.0006240N+ 0.0049609 0.0049609
V2CS+-0.0006258-0.0006258N+ 0.0049607 0.0049607
V3CS+-0.0002066-0.0002066N+ 0.0049957 0.0049957
V4CS+-0.0002067-0.0002067N+ 0.0049957 0.0049957
V5CS+ 0.0002067 0.0002067N+ 0.0049957 0.0049957
V6CS+ 0.0002066 0.0002066N+ 0.0049957 0.0049957
V7CS+ 0.0006258 0.0006258N+ 0.0049607 0.0049607
V8CS+ 0.0006240 0.0006240N+ 0.0049609 0.0049609
**
**  WID  COH  FRN  DIL  FCOH  FFRN  RDIL  TCUT  DNCR CSOFT TSOFT#  LAMDA    VP1    VP2
CM   0.0  2.20  44.0   0.0  0.11  38.0   0.0  2.20  0.12  1.00 10.00     1.0 0.00000    1.0
CV   0.0  6.40  40.0   0.0  0.12  36.0   0.0  6.40  0.09  1.00 10.00     1.0 0.00000    1.0 0.00000    1.0
**
**STEP MSKIP MXINC MXSTP TSTEP  TTOL  DTOL MAXIT   SOR C S
!PLD00   10   300    1  6.00 0.005   0.0   250   0.4 B #   SAMPLE.
I PIDT.FSG
RX
RS
RG   1  51    0.00  -75.00    0.0    0.0    3.00
RG  51   1  -75.00    0.00    0.0    3.0    0.00
RG   1   2    0.00  -19.05    0.0    0.0   38.10
RG   2   1  -19.05    0.00    0.0   38.10    0.00
**
!PL010   10   300    1  6.00 0.005   0.0   250   0.4 B #   SAMPLE.
AM
RA
RG   1  51    0.00  -75.00    0.0    0.0    3.00
RG  51   1  -75.00    0.00    0.0    3.0    0.00
RG   1   2    0.00  -19.05    0.0    0.0   38.10
RG   2   1  -19.05    0.00    0.0   38.10    0.00
```

Figure B.7 .DAT file used for simulating the IDT test

B.3.4 Output File (*.OUT)

The OUT file contains the analysis result obtained from DIGS. The OUT file first echoes the information in the DAT file and subsequently reports the requested output variables at elements and field points for each load step.

- Output variables at element: angle measured from Y-axis to Z-axis; local tangential stress yy components on both positive and negative sides; local shear stress yz and zz components; local normal stress zz component; cohesion strength; sliding crack displacement; opening crack displacement; local displacement in both y and z directions.
- Output variables at field point (req.1): major and minor principal stresses; major angle measured from Y-axis to Z-axis; global displacements in both Y and Z directions; distance to a Mohr-Coulomb envelope; strain energy density.
- Output variables at field point (req.2): normal stress YY component in global Cartesian coordinates; shear stress YZ component in global Cartesian coordinates; normal stress ZZ component in global Cartesian coordinates; displacements in both Y and Z directions in global Cartesian coordinates.

REFERENCES

Abdalla H.M. & B.L. Karihaloo. "Determination of size-independent specific fracture energy of concrete from three-point bend and wedge splitting tests". *Magazine of Concrete Research*, Vol.55, pp. 133-141, 2003.

Abdulshafi A.A. & K. Majidzadeh. "J-Integral and Cyclic Plasticity Approach to Fatigue and Fracture of Asphaltic Mixtures". *Transportation Research Record.* 1034, pp. 112-123, 1985.

Ackermann F. "Digital image correlation: performance and potential application in photogrammetry". *Photogrammetric record.* Vol. 11(64), pp. 429-439, 1984.

Aglan A. Hesmat. "Polymer Modifiers for Improved Performance of Asphaltic Mixtures". *Asphalt Science and Technology*. Arthur Usmani, 1997.

Airey G.D. "Styrene Butadiene Styrene Polymer Modification of Road Bitumens". *Journal of Materials Science.* Vol. 39, pp. 951-959, 2004.

Anderson T.L. "Fracture Mechanics – Fundamental and Applications – 2nd ed". *CRC Press, 688 pp,* 1995.

ASTM E399-90. "Standard Test Method for Plane-Strain Fracture Toughness of Metallic Materials". *Annual Book of ASTM Standards.* Vol. 03.01, pp. 443-473, 2002.

ASTM E1820-01. "Standard Test Method for Measurement of Fracture Toughness". *Annual Book of ASTM Standards.* Vol. 03.01, pp. 1031-1076, 2002.

Bahia H.U., D.I. Hanson, M. Zeng, H. Zhia, M.A. Khatri and R.M. Anderson. "Characterization of Modified Asphalt Binders in Superpave Mix Design". *NCHRP Report 459*, 2001.

Bazant, Z. P. Mechanics of Distributed Cracking. *Applied Mechanics Review*, Vol. 39, No. 5, pp. 675-705, 1986.

Barenblatt G.I. "The Mathematical Theory of Equilibrium Cracks in Brittle Fracture". *Advances in Applied Mechanics.* Vol. VII, pp. 55-129, 1962.

Birgisson B, C. Soranakom, J.A.L. Napier and R. Roque. "Microstructure and Fracture in Asphalt Mixtures Using a Boundary Element Approach". *ASCE Journal of Civil Engineering Materials*, New York, 2002

Birgisson B., C. Soranakom, J.A.L. Napier and R. Roque. "Simulation of Fracture Initiation in Hot Mix Asphalt Mixtures". *Transportation Research Record 1849, TRB, National Research Council.* Washington, DC, pp.183-190 , 2003.

Bruck H.A., S.R. McNeill, M.A. Sutton and W.H.I. Peters. "Digital Image Correlation Using Newton-Raphson Method for a Partial Differential Correction". *Experimental Mechanics.* Vol. 28(3), pp. 261-267, 1989.

Buttlar W.G. & R. Roque, "Development and Evaluation of the Strategic Highway Research Program Measurement and Analysis System for Indirect Tensile Test at Low Temperatures". *Transportation Research Record 1454, TRB, National Research Council.* Washington, DC, pp.163-171, 1994.

Carpinteri A. & G. Ferro. “Size effects on tensile fracture properties: a unified explanation based on disorder and fractality of concrete microstructure”. *Materials and Structures.* Vol. 28, pp. 563–571, 1994.

Carpinteri A. & G. Ferro. “Scaling behavior and dual renormalization of experimental tensile softening responses”. *Materials and Structures.* Vol. 31, pp. 303–309, 1998.

Carpinteri A., B. Chiaia, S. Invernizzi. “Numerical Analysis of Identation Fracture in Quasi-Brittle Materials”. *Engineering Fracture Mechanics.* Vol. 71(4-6), pp. 567-577, 2003.

Chehab G.R., Y. Seo, Y.R. Kim. “Viscoelastoplastic Damage Characterization of Asphalt-Aggregate Mixtures using Digital Image Correlation”. *International Journal of Geomechanics*. Vol. 7, No. 2, pp. 111-118 , 2007.

Choi S. and S.P. Shah. “Measurement of Deformations on Concrete Subjected to Compression using Image Correlation”. *Experimental Mechanics.* Vol. 37(3), pp.307-313, 1997.

Chu T.C., W.F. Ranson, W.H. Peters and M.A. Sutton. “Applications of Digital-Image-Correlation Techniques to Experimental Mechanics”. *Experimental Mechanics.* Vol. 25(3), pp. 232-245, 1985

Collop A. & D. Cebon. “A Theoretical Analysis of Fatigue Cracking in Flexible Pavements”. *Proceedings of the Institution of Mechanical Engineers.* Vol. 209, pp. 345-361, 1995.

Crawford A.M. & J.H. Curran”. Higher-Order Functional Variation Displacement Discontinuity Elements”. *International Journal of Rock Mechanics and Mining Sciences*. Vol.19, pp.143-148, 1982

Crippa B, G. Forlani and A. de Haan. “Automatic deformation measurement from digital images”. *Optical 3-D Measurement Techniques II*, Gruen/Kahmen (Ed's), Wichman Verlag, Karlsruhe, pp.557-563, 1993.

Crouch S.L. and A.M. Starfield. *Boundary Element Methods in Solid Mechanics*, George Allen & Unwin, London, U.K, 1983

Deacon J.A., A. Tayebali, Harvey J.T. and C.M. Monismith. “Influence of Binder Loss Modulus on the Fatigue Performance of Asphalt Concrete Pavements”. *Journal of the Association of Asphalt Paving Technologists.* Vol.66, pp.633, 1997.

Dugdale D.S. “Yielding of Steel Sheets Containing Slits”. *Journal of the Mechanics and Physics of Solids.* Vol. 8, pp. 100-108, 1960.

Elber W. “Fatigue Crack Closure Under Cyclic Tension”. *Engineering Fracture Mechanics.* Vol. 2, pp. 37-45, 1970.

Elices M., G.V. Guinea, J. Planas “Measurement of the fracture energy using the three point bend test: Part 3 – Influence of cutting the P-δ tail”. *Materials and Structures.* Vol. 25, pp. 327-334, 1992.

Ewalds H.L. & R.J. Wanhill. “Fracture Mechanics-Delft”. *Delftse U.M., London,* 1986.

Foreman R.G., V.E. Keary & R.M. Engle. “Numerical Analysis of Crack Propagation in Cyclic-Loaded Structures”. *Journal of Basic Engineering.* Vol. 9, pp. 459-464, 1967.

Forstner W. “On the geometric precision of digital image correlation”. *IAPRS.* Vol. 24 (3), pp. 176-189, 1982.

Freeman R.B., J.K. Newman and R.A. Ahlrich. "Effect of Polymer Modifiers on Dense-Graded, Heavy-Duty Mixtures". *Eighth International Conference on Asphalt Pavements*. Seattle, Washington, 1997.

Grédiac M. "The use of full-field measurement methods in composite material characterization: interest and limitations. Composites, Part A". *Applied Science and Manufacturing.* Vol. 35, pp.751-761, 2004.

Griffith A.A. "The Phenomena of Rupture and Flow in Solids". *Philosophical Transaction, Series A.* Vol. 221, pp.163-198, 1920.

Gruen A.W. "Adaptive Least Squares Correlation: a Powerful Image Matching Technique". *South African Journal of Photogrammetry, Remote Sensing and Cartography.* Vol. 14, No. 3, pp. 175-187, 1985.

Harvey J.T., J.A. Deacon, B. Tsai and C.L. Monismith. "A Fatigue Performance of Asphalt Concrete Mixes and its Relationship to Asphalt Concrete Pavement Performance in California". *California Department of Transportation.* Report No. RTA-65W485-2, 1995.

Harvey J.T., J.A. Deacon, A.A. Tayebali, R.B. Leahy and C.L. Monismith. "A Reliability-Based Mix Design and Analysis System for Mitigating Fatigue Distress". *Eighth International Conference on Asphalt Pavements*. Seattle, Washington, 1997.

Helms K.L.E., D.H. Allen and L.D. Hurtado. "A Model for Predicting Grain Boundary Cracking in Polycrystalline Viscoplastic Material Including Scale Effects". *International Journal of Fracture,* Vol. 95, pp. 175-194, 1999.

Hillerborg A., M. Modeer & P.E. Petersson. "Analysis of crack formation and crack growth in concrete by means of fracture mechanics and finite elements". *Cement Concrete.* Res 6, pp. 773–782, 1976.

Hillerborg A., "Results of Three Comparative Test Series for Determining the Fracture Energy G_F of Concrete". *Materials and Structures.* Vol.18, No. 107, pp. 407-413, 1985.

Hossain M., S. Swartz, E. Hoque. "Fracture and Tensile Characteristics of Asphalt-Rubber Concrete". *Journal of Materials in Civil Engineering.* Vol. 11, issue 4, pp. 287-294, 1999.

Hu X.Z. and F.H. Wittmann. "Fracture Energy and Fracture Process Zone". *Materials and Structres*. Vol. 25, pp. 319-326, 1992.

Isacsson U., & X. Lu. "Testing and appraisal of polymer modified road bitumens—state of the art". *Materials & Structures.* Nol. 28, No. 3, pp.139-159, 1995

Jacobs M.M.J. "Crack Growth in Asphaltic Mixes". *Ph.D. Dissertation.* Delft Universiy of Technology, Road and Railroad Research Laboratory, 1995.

Jacobs M.M.J. "P.C. Hopman & A.A.A. Molenaar. "Application of Fracture Mechanics Principles to Analyze Cracking in Asphalt Concrete". *Journal of the Association of Asphalt Paving Technologists.* Vol.65, pp. 1-39, 1996.

Jenq Y.S. & J.D. Perng. "Analysis of Crack Propagation in Asphalt Concrete Using a Cohesive Crack Model". *Transportation Research Record.* No. 1317, pp. 90-99, 1991.

Kaloush K.E., W.M. Witczak, G.B Way. "Performance Evaluation of Arizona Asphalt Rubber Mixtures using Advanced Dynamic Material Characterization Tests". *Final Report Submitted to Alberta Transportation.* Edmonton, Alberta, June 2003.

Khattak M.J. & G.Y. Baladi. "Engineering Properties of Polymer Modified Asphalt Mixture". *Transportation Research Record.* TRB No. 1638, pp.12-22, , 1998.

Khattak M.J., G.Y. Baladi and L.T. Drzal "Low Temperature Binder-Aggregate Adhesion and Mechanistic Characteristics of Polymer Modified Asphalt Mixtures". *Journal of Materials in Civil Engineering.* Vol. 19, issue 5, pp. 411-422, 2007.

Kim Y.R., D.L. Little and F. Benson. "Chemical and Mechanical Evaluation on Healing Mechanism of Asphalt Concrete". *Journal of the Association of Asphalt Paving Technologists.* Vol.59, pp. 240-276, 1990.

Kim Y.R., S.L. Whitmoyer and D.N. Little "Healing in Asphalt Concrete Pavements: is it real?". *Transportation Research Record.* 1454, pp. 89-96, 1994.

Kim Y.R., Y.C. Lee and H.J. Lee "Correspondence Principle for Characterization of Asphalt Concrete". ". *Journal of Materials in Civil Engineering.* Vol. 7, issue 1, pp. 59-68, 1995.

Kim K.W. & El Hussein. "Variation of Fracture Toughness of Asphalt Concrete under Low Temperature". *Construction & Building Materials.* Vol.11, pp. 403-411, 1997.

Kim Y.R., H.J. Lee and D.N. Little. "Fatigue Characterization of Asphalt Concrete using Viscoelasticity and Continuum Damage Theory". *Journal of the Association of Asphalt Paving Technologists.* Vol.66, pp. 520-569, 1997.

Kim Y.R. and Wen H. "Fracture Energy from Indirect Tension Test". *Journal of the Association of Asphalt Paving Technologists.* Vol.71, pp. 779-793, 2002.

Kim B., Roque R., Birgisson B. "Effect of Styrene Butadiene Styrene Modifier on Cracking Resistance of Asphalt Mixture". Transportation Research Record. No. 1829, pp. 8-15, 2003.

King G.N, H.W. King, O. Harders, W. Arand and P. Planche. "Influence of Asphalt Grade and Polymer Concentration on the Low-Temperature Performance of Polymer Modified Asphalt". *Journal of the Association of Asphalt Paving Technologists.* Vol.62, pp. 1-22, 1993.

Klesnil M. & P. Lukas. "Influence of Strength and Stress History on Growth and Stabilization of Fatigue Cracks". *Engineering Fracture Mechanics.* Vol. 4, pp. 77-92, 1972.

Krans R.L., F. Tolman, M.F.C. Van de Ven. "Semi-Circular Bending Test: a Practical Crack Growth Test using Asphalt Concrete Cores". *3rd International RILEM Conference on Reflective Cracking in Pavements.* Maastricht, October 1996.

Kuijpers J.S. & J.A.L. Napier. "Effective Growth Rules for Macrofracture Simulation in Brittle Rock under Compression". *Eurorock '96* (edited by G. Barla), Balkema, Rotterdam, pp. 469-479, 1996.

Lee, H.J. & Y.R. Kim. "Viscoelastic Constitutive Model for Asphalt Concrete under Cyclic Loading." *Journal of Engineering Mechanics*. Vol. 124, No 1, pp. 32-40, 1998a.

Lee, H.J., & Y.R. Kim. "Viscoelastic Continuum Damage Model of Asphalt Concrete with Healing". *Journal of Engineering Mechanics.* Vol. 124, No. 11, pp. 1224-1232, 1998b.

Li X. & M. Marateanu. "Evaluation of the Low Temperature Fracture Resistance of Asphalt Mixtures using the Semi Circular Bend Test". *Journal of the Association of Asphalt Paving Technologists.* Vol.73, pp. 401-426, 2004.

Li X. and M. Marasteanu. "Study of Temperature Cracking in Asphalt Mixtures using Mechanical Testing and Acoustic Emission Methods". *Journal of the Association of Asphalt Paving Technologists.* Vol.76, pp. 427-454, 2007.

Lim I.L., I.W. Johnston, S.K. Choi, J.N. Boland. "Fracture Testing of a Soft Rock with Semi-Circular Specimens under Three Point Bending" Part I and II. *International Journal of Rock Mechanics and Mining Science & Geomechanics Abstracts.* Vol.31, No 3, pp.185, 1994.

Little D.N., J.W. Button, R.M. White, E.K. Ensley, Y. Kim, S.J. Ahmed. "Investigation of Asphalt Additives". Texas Transportation Institute, Report no FHWA/RD-87/001, 1987.

Little D.L., R. Lytton, D. Williams, Y.R. Kim. "Propagation and Healing of Microcracks in Asphalt Concrete and Their Contributions to Fatigue". *Asphalt Science and Technology, Usmani.* pp. 149, 1997.

Lu H. and P.D. Cary. "Deformation measurements by digital image correlation: implementation of a second-order displacement gradient". *Experimental Mechanics* Vol. 40, pp. 393-400, 2000.

Lu X. & U. Isacsson. "Rheological Characterization of Styrene-Butadiene-Styrene Copolymer Modified Bitumens". *Construction and Building Materials.* Vol.11, issue 1, pp. 23-32, 1997.

Lu X., U. Isacsson, J. Ekblad. "Influence of Polymer Modification on Low Temperature Behaviour of Bituminous Binders and Mixtures. *Materials and Structures* Vol. 36, pp.652-656, 2003.

Lundström R. & U. Isacsson. "Linear Viscoelastic and Fatigue Characteristics of Styrene-Butadiene-Styrene Modified Asphalt Mixtures". *Journal of Materials in Civil Engineering.* Vol.16, issue 6, pp. 629-638, 2004.

Majidzadeh K. E.M. Kaufmann, and D.V. Ramsamooj. "Application of Fracture Mechanics in the Analysis of Pavement Fatigue". *Journal of the Association of Asphalt Technologists*. Vol.40, pp.227-246, 1971.

Malan D.F. & J.A.L. Napier. "Computer Modeling of Granular Material Microfracturing". *Tectonophysics.* Vol. 248, pp. 21-37, 1995.

Marasteanu M.O., J.F. Labuz, S. Dai and X. Li. "Determining the Low-Temperature Fracture Toughness of Asphalt Mixtures". *Transportation research Record.* No. 1789, pp. 191-199, 2002.

McEvily A.J. "On Closure in Fatigue Crack Growth". *ASTM STP 982, American Society for Testing and Materials.* Philadelphia, pp. 35-43, 1988.

Melrose P, R. Lopez-Anido, L. Muszynski. "Elastic Properties of Sandwich Composite Panels using 3-D Digital Image Correlation with the Hydromat Test System". *SEM XII International Congress and Exposition on Experimental Mechanics and Applied Mechanics,* Costa Mesa, CA, 2004

Mier J.G.M & M.R.A. van Vliet. "Effect of strain gradients on the size effect of concrete in uniaxial tension". *International Journal of Fracture.* Vol.94, pp. 195–219, 1999.

Mihashi H., H. Takhashi and F.H. Wittmann. "Tension-Softening Curve Measurements for Fracture Toughness Determination in Granite". *Proceedings of the International Workshop on Fracture Toughness and Fracture Energy-Test Methods for Concrete and Rock.* Balkema, Rotterdam, pp.47-55, 1989.

Mobasher B.M., M.S. Mamlouk and H.M. Lin. "Evaluation of Crack Propagation Properties of Asphalt Mixtures". *ASCE Journal of Transportation Engineering.* Vol. 123, No. 5, pp. 405-413, 1997.

Molenaar A.A.A., A. Scarpas, X. Liu and G. Erkens. "Semi-Circular bending Test; Simple but Useful?". *Journal of the Association of Asphalt Technologists*. Vol.71, pp.794-815, 2002.

Mull M.A., K. Stuart, A. Yehia. "Fracture Resistance Characterization of Chemically Modified Crumb Rubber Asphalt Pavement". *Journal of Material Science.* Vol. 37, pp. 557-566, 2002.

Muszynski L, R. Lopez-Anido and S.M. Shaler. "Image Correlation Analysis Applied to Measurement of Shear Strains in Laminated Composites". *SEM XI International Congress on Experimental Mechanics*, Orlando, FL, 2000.

Muszynski L. , F. Wang and S.M. Shaler. "Short Term Creep Tests on Phenol Resorcinol Formaldehyde (PRF) Resin Undergoing Moisture Cement". *Wood and Fiber Science.* Vol. 34 (4), pp. 612-624, 2002.

Myers L. "Development and Propagation of Surface-Initiated Longitudinal Wheel Path Cracks in Flexible Highway Pavements". *Ph.D. Dissertation.* University of Florida, 2000.

Myers L., R. Roque & B. Birgisson. " Propagation Mechanisms for Surface-Initiated Longitudinal Wheel Path Cracks". *Transportation Research Record.* No. 1778, pp. 113-121, 2001.

Napier J.A.L. "Modelling of Fracturing near Deep Level Gold Mine Excavations Using a Displacement Discontinuity Approach". *Proceedings of the Second International Conference on Mechanics of Jointed and Faulted Rock* (Edited by H. P: Rossmanith), Balkema, Rotterdam, pp. 709-715, 1990.

Napier J.A.L and M.W. Hildyard. "Simulation of Fracture Growth Openings in Highly Stressed Brittle Rock". *Journal of the South African Institute of Mining and Metallurgy*. Vol. 92, pp. 159-168, 1992.

Napier J.A.L. & A.P. Peirce. "Simulation of Extensive Fracture Formation and Interaction in Brittle Materials". *Mechanics of Jointed and Faulted Rock;* (edited by H. P. Rossmanith), Balkema, Rotterdam , pp. 63-74, 1995.

Napier J.A.L & D.F. Malan. "A Viscoplastic Discontinuum Model of Time-Dependent Fracture and Seismicity Effect in Brittle Rock". *International Journal of Rock Mechanics and Miming Sciences*. Vol. 34, pp. 1075-1089, 1997.

Napier, J.A.L, A. Daehnke, T. Dede, M. W. Hildyard, J. S. Kuijpers, D. F. Malan, E. J. Sellers, and P. A. Turner. "Quantification of Stope Fracture Zone Behaviour in Deep Level Gold

Mines". *Journal of the South African Institute of Mining an Metallurgy*. Vol. 97, pp. 119-134, 1997.

Newman J.K. "Polymer Modification of Asphalt Mixtures Designed for Military Airfield Pavements; Fatigue Properties according to AASHTO TP-8". *Transportation System 2000 Workshop.* San Antonio, Texas, February 28-March 3, 2000.

Paris P.C. & F. Erdogan. "A Critical Analysis of Crack Propagation Laws". Transactions of the ASME, *Journal of Basic Engineering.* Vol. 85, pp. 528-534, 1963.

Pucci T., A.G. Dumont, H. Di Benedetto. "Thermomechanical and Mechanical Behavior of Asphalt Mixtures at Cold Temperature. Road and Laboratory Investigations". *Road Materials and Pavement Design.* Vol. 5, issue 1, pp. 45-72, 2004.

Ramsamooj D.V. "Fatigue Cracking of Asphalt Pavements". *Journal of Transportation Research Record.* No. 756, pp.43-48, 1980.

Ramssamooj D.V. "Prediction of Fatigue Life of Asphalt Concrete Beams from Fracture Test". *Journal of Testing and Evaluation.* Vol.19, No. 3, pp. 231-239, May 1991.

Ramssamooj D.V. "Fracture of Highway and Airport Pavements". *Journal of Engineering Fracture Mechanics.* Vol. 44, No. 4, pp. 609-626, 1993.

Ranson W.F., M.A. Sutton and W.H.I. Peters. "Holographic and Spackle Interferometry" *SEM Handbook of Experimental Mechanics*, New Jersey: Prentice-Hall, Inc, pp. 388-429, 1987.

Rice J.R. "A Path Independent Integral and the Approximate Analysis of Strain Contration by Notches and Cracks". *Journal of Applied Mechanics.* June, pp. 379-386, 1968.

RILEM Technical Committee 50. " Determination of Fracture Energy of Mortar and Concrete by means of three-point bend tests on notched beams". *Materials and Structures.* Vol. 18, pp. 287-290, 1985.

Romero P., K.D. Stuart and W. Mogawer. "Fatigue Response of Asphalt Mixtures tested by the Federal Highway Administration's Accelerated Load Facility". *Journal of the Association of Asphalt Technologists*. Vol.69, pp.212, 2000.

Roque R. & W.G. Buttlar. "The Development of a Measurement and Analysis System to Accurately Determine Asphalt Concrete Properties Using The Indirect Tensile Mode". *Journal of the Association of asphalt Technologists*. Vol.61, pp.304-332, 1992

Roque R., Z. Zhang and B. Sankar. "Determination of Crack Growth Rate Parameters of Asphalt Mixtures using the Superpave Indirect Tension Test (IDT)". *Journal of the Association of Asphalt Paving Technologists.* Vol.68, pp. 404-433, 1999.

Roque R., B. Birgisson, S. Sangptegnam, Z. Zhang. "Asphalt Fracture Mechanis: A Fundamental Crack Growth Law for Asphalt Mixtures". *Journal of the Association of Asphalt Paving Technologists.* Vol.71, pp. 816-827, 2002.

Roque R., B. Birgisson, C. Drakos, B. Dietrich. "Development and Field Evaluation of Energy-Based Criteria for Top-down Cracking Performance of Hot Mix Asphalt". *Journal of the Association of Asphalt Paving Technologists.* Vol.73, pp.229-260, 2004.

Sargand S.M. & S.S. Kim. "Performance Evaluation of Polymer Modified and Unmodified Superpave mixes". *Second International Symposium on Maintenance and Rehabilitation of* Pavements and Technological Control. Auburn, AL, 2001.

Schapery R.A. "A Theory of Crack Growth in Visco-Elastic Media". Report MM 2764-73-1, Mechanics and Materials Research Center. Texas A&M University, College Station, TX, 1973.

Schapery R.A. "A Theory of Crack Initiation and Growth in Visco-Elastic Media, I: Theoretical Development, II: Approximate Methods of Analysis, III: Analysis of Continuos Growth". International Journal of Fracture. Vol. 11, No. 1, pp. 141-159. Vol. 11, No. 3, pp 369-388 and Vol. 11, No. 4, pp. 549-563, 1975.

Schapery R.A. "A Method for predicting Crack Growth in Non-Homogeneous Visco-Elastic Media". International Journal of Fracture. Vol. 14, No. 3, pp. 293-309, 1978.

Schapery R.A. "Correspondence Principles and a Generalized J-Integral for Large Deformation and Fracture Analysis of Viscoelastic Media". *International Journal of Fracture.* Vol. 25, pp. 195-223, 1984.

Schwarz C.R. & J.J. Kok. Blunder Detection and Data Snooping in LS and Robust Adjustments. *Journal of Surveying Engineering* Vol. 119(4), pp. 127-136, 1993.

Seo Y., Y.R. Kim, R. Schapery, M. Witczac, R. Bonaquist. "A Study of Crack-Tip Deformation and Crack Growth in Asphalt Concrete using Fracture Mechanics". *Journal of the Association of Asphalt Paving Technologists.* Vol.73, pp. 697-730, 2004.

Steen B.V.D., A. Vervoort and J.A.L. Napier. Numerical Modeling of Fracture Initiation and Propagation in Biaxial Tests on Rock Samples. *International Journal of Fracture*, Vol. 108, pp. 165-191, 2001.

Sulaiman S.J, A.F. Stock. "The Use of Fracture Mechanics for the Evaluation of Asphalt Mixes". *Journal of the Association of Asphalt Paving Technologists.* Vol.64, pp. 500-533, 1995.

Sutton M.A., W.J. Wolters, , W.H. Peters, W.F. Ranson, and S. R. McNeil. "Determination of Displacements Using an Improved Digital Correlation Method". *Image and Vision Computing*, Vol. 1, issue 3, pp. 133-139, 1983.

Sutton M.A., M.Q. Cheng, W.H. Peters, Y.J. Chao and S.R. McNeill. "Application of an Optimized Digital Correlation Method to Planar Deformation Analysis". *Image and Vision Computing*. Vol. 4, issue 3, pp. 143-151, 1986.

Sutton M.A., S.R. McNeill, J. Jang and M. Babai. "Effects of Subpixel Image Restoration on Digital Correlation Error". *Journal of Optical Engineering.* Vol. 27(10), pp. 870-877, 1988.

Swartz S.E. & T.M.E. Refai. "Influence of Size Effects on Opening Mode Fracture Paramters for Precracked Concrete Beams in Bending". *Proceedings of the SEM/RILEM International Conference on Fracture of Concrete and Rock.* Huston, 1987.

Van de Ven M.F.C., A. Smit, R. L. Krans. "Possibilities of a Semi-Circular Bending Test". *8^{th} International Conference on Asphalt Pavements.* Seattle, August, 1997.

Van den Heuvel F, Kroon R. "Digital Close-Range Photogrammetry using Artificial Targets". *IAPRS* 29(5), pp. 222-229, 1992

Van der Burg M.W.D. and E. Van der Giessen; *Delanuay-Network Modelling of Creep Failure in Regular Polycrystalline Aggregates by Grain Boundary Cavitations.* Delft University of Technology, LMT Report No. 1004,1993.

Wagoner M.P., W.G. Buttlar and G.H. Paulino. “Development of a Single-Edge Notched Beam Test for the Study of Asphalt Concrete Fracture”. *ASTM Journal of Testing and Evaluations.* Vol. 33, No 6, 2005a.

Wagoner M.P., W.G. Buttlar and G.H. Paulino. “Disk-shaped Compact Tension Test for Asphalt Concrete Fracture”. *Experimental Mechanics.* Vol. 45, No. 3,pp.270-277, 2005b.

Wagoner M.P. and W.G. Buttlar. “Influence of Specimen Size on Fracture Energy of Asphalt Concrete”. *Journal of the Association of Asphalt Paving Technologists.* Vol.76, pp. 391-426, 2007.

Wendling L., E. Xolin, D. Gimenez, P. Reynaud, C. De La Roche, J. Chevalier & G. Fantozzi. “Characterization of Crack Propagation in Bituminous Mixtures”. *5th International RILEM Conference on Cracking Pavements.* Limoges, Fance, RILEM Pubblications, pp. 639-646, 2004.

Weertman J. “Rate of Growth of Fatigue Cracks Calculated from the Theory of Infinitesimal Dislocations Distributed on a Plane”. *International Journal of Fracture Mechanics.* Vol. 2, pp. 460-467, 1966.

Winnie D.H. & B.M. Wundt. “Application of the Giffith-Irwin Theory of Crack Propagation to the Bursting Behavior of Disc, Including Analytical and Experimental Studies”. *Transaction ASME.* Vol. 80, pp. 1643-1655, 1958.

Wittmann F.H. “Fracture Toughness and Fracture Energy of Concrete”. *Proceedings of the International Conference on Fracture Mechanics of Concrete.* Lausanne, Switzerland, 1986.

Wittmann F.H., H. Mihashi, N. Nomura. “Size effect on fracture energy of concrete”. *Engineering Fracture Mechanics.* Vol.35, pp. 107-115, 1990.

Wnuk M.P. “Subcritical Growth of Fracture”. *International Journal of Fracture Mechanic.* Vol. 7, pp. 383-486, 1971.

Xu S. & G. Zhao. “Fracture Energy of Concrete and its Variational Trend in Size Effect studied by using Three Point Bending Beams”. *Journal of Dalian University of Technology.* Vol.31, No. 1, pp. 79-86, 1991.

Zhang Z., R. Roque, B. Birgisson & B. Sangpetgnam. “Identification and Verification of a Suitable Crack Growth Law”. *Journal of the Association of Asphalt Paving Technologists.* Vol.70, pp. 206-241, 2001.